ProQuest LLC.
789 East Eisenhower Parkway
P.O. Box 1346
Ann Arbor, MI 48106 – 1346

CORROSION AND PASSIVATION OF MOLYBDENUM-BEARING ALLOYS

by

Xiaofan Yang

Department of Materials Science and Engineering
University of Surrey
Guildford Surrey
U.K.

A Thesis Submitted to the University of Surrey for the Degree of Doctor of Philosophy

December 1995

ABSTRACT

Molybdenum-bearing alloys are widely used in industry because of their excellent corrosion resistance. However, the role of molybdenum in passivation is a subject which has been a matter for discussion and controversy for many years. In the previous work carried out in this laboratory, Professor Castle and Dr Qiu suggested that molybdenum oxide might provide the nuclei for formation of the passive film. This hypothesis is the basis of the present work.

In order to find out the evidence for the existence of the molybdenum oxide nuclei, furthermore, to establish a model of passivation for the molybdenum-bearing alloys, the passivation of molybdenum-bearing alloys are investigated by X-ray photoelectron spectroscopy (XPS) and atomic force microscopy (AFM), especially in-situ AFM, in conjunction with SEM and TEM.

During the passivation study, it was found that the chemical composition on anodically polarised surfaces varied with potential. For 516 alloy, the peak value of molybdenum in the surface is at the low potential of the passive region close to the Flade potential. Therefore, molybdenum exerts its greatest function in this potential region. A further AFM study at this potential revealed, surprisingly, that a platelet layer formed on the passivation surface. The dendritic

structure on the surface of the platelets presented under the high resolution of STM, which shows the crystallization property of the platelets. These platelets are mainly composed of chromium and molybdenum oxides and they are only found in the passivation of the molybdenum-bearing alloy, so the formation of the platelets may be associated with molybdenum nucleation in passivation.

The in-situ AFM studies provide the evidence for the formation and disappearance of the platelets during the passivation of molybdenum-bearing alloys, i.e. the platelets form at the early stage of passivation and they gradually merge into the passive film if they are not disturbed by the environment.

Based on the above finding, the role of molybdenum in passivation is proposed as following: molybdenum oxide precipitated on the surface seeds chromium oxide to form platelets at the early stage of passivation and the formed platelet layer prohibits the dissolution of the passive species from the metal. By this way, molybdenum facilitates the formation of the passive film on alloys.

Using Fe-Cr-Mo duplex stainless steels, the corrosion of molybdenum-bearing alloys are studied in HCl and the kinetics of the corrosion are traced by in-situ AFM. During corrosion, it was observed that the ferritic phase in duplex stainless steel dissolves more rapidly than the austenitic phase and the dissolution occurs on the austenite preferentially along grain boundaries, sub-grain boundaries and the planes with high energy. By switching the electrochemical condition from active dissolution to passivation and then changing it back, it is found that under the passivation condition after the active dissolution, the corrosion changes from selective dissolution of the crystallographic feature to general corrosion. This situation persists even though the electrochemical

condition changes back to the active condition from the passivation condition.

Since AFM is a new technique and this is one of the first attempts at applying it to a corrosion study, an in-depth explanation of the images obtained from a corroded rough surface is an important topic on which so far little work has been reported. In this study, therefore, the artifacts and the reality of the structure in AFM images obtained in the corrosion study are discussed.

ACKNOWLEDGEMENTS

First of all, I am very grateful to my supervisor, Professor J.E.Castle, for his guidance, encouragement and continuous support throughout of my Ph.D study. I would like also to thank Dr J.F.Watts for his guidance in operating ESCA3 and conducting XPS analysis, and Dr P.A.Zhdan for his advice in using AFM. Thanks are also extended to all the members of the Surface Interface Reactions Group for their assistance and cooperation in my work and among them, Mr S.J.Davis, Mr S.J.Greaves, and Mrs L.Sun particularly deserve to be mentioned.

I wish to acknowledge Miss D.Chescoe, Mrs G.I.Gibbs, Mrs R.Powell, Dr M.J.Whiting and Dr G.S.Shao for their expertise and assistance in SEM and TEM studies.

I also wish to express my special gratitude to the secretaries and all the staff of the Department of Materials Science and Engineering for their kindness and generous help in many ways and among them, Mrs J.Gilbert and Mrs P.Briggs are greatly acknowledged. I also owe special thanks to Dr L.Boniface for her valuable comments and advice in my English writing of this thesis.

My special acknowledgement is also made to the British Gas company for

providing me a studentship.

Last but not least, I must thank my parents and my husband, H.D.Liu, for their love and support throughout the course of my Ph.D study.

CONTENTS

LIST OF ACRONYMS

AES	-	Auger Electron Spectroscopy
AFM	-	Atomic Force Microscopy
CAE	-	Constant Analyzer Energy
CHA	-	Concentric Hemispherical Analyzer
EDX	-	Energy Dispersive X-ray Analysis
EPMA	-	Electron Probe Micro-Analysis
ESCA	-	Electron Spectroscopy for Chemical Analysis
FWHM	-	Full Width at Half Maximum
GDOS	-	Glow Discharge Optical Spectrometry
PRE_N	-	Pitting Resistance Equivalent
SAM	-	Scanning Auger Microscopy
SCE	-	Saturated Calomel Electrode
SEM	-	Scanning Electron Microscopy
SHE	-	Standard Hydrogen Electrode
SPM	-	Scanning Probe Microscopy
SIMS	-	Secondary Ion Mass Spectroscopy
STM	-	Scanning Tunnelling Microscopy
TEM	-	Transmission Electron Microscopy
UHV	-	Ultra High Vacuum
XPS	-	X-ray Photoelectron Spectroscopy

CHAPTER 1

INTRODUCTION

Stainless steel was produced for the first time in the last century and since then it has played an increasingly important role in industry and daily life. As one of important properties of stainless steels is their excellent corrosion resistance, understanding the corrosion behaviour of stainless steels in corrosion environments is very important.

It is known that corrosion resistance of stainless steels results from passivation properties of alloys which are able to form a compact oxide film on their surfaces to protect alloys from corrosion under various conditions. However, passive films only form in a certain potential range, for example, in the active potential region, alloys suffer active dissolution and in the transpassive region, a passive film is dissolved. Even in the passive region, a passive film in a corrosive environment is frequently damaged by localised corrosion, which then leads to the damage of alloys. In this case, the rapid repair of the local damage of the passive film will prolong the life of the steels significantly. Therefore, studying passivation and repassivation is a practical subject. In this thesis, passivation in acidic

electrolytes is mainly concerned.

Among stainless steels, molybdenum-containing alloys have a high reputation for resistance to localized corrosion, such as pitting corrosion in a solution with chloride ions, but the role of molybdenum in passivation is not clear. Therefore, attention has been paid in this study to the corrosion and passivation of molybdenum-bearing alloys to investigate the role of molybdenum in the passivation of molybdenum-bearing alloys.

In the literature, it is shown that a lot of work has been done in this field. As pronounced enrichment of molybdenum in the surface film is observed in the low potential region, i.e. the active potential region and the lower potential range of the passive region, it is suggested, accordingly, that molybdenum probably facilitates passivation prior to the formation of passive films by increasing the overvoltage or reducing the activity of active sites on the surface (Asami *et al* 1980, Hashimoto *et al* 1979[1,2], Sugimoto and Sawada 1977). In the previous study, Castle and Qiu (1989, 1990), using XPS and solution analysis, found that iron and nickel dissolve into solution in passivation while chromium and molybdenum oxides accumulate in surfaces, and also, molybdenum in the surface influences the proportion of chromium retained in the film. Thus, they assumed that molybdenum oxide may provide the nuclei for the passive films on molybdenum-bearing alloys. The central work of this study is to prove this assumption.

Since molybdenum exerts its greatest function only when it enriches in the surface, a surface analytical technique is necessary to define the maximum enrichment condition. In this study, X-ray photoelectron spectroscopy (XPS) is used for analyzing the compositions of polarised surfaces as it can provide both

elemental and chemical state information of the surface at a nanometre level.

During passivation study, a simple and direct question is: what is the appearance of a passive film and what is the appearance of a passivation surface? A passive film cannot be observed in SEM, because it is only a few nanometres thick. Though a stripped passive film can be inspected in TEM, the stripping process may damage, more or less, the topography of passive films. Therefore, the passivated surface was never observed in the past. Atomic force spectroscopy (AFM) is new equipment which has been developed rapidly in the past ten years. As it can scan a surface down to an atomic scale it is possible to study the topography of passive films by AFM. Furthermore, an electrochemical cell attached to AFM offers an opportunity to investigate the kinetics of passivation. It is expected to be possible to investigate the transient phenomena occurring during passivation and to find out the further aspects of the mechanism of the passivation of molybdenum-bearing alloys. In particular, the possibility of the molybdenum nucleation of passive film may be proved by the AFM study.

In addition to passivation, active corrosion of duplex stainless steels is another topic of this thesis. Cr-Mo-Ni duplex stainless steels, as a family of molybdenum-bearing alloys, have been developed in the past few decades and have attracted the interest of engineers due to their excellent corrosion resistance, especially in chloride environments, and their relatively low cost. Duplex stainless steels are not used in HCl, but HCl solution is always used as a test medium in industry. Therefore, in this study, HCl is utilized as the electrolyte for studying the corrosion of duplex stainless steels.

Although the topography of corroded surfaces of duplex stainless steels

has been studied in different environments by many authors and the fact that the ferritic and austenitic phase in duplex stainless steels etch at different rates has been found, a surface undertaking active corrosion has not been observed in the past because of rapid oxidation of a sample when it is removed from solution. Moreover, the gradual exposure of grains during active dissolution cannot be followed by ex-situ study. As AFM can give images at high magnification beneath the surface of an aqueous medium, it makes possible to do the in-situ study of active corrosion. Furthermore, we can inspect the surface change not only under a constant electrochemical condition, but also between the different electrochemical conditions by switching a potentiostatic control using in-situ AFM. Therefore, it is possible to use in-situ AFM to study passivation occurring on an active surface or to study a passivation surface undertaking active dissolution. This study may lead to a new finding on the role of molybdenum in the passivation.

CHAPTER 2

LITERATURE SURVEY

2.1 Interpretation of corrosion

2.1.1 Corrosion phenomena

Almost all metals are thermodynamically unstable in most oxidizing environments and this instability leads to a reaction occurring between metal surface and its environment. The resultant reaction is corrosion. Rust on iron is one example which we are familiar with. There are two types of corrosion: general corrosion and localized corrosion. General corrosion describes a type of corrosion which occurs evenly over the whole exposed surface and leads to a bulk loss in thickness. Localized corrosion, however, is characterized by occurring at different corrosion rates, for example, the corrosion rate at a particular site may be much more rapid than that surrounding. Localized corrosion can be sub-divided into pitting, crevice corrosion and intergranular corrosion, to name but a few examples.

In corrosion, metal can either be dissolved into environments from bulk alloys or metal ions form a reaction product layer on surfaces. The layer may be a compact layer limiting the rate of corrosion or a loose one dissolved subsequently. (Baer and Thomas, 1981)

2.1.2 Corrosion process

Most aqueous corrosion incorporates electron transfer and an aqueous corrosion reaction consists of two partial reactions: anodic oxidation and cathodic reduction. The partial reactions occur simultaneously at separate sites and they take place independently.

In corrosion, the anodic reaction is oxidation of metals.

$$Me \text{ ---- } Me^{n+} + ne^-$$

For stainless steel, the formula could be written as:

$$Fe \text{ --- } Fe^{+2} + 2e$$

$$Cr \text{ --- } Cr^{+3} + 3e$$

$$Ni \text{ --- } Ni^{+2} + 2e$$

The molybdenum and chromium in stainless steels may react with water and form $MoO_4^=$ and $CrO_4^=$.

Cathodic reactions in acidic solution include the reduction of hydrogen and the reduction of metal ions:

$$2H^+ + 2e^- \text{ --- } H_2$$

$$Cu^{++} + 2e^- \text{ --- } Cu$$

2.1.3 Polarisation of metals

2.1.3.1 Introduction

When a net current flows across an anodic and a cathodic electrode, the electrode is no longer in equilibrium. The change of potential caused by the net current to or from an electrode is called polarisation.

Figure 2-1 Polarisation in corrosion system, x-axis: current density, y-axis: potential, E_A: anode potential, E_C: cathode potential, E_{corr}: corrosion potential (Evans, 1960).

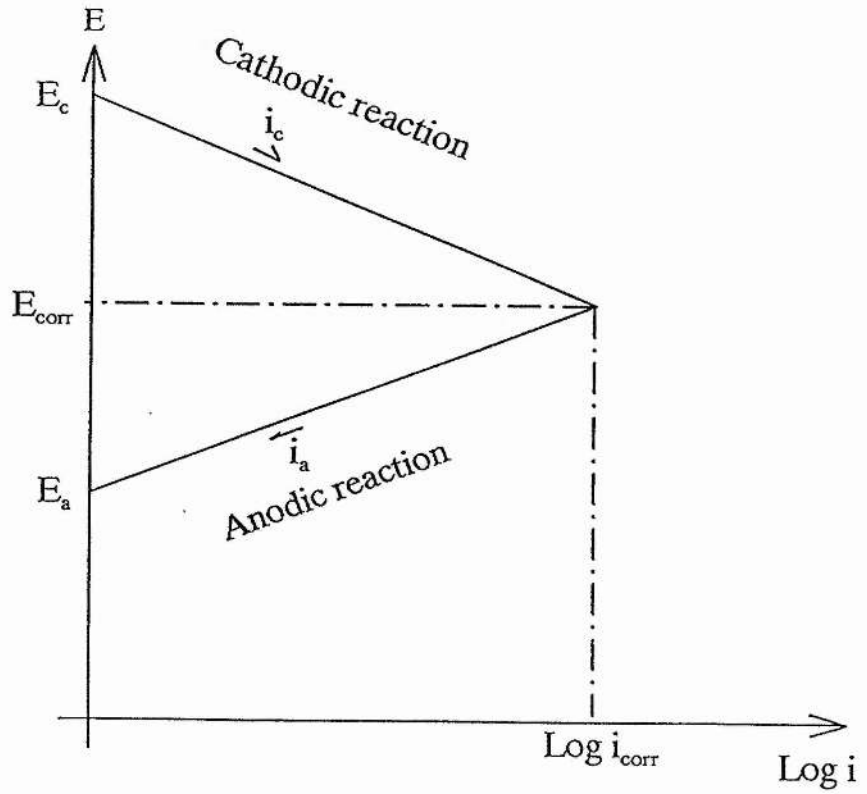

The direction of the potential change always opposes the flow of the current, that is, the anode always becomes more cathodic in potential (anodic polarisation) and the cathode always becomes more anodic (cathodic polarisation). The corrosion potential is the mixed potential of the polarised anode and cathode (Figure 2-1).

2.1.3.2 Influence of polarisation on corrosion system

Both resistance of electrolyte and polarisation of electrodes limit the magnitude of current produced by a galvanic cell. When polarisation occurs mostly at the anode, the corrosion rate is anodically controlled and the corrosion potential is near the open circuit potential of the cathode. When the polarisation occurs mostly at the cathode, the corrosion is controlled cathodically and then the corrosion potential is near the open circuit potential of the anode. When the resistance of the electrolyte is so high that the resultant current is too small to polarise the anode or the cathode sufficiently, it is called resistance control. If both the anode and the cathode are polarised to some degree, the situation is termed mixed control. Figure 2-2 shows the types of corrosion control under different conditions.

Figure 2-2 Types of corrosion control (Uhlig, 1971).

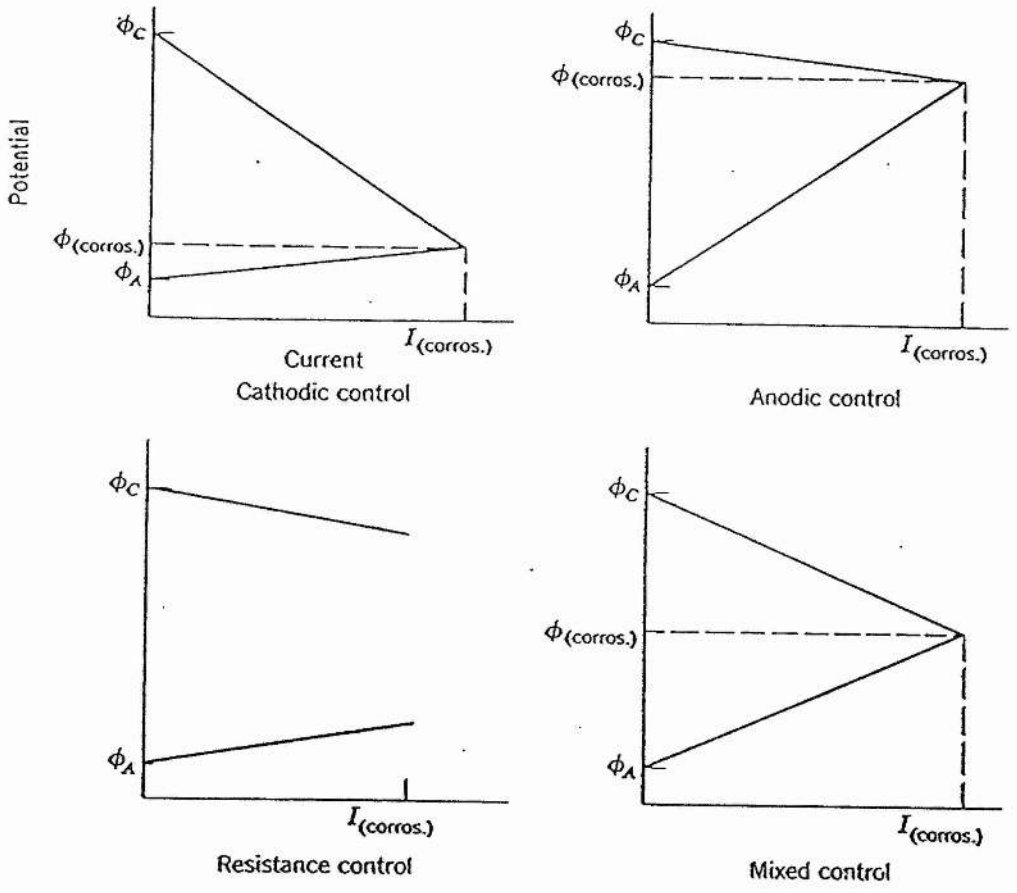

2.1.3.3 Polarisation curve of stainless steel

Figure 2-3 shows a typical polarisation curve of stainless steels, which is a potential current-density variation diagram. By increasing potential in the noble direction step by step and recording resultant currents, a polarisation curve is obtained. The curve below the corrosion potential E_{corr} is a cathodic polarisation curve because cathodic reduction occurs in this area. At the corrosion potential,

the external current is zero. The curve above the corrosion potential is an anodic polarisation curve. According to corrosion behaviour of steels, the curve can be divided into four regions and they are marked by four special potentials: E_{corr}--corrosion potential, E_{pp}--passivation potential, E_f--the Flade potential and E_t--transpassive potential.

(1) The region between E_{corr} and E_{pp} is an active region where the current density increases with increasing potential sharply and the metal is dissolved into solution at a rate which depends on an activation process. The current ceases to increase at the primary passivation potential E_{pp} at which the corresponding current is called critical current i_{crit}.

(2). The potential region between E_{pp} and E_f is a region of active-passive transition. When the applied potential reaches E_{pp}, a barrier layer begins to form on the surface. Any further slight increase in potential will increase the thickness or coverage of the barrier film which cause the anodic current density to drop significantly. In consequence of a sudden change of the current density in this potential region, the surface state is unstable and the metal cannot be protected.

(3) A passive region lies above the Flade potential E_f (Bockris and Reddy, 1970), within which the current density on the surface of the metal remains at a low value and its change is independent of potential. The passive current, i_{pass} is, generally, less than the critical current in three magnitudes, thus the metal is anodically protected in this potential region. There is a pitting potential, E_p, near the upper limiting potential of the passive region. Though the current density remains at a low value above the potential E_p, a pitting type of localized corrosion occurs there.

Figure 2-3 Typical anodic polarisation curve of stainless steels.

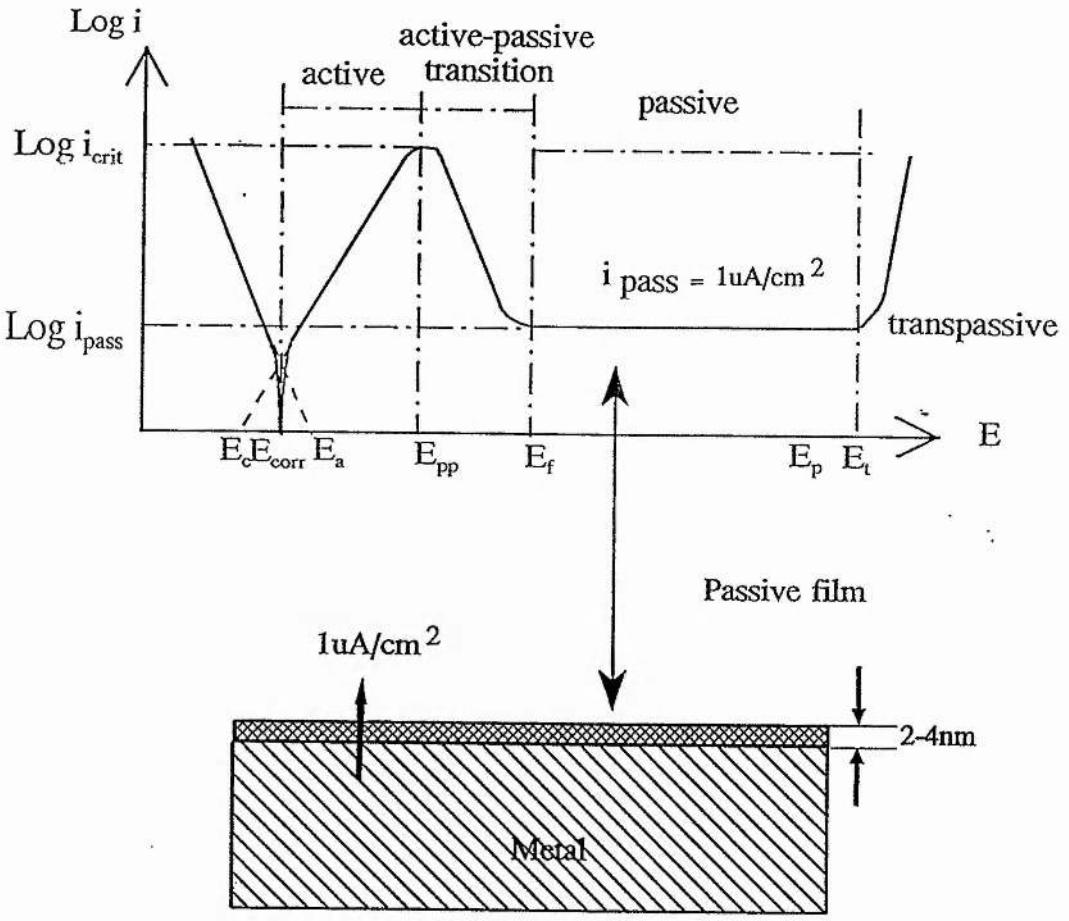

(4) On continuing to increase the applied potential to another critical potential E_t, the fourth region - the transpassive region is reached. Transpassivity is characterized by a sudden increase in dissolution current and it results from a new electrode reaction which dissolves solid surface films.

Since polarisation curves describe the electrochemical characters of

stainless steels in given environments, they are very valuable in an industrial situation for selecting suitable material/environment combinations so as to enable the use of the material in a safe potential range during operation.

2.1.4 Influence of environment on corrosion rate

2.1.4.1 Concentrations of solutions

The concentrations of the solution affect the corrosion rate of metals significantly. Figure 2-4 gives an example, when the concentration of H_2SO_4 increases from 1 N to 10 N, the i_{crit} and the i_{pass} of Fe18Cr8Ni increase more than ten fold.

Figure 2-4 Anodic polarisation curves of Fe-18Cr-8Ni stainless steel in H_2SO_4 solutions of different concentrations, both i_{crit} and i_{pass} increasing with concentration (Fontana and Greene, 1967).

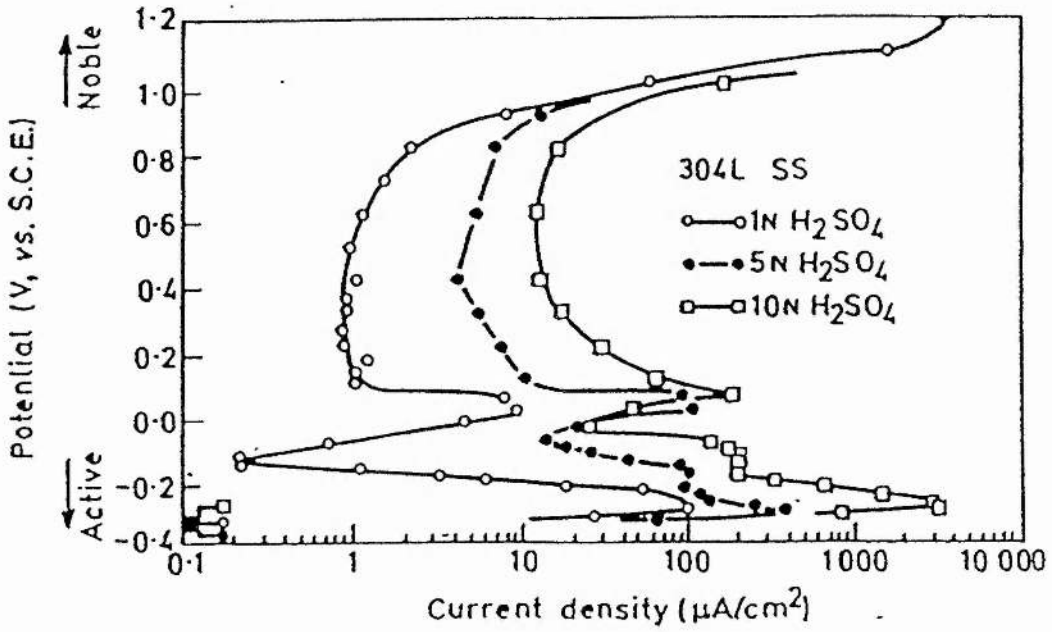

2.1.4.2 Chloride ion

Chlorine can damage passive films and facilitate the occurrence of pitting corrosion. Figure 2-5 is a schematic diagram to show the possible influence of chloride ions on polarisation curves of stainless steels. It can be seen from the diagram that the concentrated chloride ions narrow the passive region, lower the pitting potential and increase the passive and critical current of the alloy.

Figure 2-5 Schematic diagram showing the influence of chlorine on polarisation curves of stainless steels (Sedriks, 1979).

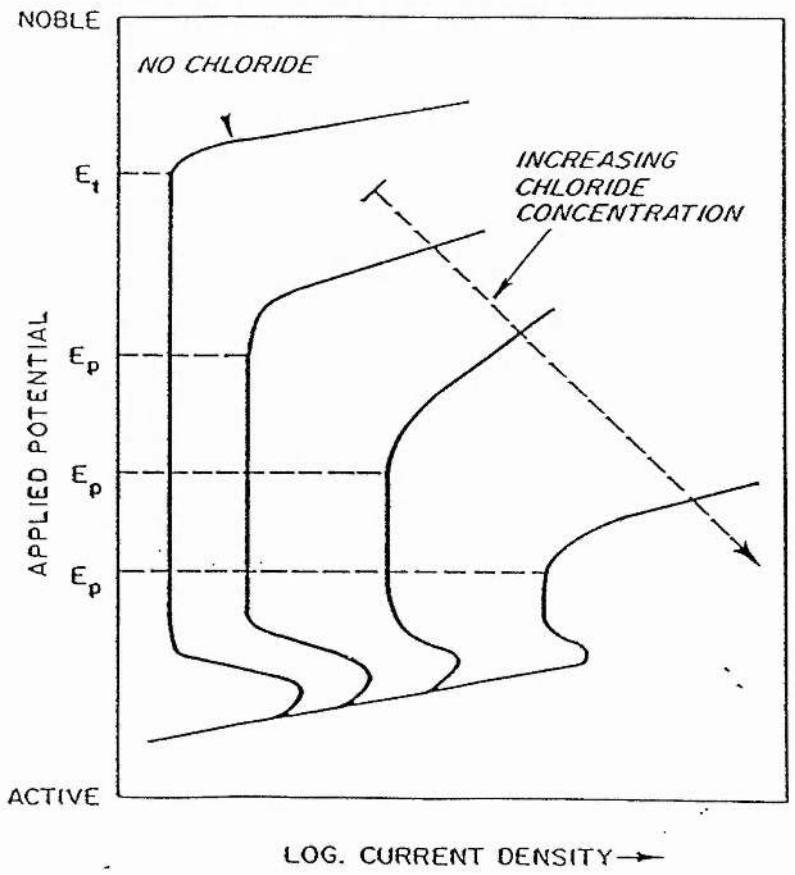

Marcus and Herbelin (1993) measured the polarisation curves of Ni in 0.05M H_2SO_4 with different concentrations of Cl^- and the results show the similar situation to Figure 2-5 (Figure 2-6).

Figure 2-6 Polarisation curves of nickel in 0.05 M H_2SO_4 with various concentrations of Cl^-: 10^{-4}, 10^{-3}, $5x10^{-3}$, 10^{-2}, $5x10^{-2}$M and Ni (100) in the solution with $5x10^{-3}$M Cl^-.

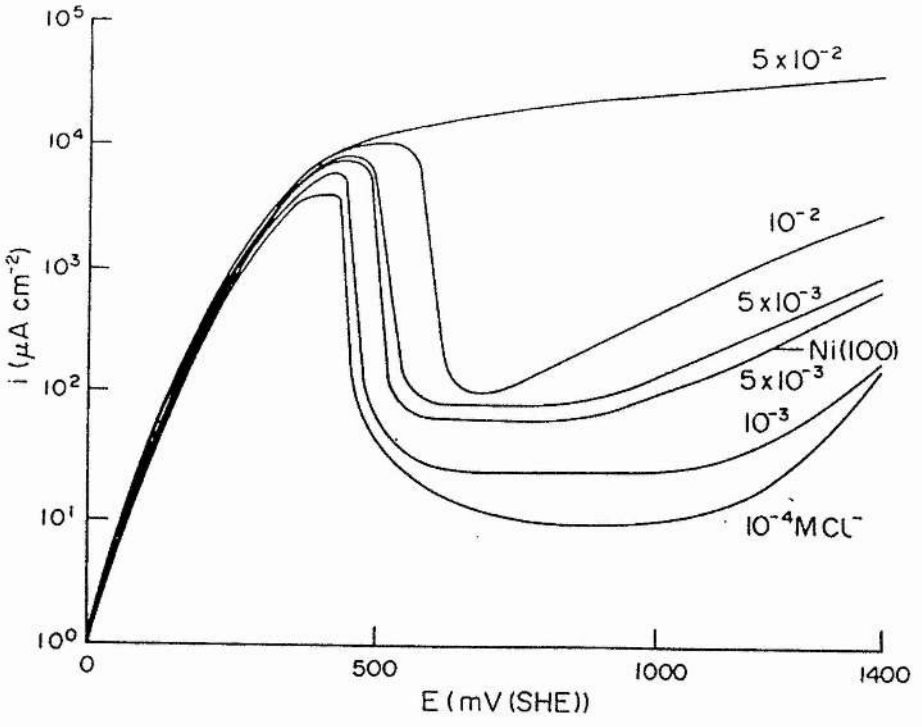

Scully (1990) explained that such behaviour is attributed to the capacity of chloride ions to form soluble species and to produce lattice defects in films. Okamoto's model for the effect of chloride ions is given in Figure 2-7 which describes how chloride ions prohibit the bridging action by replacing water molecules to facilitate pitting corrosion.

Figure 2-7 a) Metal ions forming a film through the formation of bridging via the OH bond, b) chloride ions replace water molecules and inhibit the bridging action to facilitate pitting corrosion.

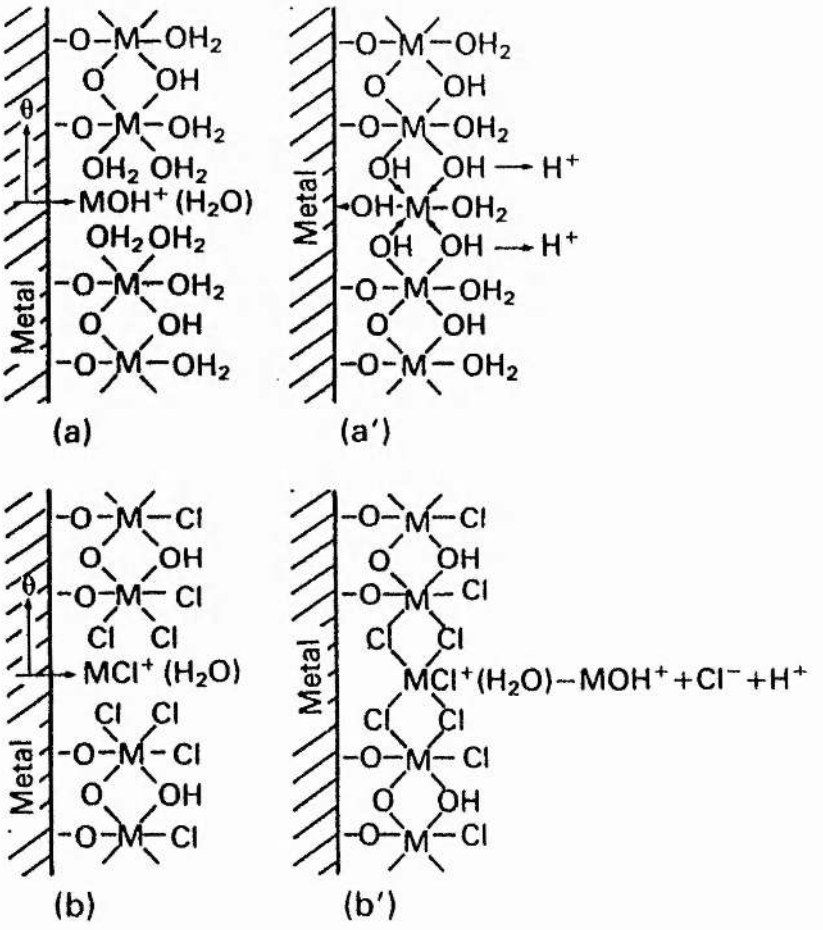

Marcus and Herbelin (1993) studied the effects of chlorine ions on the passivation of nickel and they found that below the pitting potential in the passive region, Cl^- ions are incorporated in the outer hydroxide layer where Cl^- replaces limited OH^- in the film. However, above the pitting potential, Cl^- ions infiltrate into the inner part of the film - the oxide layer - and the pitting corrosion will be initiated when a critical concentration of Cl^- reaches about $10x10^{-3}$ mol cm^{-3} in the inner oxide part of the passive film.

2.1.5 Corrosion of duplex stainless steels

Duplex stainless steels comprise a family of grades with a wide range of corrosion resistance. They are called duplex stainless steels because their alloy microstructures contain austenitic and ferritic phase and the ratio of the two phases is approximate 50% austenite to 50% ferrite in modern grades (Soulingnac and Dupoiron, 1990). As their compositions typically enrich chromium (18-27%), which is higher than that in corrosion-resistant austenitic stainless steels and they have molybdenum content as high as 4.5%, the higher chromium plus molybdenum combination gives the alloys good chloride pitting corrosion and crevice corrosion resistance. They are used in oil, gas and chemical engineering industries intensively today (Davison and Redmond, 1990).

In duplex stainless steels, alloying elements do not distribute evenly in bulk alloys. Ferrite stabilizing elements, such as Cr, Mo, Si, tend to enrich in the ferritic phase while austenite stabilizing elements, such as Ni, N, Cu, tend to enrich in the austenitic phase. The different chemical compositions give different corrosion properties to the two phases, so selective dissolution between the ferritic phase and the austenitic phase occurs in the active region because of galvanic

effects. Zhang (1987) considered that the ferritic phase around the austenitic phase is less noble in potential and it cathodically protects the austenitic phase from corrosion. However, Bernhardsson (1991) reported that either the austenitic or the ferritic phase can be dissolved selectively, depending on the local environment.

2.2 Passivity of Metals

2.2.1 Definition of passivity

Early investigators found that in certain condition, e.g. in concentrated nitric acid, iron reacts with the environment at an unexpectedly low reaction rate. They called it passivity. Faraday considered that a low corrosion rate alone should not be a criterion for the description of a metal as exhibiting passivity, but there is not an agreement on the definition of passivity. The two proposed definitions raised in "Corrosion Handbook" (Uhlig, 1948) are:

1. A metal is passive if it substantially resists corrosion in a given environment resulting from marked anodic polarization.

2. A metal is passive if it substantially resists corrosion in a given environment despite a marked thermodynamic tendency to react.

Definition 1 assumes that the passive potential of a metal is appreciably more noble than the active dissolution potential. Many metals have the same property: when they are polarized anodically, a sudden fall in current density will occur as a result of salt precipitation or oxide film formation.

With other cases, such as lead in H_2SO_4, metal corrodes at a low rate in spite of its relatively active position in the galvanic series, which is accounted for by a comparatively thick diffusion barrier, e.g. $PbSO_4$, covering the metal surface. This is the situation described by the Definition 2.

2.2.2 Passivity theory

There are various theories explaining the passivation of metals. The most fundamental and generally accepted theories are the oxide film theory and the adsorption theory.

The first proposal of the oxide film model for passivity was suggested by Faraday (reprinted in 1965). The model was supported by many scientists such as Gmelin (1929-1932), Haber (1904), Heathcote (1907) and Flade (1911) etc. In 1927, Evans (1927) confirmed the existence of oxide films by stripping an oxide film from Fe which was exposed in air and passivated in chromate solution. In 1934, Tronstad and Borgmann (1934), using an ellipsometer, proved the existence of a film on passive Fe and on 18-8 stainless steel and they suggested that the film was an oxide film.

The adsorption theory might start from Michael Faraday's alternative proposal. It described an adsorbed layer on Fe consisting of oxygen which satisfies the chemical affinities of the surface and hence reduces the reactivity of the surface. The distinction between the oxide film and the adsorbed film is in the mechanism of protection. According to the adsorption theory, the adsorbed film is associated with retarding the surface reaction rate rather than retarding the diffusion rate. This theory was developed by Langmuir (1916), Stanski and

Mutaftschiew (1929). Uhlig (Franck, 1949) proposed in 1946 that an adsorbed oxygen film is commonly the primary source of passivity by the definition 1.

As different descriptions, the oxide film model and the adsorption model have developed in parallel for many years and they complement rather than contradict each other. Since an adsorbed film in the process of thickening gradually passes into an oxide film, the retardation of the anodic process will also be complemented by the inhibition of ions passing through the protective film. The gradations depend on the given metal, environment and electrochemical conditions.

2.2.3 Passive film

2.2.3.1 Structure

There is no general agreement as to whether passivating films are crystalline or amorphous. McBee and Kruger (1972) studied a series of Fe-Cr alloys potentiostatically in 1 N H_2SO_4 and found that the improvement of the stability of passive films with the addition of chromium may be due to the change of the structure of the film, tending toward amorphous. Table 2-1 shows the results of their study (the general formula for spinel structure is AB_2O_4).

Table 2-1 The effect of chromium contents on the structure of the passive film of Fe-Cr alloys.

%Cr	Structure
0	Well-oriented spinel ($Fe^{+2}Fe^{+3}{}_2O_4$)
5	Well-oriented spinel.
12	Poorly oriented spinel.
19	Mainly amorphous.
24	Completely amorphous.

2.2.3.2 Composition

Chromium

Chromium oxide is an essential component in the passive film of stainless steels. After passivation, the chromium fraction in the passive films of Fe15-18Cr alloys increases to a range of 50 to 65% and it may increase to 90% in the passive film of Fe20Cr26 alloys (Olefjord and Brox, 1983, Mischler *et al,* 1988, Calinski and Strehblow, 1989 and Yang *et al*, 1994[2]). Asami and coworkers (1978) found that the chromium concentration in passive films increases with increasing the chromium content of alloys and a sharp increase occurs at 13% chromium alloy, which is illustrated in Figure 2-8.

Figure 2-8 The chromium concentration in the surface film and the alloy surface immediately under the surface film changes with chromium content of iron-chromium alloys.
-●- and -▲-: The alloys were polarised at 100 mV (SEC).
-○- and -△-: The alloys were polarised at 500 mV (SEC).
-▲- and -△-: atomic fraction of Cr in the alloy surface immediately under the surface film,
-●- and -○-: cationic fraction of Cr in the surface film (Asami *et al*, 1978).

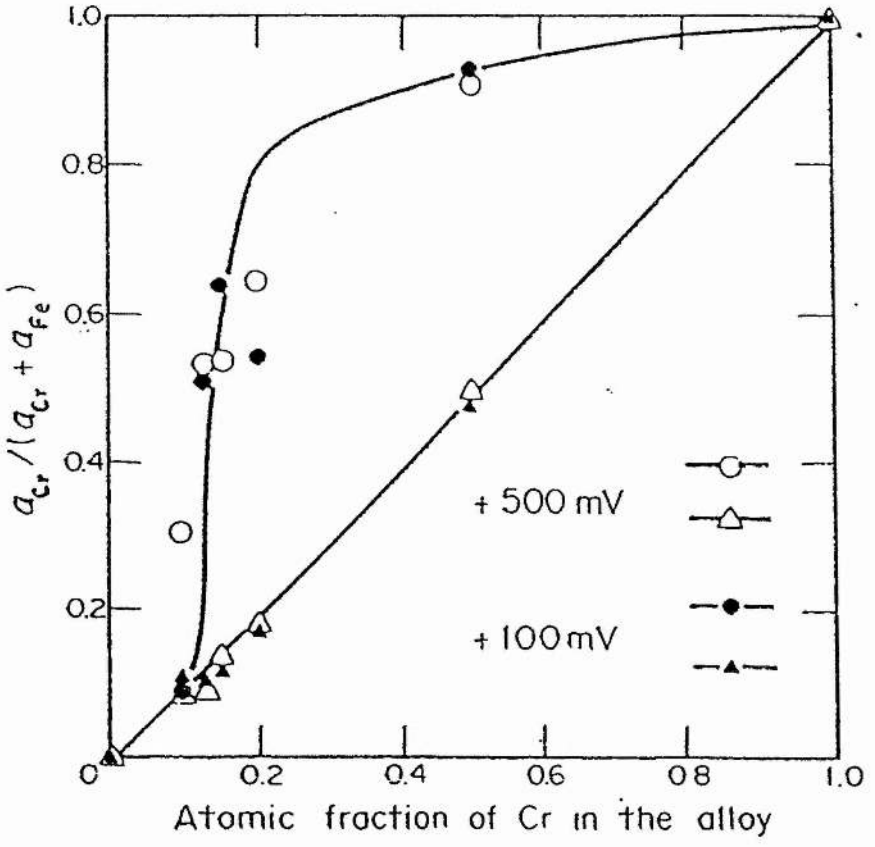

The significant enrichment of chromium is not only observed in the passive region, it is observed in active region as well (Figure 2-9) (Olefjord, 1980).

Figure 2-9 The chromium fraction in the surface film of the alloy (20.4 at% chromium, 1.7 at% molybdenum and balance iron) changes with potential in 0.1 M HCl+0.1 M NaCl. ▾ alloy composition, ▪ 2 min. exposure, ● 5 min. exposure,+ 30 min. exposure, x 60 min. exposure, (Olefjord, 1980).

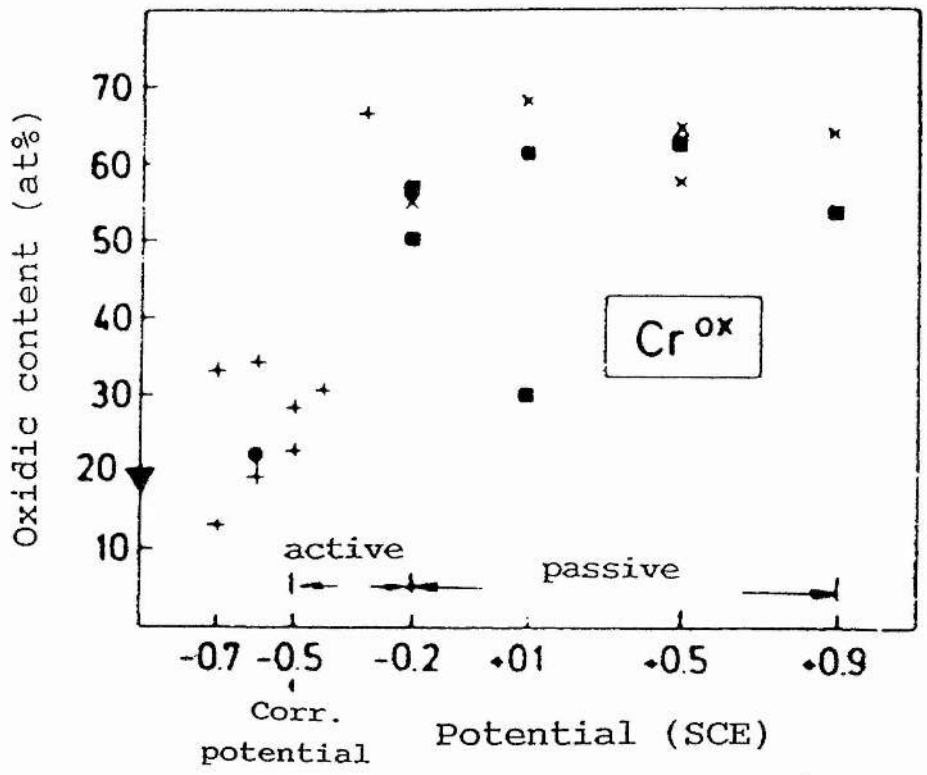

The enrichment of chromium in passive films is a function of time as well. For example, by polarising Fe-Cr alloys at 500 mV, Yang and colleagues (1994[2]) found that the enrichment of chromium in the inner layer of the film increases with increasing polarisation time.

The presence of molybdenum in an alloy can also enhance the chromium

enrichment in passive films. A comparison of the compositions between the passive films formed on 515 (Fe17Cr) alloy and 516 (Fe15Cr4Mo) alloy in 0.1M H_2SO_4 shows that the passive film of molybdenum-bearing alloy contains more chromium, especially in the outmost layer, and the enrichment factor of chromium of molybdenum-bearing alloy is about 0.8 higher than that of the molybdenum - free alloy (Figure 2-10).

Figure 2-10 a) Chromium enrichment factors in the surface of 515 alloy, b) chromium enrichment factors in the surface of 516 alloy (Castle and Qiu, 1990).

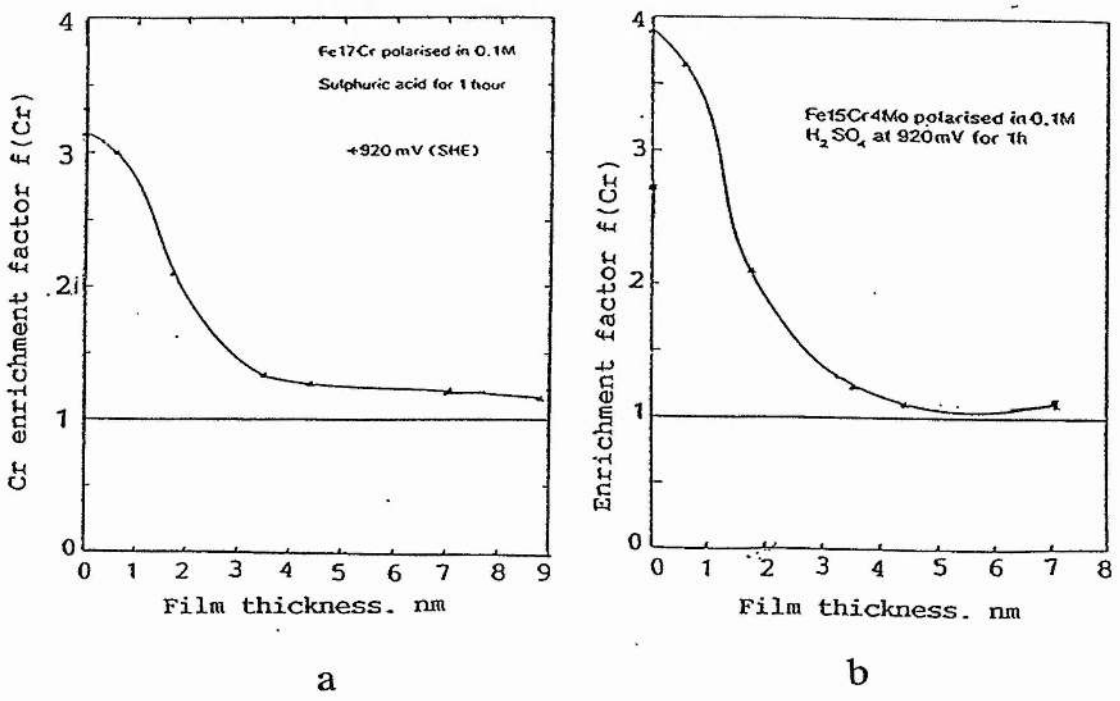

Some investigators found that chromium exists in passive films as chromium oxide, chromium oxyhydroxide or chromium hydroxide with +3 valence or +6 valence (Asami *et al*, 1980, Olefjord and Elfstrom, 1982, Clayton and Lu, 1986). However, the presence of Cr^{+6} in passive layer is still a controversial issue (Brooks *et al*, 1986, Halada and Clayton, 1991, Yang 1994[1]).

Molybdenum

Whether molybdenum is enriched or depleted in surface films of Mo-bearing alloys is a question which has been debated for many years. In 1948, Mahla and Nielsen (1948) analyzed a stripped passive film of Type 317 stainless steel which was passivated in 5% HNO_3 + 0.5% $K_2Cr_2O_7$ at 60 °C and found that Cr and Mo are enriched in the film. Later Rhodin (1956) confirmed the enrichment of the above elements in the stripped film.

Since 1970's, many investigators have explored the molybdenum concentration in passive films by surface analytical techniques. Using AES, Lumsden and Staehle (1972) studied the passive film of 316 stainless steel in a neutral chloride solution and the result showed that though an enrichment of chromium occurred to some extent in the film, the enrichments of molybdenum and silicon were not found.

On the contrary, XPS studies gave a different view. It has been found by XPS that the molybdenum concentration in a surface film is a function of polarisation potential, i.e. molybdenum is strongly enriched at the active potential region and, sometimes, the enrichment persists even during the exposure in the passive range, but the enrichment declines at high potentials (Olefjord, 1980,

Goetz and Landolt, 1984, Hashimoto *et al*, 1979[1]). Figure 2-11 and Figure 2-12 give the cationic fractions of molybdenum in the surface films in a wide potential region.

Figure 2-11 The molybdenum fraction in the surface film of the alloy (20.4 at% chromium, 1.7 at%molybdenum and balance iron) changes as a function of polarisation potential in 0.1 M HCl+0.1M NaCl. ▾ alloy composition, ▪ 2 min. exposure, + 30 min. exposure, x 60 min. exposure (Olefjord, 1980).

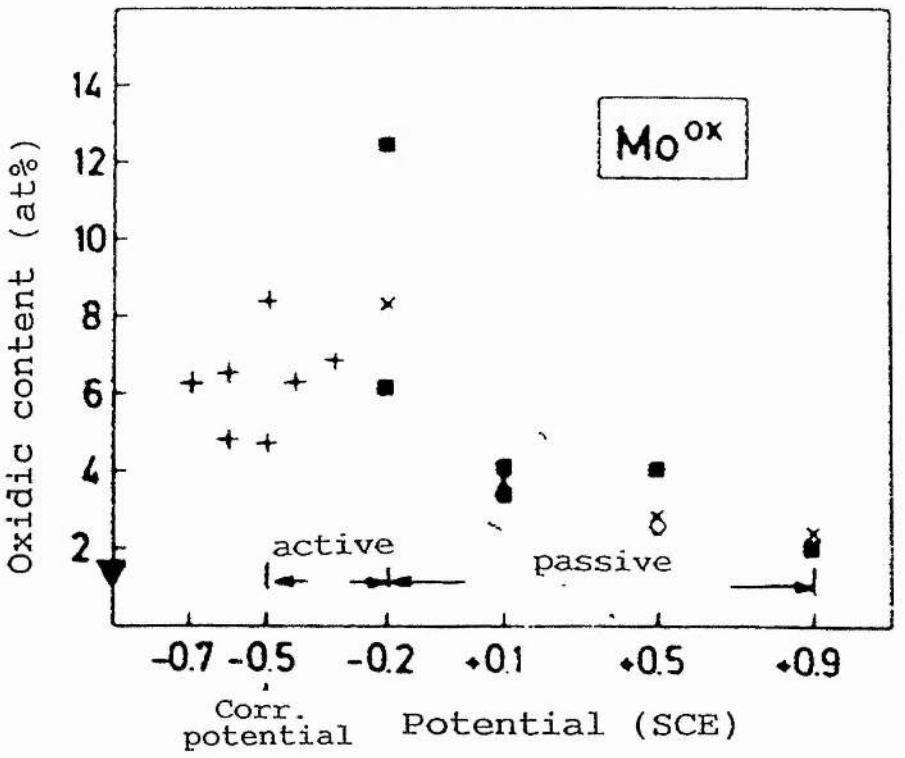

Figure 2-12 The cationic fraction of molybdenum in the surface film of Fe-25Cr-20B-xMo as a function of polarisation potential after 1 hour polarisation in 6 N HCl (Asami *et al*, 1980).

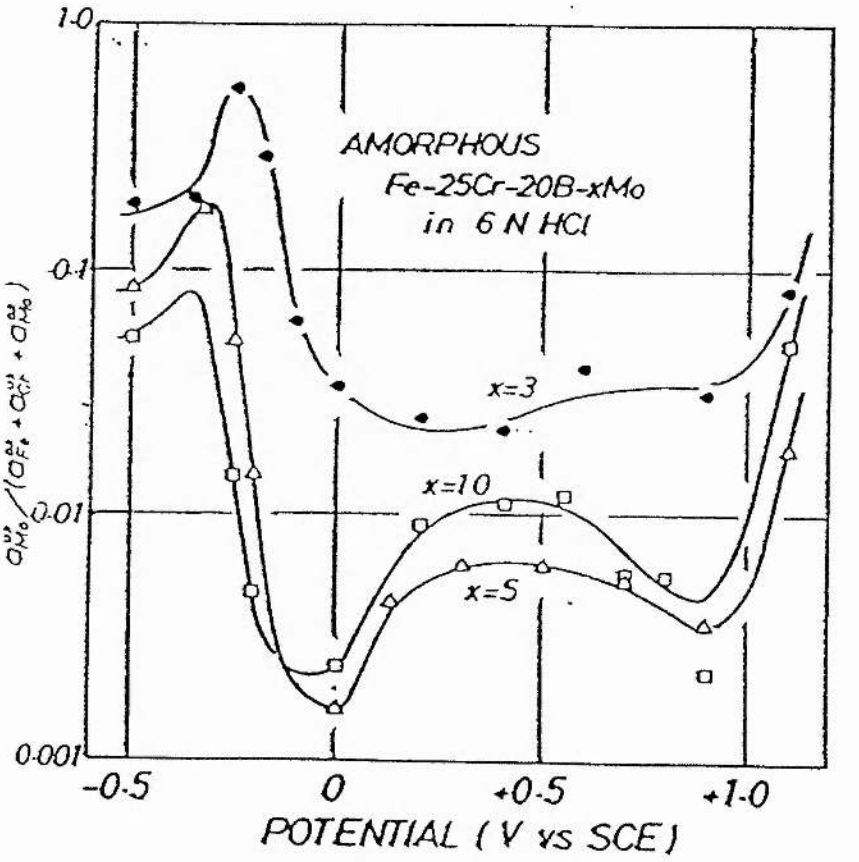

Asami and coworkers (1980) studied molybdenum enrichment regions of different alloys and they found that the enrichment of molybdenum in the surface layer is more pronounced in the active potential region of high chromium alloys and at the low potential of the passive region of low chromium alloys.

Accordingly, the enrichment or the depletion of molybdenum in a surface film is possibly determined by given alloys and applied potentials. More results

related to the investigation of molybdenum in surface films are collected in Table 2-2 (Goetz and Landolt, 1984), in which molybdenum in surface films is undetectable by AES analyses in most cases, but its enrichment is found repeatly by XPS, especially at low potentials. Thus, XPS is a satisfactory technique to investigate the molybdenum concentrations in surface films.

The chemical state of molybdenum in the film depends on the potential to which the sample was polarized. At a low potential, the film is a mixture of low valence Mo-oxide, while at a high potential (+0.5V), molybdenum is oxidized to its six valence state (Olefjord and Elfstrom, 1982).

Table 2-2 Molybdenum content in surface film.

Fe-Alloy with (weight %)	Electrolyte (25°C)	A-M	Potential mV(SHE)	Mo conc.	Author
17Cr13Ni2.3Mo0.75Si	1M NaCl + 0.1M Na_2SO_4	AES	+440(p)	n.d.	Lumsden, Staehle (1972)
26Cr3Mo	0.6M NaCl pH=2.5	AES	+900(p)	n.d.	Rondot *et al*, 1975
19Cr9Ni2.4Mo2.5Si	0.8M HNO_3 + 0.017 M $K_2Cr_2O_7$ (60°C)	AES	open cir. (p)	n.d.	Lumsden, Staehle (1976)
26Cr1Mo	0.6M NaCl, pH=2.5 (5°C)	AES	0 (p) +900 (p)	n.d. n.d.	Cunha Belo *et al*, (1977)
25Cr5.2Mo	1M NaCl + H_2SO_4 pH=3.45	AES	-1155 (c) -150 (p)	det. n.d.	Yaniv *et al*, (1977)
	0.5M H_2SO_4	AES	+60 (p)	n.d.	
17Cr5Mo	1M NaCl + H_2SO_4, pH=3.45	AES	+1250 (t)	det.	

17.5Cr4.8Mo	1 M HCl	AES	-160 (p) +40 (p)	n.d. n.d.	Galvele *et al*, (1978)
18Cr4.8Mo	1 M HCl	AES	+240 (p)	n.d.	Lumsden, (1978)
	0.5 M H_2SO_4	AES	+740 (p)	n.d.	
25Cr3Mo	0.5 M H_2SO_4 +0.5M NaCl (35°C)	AES	+240 (p) +1040 (p)	det. n.d.	Ogawa *et al*, (1978)
17Cr12Ni2Mo	0.5M H_2SO_4 (35°C)	AES	+240 (p) +1040 (p)	det. n.d.	
18Cr3Mo (monocrystalline)	0.5M H_2SO_4	AES	+40 (p) +1140 (p)	enr. same	Leygraf *et al*, (1979)
18Cr4Mo	5M HCOOH (70°C) 0.1M H_2SO_4	AES	+200 (p) +600 (p)	n.d. n.d. 1*	Berneron *et al*, (1980), Charbonnier *et al*, (1977)
17.5Cr16Ni6Mo3Cu	2.6M HNO_3	AES	open cir. (p)	det. 2*	Marcus, Charbon-nier, (1981)
22Cr24Ni2.7Mo18Cr10.5Ni2.8Mo	0.15M Cl^- (37°C) (Ringer's solution)	AES	+240 (p)	det.	Cahoon, Bandy, (1982)
Fe5Mo (binary)	0.01M NaCl in Borate Buffer, pH=8.4	XPS	+440 (p)	dep.	Ambrose, (1978)
Fe15Mo (binary)	0.1M KCl in Borate Buffer, pH=8.4	AES	+330 (pitting)	n.d. 3*	Stout *et al*, (1979)
Cr18Mo (binary) (without iron)	8M HCl	AES	-100 (a) +200 (p) +650 (p)	enr. enr. dep.	Goetz, Landolt,(1982)
20Cr25Ni5Mo	1M HCl	XPS	-110 (a) +540 (p) +940 (p)	enr. enr. dep 4*	Sugimoto, Sawada, (1977)
30Cr1.7Mo	1M HCl	XPS	-160 (a) >+40 (p)	enr. dep.	Hashimo-to *et al*, (1979[1])
18Cr3Mo (monocrystalline)	0.5M H_2SO_4	XPS	+40 (p) +1140 (p)	enr. same	leygraf *et al*, (1979)

25Cr20B10Mo (amorphous)	6M HCl	XPS	-60 (a) +240 (p) +1140 (p)	enr. dep. dep.	Asami *et al*, (1980)
20.5Cr18Ni6.3Mo 18Cr12Ni3Mo	0.1M HCl + 0.4M NaCl	XPS	-60 (a) +140 (p) +740 (p)	enr. enr. enr.	Olefjord, Elfstrom, (1982)

1* Under the same conditions, Mo was detectable with SIMS (secondary ion mass spectrometry) and GDOS (glow discharge optical spectrometry)
2* Mo was only detectable at the surface (interface of electrolyte - film) but not in the film.
3* Analysis of the unattacked surface. Within the pits, Mo was sometimes detected.
4* Mo oxide to Cr-oxide ratio relative to air-formed film.
A-M: Analysis method.
Mo conc.: the Mo concentration in the oxide film relative to the metal bulk concentration.
n.d.: undetectable,
det.: detectable,
enr.: enrichment,
dep.: depletion,
(a): active potential,
(p): passive potential,
(t): transpassive potential.

Iron

Iron is a passivating species in Fe-Mo alloy (Hashimoto *et al*, 1979[2]), but it is dissolved selectively in passivation of stainless steels. So far, many investigators have observed significant depletion of Fe in passive films of stainless steels (Olefjord and Elfstrom, 1982, Clayton and Lu, 1986, Castle and Qiu, 1990). Asami and colleagues also found that the existence of molybdenum in an alloy can enhance this depletion (Asami *et al*, 1980).

2.2.3.3 The thickness of passive films

Passive films are less than 10 nm thick. According to round robin work, the passive film of 516 stainless steel formed in 0.5M sulphuric acid is about 2 nm (Marcus and Olefjord, 1988). The thickness of a film changes with polarisation potential. For instance, the film thickness of FeCrNiMo steel is only 0.6 nm at the corrosion potential, while it increases to about 1.5 nm at the high potential

(Olefjord and Elfstrom, 1982). Castle and Qiu (1989) measured the passive films formed on 516 alloy at 920 mV and at 750 mV, the former is twice as thick as the latter. Figure 2-13 illustrates that the film thicknesses of a series of Cr-Ni stainless steels increase with shifting the potential in the noble direction.

Figure 2-13 The thickness of the film of xCr-10Ni steels as a function of potential, polarising in 0.5 kmol/m^3 H_2SO_4 with pH 0.2 (Sugimoto and Matsuda, 1988).

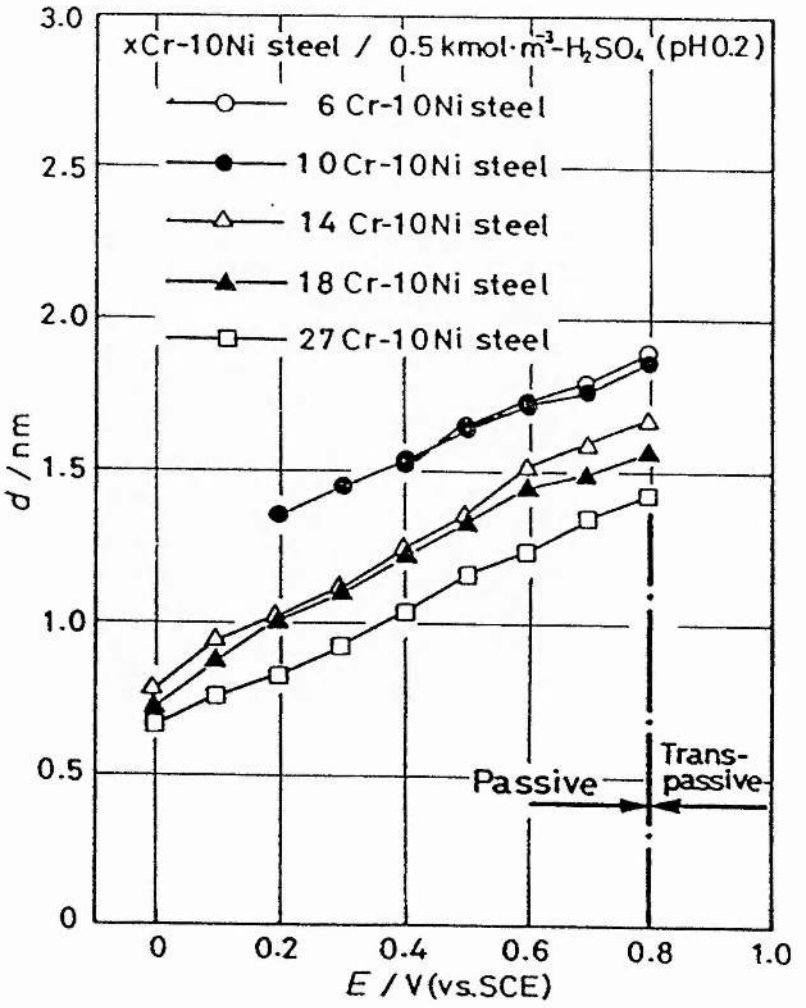

Film thicknesses also depends on passivation time. By increasing the polarisation time from 1 hour to 24 hours, the film thickness of 516 alloy increases from 2.0 nm to 8.0 nm in 0.1 M H_2SO_4 (Castle and Qiu, 1989). Similarly, from 5 minutes to over 20 hours, the 2.4 nm film on Fe-17Cr alloy formed in NaCl increases to 4.1 nm (Yang *et al*, 1994[1], 1994[2]). However, the presence of molybdenum in alloys does not cause any change in the thickness of films (Hashimoto et at 1979[1], Olefjord and Elfstrom, 1982, Castle and Qiu. 1989) and the situation is shown in Figure 2-14.

Figure 2-14 The similar thicknesses of the passive films formed on the molybdenum-bearing alloy and the molybdenum free alloy (Hashimoto et at, 1979).

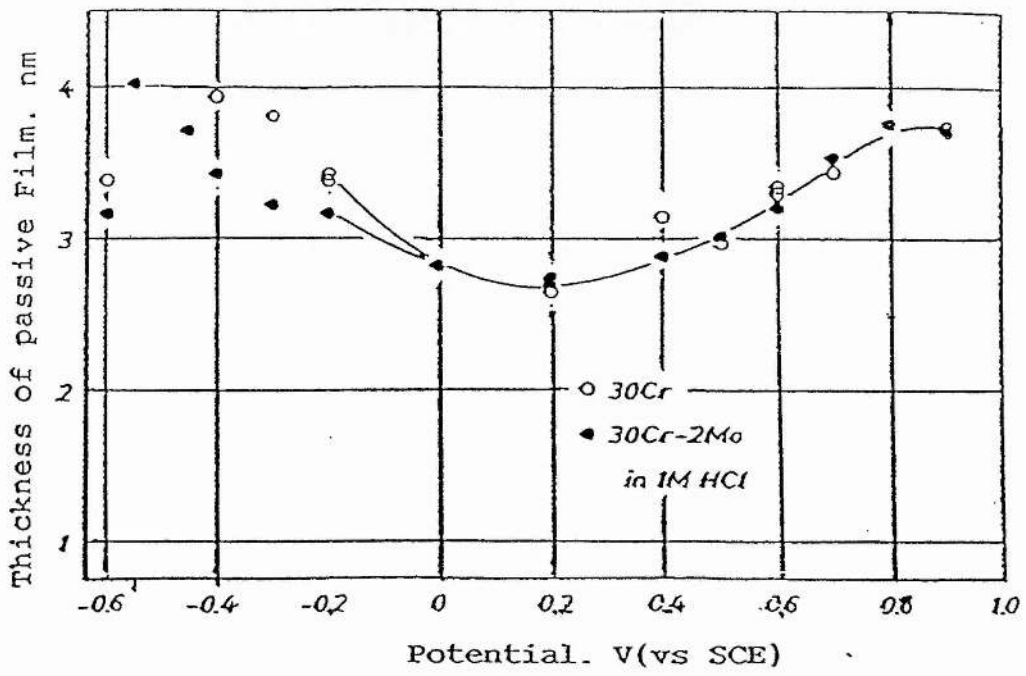

2.2.4 Effect of alloying elements on passivity

2.2.4.1 General description

Alloying is an effective way to improve the corrosion resistance of metals. As early as the beginning of this century, it was established that introducing new elements such as chromium and nickel into iron may cause the passive property of the metal to be enhanced to some extent.

Studying an anodic polarisation curve is a practical way to examine the improvement of the passivation characteristics of a metal by alloying. If alloying elements give rise to an enhancement of one or more following factors in the polarisation curve, it means that they increase the corrosion resistance of the metal (Tamashov and Chernova, 1967):

1) reduction in critical current density i_c,
2) reduction in passive current density i_p in the passive state,
3) more negative passivation potential value E_{pp},
4) more negative Flade potential value E_f,
5) more positive pitting potential value E_p,
6) more positive transpassive potential E_t,

An alloy may possess remarkable corrosion resistance while the single constituents may not. For example, though pure Fe, Ni and Mo cannot be passivated in 1 N HCl solution and Cr has the high critical and passive current, their alloy Fe20Cr25Ni5Mo, however, shows a good passivation capability with low critical current and low passive current (Sugimoto and Sawada, 1977). The

corrosion resistance of the metal, therefore, is improved greatly by the addition of the alloying elements (Figure 2-15).

Figure 2-15 Anodic polarization curves for pure Fe, Cr, Ni, Mo and their alloys 20Cr-25Ni, 20Cr-25Ni-5Mo stainless steels in 1 N HCl at 25°C.

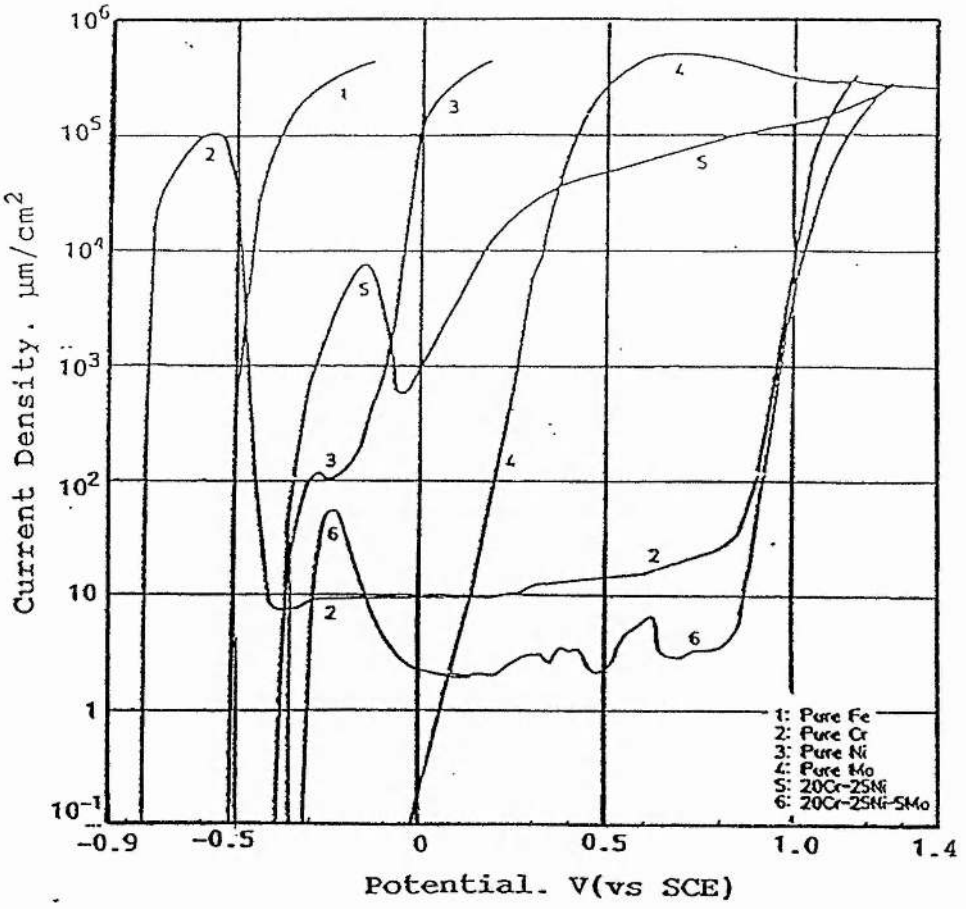

Chromium and molybdenum are the most important alloying elements which supply the necessary and beneficial passive species for passivation. Nickel

is also a beneficial element for passivation as it enables enrichment of chromium by selective dissolution (Castle and Qiu, 1990). In the following section, the effect of alloying elements on passivation is discussed in detail.

2.2.4.2 Influence of chromium

Figure 2-16 Anodic polarisation curves of 25Ni-5Mo stainless steels containing 5-20 wt%Cr in 1 N HCl at 25°C.

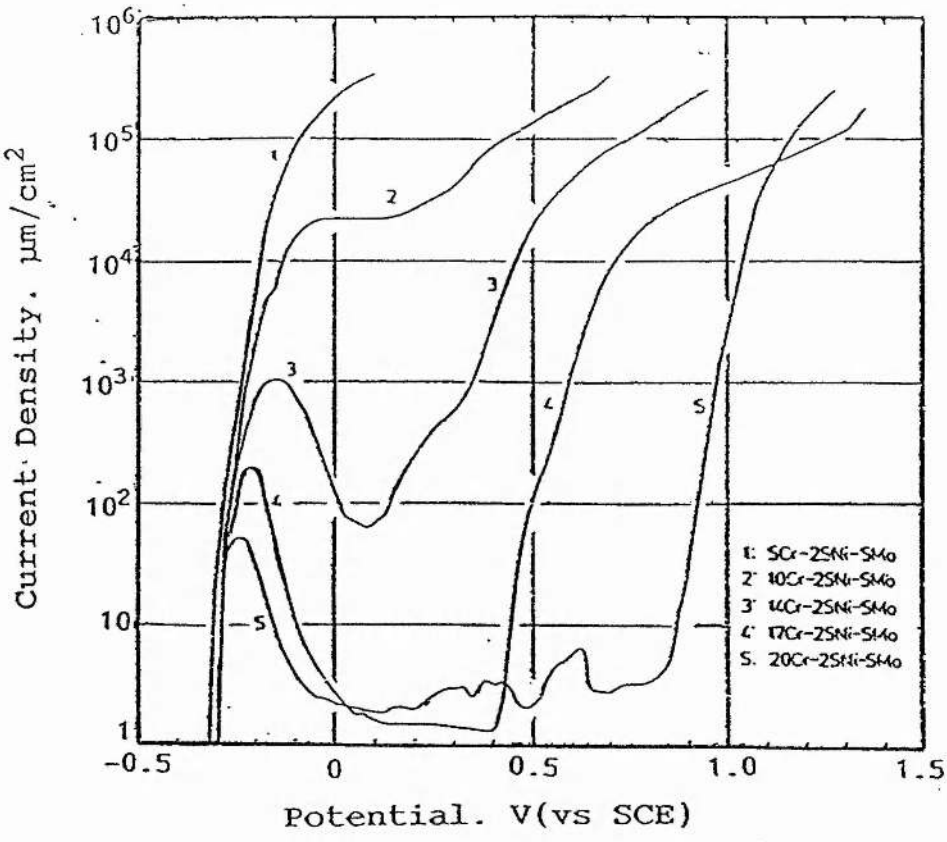

Monnartz (1911) was apparently the first who recognized the outstanding properties of passivity in Cr-Fe and Cr-Fe-Ni alloys and claimed that this property initiates at a minimum of 12% Cr. Sugimoto and Sawada (1977) measured the polarisation curves of a series of CrNiMo alloys containing chromium of 5%, 10%,

14%, 17% and 20% in 1 N HCl, the curves show that the passive region in the curves cannot be observed until chromium content in the alloy reaches 14% (Figure 2-16). The further increase in chromium content tends to decrease the critical current and the passive current and to broaden the passive region. Therefore, chromium is very important for the passivation property of steels.

2.2.4.3 Influence of molybdenum

Figure 2-17 Polarisation curves of 515 (Fe-17Cr) alloy and 516 (Fe-15Cr-4Mo) alloy in 0.5M H_2SO_4, 516 alloy showing much lower active dissolution current (Marcus and Olefjord, 1988).

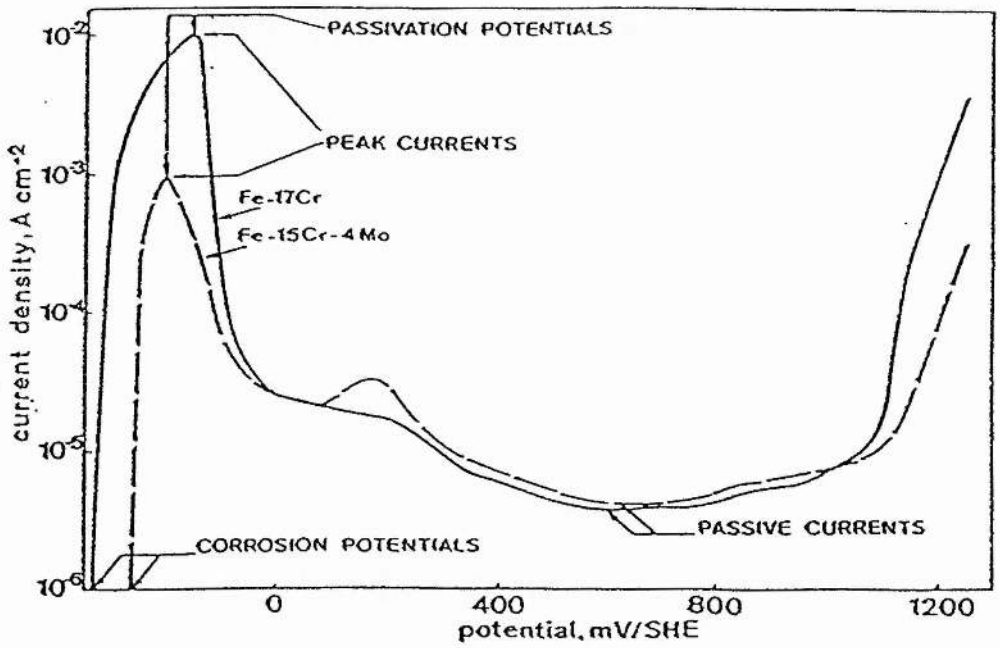

A comparison between the two polarisation curves of 515 (Fe-17Cr) alloy and 516 (Fe-15Cr-4Mo) alloy in Figure 2-17 shows that a significant difference of the two curves lies in the active potential region where the peak current

(critical current) of 516 alloy is less than that of 515 alloy in one magnitude. Therefore, molybdenum alloying element can depress the active current of the alloy in passivation significantly.

The same phenomenon is observed on Fe24Cr11Mo alloy (Figure 2-18). After 11% molybdenum is added to Fe24Cr, though the passive current does not change, the active current in active region is completely depressed (Mischler, *et al*, 1991). Hence, the function of molybdenum is likely at the active dissolution stage rather than at the passive stage.

Many investigations have concluded that pronounced enrichment of molybdenum in surface films is always observed at low potential region, i.e. active potential region and the low potential of passive region where passive films have not yet formed or newly formed (Asami *et al*, 1980, Hashimoto *et al*, 1979[1,2], Sugimoto and Sawada, 1977). Accordingly, molybdenum probably facilitates passivation prior to the formation of passive films. They suggested that the role of molybdenum in passivation is to decrease the activity of the active sites on the surface, consequently decreasing the active dissolution current density by forming a molybdenum - enriched corrosion product layer. This layer is composed of molybdenum oxy-hydroxide or chromium or iron molybdate (Hashimoto *et al*, 1979[1]) and it assists the formation of the passive film by inhibiting the dissolution of passive species (Asami *et al*, 1980, Goetzu and Landolt, 1984). In the case of localized corrosion, its function may count for reinforcing the passive film by intensifying the enrichment of chromium in films (Castle and Qiu, 1990), promoting repassivation and accelerating the repair of passive films (Leygraf *et al*, 1979). This suggestion can be used to explain the depression of the active dissolution current of molybdenum-bearing alloys.

Figure 2-18 The polarisation curves of Fe24Cr (a) and Fe24Cr11Mo (b) in the solution A: 0.1M H_2SO_4 + 0.4M Na_2SO_4 and the solution B: 0.1M H_2SO_4 + 0.4M Na_2SO_4 + 0.12M NaCl.

a

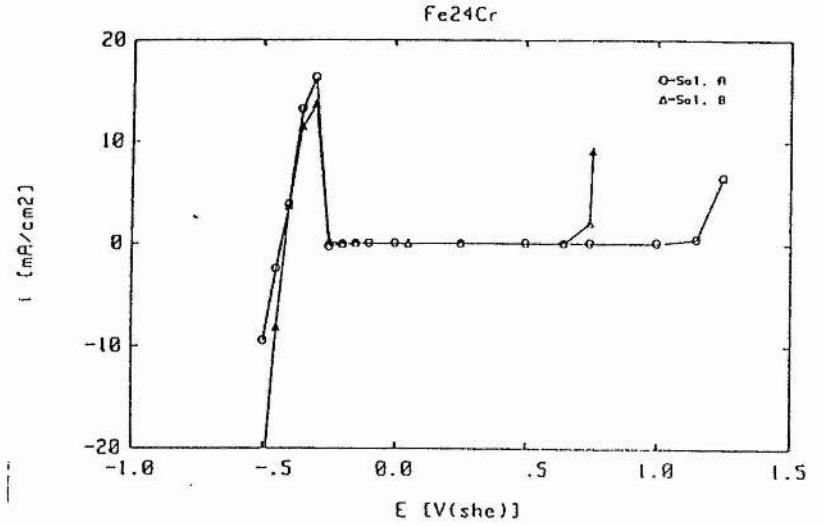

b

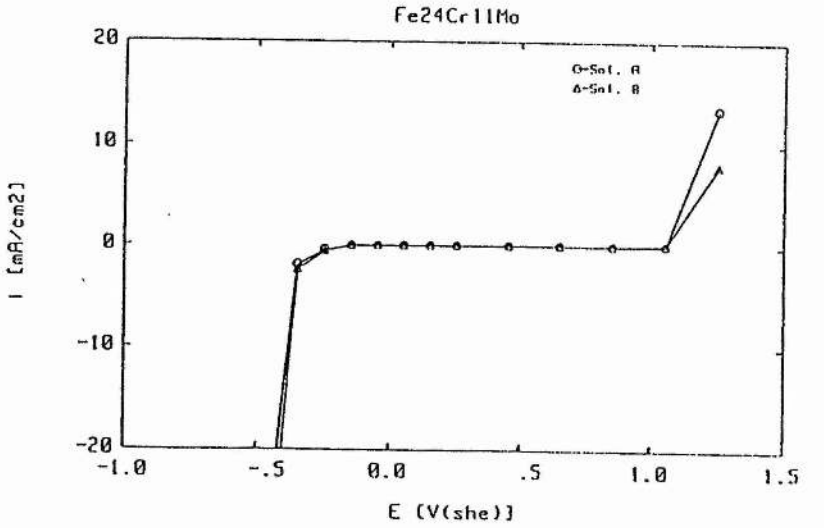

2.2.4.4 Influence of nickel

Figure 2-19 In various current-time curves of Fe-Cr, Fe-Cr-Mo, Fe-Cr-Ni alloys. Ni-bearing alloy showing the lowest passive current in 0.1M H_2SO_4.

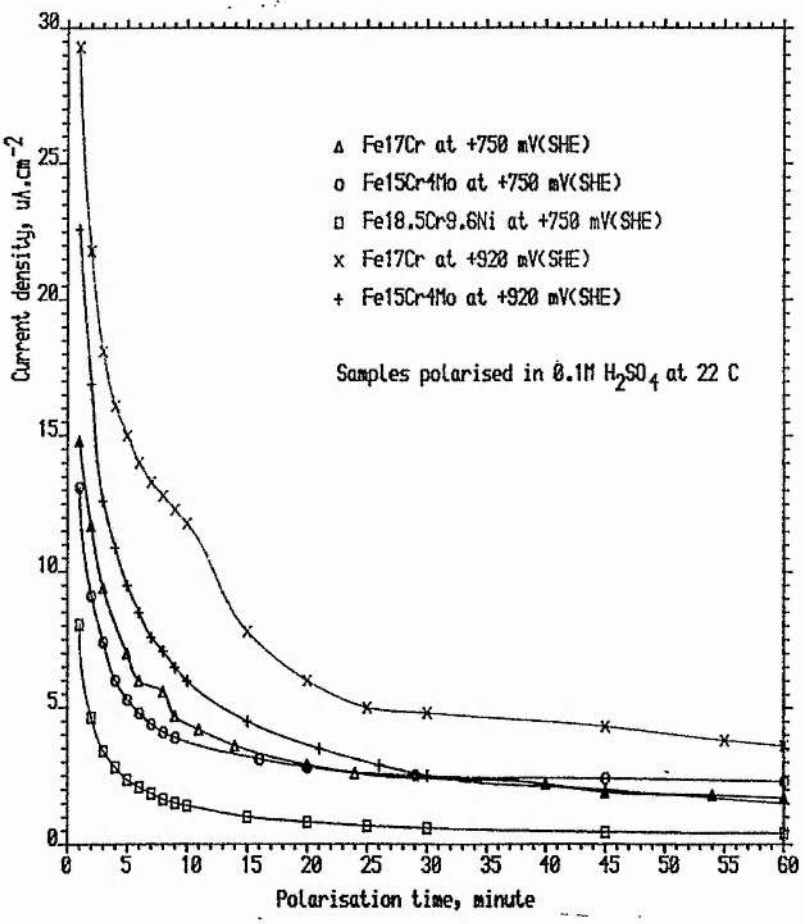

Although nickel is almost absent in passive films (Olefjord and Elfstrom, 1982, Olefjord, 1980, Castle and Qiu, 1990), its effect on passivation of stainless steels is significant. It not only suppresses critical current at the active region but also can reduces passivation time that an alloy needs and decreases passive current. As shown in Figure 2-19, the Cr-Ni alloy exhibits the lowest passive

current in various alloys (Qiu, 1989).

2.2.4.5 Cooperation function of alloying elements in passivation

Passivation occurring on stainless steels are the cooperation result of alloying elements such as chromium, molybdenum, nickel. Figure 2-20 shows chromium and molybdenum effect on the pitting potential shifting to a positive position which marked the improvement of the pitting corrosion resistance of the alloy. It can be seen that pitting potential of 18Cr is obviously higher than 13Cr alloy and this difference in the pitting potential is more significant with adding molybdenum to the alloy (Bond, 1985), i.e. when molybdenum content increases from 0 wt% to 5 wt%, the pitting potential of 13Cr-Mo alloy increases from 0.05 V to 0.3 V and the pitting potential of 18Cr alloy increases from 0.1 V to just above 0.5 V.

There are some expressions used in literature to rank relative pitting corrosion or crevice corrosion resistance of alloy steels in terms of the composition of these alloying elements (Roscoe *el at*, 1987; Suutala and Kurkela, 1984; Brandis and Kiesheyer, 1984). These expressions describe the cooperating function of alloying elements, especially chromium and molybdenum. The pitting corrosion resistance equivalent (PRE_N), the pitting index and the crevice index are good examples (Roscoe el at, 1987).

Figure 2-20 Pitting potentials 13Cr and 18Cr ferritic stainless steels in 1M NaCl at 25 °C.

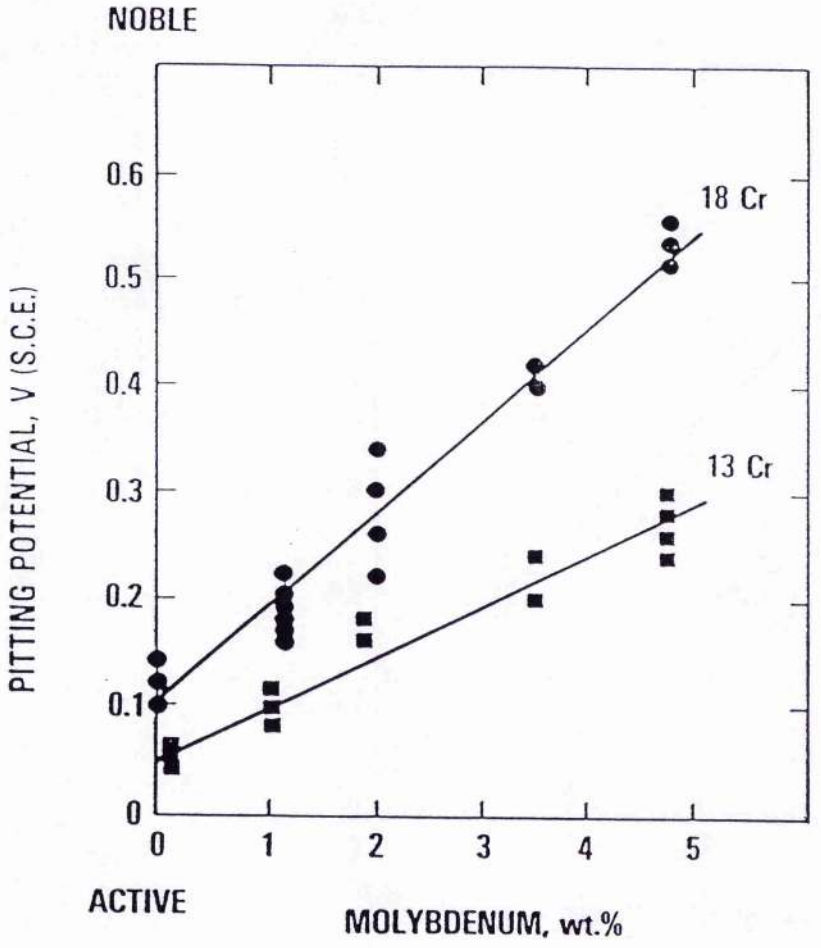

$$PRE_N = \%Cr + 3.3\%(Mo+W) + 16\%N > 40$$

When the value of PRE_N is greater than 40, stainless steels can resist localized corrosion in deoxygenated water. This requirement is met by super duplex and super austenitic stainless steels (6%Mo). The duplex stainless steels, GGR, HCE and GRY, used in this study possess the PRE_N of 34.03, 36.90 and 43.52 respectively.

The pitting index and the crevice index are used for evaluating pitting corrosion resistance and crevice corrosion resistance of steels and welds in chloride-containing environments (Suutala and Kurkela, 1985). They are defined as:

$$\text{Crevice Index} = \%Cr + 4.1\%Mo + 27\%N$$

$$\text{Pitting Index} = \%Cr + 3.3\%Mo + 13\%N$$

For the duplex stainless steels, GGR, HCE and GRY, the pitting indexes are 33.73, 36.36, 40.50 and the Crevice Indexes are 37.61, 41.55 and 46.47 respectively. Using Figure 2-21 and 2-22, the critical pitting temperature and the critical crevice temperature of the alloys can be defined.

Figure 2-21 Critical crevice corrosion temperature as a function of %Cr +4.1x%Mo +27x%N (Sugimoto, 1984, Olefjord and Brox, 1983, Azzerri et al, 1982,Olefjord and Wegrelius, 1990, Miyasaka and Ogawa, 1990, Kruger, et al 1990, Mastsuda, et al, 1990, Suutala and Kurkela, 1985).

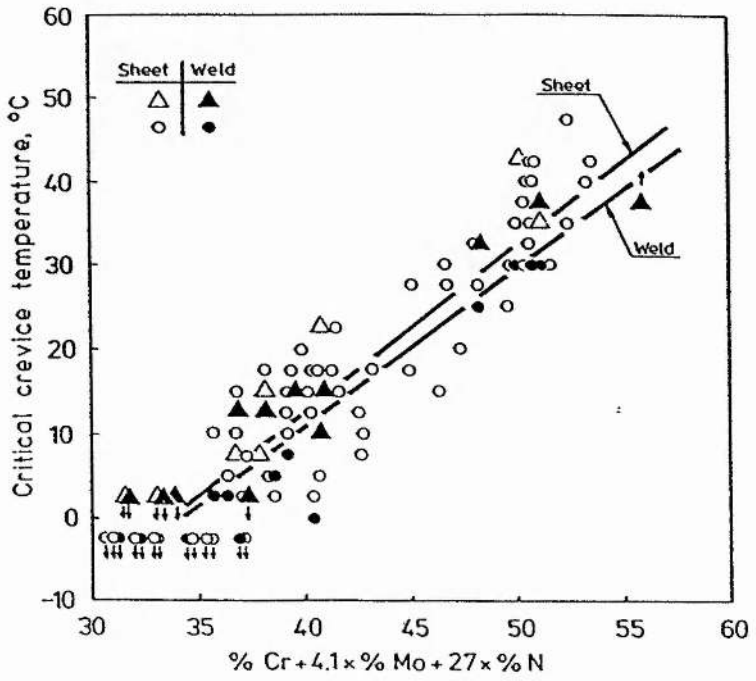

Figure 2-22 Critical pitting temperature as a function of %Cr +3.3x%Mo +13%N (Sugimoto, 1984, Olefjord and Brox, 1983, Azzerri et al, 1982, Miyasaka and Ogawa, 1990, Degerbek, et al, 1979, Kruger, et al 1990, Suutala and Kurkela, 1985).

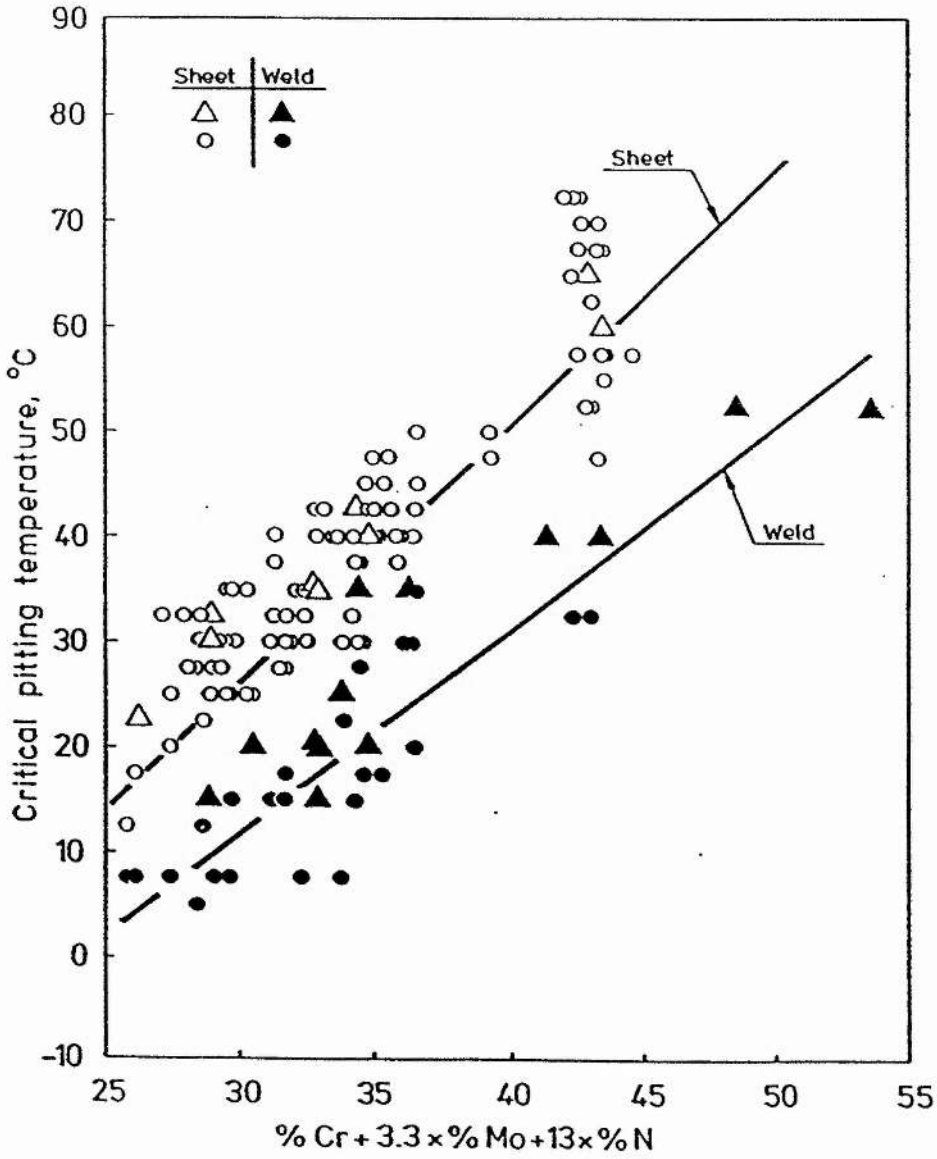

It is observed in Figure 2-21 and Figure 2-22 that the higher the value of the index the alloy possesses, the higher critical crevice temperature and the higher pitting temperature the alloy has.

Figure 2-23 Influence of 'efficiency sum': %Cr + 3.3x%Mo on critical pitting temperature, in 10% $FeCl_3$ (Brandis and Kiesheyer, 1985)

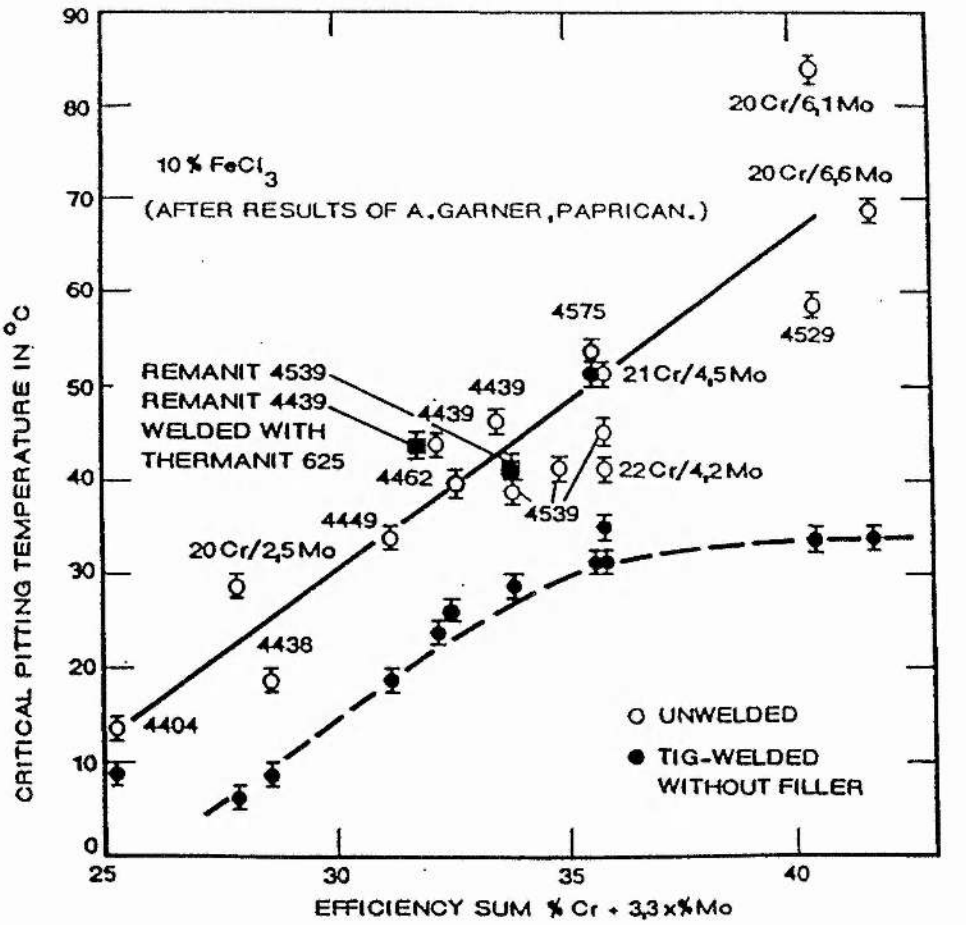

Using the "efficiency sum": %Cr +3.3xMo is another way to evaluate the pitting behaviour of steels. Increasing the "efficiency sum" of the alloy can raise the pitting potential and the critical pitting temperature of the alloy significantly. The effect of "efficiency sum" on localized corrosion is illustrated in Figure 2-23 and 2-24 (Brandis and Kiesheyer, 1985).

Figure 2-24 Influence of "efficiency sum": %Cr + 3.3x%Mo on pitting potentials, in aerated 3% sodium chloride solution (Brandisand Kiesheyer, 1985).

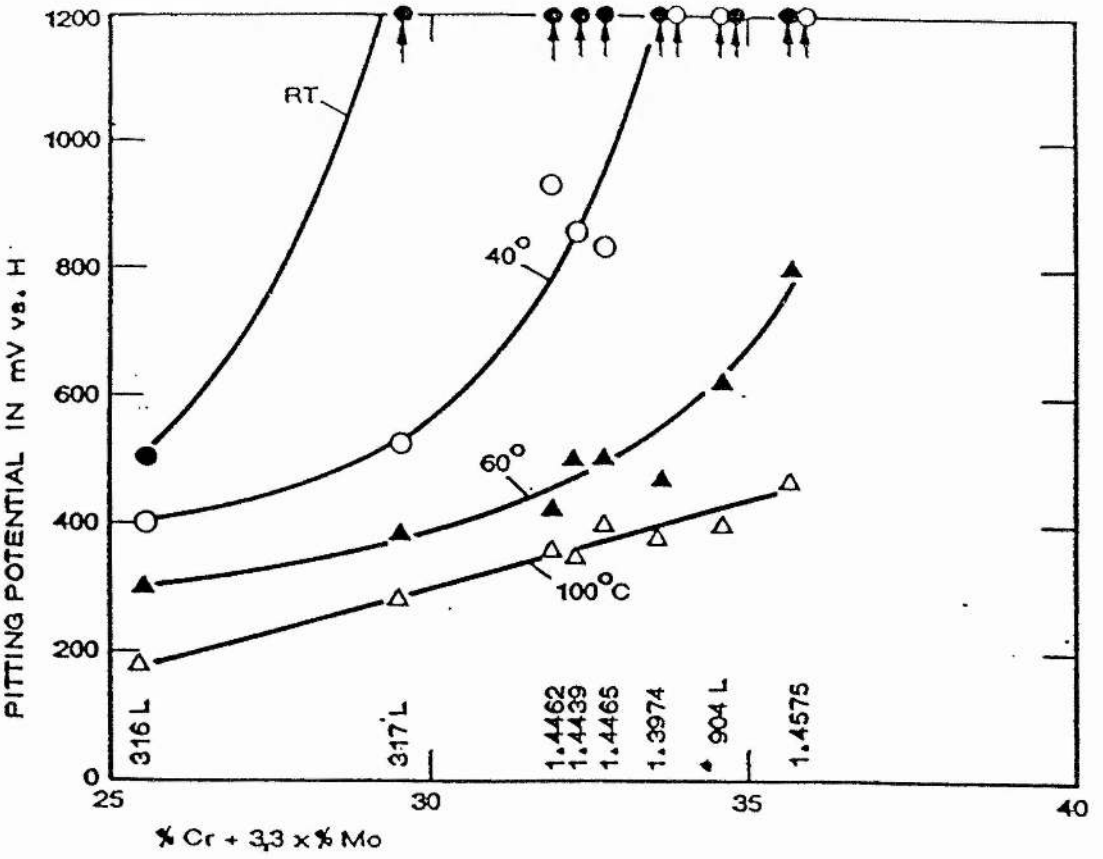

2.2.5 Kinetics of passivation

Kinetics of passivation is a subject of much discussion. Müller (1927) seems to have been amongst the first to suggest that an initial film should be produced by a dissolution-precipitation process. In the early stage of passivation, metal is dissolving into solution until a supersaturation concentration is reached in the vicinity of an anode and the deposits gradually block the metal surface.

The other model is associated with a solid state reaction which involves the formation of passive films. This model describes the growth of a passive film by a direct attack with anions on a metal instead of by dissolution and precipitation of metal ions, e.g. anions O^{-2} from H_2O react with the metal directly without the metal cations entering the solution. According to this model, the initial film is non-uniform, consisting of discrete nuclei, and after long time exposure, the nuclei coalesce and form a continuous film varying in thickness from one monolayer to thousands of monolayers. When a metal is passivated by the second model, metal dissolution always occurs, especially at the active potential region, in parallel with a solid state reaction (Armstrong, 1971).

2.3 Objective

The central work of this thesis is to study the passivation of 516 alloy. In the previous work of this laboratory, an assumption of molybdenum nucleation in passivation was made. The task of this study is to find out the evidence of molybdenum nucleation, to establish the role of molybdenum in passivation of stainless steels and to propose a model for the passivation of molybdenum-bearing alloys. For this purpose, XPS is used to study the composition of passive films formed under different electrochemical conditions furthermore to find out the potential region where molybdenum concentration reaches maximum and also to measure the thickness of the passive film in that potential region. Then, the topography of passivation surfaces and the kinetic of passivation is investigated by AFM, especially in-situ AFM. It is expected that by this study, the evidence of nucleation can be found and the foundation of a model for the passivation of molybdenum-bearing alloys can be provided.

Following the in-situ AFM study of passivation and the indication that Mo functions by nucleating the oxide phase it becomes of interests to study active corrosion. AFM is very valuable for the study of surfaces which corrode at non-uniform rates, as it can estimate the differential etching rate by measuring the change in height of the feature whereas only a mean etching rate can be obtained by traditional electrochemical methods. This investigation is undertaken using molybdenum-containing duplex stainless steels which are of interest to British Gas and it starts with in-situ AFM study of the kinetics of corrosion in HCl. By the electrochemical facility in AFM, an attempt is going to be made to investigate the change of the surface jumped between two different potentials, i.e. to investigate passivation occurring on an active surface

or the behaviour of a passivation surface under active dissolution conditions.

The use of AFM at moderate magnification in solution is still new and there is little literature dealing with the study of very rough surface. Therefore, artifacts in AFM images, which may be created by unsatisfactory sharpness of the tip and the improper use of parameters is discussed.

CHAPTER 3

X-RAY PHOTOELECTRON SPECTROSCOPY

3.1. Introduction

Hertz (1887) was the first worker who used X-rays as an exciting photo source to investigate the photo-electric effect. It was not until the 1950's that Siegbahn and colleagues (Siegbahn, 1957) obtained the first X-ray photoelectron spectrum from cleaved sodium chloride using a high-energy resolution spectrometer in 1954 and found a chemical shift effect on core-level binding energies in 1958 (Nordling at el, 1958). Their findings established the importance of this technique in chemical analysis, and hence X-ray Photoelectron Spectroscopy (XPS) is also known as Electron Spectroscopy for Chemical Analysis (ESCA). Since then, the technique has been developed very rapidly in both instrumentation and applications. In recent years, new types of advanced XPS equipment have been produced and applied in many research fields. Small area XPS improves the XPS resolution from a few 10 mm to 50 μm and imaging XPS can collect a map of the chemical composition of the surface with a resolution of < 10μm. Nowadays XPS, like other mature surface analytical methods, e.g. AES and SIMS, is widely used in metallurgy, corrosion science,

microelectronics, semiconductor materials and other fields.

Corrosion is a chemical or an electrochemical reaction occurring on metal surfaces and it gives rise to the change of surface properties, such as chemical composition and reaction activity. Therefore, surface analysis is very important to corrosion study. In the early 1970's, once XPS was available as a technique in the surface analysis field, Castle (1977,1980) recognized its potential application to corrosion science and electrochemistry. In the past twenty years, Castle and coworkers have made significant contributions in the study of corrosion by means of surface analysis.

3.2 Basic principle of the electron emission process

When X-ray photons are incident on a sample and their energy, $h\nu$, exceeds the binding energies of the electrons in the atoms, the electrons are ejected from the core levels. The resultant free electrons are called photoelectrons which are identified by their kinetic energies as they derived from. For example, a 1s photoelectron is an electron which is excited by an X-ray photon from the K shell directly into a free electron level so that it has the characteristic kinetic energy of its appropriated 1s level. The electron emission process is illustrated in Figure 3-1.

In XPS analysis, though the kinetic energy (E_K) of an emitted photoelectron is measured by the spectrometer, it is dependent on the energy of the X-ray source used. The binding energy (E_B), however, is an intrinsic material property by which the photoelectron is bound to its parent atom. Therefore, the

XPS spectrum is normally scaled using binding energy. The relationship between E_K and E_B is described by the following equation:

$$E_B = h\nu - E_K - W \qquad (3\text{-}1)$$

where $h\nu$ is the energy of the incident photon, E_K is the kinetic energy of the emitted electron and W is the spectrometer work function. From the known and the measurable parameters on the right hand side of the equation, the binding energy (E_B) of the electron can be simply calculated. All detected photoelectrons from the sample contribute to an XPS spectrum.

Figure 3-1 Photoelectron emission process

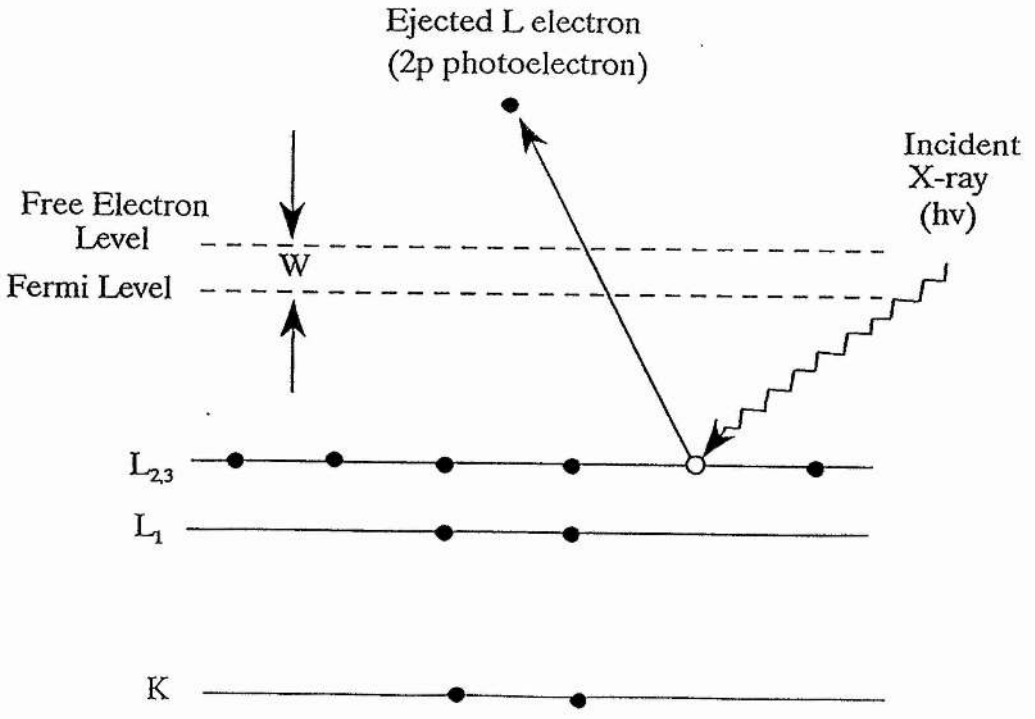

3.3 XPS Instrumentation

3.3.1 General description of XPS

A typical XPS spectrometer consists of an ultra-high vacuum (UHV) system, an X-ray source, an electron energy analyzer, a detection system and a data processing system. The XPS instrument used in this study is an ESCA3 MarkII photoelectron spectrometer made by VG Scientific Limited, U.K.. Figure 3-2 illustrates the working system of ESCA3.

An X-ray gun used for XPS analysis is located in an analysis chamber which is under a UHV condition at all times. A sample preparation chamber is attached to the analysis chamber and these two chambers can be isolated from each other by a gate valve.

Figure 3-2 Working system of ESCA3 MarkII.

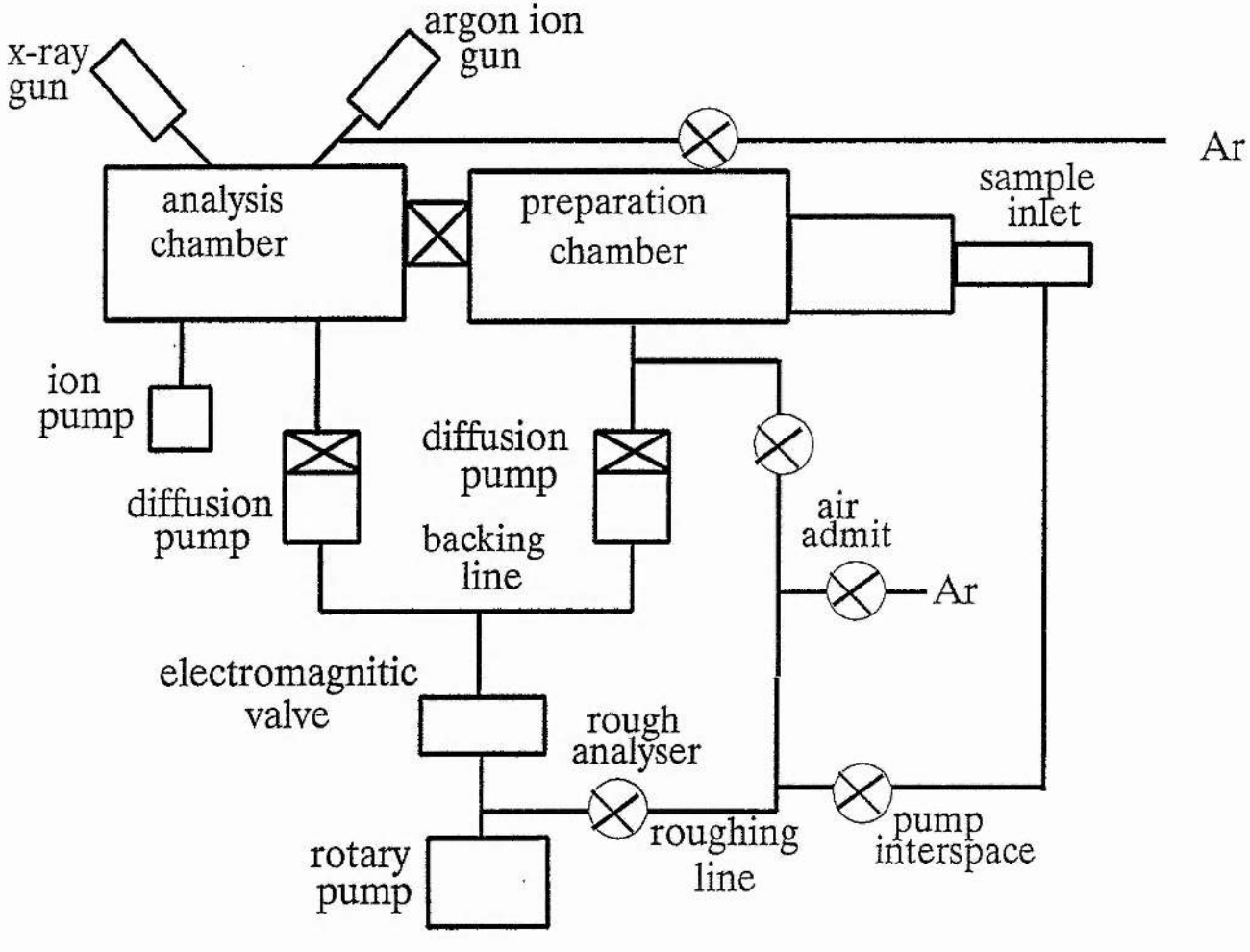

3.3.2 Vacuum system

XPS is a surface sensitive technique which requires 10^{-9} to 10^{-10} mbar of vacuum during its operation, since, according to gas kinetics, a monolayer of gas can be adsorbed on the sample surface in about one second even under 10^{-6} mbar vacuum condition (Watts, 1990). To control the residual gas concentration in the chamber to an acceptable level, a UHV system is an essential requirement for XPS analysis.

The UHV condition is achieved by a pumping system which contains a rotary pump, two diffusion pumps and an ion pump in ESCA3. The rotary pump is used either for establishing a basic vacuum (10^{-2} 10^{-3} mbar) by pumping the chamber directly or for maintaining the UHV by forming a two-stage pumping system with the diffusion pumps. A liquid nitrogen cold trap (Vacuum System CCT Type) is placed above each oil diffusion pump to prevent the oil backstreaming into the vacuum chamber. An ion pump is fixed on the analysis chamber to ensure that the experiment is running under an optimal vacuum condition.

3.3.3 X-ray source

An X-ray source is a device for producing a sufficient flux of x-ray photons with the characteristic energy. Anode materials for X-ray sources must possess two properties: a high enough photon energy (typically above 1 KeV) to excite the photoelectrons from all elements and a narrow natural X-ray line width (normally less than 1 eV) to achieve necessary resolution. AlKα ($h\nu$ = 1486.6 eV, line

width is 0.85 eV) and MgKα ($h\nu$ = 1253.6 eV, line width is 0.7 eV) are the typical anode materials which posses these two properties although other materials such as SiKα ($h\nu$ = 1739.5, line width is 1.0 eV) and AgLα (2984.3 eV, line width is 2.60 eV) have also been used (Watts, 1990).

The X-ray source fitted in the ESCA3 is a twin anode. One anode is AlKα and the other is MgKα. By turning a change-over switch on the control console, the anode can be chosen conveniently.

3.3.4 Electron energy analyzer

The heart of a spectrometer is the electron energy analyzer, which is used for measuring the energies of electrons emitted from the surface. The typical analyzer used in XPS is a concentric hemispherical analyzer (CHA) which is normally operated in a constant analyzer energy (CAE) mode. Figure 3-3 shows the analysing process of the CHA analyzer of the ESCA3. The photoelectrons emitted from the surface are retarded at a slit plate before they enter the hemisphere. A constant voltage is applied to the inner and outer hemisphere during the operation and the electrons whose energies match the pass energy of the analyzer pass through the electrostatic field between the hemispheres, reach the detector and are measured by the spectrometer, while those electrons whose energies are too high or too low strike the outer or inner hemisphere respectively in the curve path. The pass energies available are 10, 20, 50 or 100 eV.

By narrowing the slit, the resolution can be improved. For ESCA3, the resolution of the peak is given by the following equation (Qiu, 1989):

$$dE = WE/2R \qquad (3\text{-}2)$$

Where dE is the full width at half maximum height (FWHM) of the peak, E is the pass energy, W is the slit width and R is the mean radius of the hemispherical sector (10 cm), For a pass energy of 50 eV and a slit width of 2 mm, the nominal analysing resolution of 0.5 eV is achieved.

Figure 3-3 The concentric hemispherical analyzer and the analysis chamber in ESCA3.

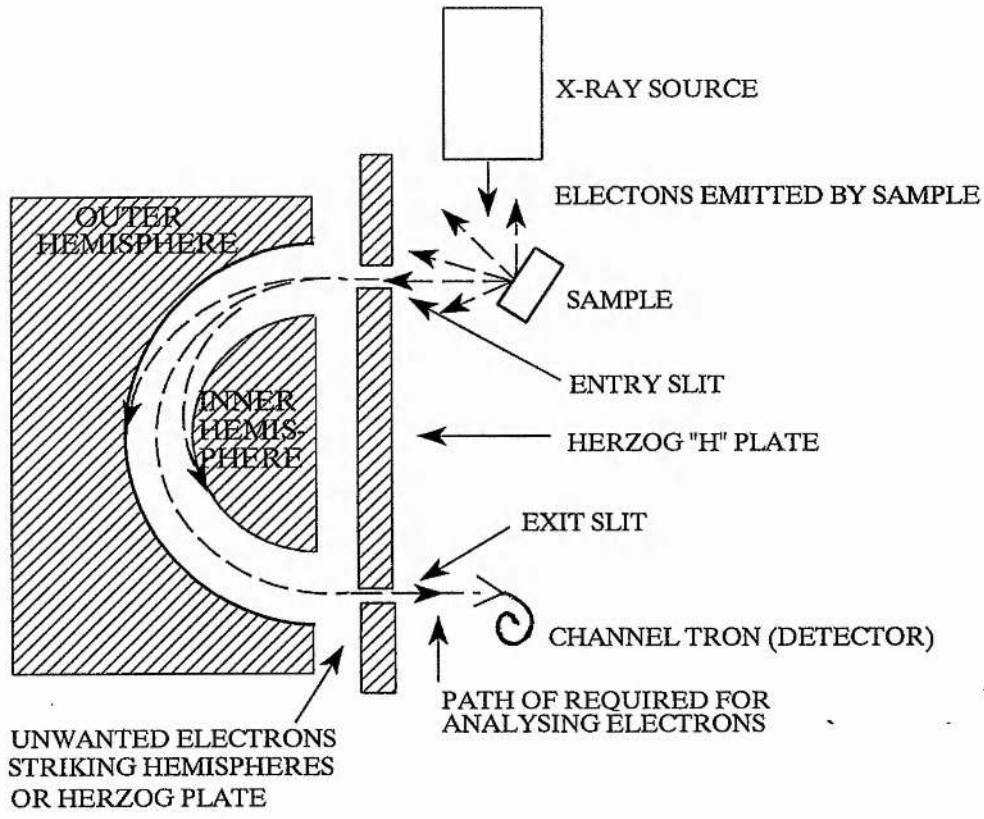

3.4 Interpretation of XPS spectra

3.4.1 General information

An XPS spectrum contains characteristic peaks which are contributed by the photoelectrons without energy loss and the energy loss background structure created by the scattered electrons.

The peaks in the spectrum present the orbital energy levels of the elements against the number of the photoelectrons in a fixed small energy interval. A survey scan spectrum is obtained by scanning, generally, 0 - 1000 eV binding energy range to cover all strong peaks for all elements in the periodic table and it provides the chemical composition information of the surface. Figure 3-4 is a survey scan spectrum of a passive film formed on 516 alloy.

Electrons which are scattered inelastically on the way out of the sample contribute to the background of a spectrum. The signal from the outermost layer owns a horizontal background or one with a slightly negative slope while the signal from a buried phase possesses a background with a positive slope (Castle, *et al*, 1985).

Figure 3-4 XPS survey scan spectrum of passive film formed on 516 alloy after polarisation at -104mV (SHE) for 1 hour in 0.1M H_2SO_4.

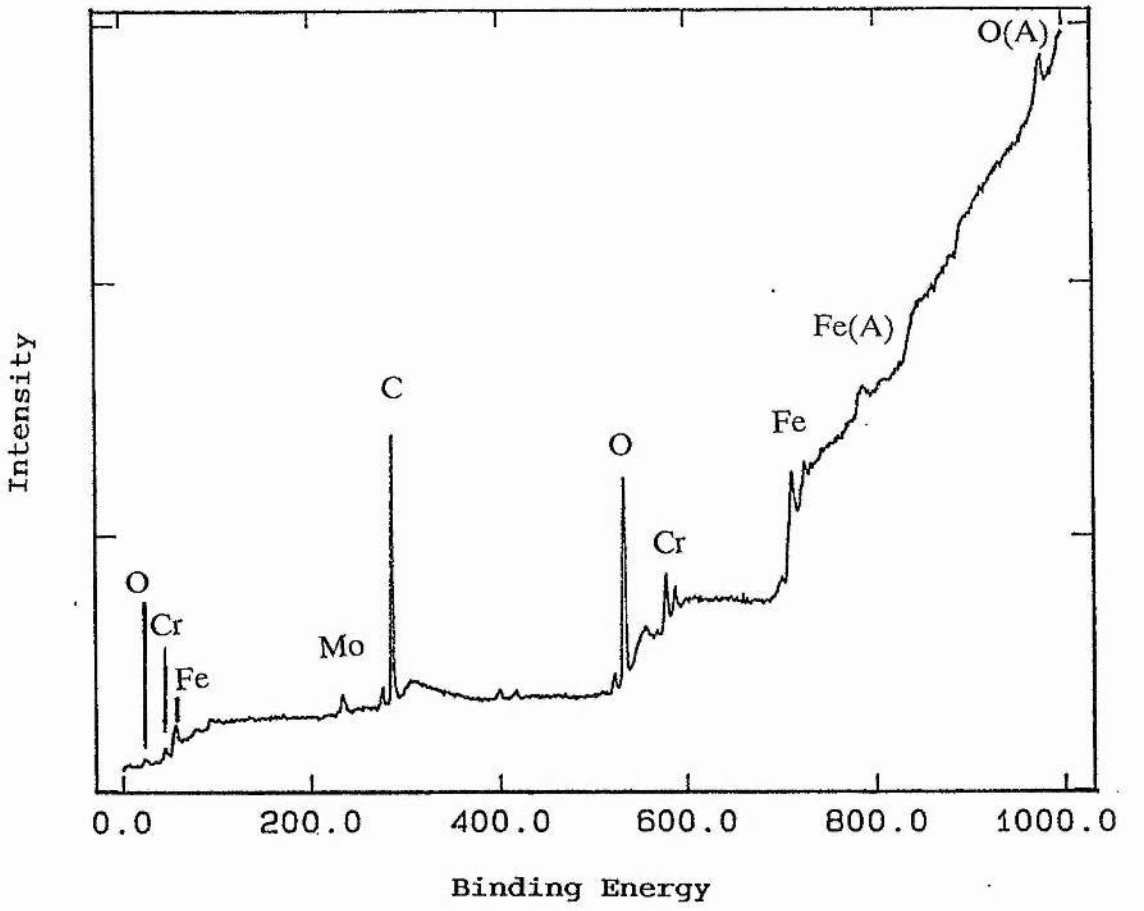

3.4.2 Chemical shift

In XPS spectra, the chemical state of an element can be determined simply by a shift of the photoelectron peak. Figure 3-5 shows the standard iron spectra, where (a) is a group of Fe2p metallic peaks and (b) is a group of Fe2p oxide peaks which shifts about 4 eV to a higher binding energy position.

Figure 3-5 Fe2p XPS spectra: a) Fe2p metallic peaks, b) Fe2p oxide peaks, the oxide peaks shifting towards high energy positions (Wagner *et al*, 1979).

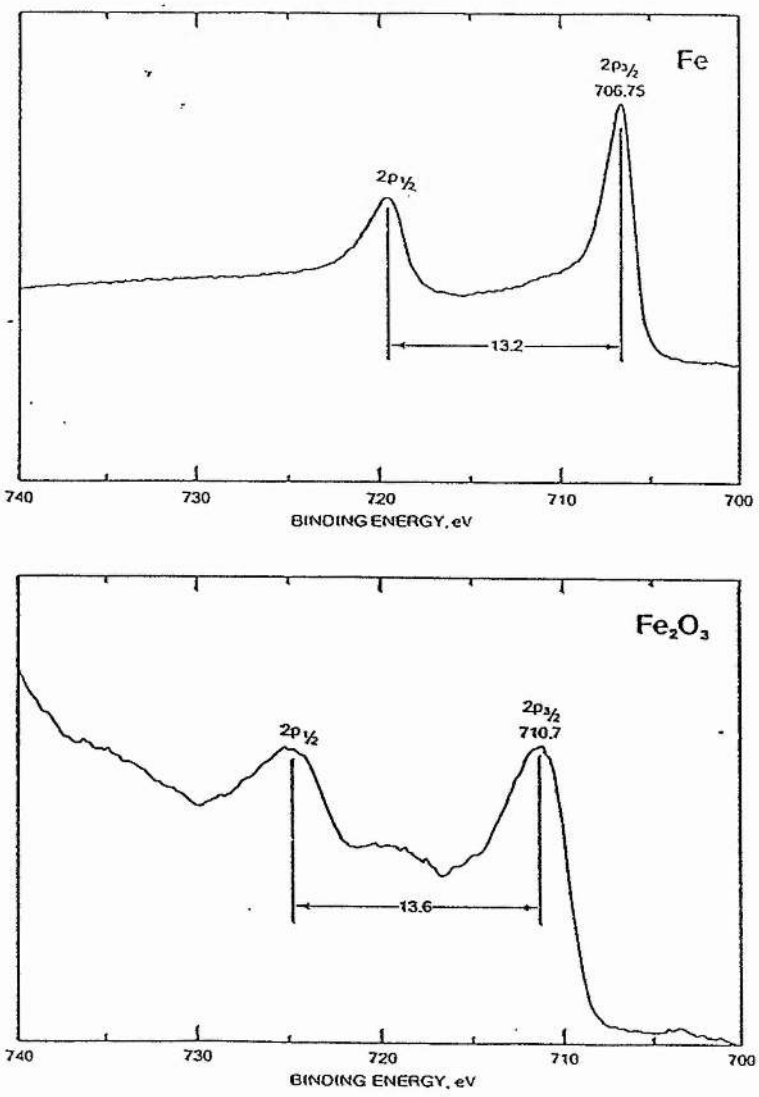

In addition to chemical shifts, shake-up satellites are also used to indicate the chemical state of the elements. Shake-up satellites show up at a few electron volts above the core level position in the binding energy scale, which is caused by an interaction of photoelectrons with valence electrons. Figure 3-6 shows the satellites of Fe2p peak.

Figure 3-6 Satellites in Fe2p XPS spectrum (Castle *et al*, 1990).

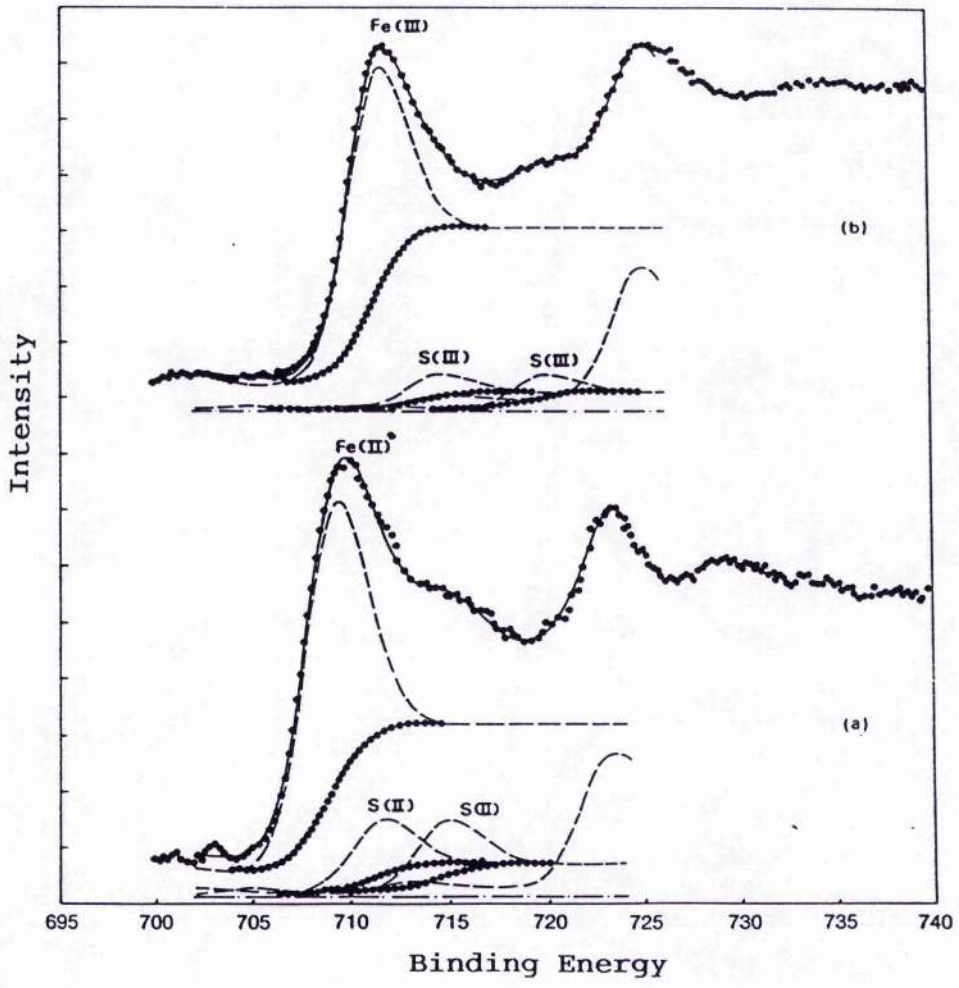

3.5 Quantitative analysis

In the quantification of XPS, the relative concentration of a component detected by the XPS spectrometer can be determined by calculating the integral intensities, i.e. the peak areas of those interrelated elemental photoelectron peaks with their sensitivity factors. For example, the atomic percentage of the element A in an given sample can be calculated using the following equation:

$$[A]atomic = \{\frac{(I_A/F_A)}{\Sigma(I/F)}\} \; x \; 100\% \qquad (3\text{-}3)$$

where $[A]_{atomic}$ is the atomic percentage of the element A in the system, I_A is the peak area of element A and F_A is the sensitivity factor of the element A (Briggs and Seah, 1987).

Values of sensitivity factors are determined experimentally by individual laboratories for given equipment, therefore they change from one laboratory to another. The sensitivity factors used in the current study are taken from the surface and interface reaction group of University of Surrey.

Table 3-2 Sensitivity factors used in the Surface Analysis Laboratory of Surrey University

Element	Symbol	Line	Sensitivity factor
Iron	Fe	2p3/2	1.8
Chromium	Cr	2p3/2	1.1
Molybdenum	Mo	3d	2.75
Carbon	C	1s	0.27
Oxygen	O	1s	0.60

3.6 Compositional depth profile

A compositional depth profile of XPS analyses can be obtained by the destructive depth profile method which sputters the sample surface with inert gas ions or the non-destructive depth profile method which changes the analysing depth by altering the take-off angles during the experiment. As the second method is suitable for analysing thin layers less than 10 nm thick and avoids errors created by ion sputtering, it is used in this study to discover the character of passive films.

A signal obtained from an atomic layer within material is attenuated exponentially by overlying layers. To determine the relationship between take-off angle and depth, it is assumed that I_0 is the intensity from an infinitely thick and clean substrate, which is independent of collection angle except at low angles. If d_1 is the thickness of an outer layer and d_2 is the thickness of an inner layer, then the relative intensity in the following three cases, as described in Figure 6-10, can be easily determined based on Beer-Lambert equation (Seah and Dench, 1979):

(1) The relative intensity from an underlying substrate:

$$I/I_0 = \exp(-d_1/\lambda\sin\theta) \qquad (3\text{-}4)$$

(2) The relative intensity from an overlying layer:

$$I/I_0 = 1 - \exp(-d_2/\lambda\sin\theta) \qquad (3\text{-}5)$$

(3) The relative intensity from a thin overlying layer when covered with a second layer:

$$I/I_0 = \exp(-d_1/\lambda\sin\theta) - \exp[-(d_1+d_2)/\lambda\sin\theta] \qquad (3\text{-}6)$$

In this study, XPS analysis is carried out to determine the chemical compositions, the chemical states and also the thickness of surface films. In addition to XPS, AFM is the other main technique used in this study and it is introduced in the next Chapter.

Figure 3-10 Three typical cases to be studied by Beer-Lambert equations.

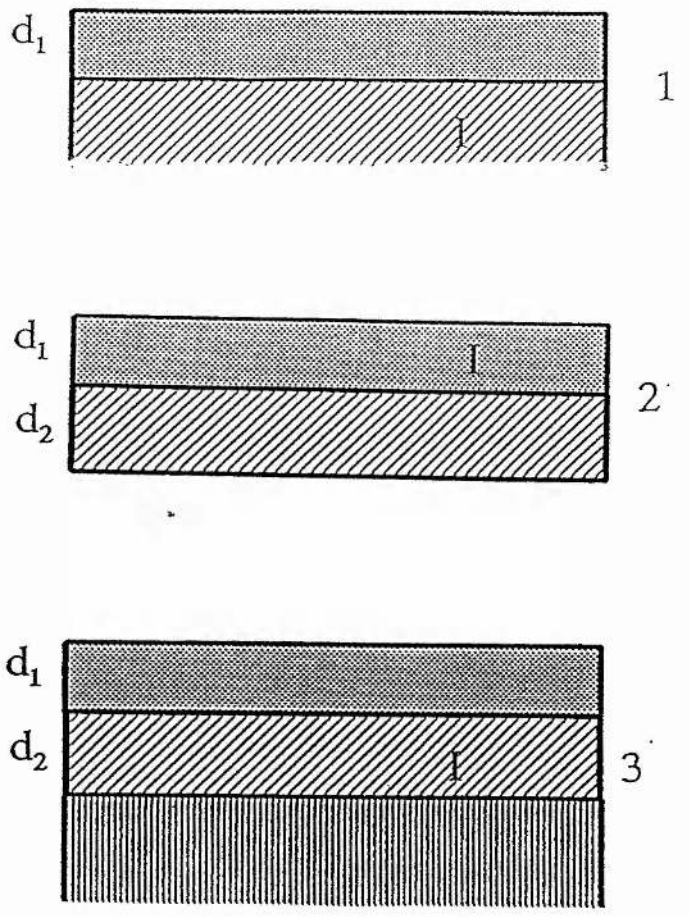

CHAPTER 4

ATOMIC FORCE MICROSCOPY

4.1 Introduction

Atomic Force Microscopy (AFM) was originally introduced by Garde Binnig, Calvin Quare and Christopher Gerber in 1986, (Binnig *et al*, 1986) when they calculated the forces between atoms and found that it is possible to make a cantilever which has a weaker spring constant than that of an equivalent spring between atoms (Rugar and Hansma,1990). This is because the interatomic spring constant of an atom bound in a molecule or in a crystalline solid can be determined by $\omega^2 m$, where m is the mass of the atom ($m = 10^{-25}$ kg) and ω is the vibration frequency of the atom ($\omega \approx 10^{13}$ Rad), so its typical value is 10 N/m and a smaller value at $\omega^2 m$ can be obtained by using a small piece of metallic wire with a diameter of the order of 10 microns and a length of several hundred microns. Therefore, by attaching a sharp tip to this type of cantilever, approaching the tip to a surface and detecting the deflection of the cantilever during the scan of the surface under the tip, it is possible to image an atomic scale topography without pushing atoms out of their atomic sites and damaging

the surface.

Like STM, AFM can be used to resolve surface details down to an atomic level, but its distinct advantage superior to STM lies in that it can also be applied to insulators. The atomically short depth of resolution and the three dimensional nature description of surface features are the merits which distinguish AFM from scanning or transmission electron microscopy and make it invaluable for surface studies. Another advantage of AFM is that it can scan in air, in oil (Marti *et al*, 1987) and in water (Drake *et al*, 1989) whereas SEM and TEM cannot. Therefore, with the aid of an electrochemical cell and a potentiostat attached to the AFM, an electrochemical or chemical process occurring on a sample surface in solution can be investigated directly. Currently, AFM is widely used in physics, chemistry and biological studies.

4.2 Principle of AFM

In AFM, a probing tip is attached to a cantilever-type spring which is deflected in response to the force between the tip and the sample. Images are taken by scanning the sample and digitizing the deflection of the cantilever or the z-movement of the piezo translator as a function of the lateral position x and y.

The AFM used in the current study is operated by the optical lever technique (Alexander *et al*, 1989, Amer *et al*, 1988, Meyer and Amer, 1988). Figure 4-1 illustrates its working process (Gould *et al*, 1990, Maivald *et al*, 1991): a sample is mounted on an XYZ translator (Smith and Binnig, 1986) which moves the sample under the tip. A laser beam passes through a lens and focuses on the

Figure 4-1 Workingprocess of AFM.

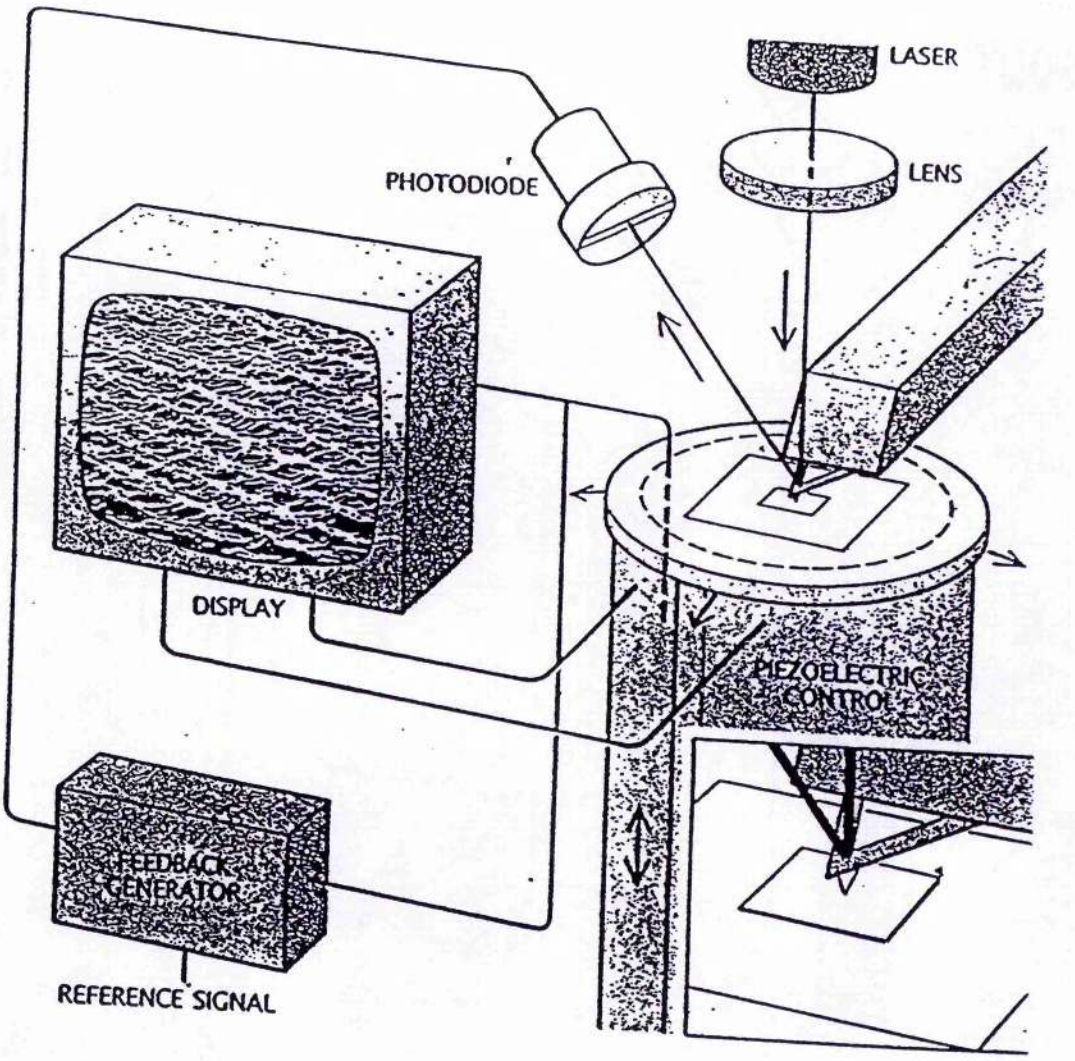

back of the cantilever on which the tip is mounted and the reflection of the laser beam is picked up by a photodiode. When the tip approaches the sample surface, the atomic force between the tip and the sample surface bends the cantilever, which consequently deflects the reflected beam. The instantaneous intensity of the beam is detected by a two-segment photodiode and is converted into the AFM image. A feedback loop controls the motion in the Z direction of the XYZ translator.

During operation, two modes are available: a height mode scan and a force mode scan. In the height mode (constant force mode) of operation, the deflection of the cantilever is held constant and the image is obtained by adjusting the vertical distance between the tip and the sample with the feedback loop. That is, when an increase or a decrease in the deflection is detected, the piezoelectric translator moves the sample down or up to fix the force at a constant value and the distance is recorded in order to reconstruct the surface topography. In the second implementation -- the force mode (variable force mode) scan, the piezoelectric translator does not move the sample up and down but the deflection variations are recorded as a change of the atomic force during scanning, which is then used to reconstruct the surface topography.

4.3 Instrumental

4.3.1 Overview of AFM

Figure 4-2 Schematic diagram of AFM.

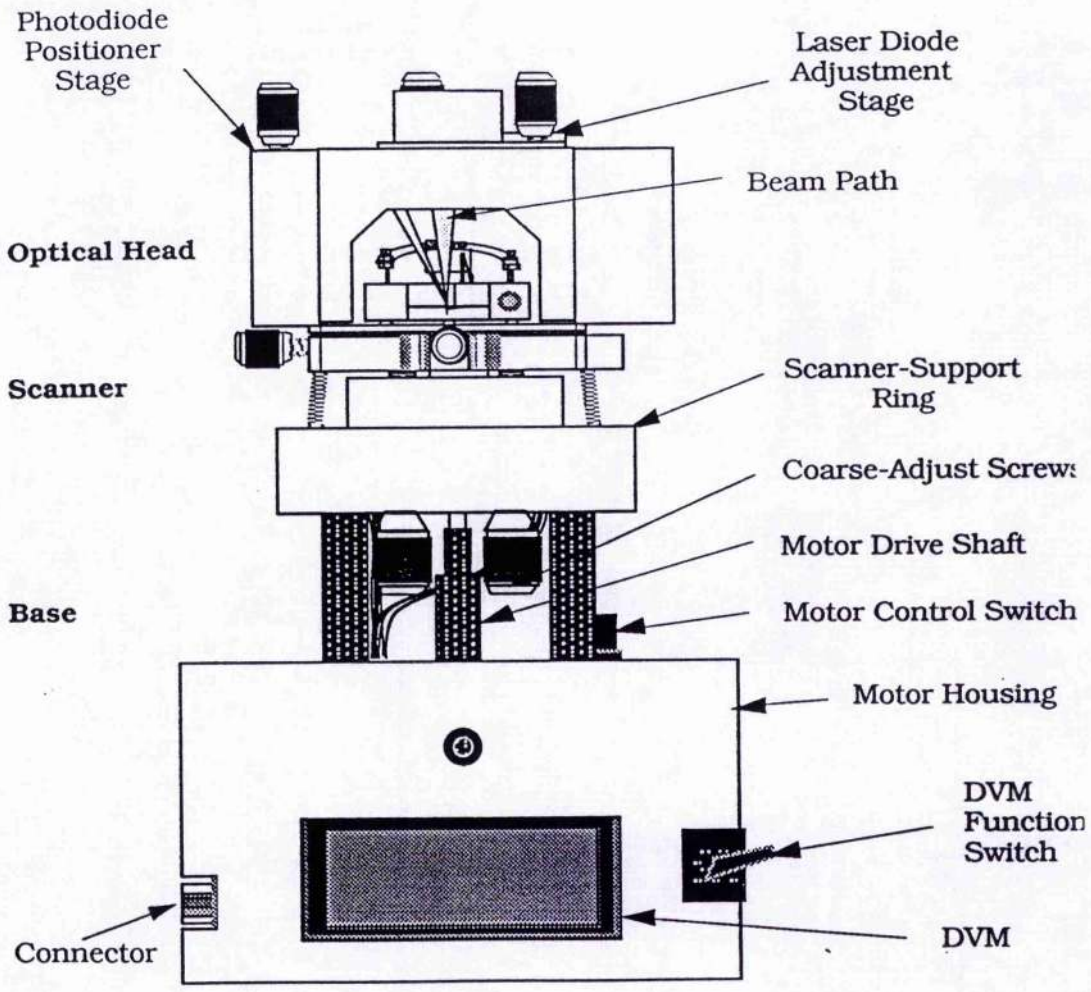

The AFM used in this study is a Nanoscope II made by Digital Instruments Inc. in U.S.A. Figure 4-2 shows a schematic diagram of the AFM. Like other atomic force microscopes, Nanoscope II consists of five essential components:

1. A sharp tip mounted on a soft cantilever spring
2. A means of sensing the cantilever's deflection
3. A feedback system to monitor and control the deflection
4. A mechanical scanning system (piezoelectric)
5. A display system that converts the measured data into an image

Additionally, a potentiostat is attached to the AFM and it is used for in-situ electrochemistry measurement in AFM studies.

4.3.2 Cantilevers and tips

Early cantilevers used in the initial measurements in atomic force microscopy were made of either metal wires or foils, while modern cantilevers are microfabricated from silicon, silicon oxide or silicon nitride with typical dimensions of the order of 100 microns in diameter and 1 micron in thickness. In this condition, the spring constants of the cantilever are in the range of 0.1-1 N/m or even less.

A tip is one of the critical component of AFM, as the resolution of AFM greatly depends on its quality. Today several types of tips are commercially available. In this study, silicon nitride tips and silicon tips are used. The silicon nitride tip has a pyramidal shape and it has been widely used in general AFM studies. The silicon tip is a new type tip which is sharper than the silicon nitride tip because of its smaller radius and open angle. Figure 4-3 shows the pictures

of both cantilevers.

Figure 4-3 a) Silicon nitride tip, b) silicon tip.

a)

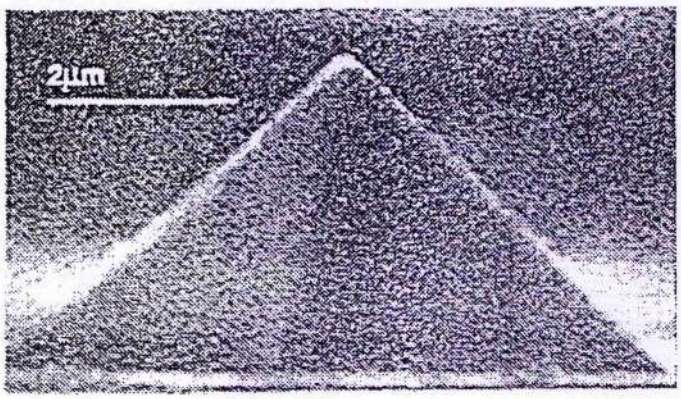

b)

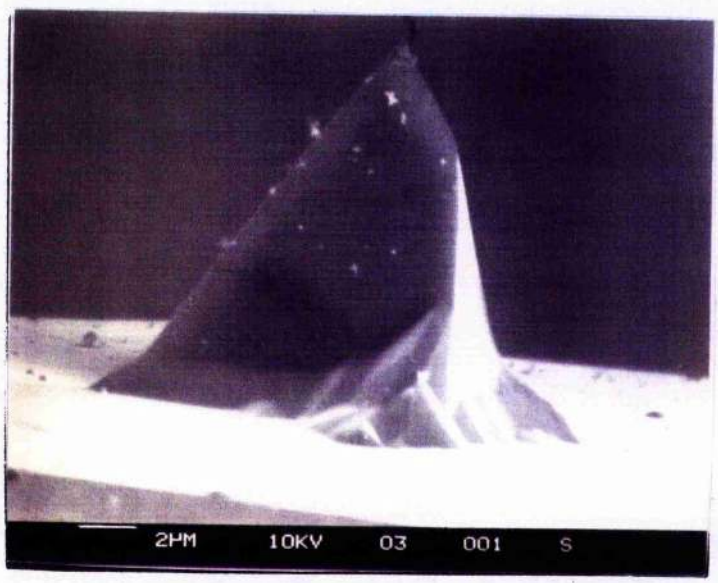

Figure 4-4 Fabrication of a pyramidal silicon nitride cantilever.

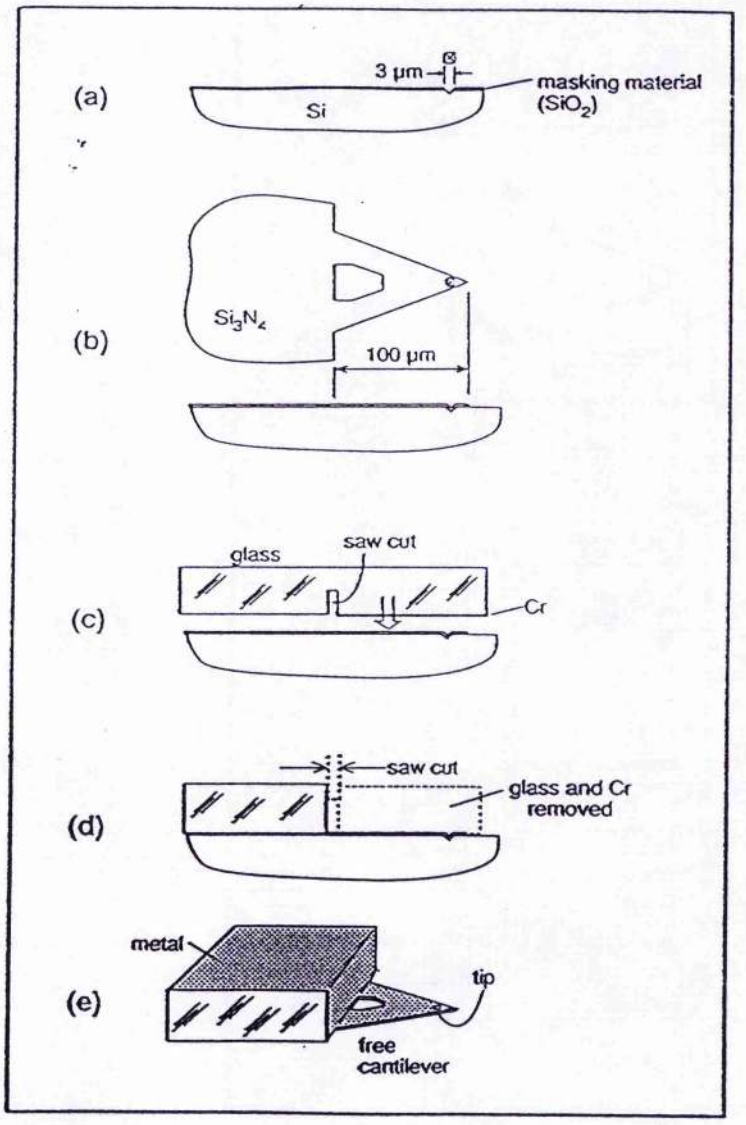

Figure 4-4 shows a commercial method, described by Albrecht (1989), for the production of pyramidal silicon nitride cantilevers. A SiO_2 mask is deposited on a Si (100) substrate and 3 x 3 μm square windows are then opened in the mask to expose the silicon substrate. Following this the silicon is etched anisotropically through the windows to form the pyramidal pits, and afterwards

the SiO_2 mask is removed and a Si_3N_4 layer is deposited over the surface conforming to the shape of the pyramidal pits. The cantilever is produced by patterning its shape on the nitride film, bonding a glass plate to the film, etching the silicon substrate away and coating gold on the back of it. Figure 4-5 shows the cantilever on the glass plate and Table 4-1 gives the spring constant values of these cantilevers.

Table 4-1 Spring constant values of the cantilevers

Cantilever Type	K(N/m) (narrow legs)	K(N/m) (wide legs)
100 micron triangular	0.38	0.58
200 micron triangular	0.06	0.12

Figure 4-5 A silicon nitride cantilever as used in this study.

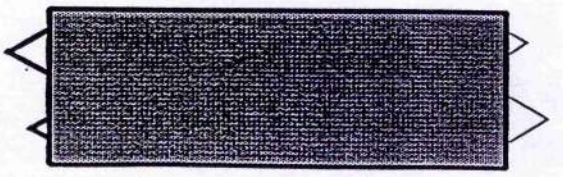

The 200 μm cantilever is for general usage and the 100 μm triangular cantilever is very useful for atomic scale images. In the in-situ electrochemical AFM study, however, the charging and refreshment of the electrolyte during the experiment places a considerable load on the cantilever. In this case, the 200 μm cantilever with the wide legs is the best choice.

4.3.3 Deflection detector

In addition to the tip, the sensor is another critical component of AFM. The first deflection sensor used by Binnig was based on the electron tunnelling principle (Binnig and Rohrer, 1982). In this implementation, a tip is brought into tunnelling range behind the cantilever during operation and the deflection of the cantilever caused by scanning the sample under the cantilever changes the tip-cantilever tunnel current which is detected as a signal. Although atomic resolution was achieved by this technique, the tunnelling tip may exert a force on the cantilever separated in a few angstroms and the force may affect the sensitivity of the sensor. Additionally, contamination of the tunnelling surfaces will also degrade the sensitivity of the sensor in practical use (Binnig *et al*, 1986, Albrecht and Quare, 1987, Meyer *et al*, 1988, Marti *et al*, 1987).

For these reasons, some other techniques have been introduced. Among them, the optical lever method is the simplest technique which is used in Nanoscope II. In this implementation (Meyer and Amer, 1988, Amer *et al*, 1988, Alexander *et al*, 1989), the deflection of the laser beam caused by bending of the cantilever is detected by a two-segment photodiode and the change of intensity is recorded as a signal to be converted into an AFM image. In contrast to the tunnelling method, the deflection sensor used in the optical technique is

far from the lever at distances of the order of centimetres. This technique has a standard resolution of the order of 0.1 angstrom.

4.3.4 Cantilever mount

There are two cantilever mounts used in Nanoscope II: a metal mount and a glass mount. The metal mount is used for operation in air and the glass mount can be used as an electrochemical cell for operation in solutions. As the most AFM studies in this thesis are carried out in solutions, the glass mount which is not commonly used is described here in detail.

The glass mount contains a counter electrode made of a piece of platinum wire and a reference electrode made of a piece of lead wire; the reference electrode which forms a $Pb/PbSO_4$ electrode in sulphuric acid with a value of 0mV (E_{H2SO4})=-126 mV (E_H) in 0.1 M H_2SO_4 (Figure 4-6 a). During operation, the glass cantilever mount is placed above the sample and a plastic ring forms the wall of the cell. The laser beam passes through the transparent mount matrix and falls on the end of the cantilever, so the reflection can be detected as in air. Fluid is injected in or drawn out during the experiment from the inlet and the outlet in the mount matrix (Figure 4-6 b). If required, a potential can be applied to the sample by switching on an attached potentiostat.

Figure 4-6 a) Glass cantilever mount.

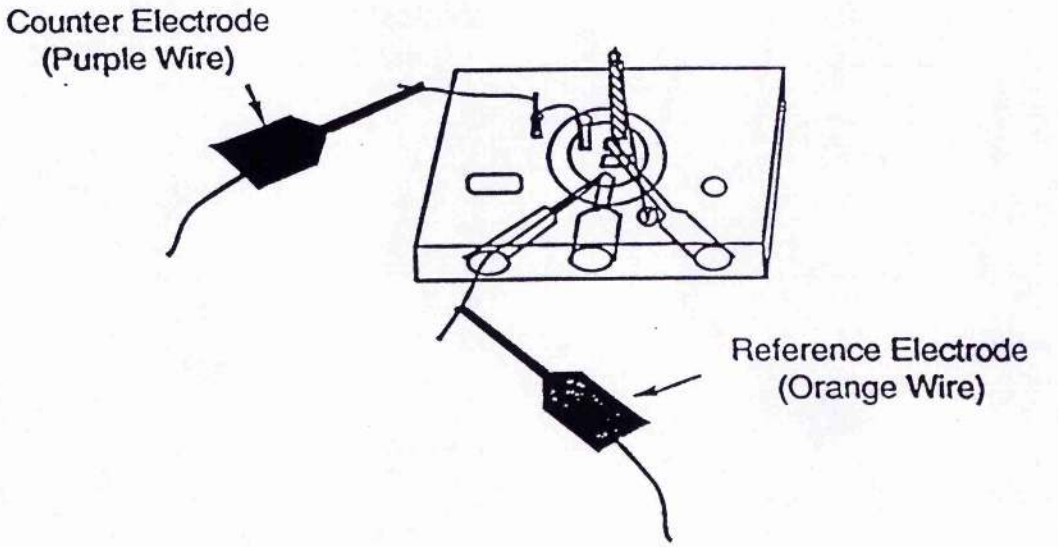

Figure 4-6 b) Operation in solution by the glass cantilever mount.

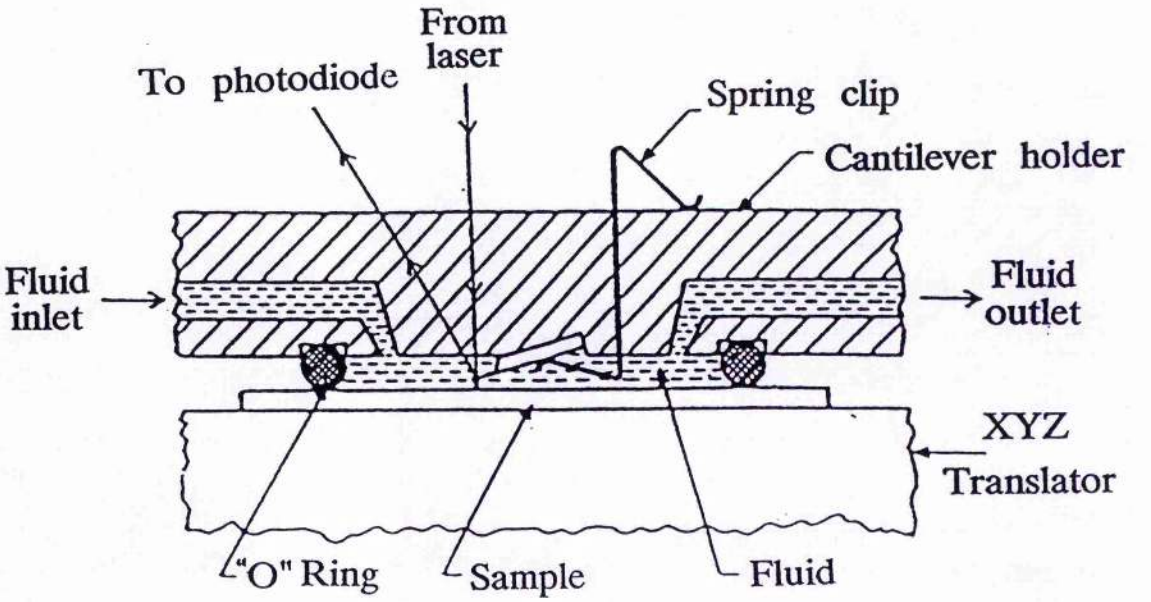

4.4 AFM image

As mentioned previously, the Nanoscope II AFM can be operated in two measurement modes: the height mode and the force mode, under which the corresponding images are available. Figure 4-7 shows the surface of a corroded duplex stainless steel in HCl, in which Figure 4-7a is the force mode image and Figure 4-7b is the corresponding height mode image. By comparing these two images, it can be seen that the resolution of the height mode image is not as good as that of the force mode image, but the former can be displayed as a three dimensional image, which gives not only good planar resolution but also good depth resolution (Figure 4-7c). Thus a complete nature of the surface feature can be presented in height mode images and its size can also be measured. Figure 6-8 is an example: the measurement of a corroded feature in Figure 6-7 shows that it is 1338 nm wide, 479.3 nm high and the gradient of the sidewall is 37.82 degree. Not only surface features, surface roughness is measurable in AFM as well. Figure 4-9a shows a corroded surface and the roughness of the surface is measured in Figure 4-9b. Following the measuring line, the characteristic period of the roughness is 1000 nm, i.e. this is that occurred most frequently.

Figure 4-7 a) A force mode image, b) a height mode image, c) a height mode image in three dimensional display mode.

a)

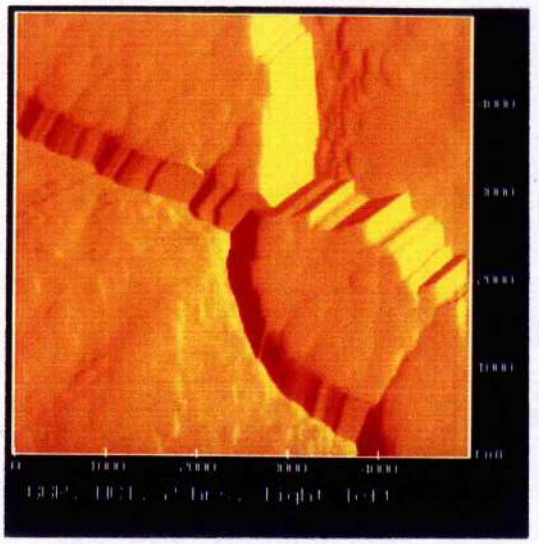

b)

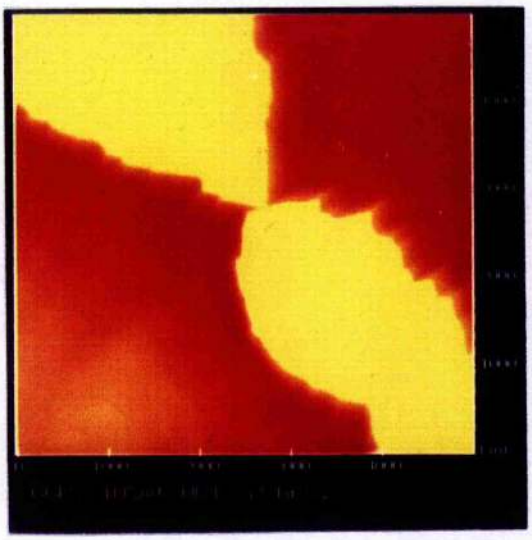

c)

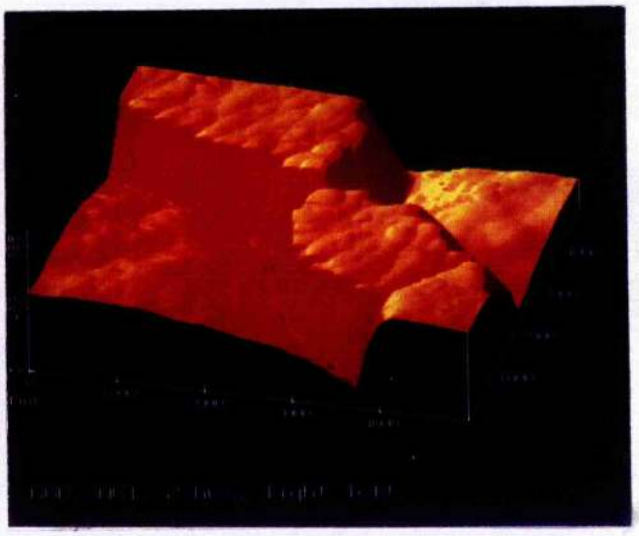

Figure 4-8 Three dimensional measurement of the surface feature.

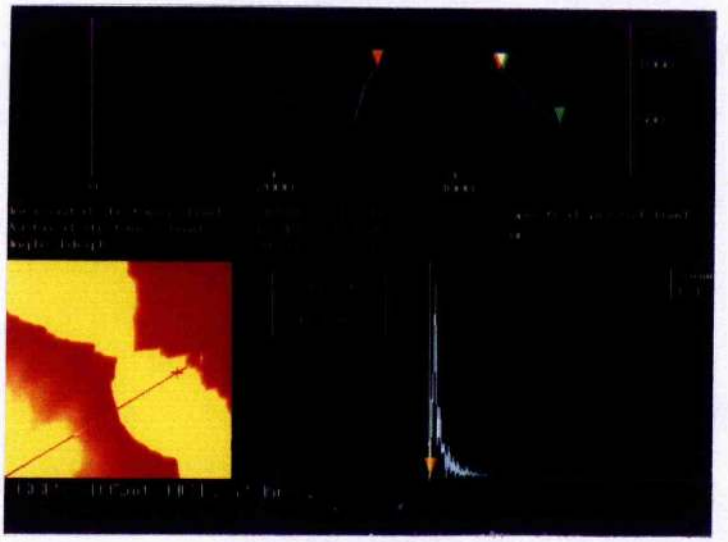

Figure 4-9 AFM measurement of the surface roughness, a) a rough surface, b) roughness measurement by the height mode image.

a)

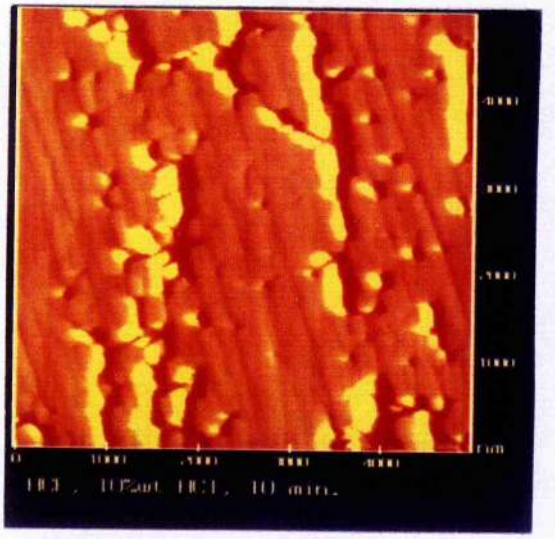

b)

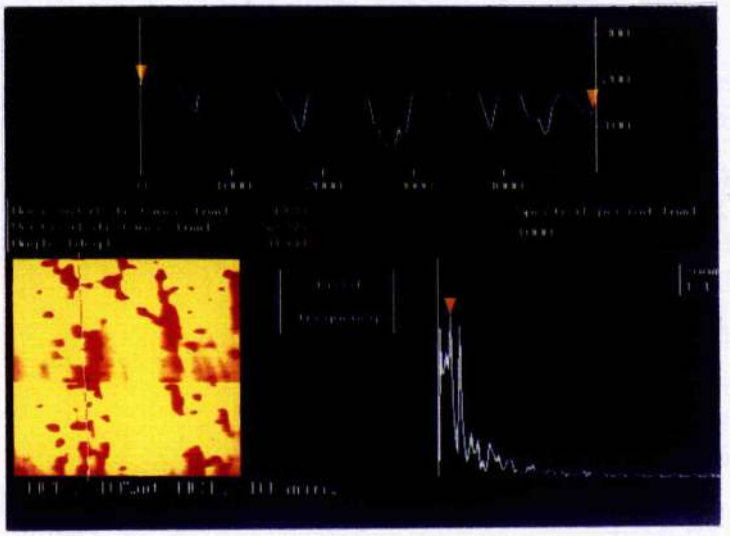

Though pyramidal tips can provide high resolution images, even atomic images, several papers have reported the distortion of AFM images caused by unsatisfactory tip sharpness (Hellemans *et al*, 1991, Allen *et al*, 1992, Grütter *et al*, 1992, Keller *et al*, 1992, Schwarz, 1994). For example, sharp features may be broadened and the vertical sidewalls may appear as steeply slopping sidewalls. Keller and his colleagues defined the "sharpness" of SPM tips by two parameters: a) the radius of the tip end, R, and b) the "cone angle" or "opening angle", which can be described as a radius of curvature,R,' indicates the increasing rate of the tip diameter upwards from the point (Keller, 1991, Keller *et al*, 1992). If a tip has an end radius,R, and a radius of curvature,R', the corresponding feature in the image will have an apparent radius of curvature,R+R'. Therefore, when a tip scans a steep sidewall whose gradient (from the vertical) is smaller than the tip angle, the sidewall in the image will appear to have the tip angle rather than the true sidewall angle. Figure 4-10 demonstrates the possible distortion of the steep sidewall. The area where the tip cannot scan properly was named as "hole

region" by Keller (1991). This is an area of investigation in this thesis since corrosion often produces very rough surfaces. In work to be described, different tips have been used to assess the impact of tip shape on the observed features. The tip radius can also distort roughness measurements (Figure 4-11), when the tip is unable to follow the surface topography exactly because of its end radius or its open angle.

Figure 4-10 The vertical sidewall shown as a steep sidewall by the tip with a large open angle (Grigg *et al* 1992).

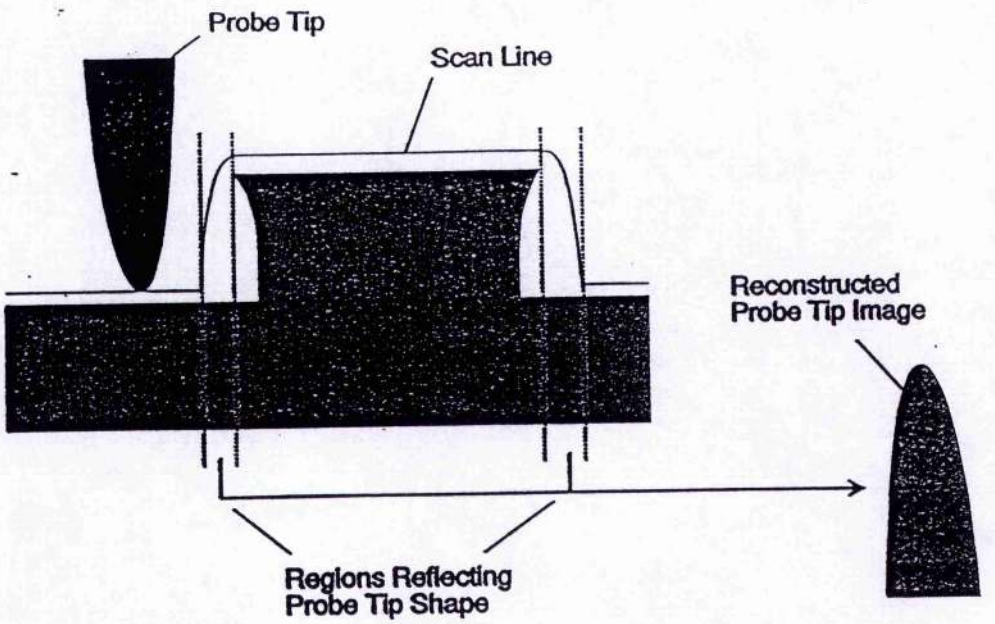

Figure 4-11 Possible distortion in AFM roughness measurement caused by tip radius and tip cone angle (Gise and Smith 1992).

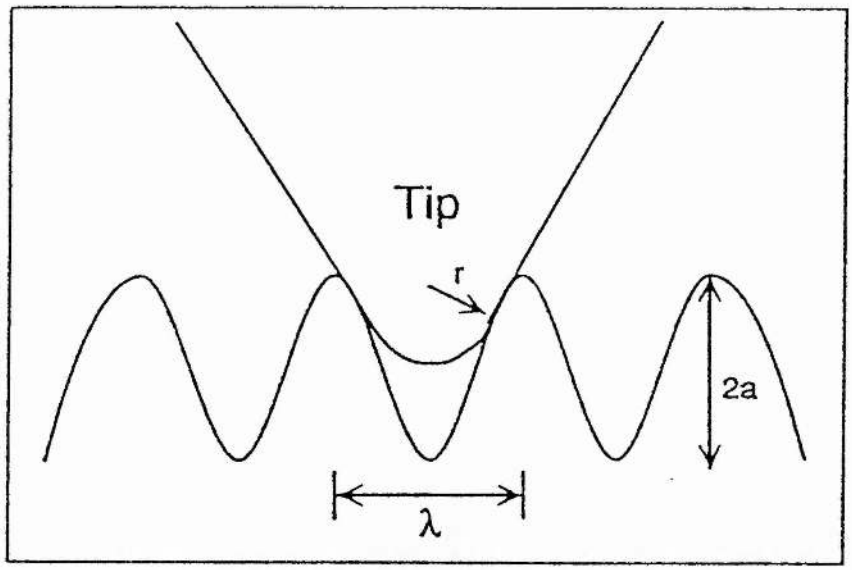

AFM is a valuable technique for surface study, but because it is a new technique, various problems may occur during the study. Therefore, it is an important topic for scientists to understand contrast obtained during AFM scans. In this study, the reality of structures on the corroded surface showing in AFM images is investigated and the results are shown and discussed in Chapter 6.

Prior to XPS analysis and ex-situ AFM study, the electrochemical measurements are carried out and the process is indicated in Chapter 5 step-by-step.

CHAPTER 5

ELECTROCHEMICAL MEASUREMENT

5.1 Introduction

Studying electrochemical corrosion can be traced back to the 19th century, but little progress was made until the 20th century. At the beginning of this century, Whitney (1903) found electro-current in the aqueous corrosion of iron for the first time, which revealed that corrosion could be an electrochemical process. Wagner and Traud (1938), then, raised the famous mixed potential theory and Pourbaix (1945) published potential - pH diagrams. In 1955, the first polarization curve of Fe-Cr alloy was presented by Oliver (1955) and as an essential method, it has been commonly accepted and widely used today to investigate the electrochemical property of materials. Computer techniques have greatly benefitted the study of corrosion. All the advanced equipment for electrochemistry study nowadays is controlled by computer and using such equipment, electrochemical curves can be recorded automatically.

Since corrosion is a process occurring on metal surfaces, some attempts have been made to connect an electrochemical cell to a surface analytical

instrument to obtain real-time information of a sample surface during its exposure under electrochemical conditions. For example, Olefjord (1980) fitted an electrochemical cell on XPS or SAM equipment to analyze the composition of surface films formed under different electrochemical conditions. In the current study, an electrochemical cell attached to an AFM allows the surface topography and the kinetics of corrosion and passivation to be studied in mediums by continuous scanning under controlled electrochemical conditions.

Potential difference on a surface may cause pitting or other types of localized corrosion, which attracts scientists' attention and they try to measure the potential at the interesting site. However, traditional electrochemical methods only provide an even etching rate of the surface. Though AFM cannot measure the potential difference in the different parts of the surface, it can draw a three dimensional picture of the corroded surface to estimate the differential etching rate caused by potential difference. Therefore, the AFM with an electrochemical facility is very valuable for studying the alloy surface etched by different rates.

5.2 Instrumentation

5.2.1 Potentiostat

A potentiostat Model 173 EG & Go made by Princeton Applied Research was used in this study to measure the polarisation curve of 516 alloy. It was controlled by an Apple II micro computer and the experiments ran with a corrosion software of Model 332 SoftCorr. Another potentiostat, Model LT78, was also used for the potentiostatic experiments to record the current-time curves at anodic potentials. A potentiostat for in-situ AFM studies was attached to the

AFM and was controlled by a computer linked with the AFM. During polarisation, the instantaneous current was shown on the screen of the computer at intervals.

5.2.2 Electrochemical cell

A traditional three-electrode cell was used for polarisation of the samples for XPS analyses or ex-situ AFM studies (Figure 5-1). The reference electrode was a 0.1 M mercury-mercurous sulphate electrode having a value of $0mV(E_{Hg2SO4})$ = 676 mV (E_H) in 0.1 M H_2SO_4.

During operation, a sample was hung in the cell vertically as a working electrode and it formed a circuit in solution (with a counter electrode made of 1 cm^2 platinum foil). The reference electrode which was in a separated tube approached the sample surface by means of a probe to measure applied potentials controlled by a potentiostat.

Figure 5-1 Three electrode electrochemical cell.

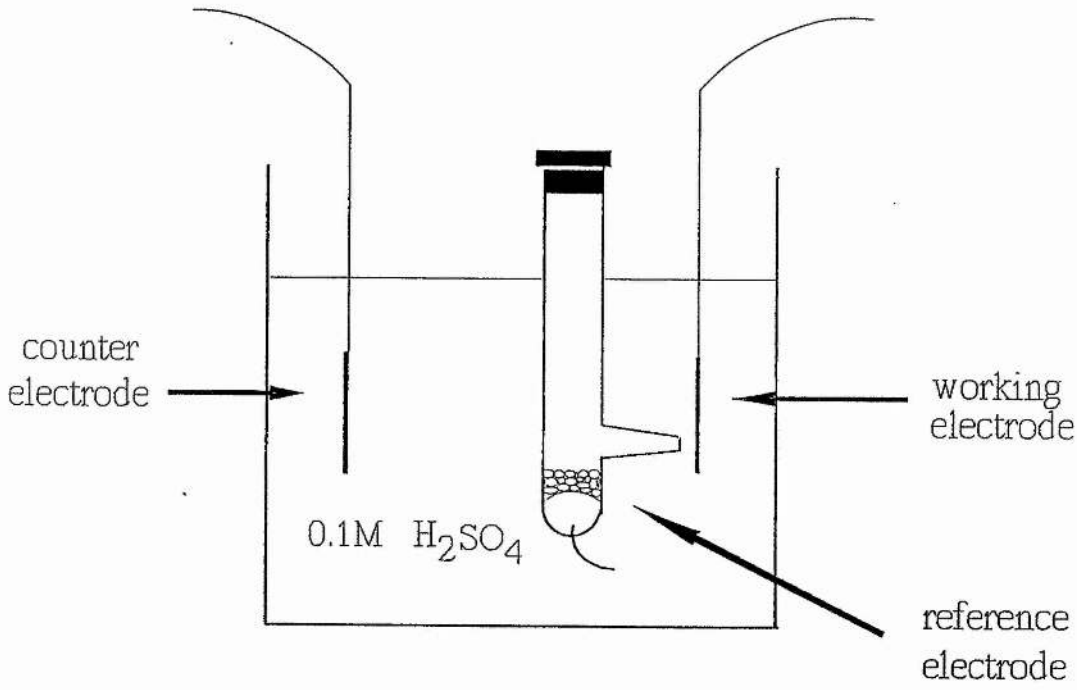

The electrochemical cell for in-situ AFM studies was a transparent cantilever mount which has been described in Chapter 4 (Figure 4-11). Instead of standing in a vertical position, the sample was placed horizontally forming the bottom of the cell which has a working area of 0.41 cm^2. The reference electrode was a piece of lead wire which forms a $Pb/PbSO_4$ electrode in sulphuric acid with a value of

0 mV ($E_{Pb/PbSO4}$) = -126 mV (E_H) in 0.1M H_2SO_4.

5.3 Sample preparation

In order to obtain an even electric field on the sample surface, the sharp edges of the sample are avoided. Figure 5-2 shows an elliptic sample for ex-situ studies, which has a area of 1.3 cm^2 and has a long handle to keep connection wires out of the solution. The non - working area of the surface is sealed by Lacomit. Samples for in-situ AFM studies, however, are circular samples with a diameter of 1.0-1.5 cm to fit the sample stage in AFM.

Figure 5-2 Samples.

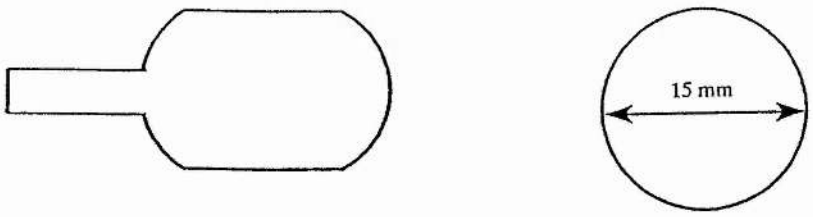

Ex-situ sample **In-situ sample**

All the samples were ground on 320, 500 and 1000 grit emery papers and polished on 6μm, and 1μm polishing plates to an 1μm finish before ex-situ and in-situ studies.

5.4 Experimental procedure

The electrochemical experiments for passivation studies were carried out in both the traditional cell for ex-situ studies and the AFM electrochemical cell

for in-situ AFM studies. The solution used was 0.1 M sulphuric acid, though other concentrations (0.05 M and 0.5 M) were also used in pre-investigations. The electrochemical treatments in this study followed the process used in the European Federation of Corrosion (EFC) round robin work (Marcus and Olefjord 1988) as closely as possible, i.e. before a passivation experiment started in the traditional cell, the sample was pretreated by cathodic polarisation at -5 mA/cm^2 for 5 minutes to remove the surface film formed in air and then the sample was exposed at the corrosion potential for another 5 minutes to desorb hydrogen formed during the cathodic polarisation. However, the pretreatment in AFM cell for in-situ study was modified, because the rapid production of bubbles during the cathodic reduction damaged the cantilever. The cathodic polarisation, therefore, was replaced by mechanical polish for oxide removal.

Electrochemical experiments in this study included potentiodynamic polarisation and potentiostatic polarisation. In the potentiodynamic polarisation, a wide potential region including the cathodic region, the active region, the passive region and the transpassive region was scanned at a scan rate of 0.33 mV/s or about 20 mV/min. The potentiostatic polarisations started by jumping the potential from the corrosion potential to an anodic potential in the active or the passive region and the potential was held for a given time. The sample was then removed from the solution immediately, rinsed in water and dried in air.

For in-situ AFM study, the polished samples were loaded on the sample stage in the AFM and scanned in pure water to adjust the laser beam and other parameters until the satisfactory images were obtained. By this way, the corrosion was minimized at this state.

The passivation started by replacing water with 0.1 M sulphuric acid solution and applying an anodic potential. The bubbles produced during passivation were removed by changing the solution frequently with care. In in-situ corrosion study of duplex stainless steels, 10%wt HCl solution was used. When the two phases were sufficiently differentiated, if it was required, HCl was replaced by 0.1 M sulphuric acid and a passivation potential was applied to study how the passivation occurring on an active surface.

The equipment and the experimental procedures have been described in Chapters 3, 4 and 5 individually. The results obtained in this study are discussed in Chapter 6.

CHAPTER 6

RESULTS AND DISCUSSIONS

6.1 Passivation of molybdenum-bearing alloys

6.1.1 Materials

In order to study the role of molybdenum in passivation of steels, it is necessary to seek an experimental material in which molybdenum enrichment in the surface can be obtained under the given passive conditions. It has been found in the previous work of this laboratory that a Mo-enriched passive film can be obtained by polarising 516 alloy in 0.1 M H_2SO_4 (Qiu, 1989) and, therefore, this alloy is used for studying the passivation in this work. For a comparison, the other two molybdenum-free, alloys, 515 alloy (Fe17Cr) and 304 steel (Fe19Cr10Ni), are also used. The chemical compositions of the alloys are listed in Table 6-1.

Table 6-1 Chemical analysis of the samples.

Sample		516	515	304	GGR
C	wt%	0.01	0.022	<0.08	0.031
	at%	0.047	0.099	<0.36	
Si		0.045	0.047	<1.00	0.46
		0.091	0.094	<1.95	
Mn		0.0012	0.0054	1.80	1.60
		0.0012	0.005	1.79	
P		0.006	0.004	<0.04	0.02
		0.011	0.007	<0.07	
S		0.0042	0.0023	<0.03	0.01
		0.0074	0.0039	<0.05	
N		0.012	0.019	----	0.1
		0.049	0.077	----	
Al		<0.001	<0.001	----	----
		<0.0021	<0.0022	----	
Cu		----	----	<0.40	----
		----	----	<0.34	
Cr		14.9	16.8	18.5	22.2
		16.24	17.78	19.44	
Mo		4.02	<0.01	----	3.1
		2.37	<0.0055	----	
Ni		----	----	9.60	6.1
		----	----	8.94	
Fe		81.00	83.09	68.55	66.38
		81.18	81.93	67.06	

6.1.2 Exploration of molybdenum enrichment conditions

Exploring the conditions for maximum molybdenum enrichment is the first step in the investigation, as molybdenum may exert its greatest effect under this condition. Though molybdenum enrichment has been found in 0.1 M sulphuric acid, it can be changed in different solutions, potentials and polarisation times and, therefore, a preliminary study of the experimental effects on the degree of molybdenum enrichment was carried out first.

Figure 6-1 Three polarisation curves of 516 in 0.01 M, 0.1 M and 0.5 M H_2SO_4.

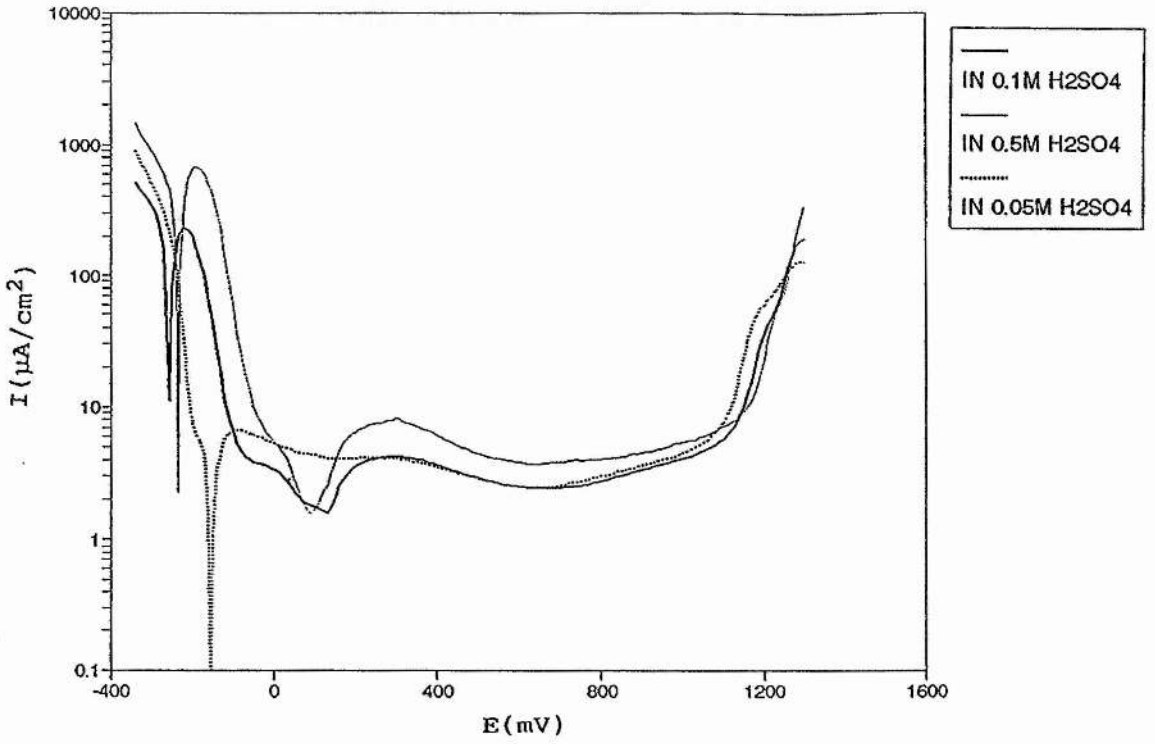

Several polarisation curves were measured in a range of solutions (0.05 M, 0.1 M and 0.5 M H_2SO_4) in order to determine the electrochemical properties of 516 alloy in the given solutions and to select the potentials in different regions for the further XPS analysis. These polarisation curves are shown in Figure 6-1 and the parameters of these three curves are listed in Table 6-2.

Table 6-2 Parameters of polarisation curve.

H_2SO4 solution	corrosion potential (mV/ SHE)	critical potential (mV/ SHE)	the Flade potential (mV/ SHE)	critical current $\mu A/cm^2$	passive current $\mu A/cm^2$
0.05 M	-154		-84		2
0.1 M	-256	-218	-104	233	2
0.5 M	-244	-202	-40	690	4

It can be seen from the polarisation curves that the major differences of these three curves are in the low potential region where the corrosion potentials, the critical currents and the passive currents are all different. For example, the active/passive transition cannot be observed in the 0.05 M H_2SO_4 curve, while the high active current in the active region (690 $\mu A/cm^2$) is clearly revealed in the 0.5 M solution curve, which is three times higher than that of the 0.1 M solution curve. On the contrary, the three curves show similar properties in the high potential of the passive region. Also, the passive currents in this region are very similar and they all reach the transpassive regions at a similar potential, i.e. around 1200 mV.

In these three curves, the following characteristic potentials were selected

for polarising the samples which were studied subsequently by XPS: the potential at the active peak (critical potential); the potential in the region of active-passive transition; the low potential in the passive region (close to the Flade potential); and the potential close to the maximum sustainable in the passive region. The exact values of the potentials which were chosen varied slightly from one solution to another but this was considered to be unimportant to the present study.

After one hour polarisation at the characteristic potentials in the three solutions, the samples were analyzed by XPS. All survey scans of XPS spectra were set in the range of 0 - 1000 eV with a pass energy of 50 eV. From the survey scans, the presence of C, O, Mo, Fe and Cr in polarized surfaces was observed and hence narrow scans of these elements were carried out following each survey scan. The scan ranges of narrow scans were around about 30 or 40 eV depending on the elements, and the pass energy was 20 eV. The peak areas of Fe, Cr and Mo, which included metallic and oxidic components, were then measured from the narrow scans for quantitative analyses.

To measure the enrichment of metal ions in the surface relative to the metal matrix, the following enrichment factors are defined. For molybdenum, F(Mo) is:

$$F(Mo) = \frac{[Mo/(Mo+Fe+Cr)]_{surface}}{[Mo/(Mo+Fe+Cr)]_{alloy}} \qquad (6-1)$$

Similarly, the enrichment factor of chromium F(Cr) is defined as:

$$F(Cr) = \frac{[Cr/(Mo+Fe+Cr)]_{surface}}{[Cr/(Mo+Fe+Cr)]_{alloy}} \qquad (6\text{-}2)$$

If the enrichment factor is larger than or less than 1, then the Mo or Cr content in the surface is either enriched or depleted, respectively. For an enrichment factor equal to 1, the Mo or Cr content in the surface equals that in the alloy.

Table 6-3 Enrichment factors of Mo, Fe and Cr in surface after one hour polarisation at the selected potentials in 0.05 M, 0.1 M and 0.5 M H_2SO_4 solutions.

solution conc.	F(M)	potentials a.p*	a-p.t**	l.p***	hp****
0.05 M	F(Mo)	1.39	1.52	1.43	1.39
	F(Cr)	1.78	1.88	1.97	3.23
	F(Fe)	0.83	0.81	0.80	0.55
0.1 M	F(Mo)	1.9	2.32	3	1.81
	F(Cr)	1.62	1.77	2.2	3.23
	F(Fe)	0.85	0.81	0.7	0.53
0.5 M	F(Mo)	1.94	2.11	2.24	0.93
	F(Cr)	1.81	2	2.11	3.31
	F(Fe)	0.81	0.77	0.73	0.54

* active peak potential
** active-passive transition potential
*** low potential of passive region
**** high potential

Table 6-3 shows the results of XPS analyses. By comparing the molybdenum enrichment factors at different potentials, it is clear that the highest one is almost always observed in 0.1 M H_2SO_4 and the enrichment is pronounced

in the low potential region in different solutions. The latter corresponds to the reports in the literature (Olefjord, 1980, Goetz and Landolt, 1984, Hashimoto et al, 1979[1]). Therefore, 0.1 M H_2SO_4 has been chosen as the electrolyte in this study and special attention is paid to the low potential region.

Table 6-4 Enrichment factors of Fe, Cr and Mo on the surface after polarisation in 0.1 M H_2SO_4 for different elapsed times.

		Time				
E(mV)	F(M)	10 min.	1 hr	2 hrs	3 hrs	24 hrs
-224	F(Mo)		1.27	1.98	2.07	2.69
(a)*	F(Cr)		1.45	1.72	1.51	1.69
	F(Fe)		0.9	0.83	0.87	0.81
-204	F(Mo)	1.9	1.9	2.36	1.9	2.96
(a.p)**	F(Cr)	1.94	1.62	1.78	1.94	2.16
	F(Fe)	0.78	0.85	0.81	0.77	0.71
-174	F(Mo)	2.07	2.32	2.03	2.62	2.31
(a-p.t)***	F(Cr)	2.02	1.77	2.06	2.43	2.48
	F(Fe)	0.77	0.81	0.76	0.68	0.68
-104	F(Mo)	1.9	3.0	3.0		
(l.p)****	F(Cr)	2.03	2.2	2.2		
	F(Fe)	0.77	0.7	0.7		

* active potential
** active peak potential
*** active/passive transition
**** low potential of passive region

In order to establish an optimum experimental time for molybdenum enrichment, a series of electrochemical experiments were carried out in the low potential region (the active potential region and the low potential of the passive region) for 10 minutes, 1 hour, 2 hours, 3 hours and 24 hours. The results in Table 6-4, which were obtained from the subsequent XPS analysis, show the

relationship between molybdenum enrichment and polarisation time. In the active potential region, the enrichment of molybdenum varies with exposure time, which probably results from poor adhesion of corrosion products under the active dissolution condition. In the passive region, F(Mo) reaches a sufficiently high value in one hour polarisation and this value remains approximately constant when the polarisation time increases to two hours. Hence, one hour polarisation is considered an ideal experimental duration for composition analysis.

Based on the above work, 0.1 M H_2SO_4 and one hour polarisation time were chosen for further XPS studies. As it can be seen from Table 6-4 the enrichment factors of Mo is significantly greater than that of Cr throughout the low potential region and it is to this region that attention is paid.

6.1.3 Nature of passive film

6.1.3.1 Elemental identification by XPS

Using the selected conditions: 0.1 M sulphuric acid and one hour polarisation time, the compositions of the surface at a series of potentials "a", "b", "c", "d", "e", "f" and "g" in the polarisation curve (Figure 6-2) were analyzed by XPS to study the change of elemental concentration with potential in the polarized surface. Of special note is that potential "a" is the critical potential (-204 mV), potential "c" is the low potential of the passive region, (-104 mV, close to the Flade potential or the completed passivation potential) and potential "g" is the potential close to the maximum sustainable potential of the passive region (900 mV).

Figure 6-2 The potentials "a", "b", "c", "d", "e", "f" and "g" are selected in the polarisation curve to polarise samples for subsequent XPS analyses.

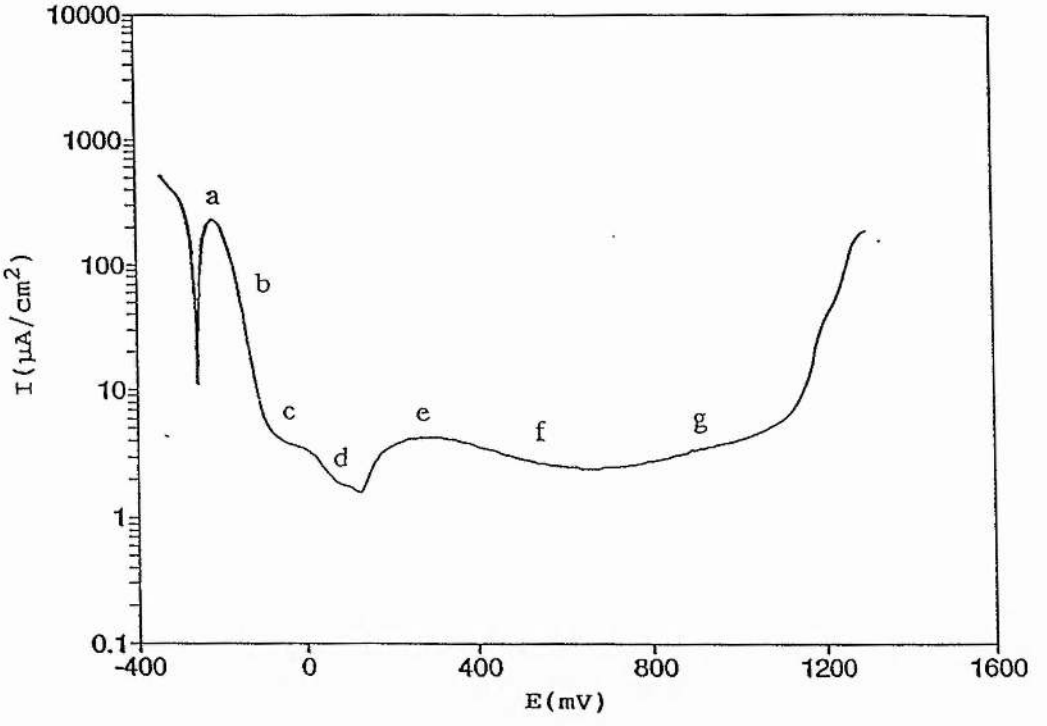

As shown in Figure 6-3, XPS analyses indicate that C, O, Fe, Cr and Mo are present in the surfaces at different potentials, but their concentrations vary with potential (Figure 6-3). For example, the chromium content increases with increasing potential, while the iron content decreases. The rising background after the iron peak at higher potentials shows that this element contributes to the spectra from beneath the surface film. The weakness of the molybdenum signal makes it impossible to inspect its change in the survey scans. The carbon peak in the spectra comes from the contamination in the air, electrolyte and vacuum involved in the transfer process.

Figure 6-3 XPS survey scan spectra of 516 alloy, after one hour polarisation at potentials "a", "b", "c", "d", "e", "f" and "g" in 0.1 M H_2SO_4.

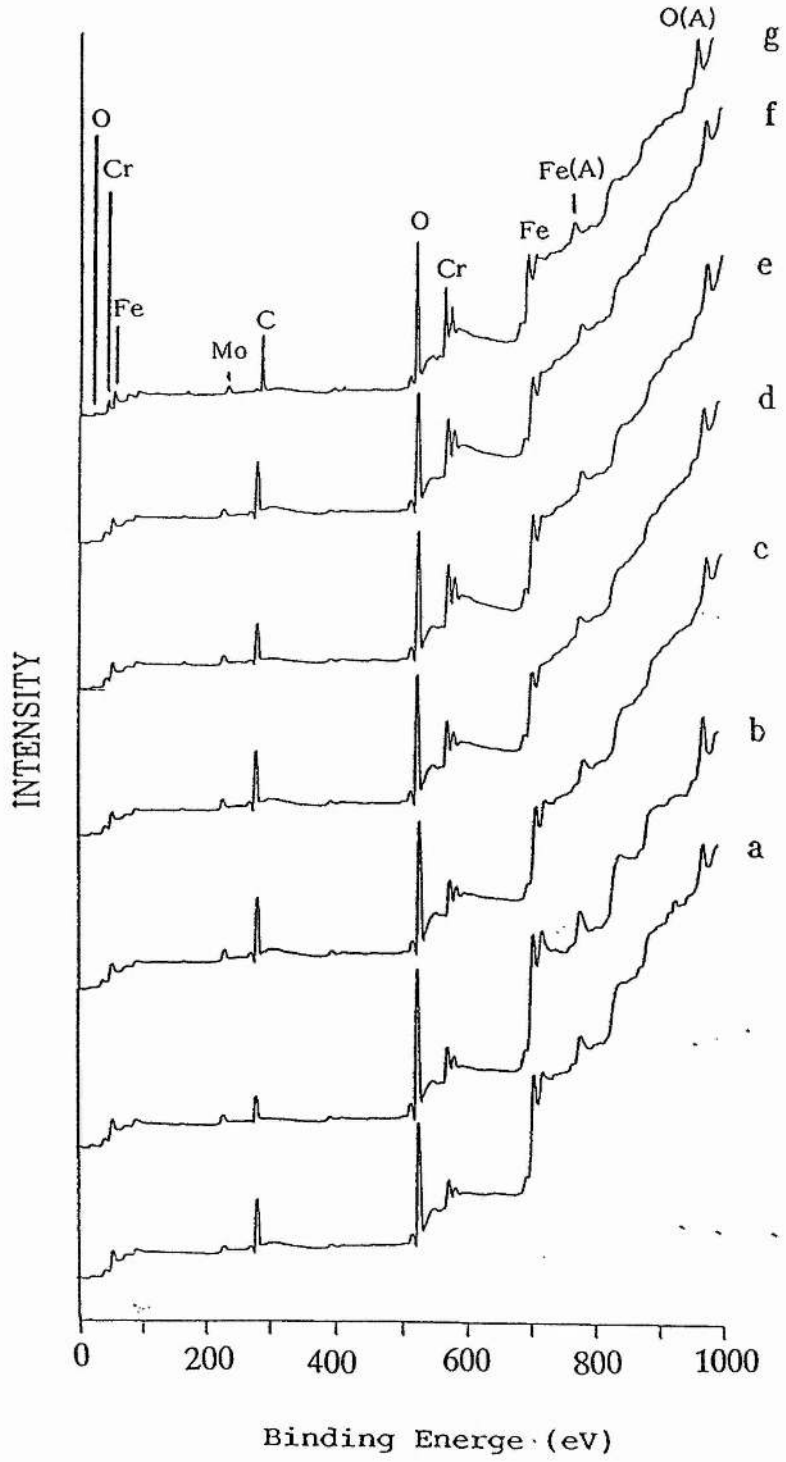

As described in the preliminary work, the surface compositions were quantified by measuring the areas of the narrow scans of Fe, Cr and Mo and the enrichment factors of Cr and Mo were determined according to equations 6-1 and 6-2. The curves of F(Mo) and F(Cr) in Figure 6-4 show the contrasting behaviour of molybdenum and chromium with regard to their concentration in the surface. Molybdenum enrichment factors clearly exceed those of chromium throughout the active region, the active/passive region and the low potential of the passive region.

Figure 6-4 Enrichment factors of molybdenum and chromium as the functions of the potential.

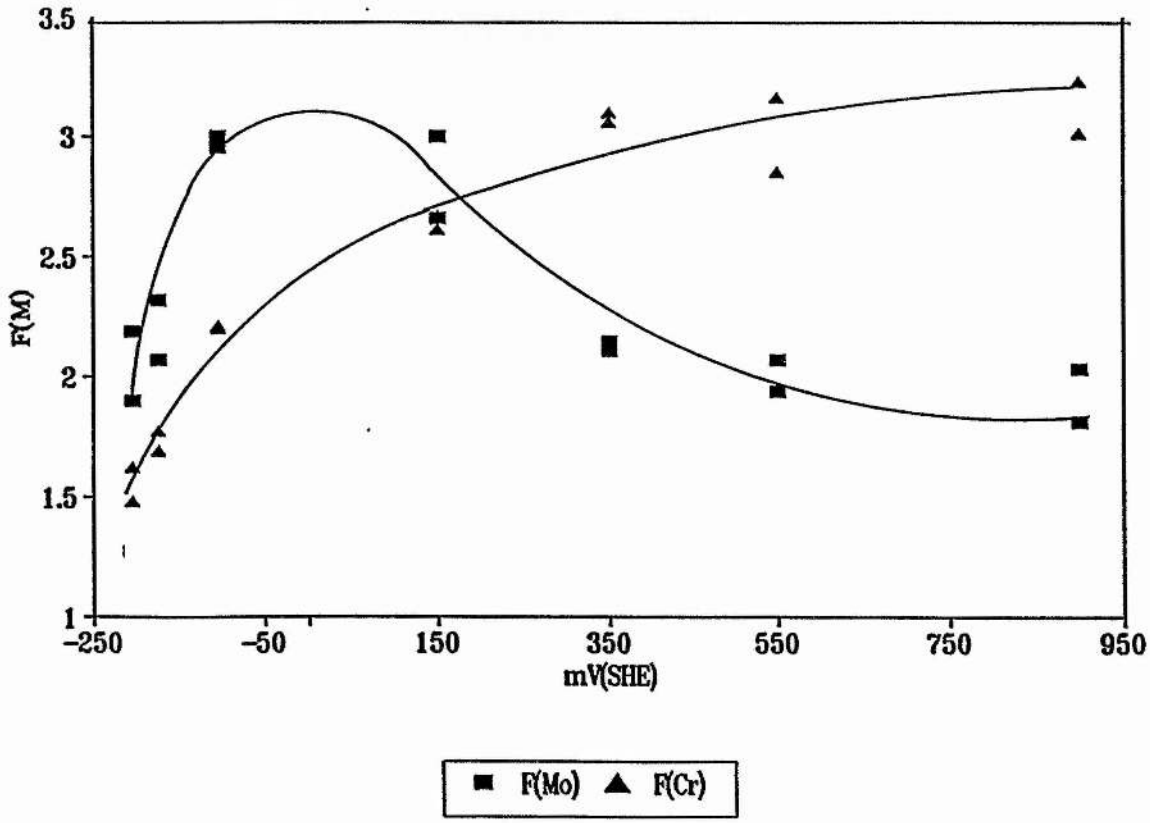

At the potential "c", the molybdenum concentration of the surface reaches a maximum value, F(Mo) of 3; i.e. molybdenum in the analyzed region is three times higher than that in the bulk alloy. The enrichment of molybdenum remains at a high value for only a limited part of the passive range. The low potential range around potential "c", is, therefore, the region where molybdenum exerts its greatest influence. The chromium content in the surface increases with the increase of potential as observed in the survey scans. At the high potential of the passive region (potential "g") , F(Cr) reaches 3.2 whereas F(Mo) is only 1.81.

Three groups of angle resolved XPS analyses show the distribution of elements in different depths of the passive films, because the signals obtained from a lower take-off angle are from the outer layers and the signals obtained from a higher take-off angle include the information from the inner layers. Figure 6-5 shows the molybdenum spectra obtained at the potentials "a", "c" and "g" and Figure 6-6 gives the relative F(Mo), where the curves "a", "c" and "g" give the enrichment factors obtained at the potentials "a", "c" and "g" respectively.

It is observed at the potentials "a" and "c" in Figure 6-6 that molybdenum concentrates at the outermost surface layer. In particular, F(Mo) reaches the maximum, 3.9, at the potential "c". However, the molybdenum concentration in the film decreases at the high potential as mentioned earlier and the decrease occurs more significantly at the outermost layer where the molybdenum concentration is close to that in the alloy.

Figure 6-5 The narrow spectra of Mo obtained from angular resolved XPS at the potentials "a", "c" and "g".

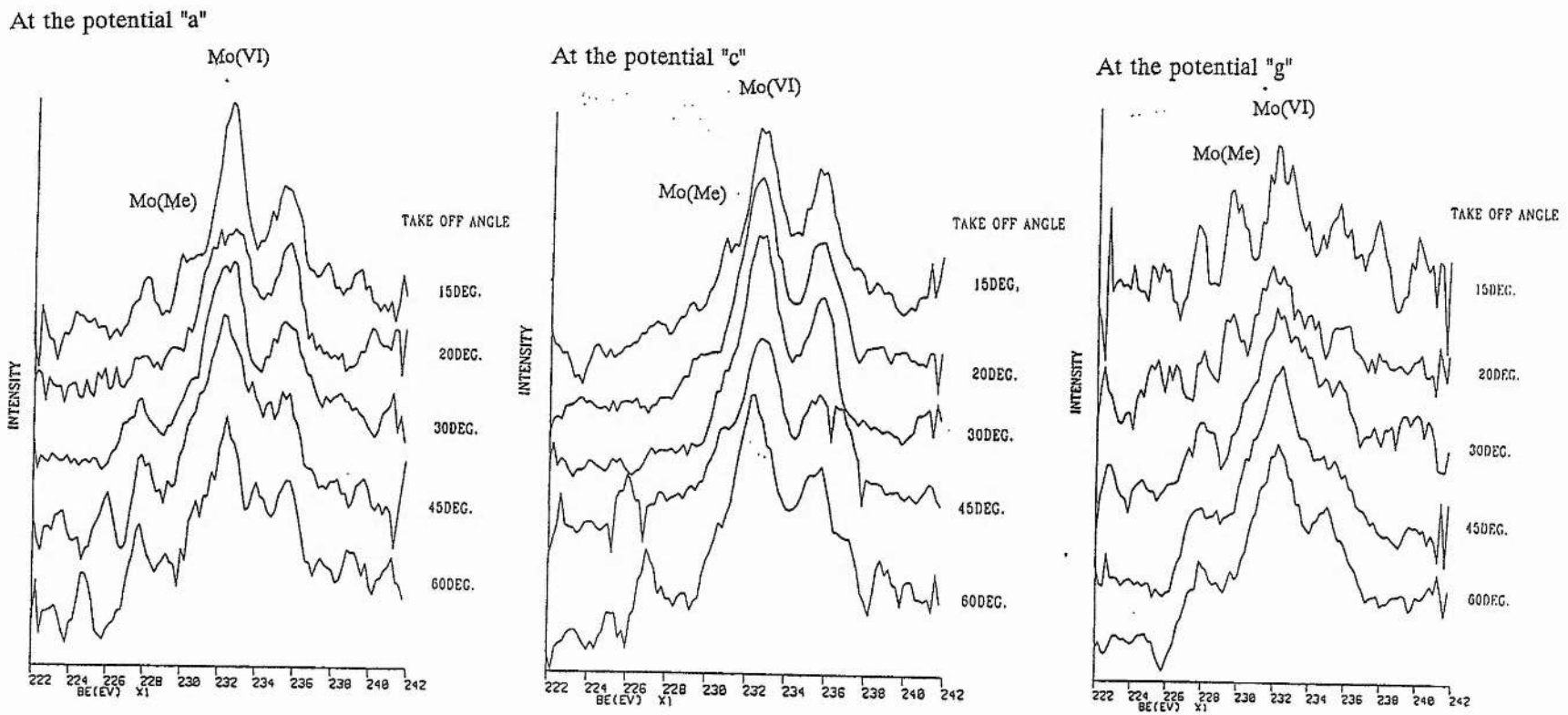

Figure 6-6 Molybdenum enrichment factors were obtained from the take-off angles 15°, 20°, 30°, 45° and 60°. The curve "a","c" and "g" were obtained at the potentials "a","c" and "g" respectively.

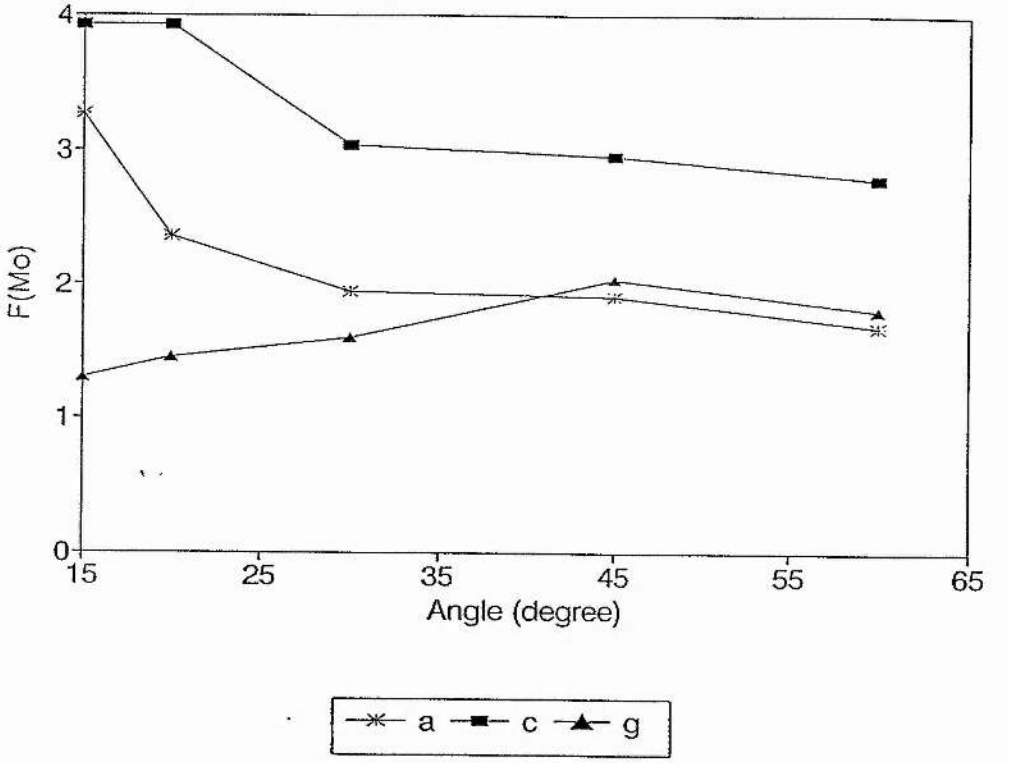

Figure 6-7 and 6-9 are the XPS spectra of chromium and iron, 6-8 and 6-10 are the corresponding enrichment factors of F(Cr) and F(Fe). It is observed that the distribution of Cr and Fe in the film is much more even in comparison with Mo. The observable changes at the high potential "g" are the obvious enrichment of chromium and the depletion of iron at the outermost layer.

Figure 6-7 The narrow spectra of Cr obtained from angular resolved XPS at the potentials "a", "c" and "g".

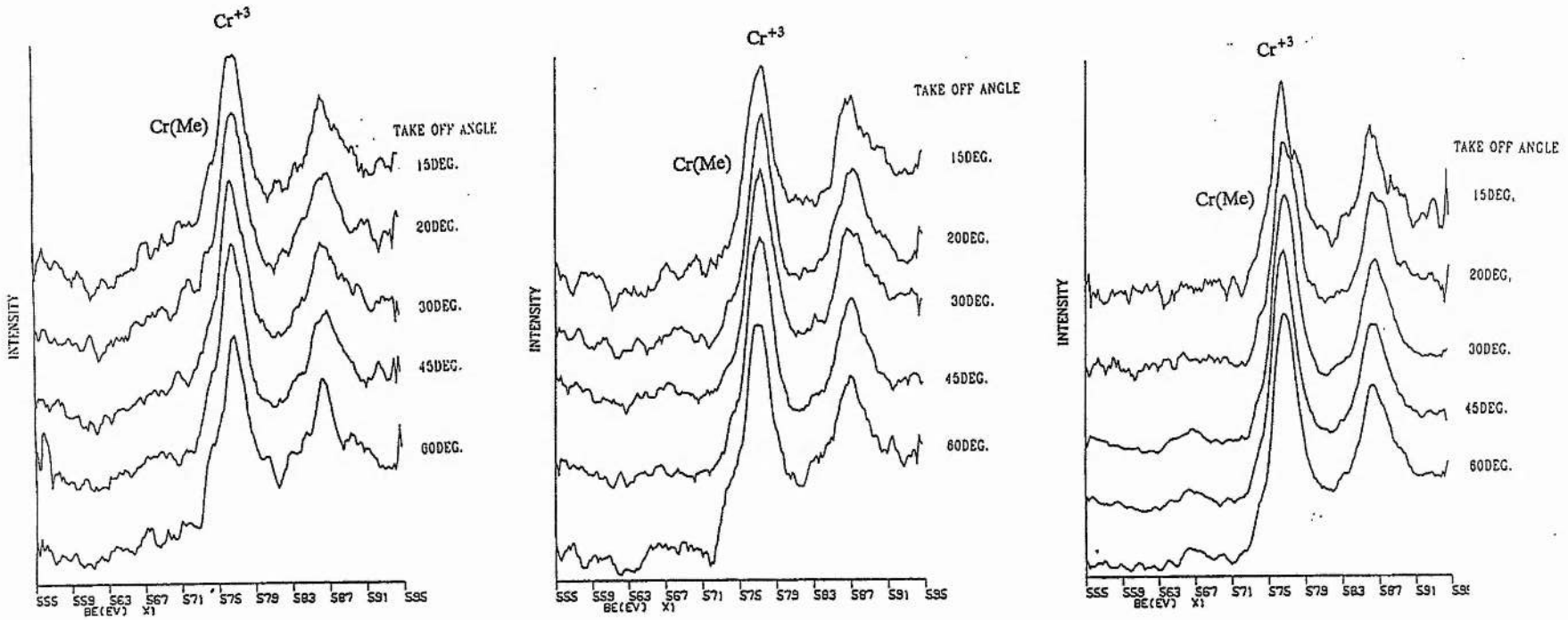

Figure 6-8 Chromium enrichment factors were obtained from the take-off angles 15°, 20°, 30°, 45° and 60°. The curve "a", "c" and "g" were obtained at the potentials "a", "c" and "g" respectively.

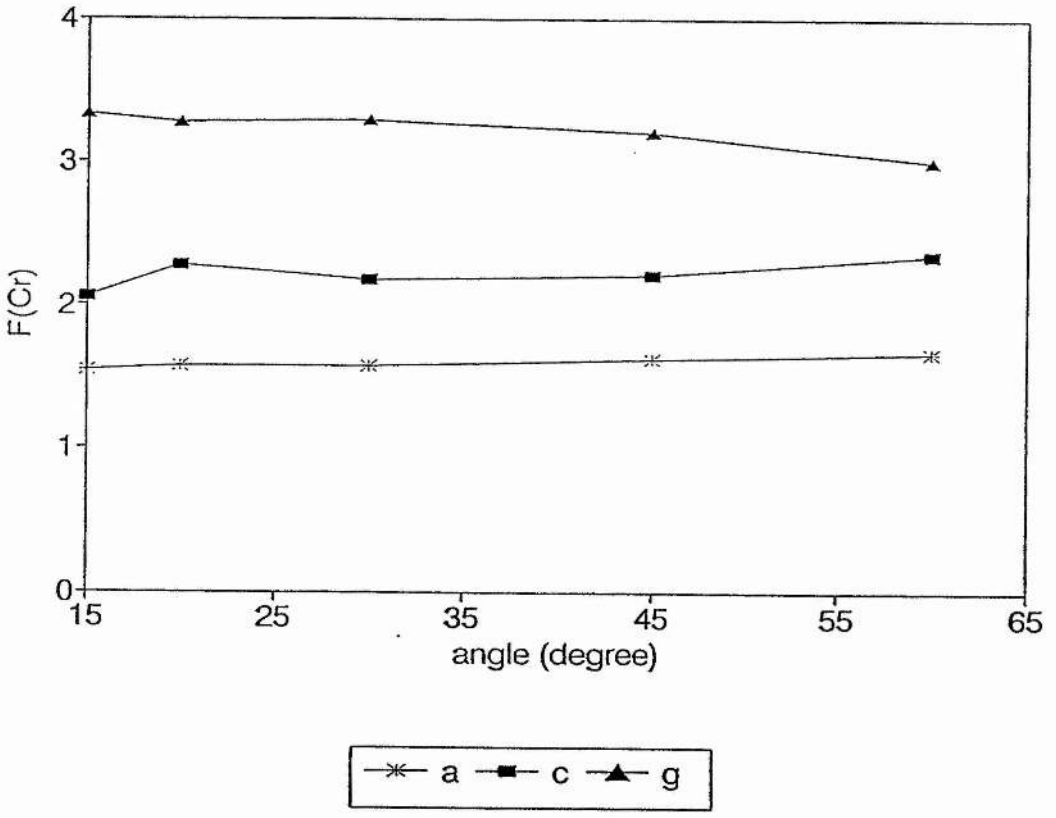

Figure 6-9 The narrow spectra of Fe obtained from angular resolved XPS at the potentials "a", "c" and "g".

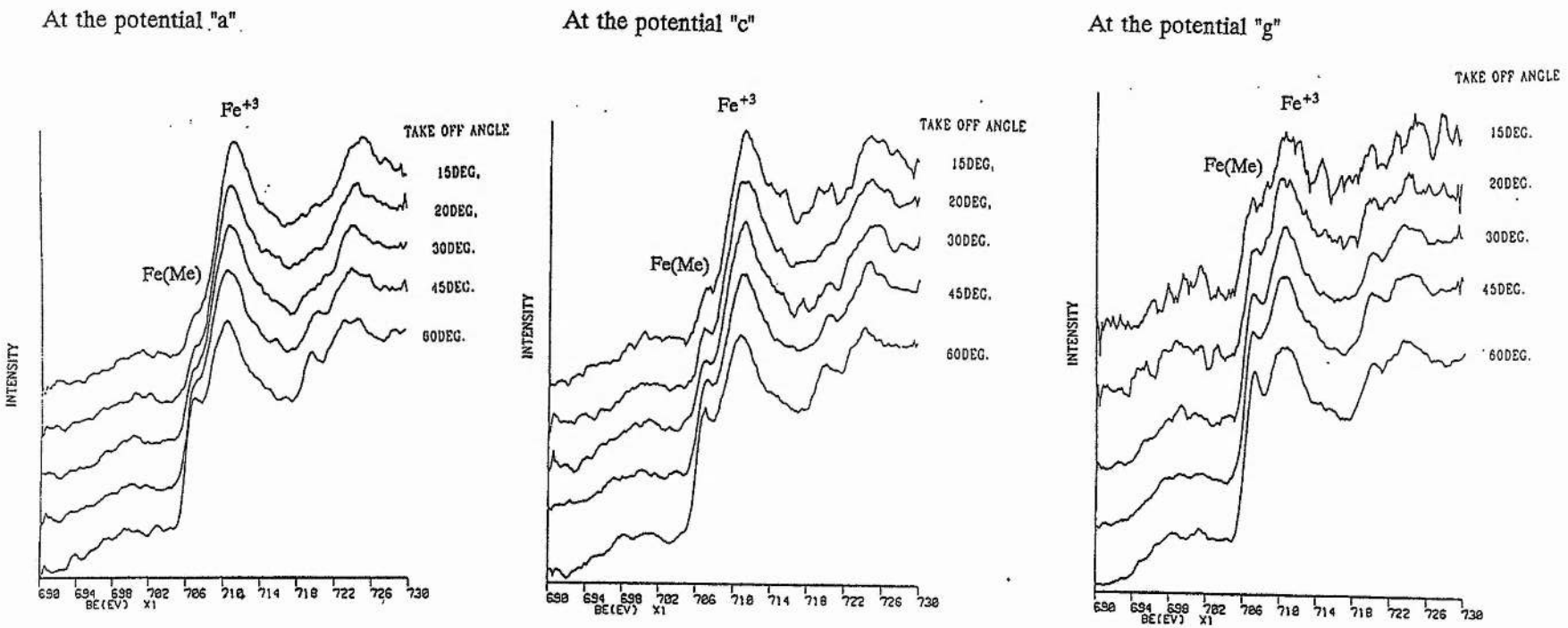

Figure 6-10 Iron enrichment factors were obtained from the take-off angles 15°, 20°, 30°, 45° and 60°. The curve "a", "c" and "g" were obtained at the potentials "a", "c" and "g" respectively.

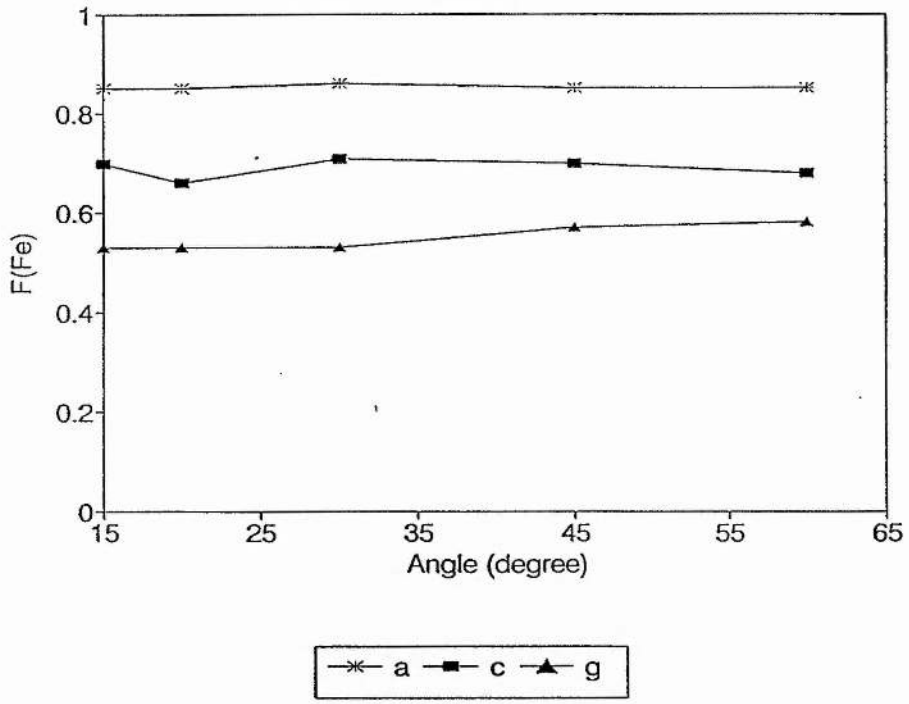

Current/time transients recorded during the polarisation of the samples for XPS analyses are shown in Figure 6-11. The three current/time curves "a", "b" and "c" in Figure 6-11a were obtained at the potentials "a", "b" and "c" respectively, in which the current in the curve "a" corresponds to the peak current in the polarisation curve, the curve "b" shows a much lower current than the curve "a" in the active-passive transition and the current of the curve "c" falls to the passivation level as the potential "c" was in the passive region. However, the values of the passive current at the different potentials (potential "c", "d", "e", "f" and "g") in the passive potential region are similar after the initial period of rapid

Figure 6-11 a) Current-time curves obtained from the critical potential "a", a potential in active-passive potential region "b" and the passive potential "c", b) the curves obtained from passive potentials "c", "d", "e", "f" and "g".

a

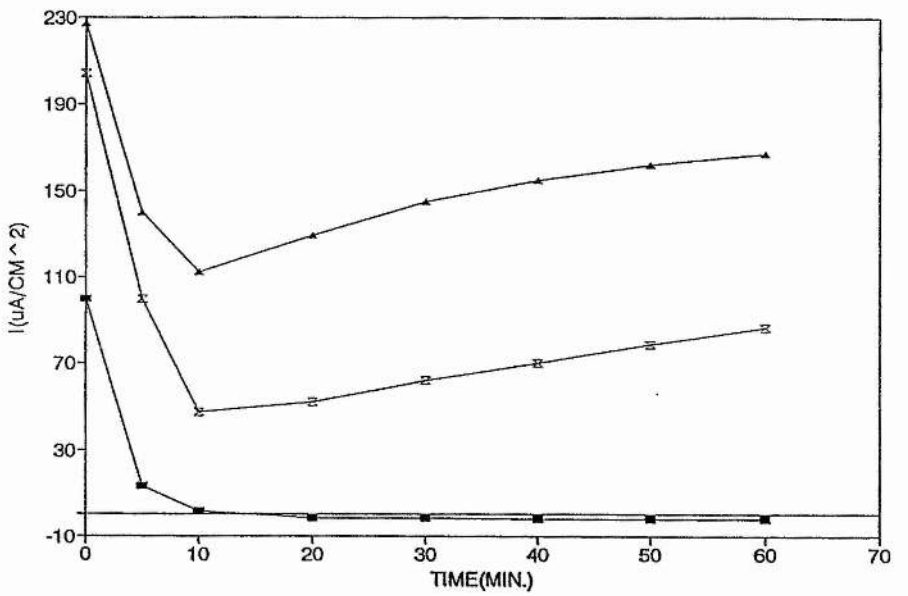

b

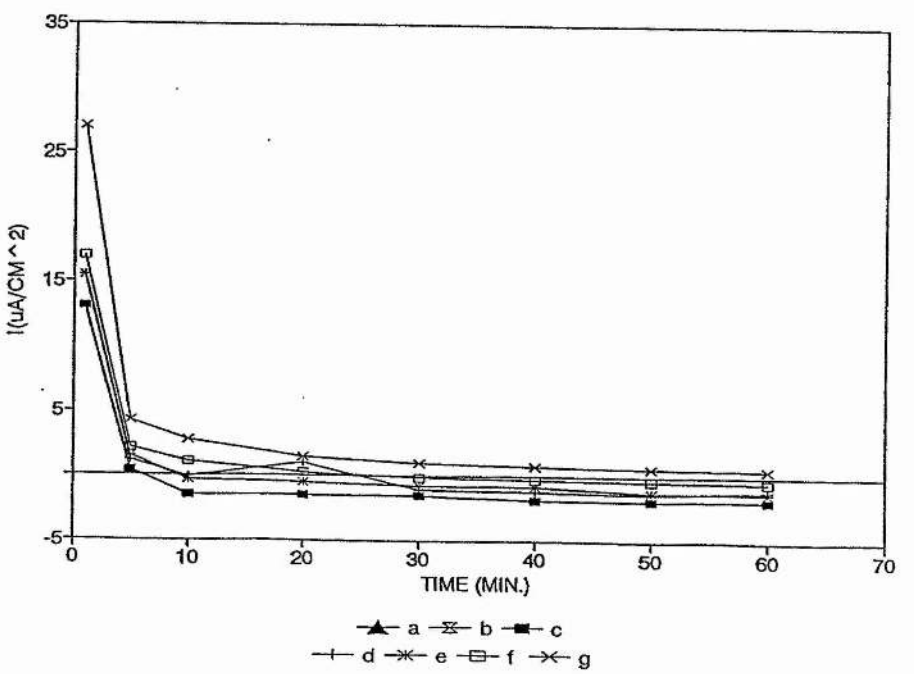

decline (Figure 6-11b). Although molybdenum does enrich on the surface at the active potentials "a" and "b", the current measured at these potentials is quite high. However the films formed at the potential "c" and above in the passive region are stable and give rise to the typical low current of passivity.

6.1.3.2 Chemical state identification by XPS

The chemical states of the detected elements can be identified by XPS chemical shifts. For example, the 2p3/2 position of the Fe peak in an XPS spectrum is at 706.8 eV on a binding energy scale while the 2p3/2 position for the Fe_2O_3 peak shifts to 710.7 eV. Therefore, the oxide ratio of the elements and its change with potential can be estimated from narrow scans.

Figure 6-12 a), b) and c) are montage XPS spectra of the narrow scans of Fe, Cr and Mo, which were obtained at the potentials "a", "b", "c", "d", "e", "f" and "g". The iron spectra show that the ratio of metallic iron increases significantly with increasing potential, which is consistent with increasing slope of the background observed in the wide scan, so at higher potentials, the iron signal in the spectrum is mainly derived from iron in the metal phase. In contrast, the chromium spectra show that at higher potentials, chromium forms the major part of the elements detected in the surface contributing to the oxide film.

The noisy molybdenum peak results from the relatively low content of Mo in the alloy and the complexity of the compounds produced from the corrosion process, such as: Mo^{+3}, Mo^{+4}, MoO_4^{-2} and MoO_3. The existence of Mo multi-compounds in the corrosion products makes it extremely difficult to determine its true chemical states by curve fitting, if possible, as there are so many peaks

Figure 6-12 a) XPS narrow scan of Fe obtained by polarising 516 alloy in 0.1 M H_2SO_4 for 1 hour.

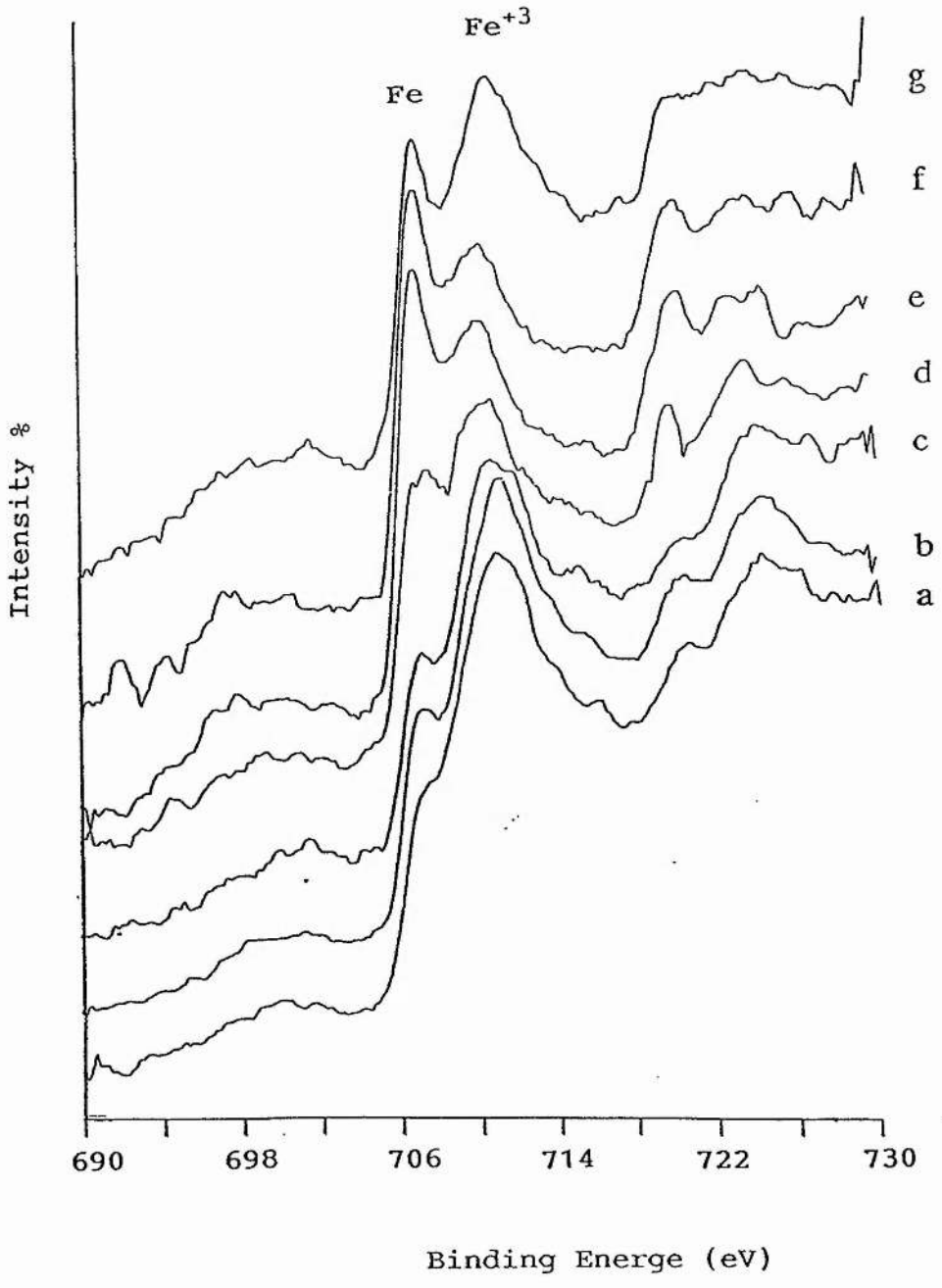

Figure 6-12 b) XPS narrow scan of Cr obtained by polarising 516 alloy in 0.1 M H_2SO_4 for 1 hour.

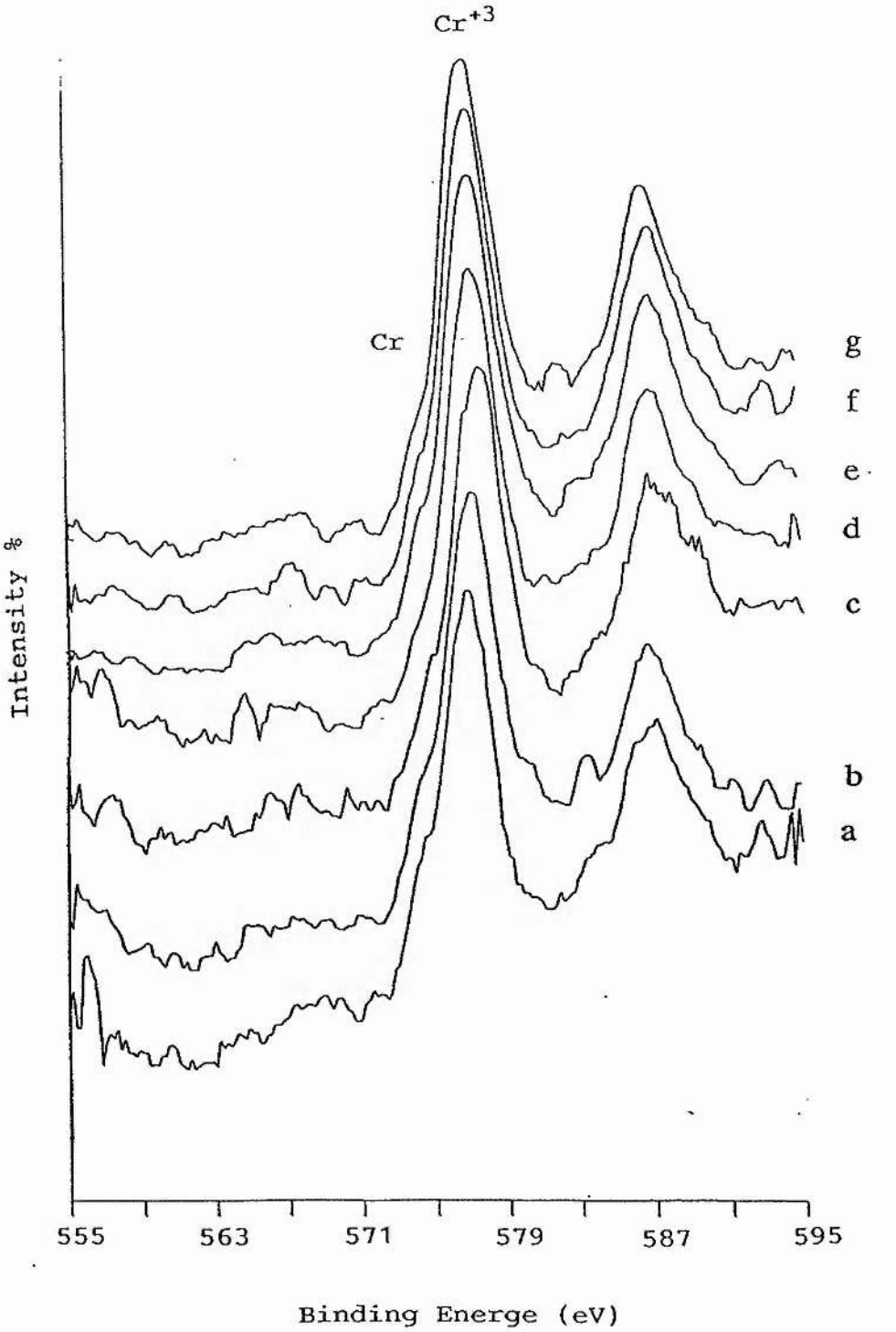

Figure 6-12 c) XPS narrow scan of Mo obtained by polarising 516 alloy in 0.1 M H_2SO_4 for 1 hour.

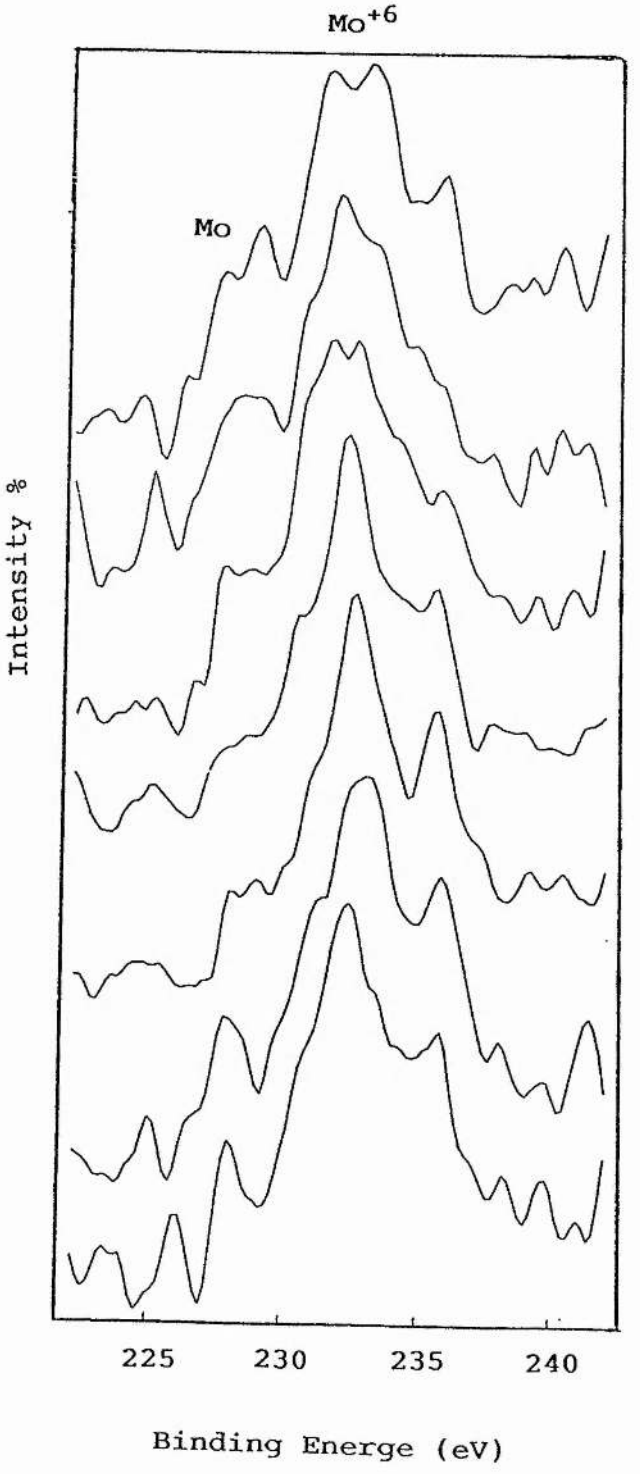

Figure 6-13 Peak fitting of Mo3d XPS spectrum, 1. Mo3d5/2 227.8 eV (metallic) 2. Mo3d3/2 230.8 eV (metallic), 3. Mo3d5/2 229.4 eV (Mo^{+3}), 4. Mo3d3/2 232.4 eV (Mo^{+3}), 5. Mo3d5/2 230.6 eV (Mo^{+4}), 6. Mo3d3/2 233.6 eV (Mo^{+4}), 7. Mo3d5/2 232.5 eV (Mo^{+6}:MoO_4^{-2}), 8. Mo3d3/2 235.5 eV (Mo^{+6}:MoO_4^{-2}), 9. Mo3d5/2 233.1 eV (Mo^{+6}:MoO_3), 10. Mo3d3/2 236.1 eV (Mo^{+6}:MoO_3).

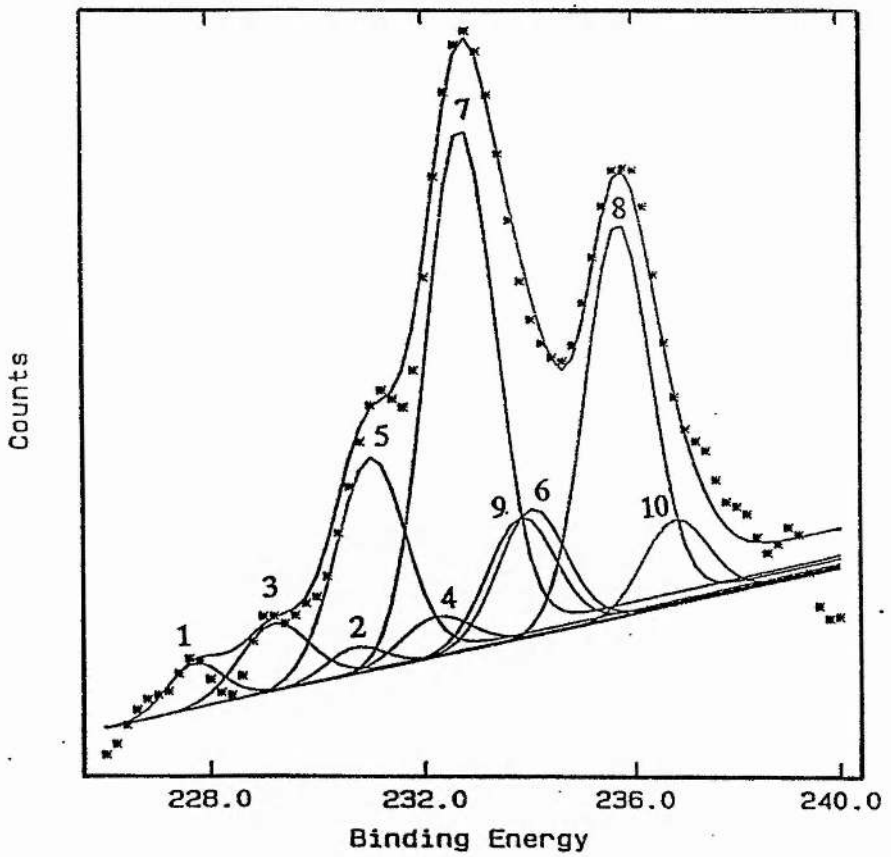

overlapped each other, the result can only be used as an estimation. Figure 6-13 is an example of the curve fitting for Mo.

An attempt is made to sum the oxidized components of molybdenum and thus to provide for resolution into metallic and oxidized components (Figure 6-14). As the maximum concentration in molybdenum oxidized components is coincident with the potential at which the maximum concentration of molybdenum occurred, it is suggested that molybdenum oxide is involved in the formation of the initial solid product on the metal surface.

Figure 6-14 By summing the oxidized components in peak fitting, maximum concentration of molybdenum oxide is found at the same potential where maximum concentration of surface molybdenum is obtained.

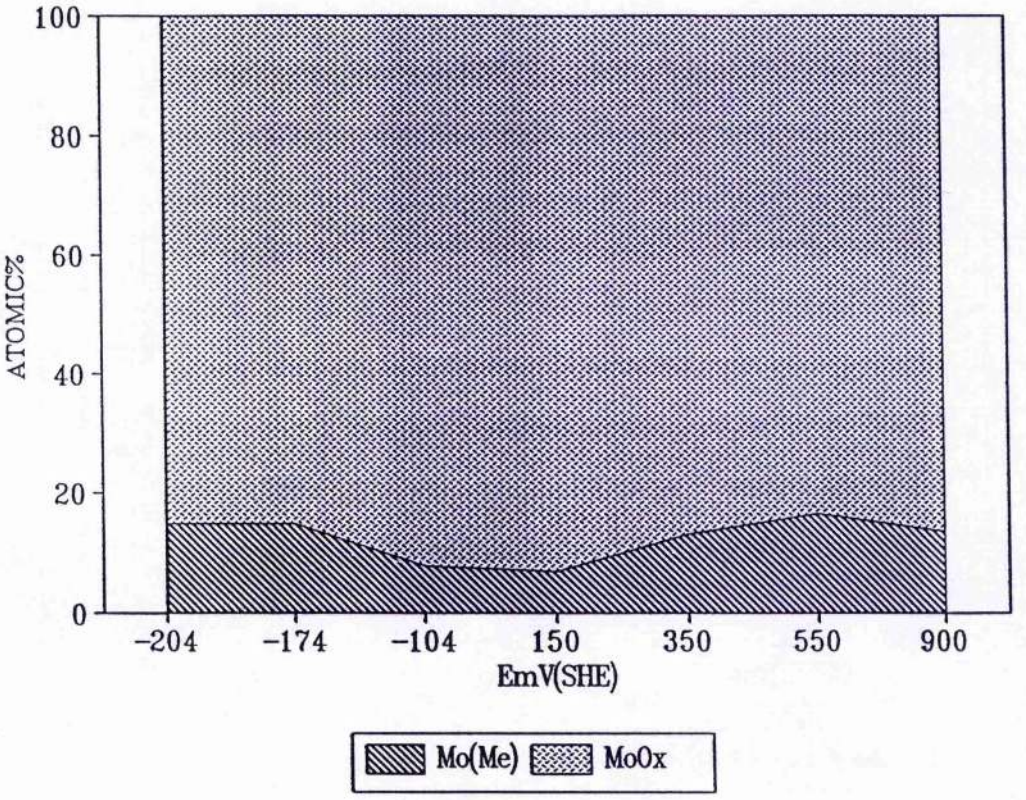

6.1.3.3 Thickness of the passive film

In addition to composition, thickness is another important characteristic of the passive film, which can be measured by XPS. In this study, the thickness of the passive film polarized at the potential "c" for 1 hour was measured by means of angular resolved XPS. According to the Beer-Lambert equation, the photoelectrons' intensity under a overlayer can be described as:

$$I/I_0 = \exp[-d/(\lambda \sin\theta)] \text{ or} \quad (6\text{-}3)$$

$$\ln I = \ln I_0 - d/(\lambda \sin\theta) \quad (6\text{-}4)$$

where I is the intensity under an overlayer, I_0 is the intensity from an infinitely thick clean surface, d is the thickness of the overlayer, λ is the inelastic mean free path of the electron and θ is the take-off angle relative to the sample surface. In the above equations I_0 is a constant, θ is chosen during the experiment and I is obtained through data processing, such as peak fitting, so the overlayer thickness, d, can then be calculated.

The Fe spectra obtained at the take-off angles of 15°, 20°, 45° and 60° are used for the measurement of the film thickness. According to Formula 6-4, $\ln I_0$ is a constant which does not affect the slope of the straight line, so it can be ignored in the calculation. I is the intensity of the metal iron in the measured area in this case. Taking lnI as the y axis and $-1/(\lambda \sin\theta)$ as the x axis, the results of the angle resolved XPS analyses will give a straight line whose slope is the film thickness, d, which is 1.3 nm (Figure 6-15). Table 6-5 gives the used parameters.

Figure 6-15 Thickness of the passive film determined by means of angle-resolved XPS.

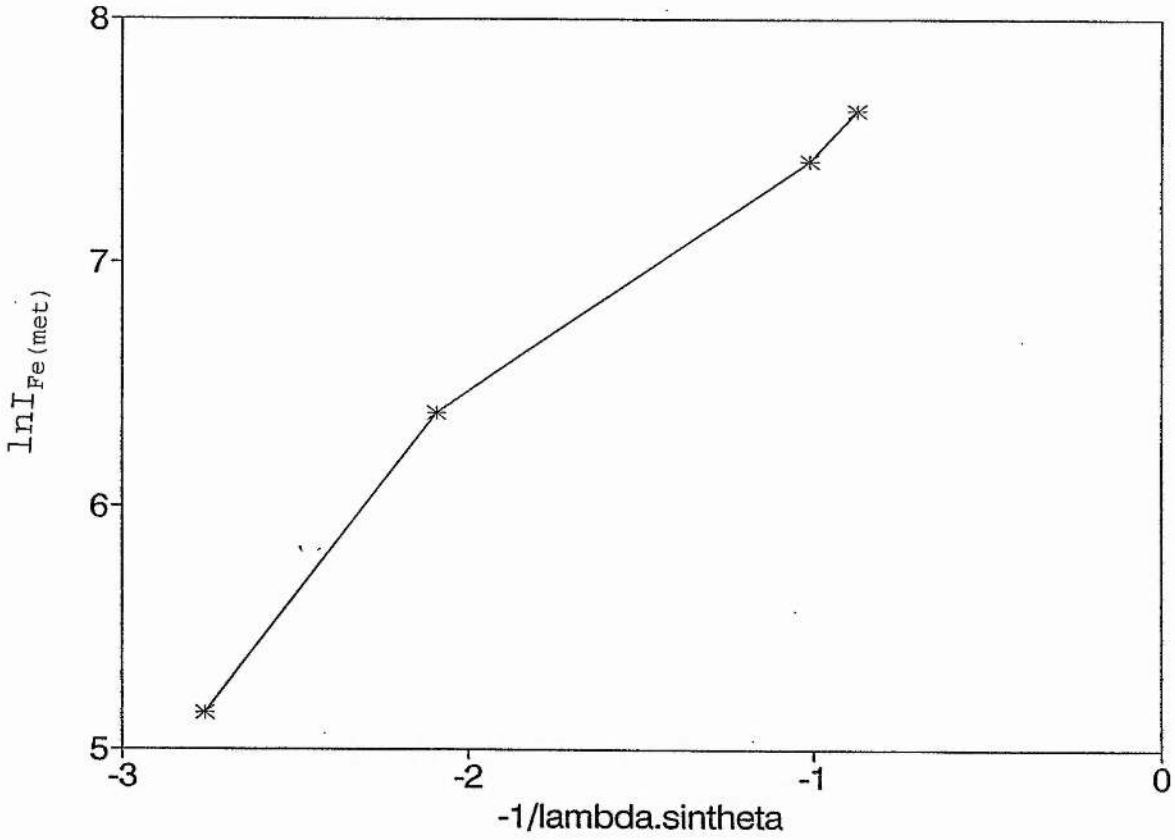

Table 6-5 Parameters used for the measurement of the film thickness.

	15°	20°	45°	60°
I_{Fe}	6870.36	8848.10	9728.86	9742.57
$I_{Fe(met)/Fe}$	2.5%	6.7%	17%	21%
$I_{Fe(met)}$	171.76	592.82	1653.91	2045.94
$I_{lnFe(met)}$	5.15	6.38	7.41	7.62
λ	1.4	1.4	1.4	1.4
$-1/(\lambda\sin\theta)$	-2.76	-2.09	-1.01	-0.82

6.1.3.4 Topography

Based on the above XPS analyses, it has shown that the potential where Mo reaches a maximum concentration in the surface is significantly different from that where the maximum enrichment of Cr occurs. The former is also close to the passivation potential at which the maximum difference in corrosion current for alloys with and without molybdenum was found (Marcus and Olefjord, 1988). This result is consistent with the view that the presence of Mo encourages the precipitation or nucleation of solid material on the metal surface. Attention was therefore transferred to an AFM study of the topography of the passivation surface under the electrochemical condition in which Mo exerts it greatest influence, i.e. at potential "c" in 0.1 M H_2SO_4. It is expected that the topographic study may provide the evidence for molybdenum nucleation of passivation. Though early investigators proposed various models to describe passive films, very few reports in the literature have shown the appearance or the topography of passive films. For this reason, an attempt is made first to study the appearance of a passivation surface using AFM at a moderate magnification.

Figure 6-16 AFM images showing a) a new polished 516 alloy surface, b) the roughness of the polished surface: the average roughness (Ra) is 0.62 nm and the maximum roughness (Rmax) is 4.49 nm.

a

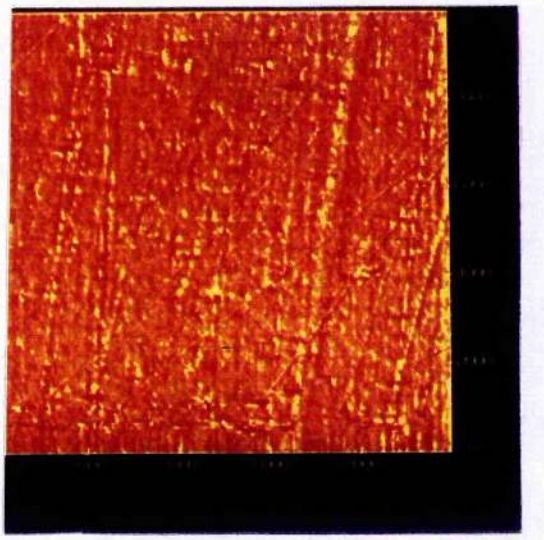

b

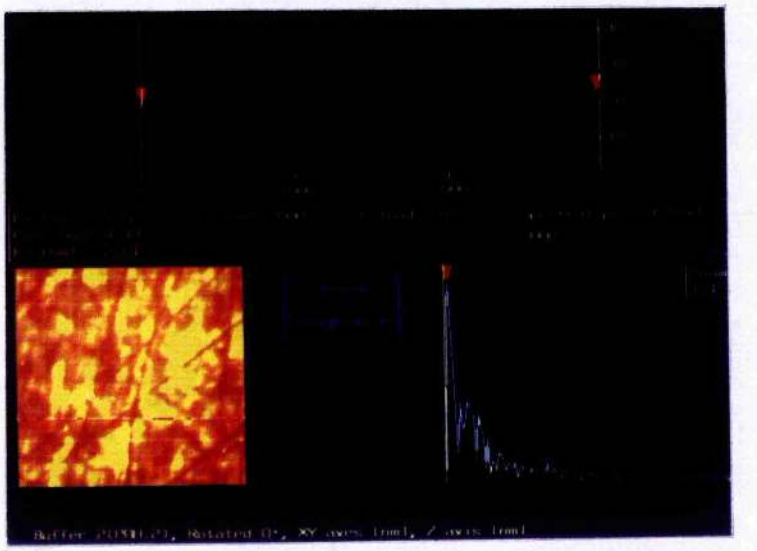

Figure 6-17 AFM images show a) a passivated surface, b) the roughness of the passivated surface: the average roughness (Ra) is 3.36 nm and the maximum roughness (Rmax) is 30.38 nm.

a

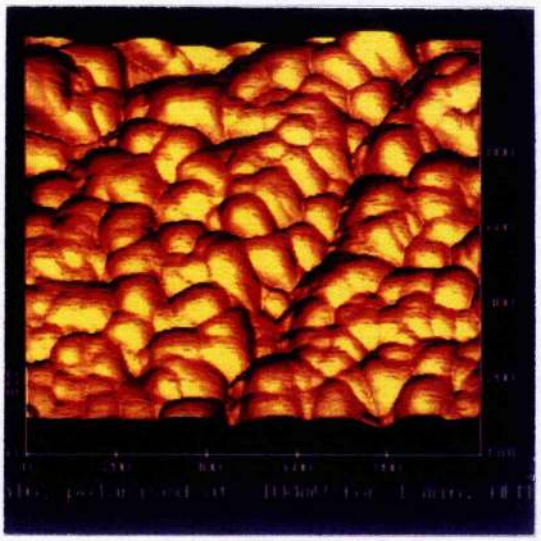

b

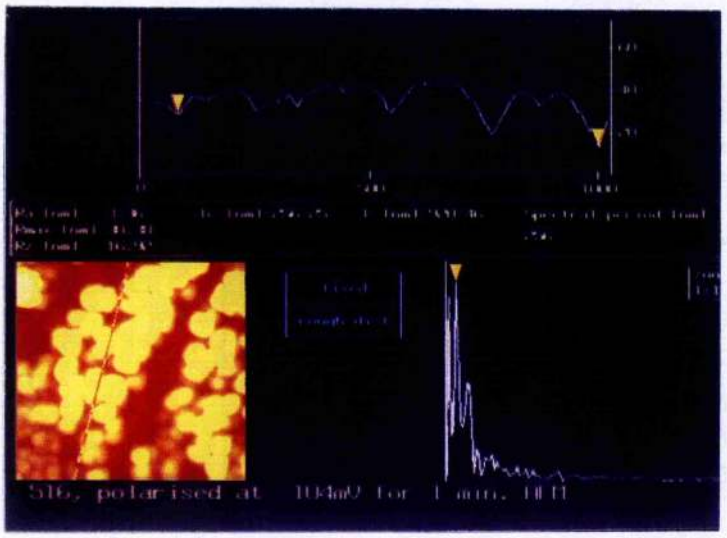

Before passivation, a newly polished surface of 516 steel was scanned in AFM (Figure 6-16a). On the polished surface, some polishing marks decorate the flat surface and give the average roughness (Ra) of about 0.62 nm (Figure 6-16b) and the maximum roughness (Rmax) of 4.49 nm.

However, the polishing marks on the surface disappear and are replaced by round features which are compactly arranged across the surface after 1 minute polarisation (Figure 6-17a). These round features increase the average roughness (Ra) of the surface to 3.36 nm (Figure 6-17b), three times greater than that of the polished surface, and the maximum roughness of the passivated surface is 30.38nm.

To identify whether the roughness of the surface is caused by the exposure of the metal structure or results from the oxide produced during passivation, an etching solution commonly used in metallography is adopted. If the roughness is derived from metal structure, it will be expected to appear after the alloy is etched in a solution. The etching solution used in this study is Fry's solution which has the following composition:

HCl	40 ml	$CuCl_2$	5g
H_2O	30ml	methanol	25ml

Etching the alloy for 30 seconds in this solution exposes the grains on the surface (Figure 6-18). As shown in this figure, most of the grains have a length of > 100μm and a width of > 50 μm. A further examination in the grains from the AFM image (Figure 6-19) does not find any sub-grains or other fine structures giving the surface the same appearance as the passivated surface.

Figure 6-18 An Optical micrograph, showing the metal grains of 516 alloy.

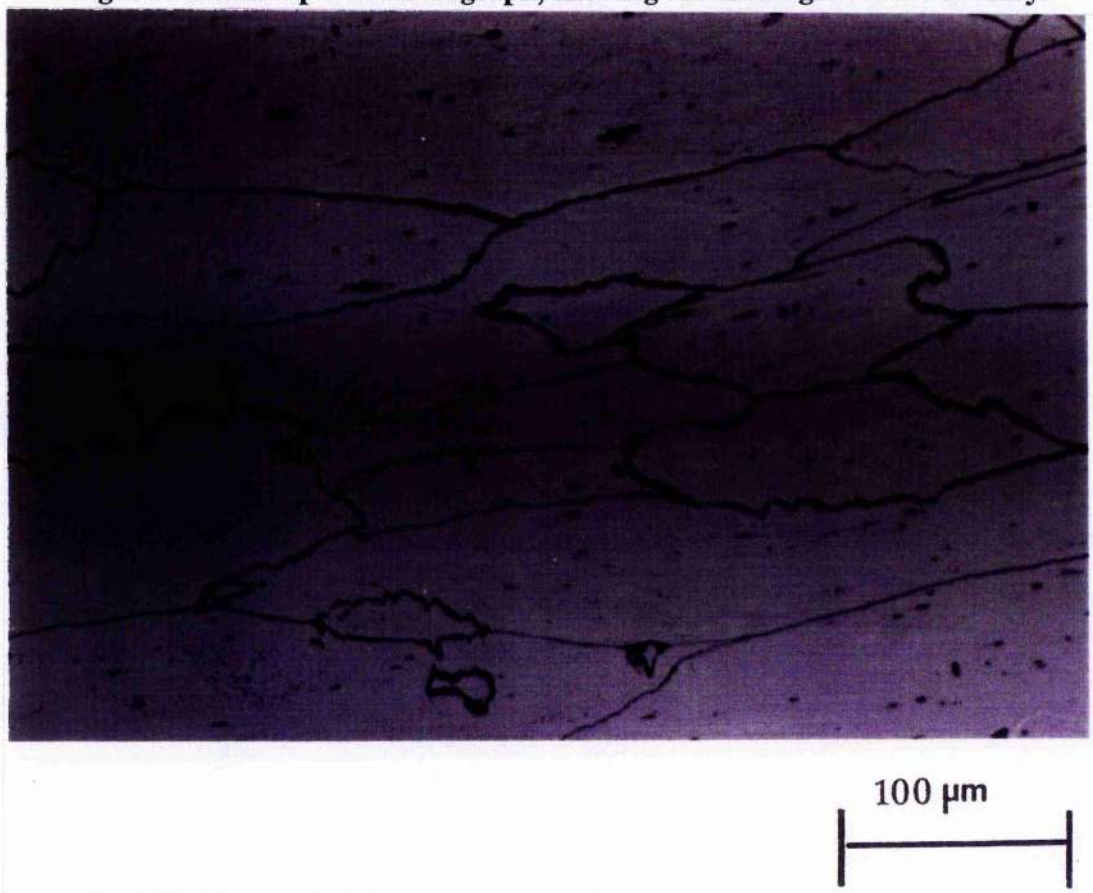

Figure 6-19 An AFM image, showing the different appearance of the metal structure from the passivation surface.

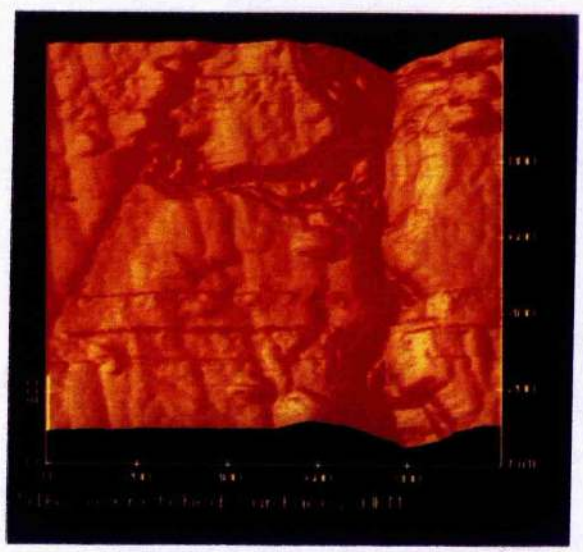

Figure 6-20 AFM images, giving the topography of the passive films of 516 alloy polarised at the potential of -104 mV/SHE for 10 minutes (A, B, C) and 1 hour (D, E, F) in 0.1 M H_2SO4 respectively.

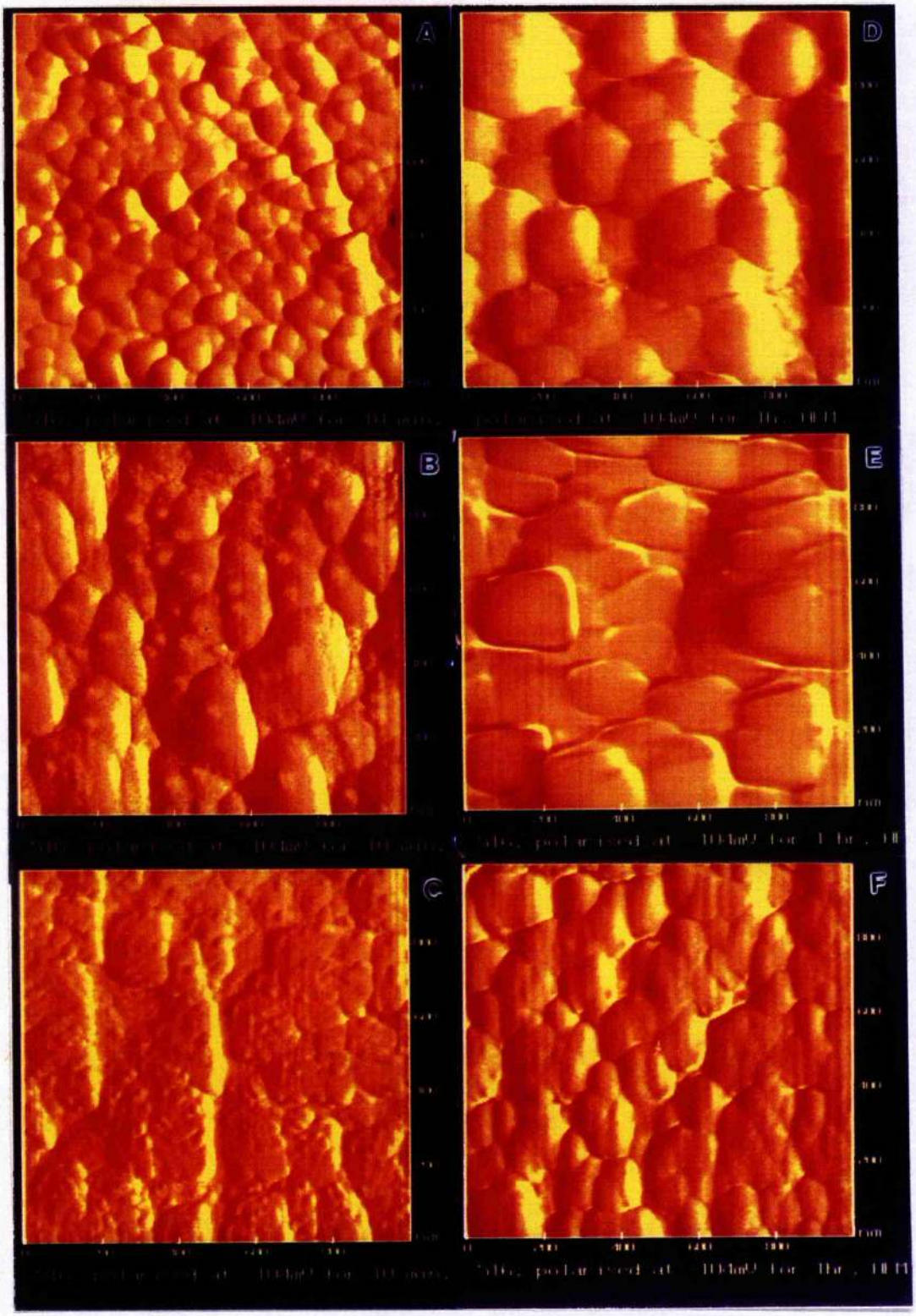

A rough surface of this type has been imaged by AFM repeatly throughout the study of passivation. A group of 1000 nm AFM images obtained from different samples after 10 minutes (A, B, C) or 1 hour (D, E, F) polarisation show reproductions of the rough surfaces (Figure 6-20).

Figure 6-21 Roughness of the surface is caused by a deposit layer, a) Ex-situ AFM, b) In-situ AFM.

a) b)

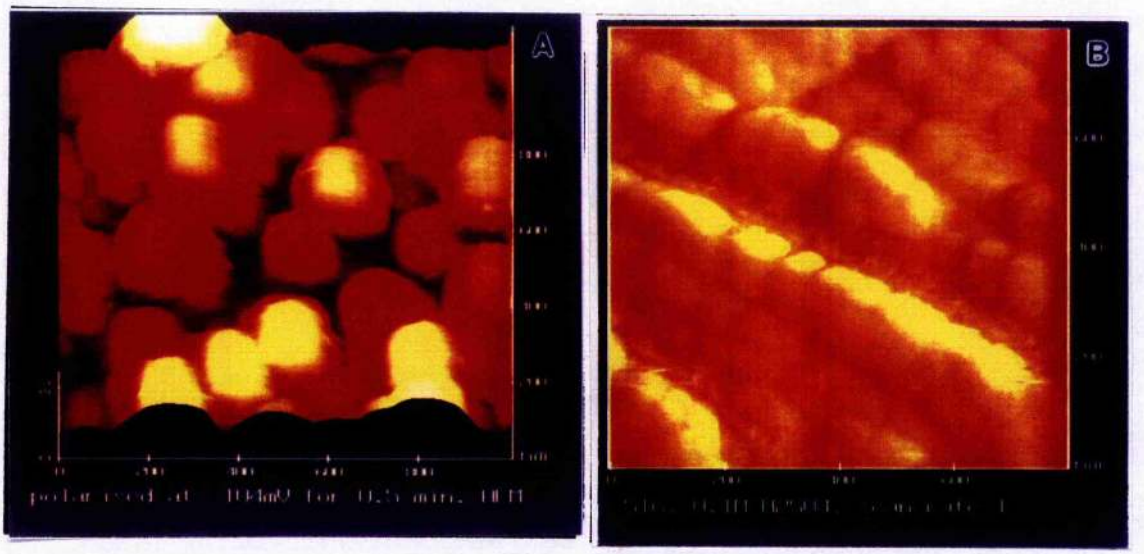

A close examination (Figure 6-21) of both ex-situ and in-situ AFM images finds that the rough surface is, very likely, induced by a deposit layer. An enlarged image of this kind of deposit layer is shown in Figure 6-22.

Figure 6-22 Enlarged deposits.

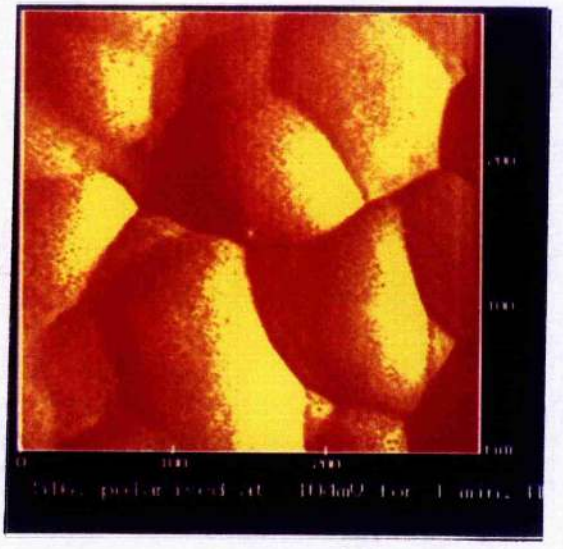

A time series of in-situ AFM images which were scanned in solution depicts the passivation of 516 steel (Figure 6-23). The deposits on the surface appear as platelets.

Figure 6-23 An In-situ AFM image shows that the deposits on the passivation surface appearing as platelets.

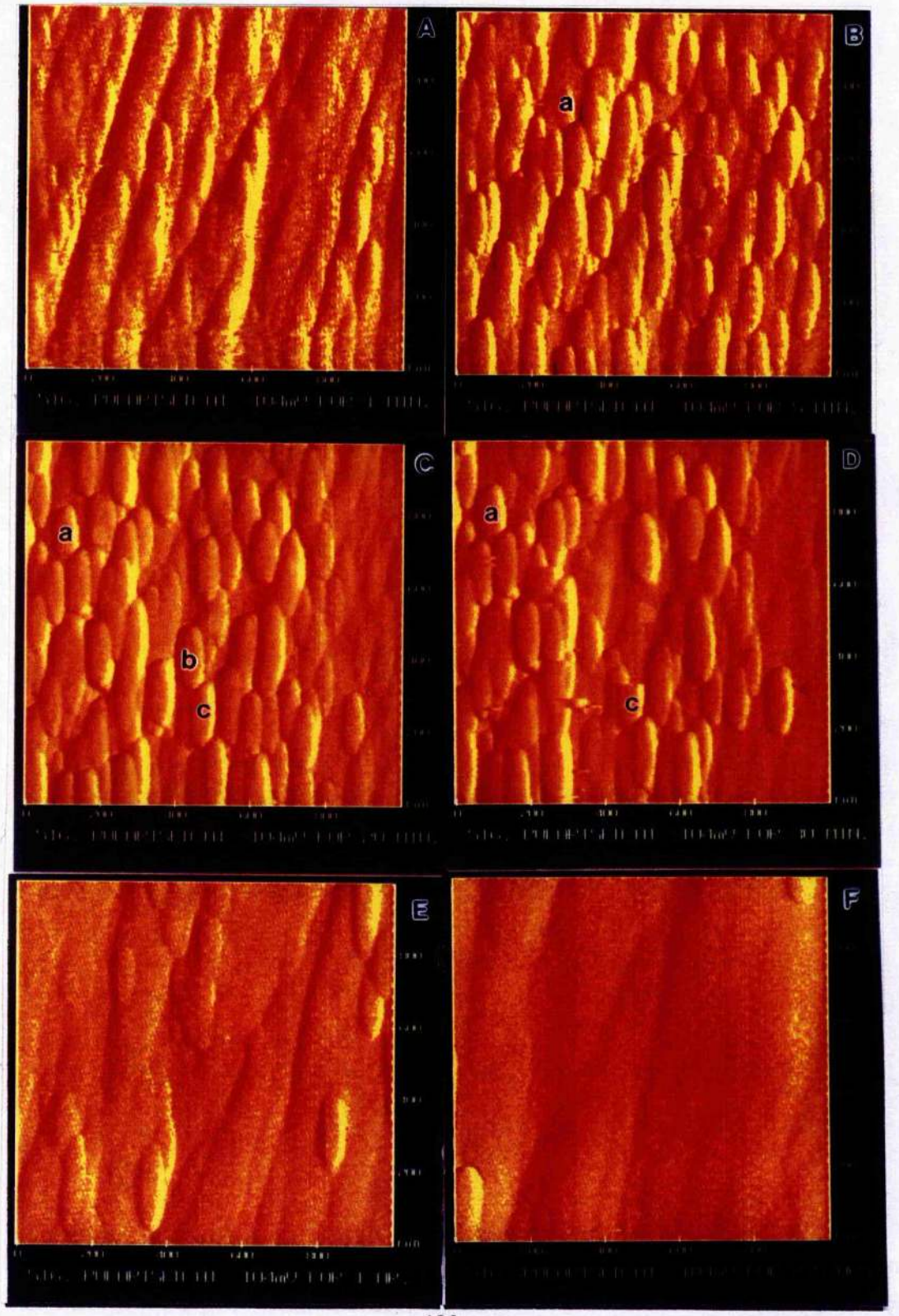

The three-dimensional nature of the platelet is illustrated by the presence of further plates beneath those which are broken in the 30 minute image of the force mode scan. Enlarging the broken platelet using the zoom facility (Fig 6-24) enables the breakage and the underlying platelet to be seen clearly.

Figure 6-24 AFM images, indicating the presence of the further platelet beneath the broken one.

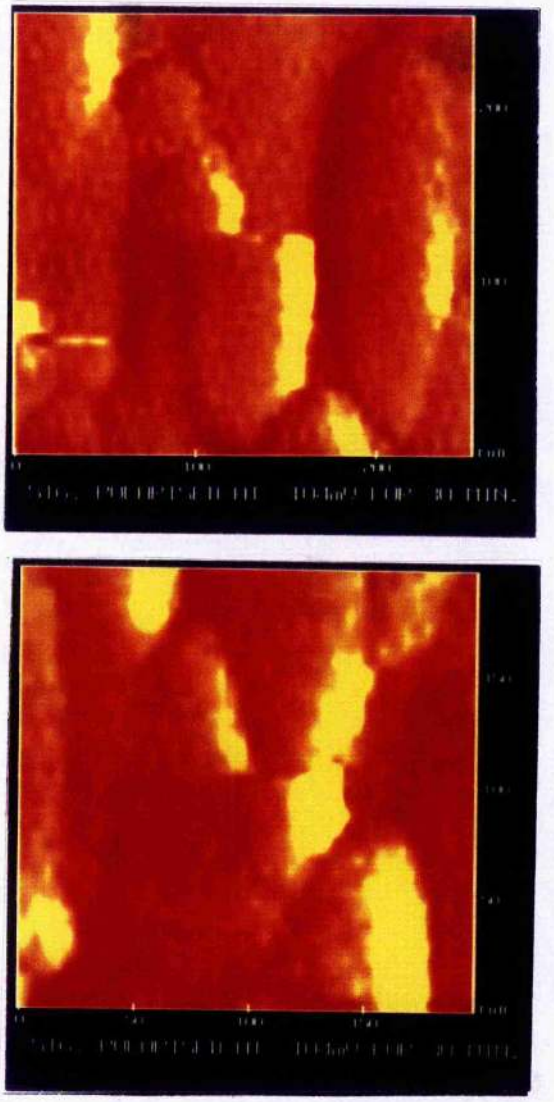

The dendritic structure on the surface of the deposits, which is hardly observed in AFM images (Figure 6-25a), is shown elegantly and dramatically under the high resolution of STM (Figure 6-25b). The dendritic appearance of the deposits is consistent with the presence of these platelets as a result of precipitation and crystallisation. Therefore, it is assumed that they are the molybdenum nucleated oxides.

Figure 6-25a An AFM image, showing faint dendritic structures on the platelets.

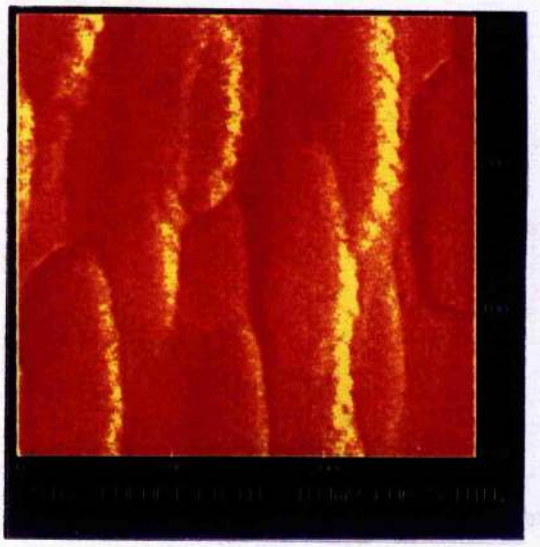

Figure 6-25b A STM image, reviewing dendritic structure on the platelets.

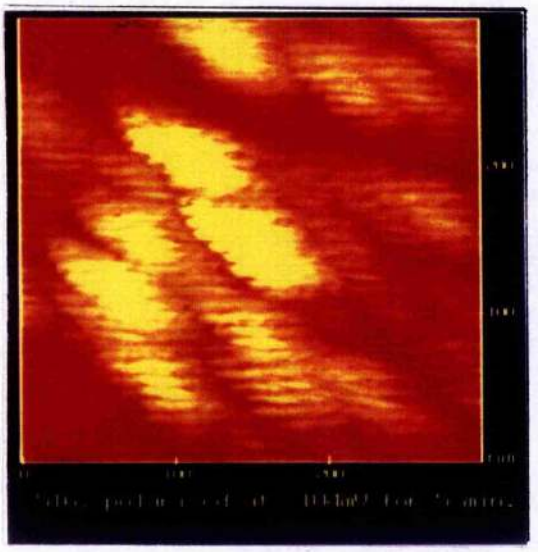

6.1.3.5 EDX analysis of the composition of the stripped passive film

In order to verify the assumption that platelets are molybdenum nucleated oxides, the composition of the platelets has to be analyzed. However, the lack of a technique with sufficient spacial and depth resolution makes it impossible to analyze a single platelet. Instead, an extraction replica of the passive film, which had been polarised for 1 hour, was made for composition analysis using TEM.

Before the film was isolated, a layer of carbon coating was sprayed on the passive film to improve its conductivity so as to meet the requirement of TEM analysis. Since a dry passive film could not be removed directly from the surface for making a conventional replica, it was stripped in an etching solution made of 40 ml bromine in 1000 ml ethyl acetate. During the process, the sample was first etched for a few minutes in the solution, and then washed in methyl alcohol and rinsed in water. An isolated film was then floated in water, which could be

mounted on a copper grid and dried in air so as to be ready for TEM analysis.

Figure 6-26 A TEM micrograph of an isolated passive film of 516 after polarisation at -104 mV in 0.1 M H_2SO_4 for 1 hour.

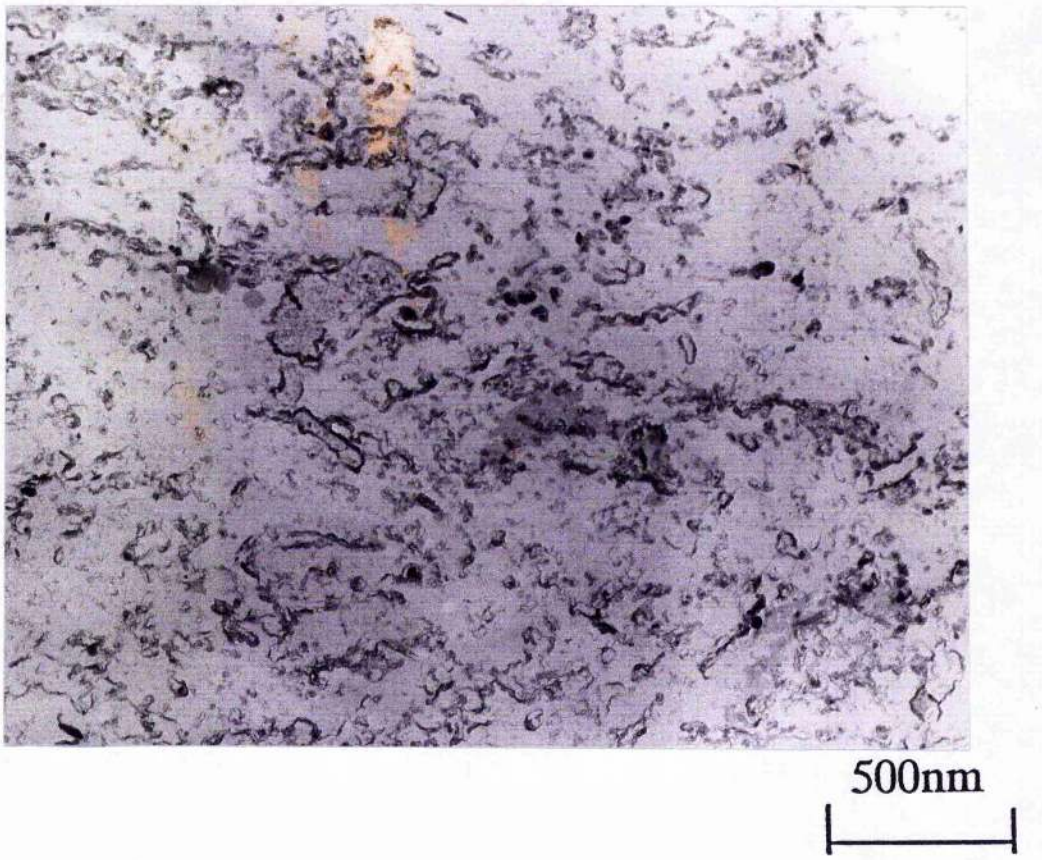

A TEM micrograph in Figure 6-26 shows the stripped passive film. By analysing patterned areas and blank areas using EDX, it is found that patterned areas contain various metal ions, such as molybdenum, chromium and iron which were derived from the film while blank areas contain only copper which was from the copper grid (Figure 6-27) so the patterned areas represent the passive film. The irregular patterns in the patterned areas, however, are difficult to define as the platelets observed in AFM images. This is probably because the platelets were damaged and broken during the isolating process.

Figure 6-27 EDX analysis: a) the blank area only contains copper from the copper grid, b) the patterned area contains metal ions derived from the passive film.

a

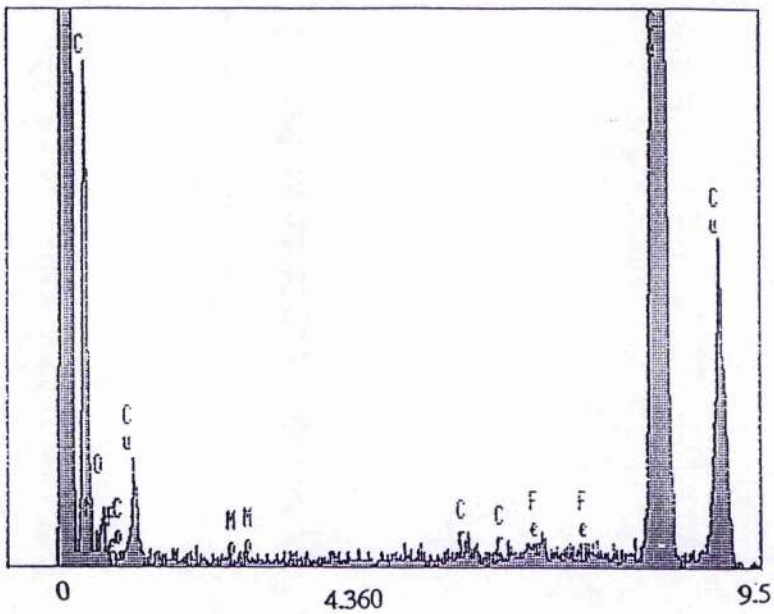

b

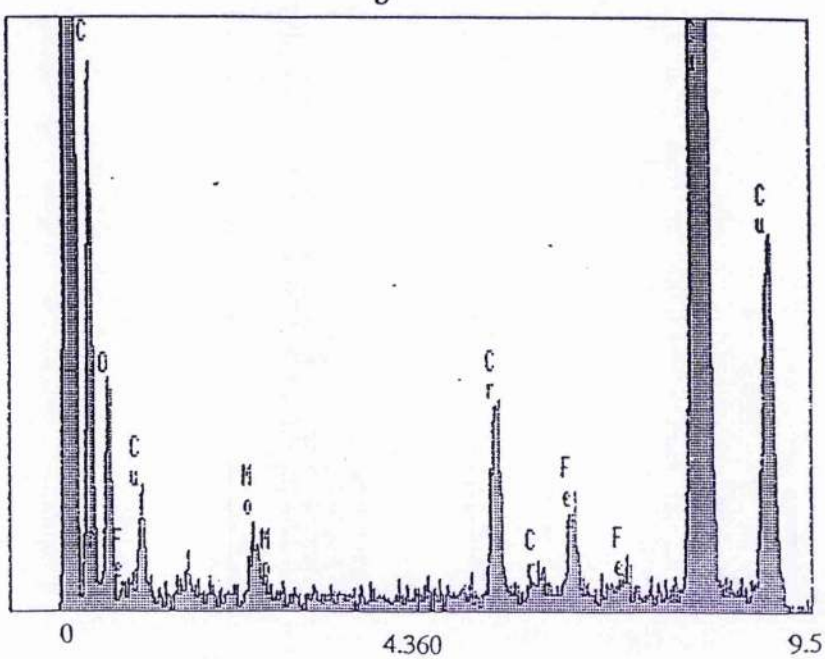

The EDX analysis also shows that the chromium and the molybdenum content in the passive film are significantly higher than those in the bulk alloy. For instance, the intensity of the chromium peak is twice as high as the iron peak in the passive film, though the iron content in the bulk alloy is 81%wt. Similar results are obtained from several patterned areas, so the platelets on the passive film are mainly composed of passive species: chromium oxide and molybdenum oxide. Therefore, it is possible that the platelets are the molybdenum nucleated oxides.

6.1.4 Discussion

6.1.4.1 Oxide nature of the platelets

Though the oxide property of the platelets has been discussed briefly in the previous section, one may consider on a counter-assumption that the "platelets" are an appearance of an etched metal surface caused by a rapid dissolution at the early period of passivation. The two possibilities are shown in Figure 6-28: (1) the rapid reaction produces passive deposits with an appearance of platelets, and (2) the rapid dissolution creates a rough surface, which is then covered by a thin passive film as the passivation goes on.

Figure 6-28 Two possible ways which may produce the rough passive surface.

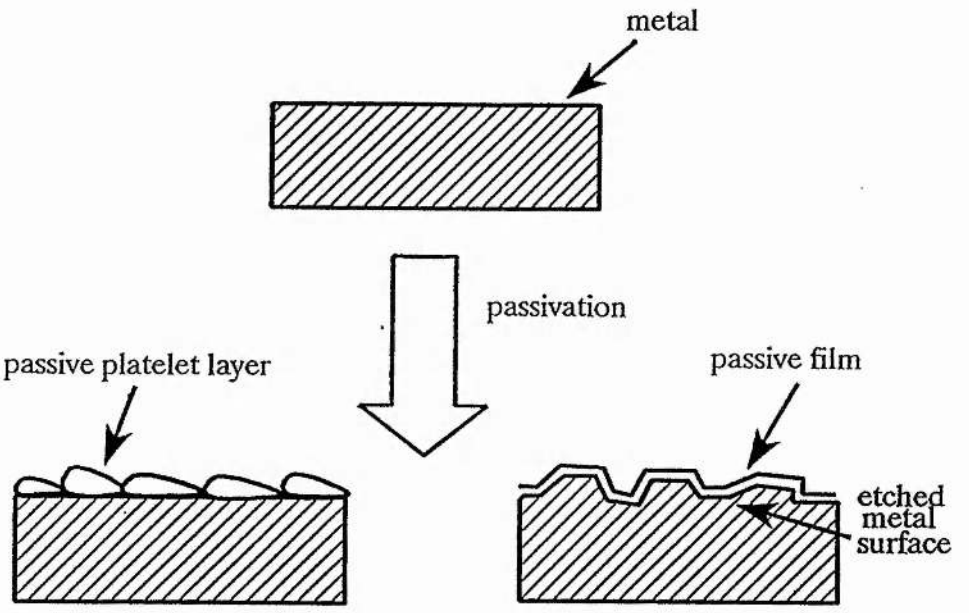

A comparison experiment was carried out to investigate the non-metallic properties of the platelets. In the experiment, two samples were polarised for 10 seconds, one was studied by AFM immediately and the other was studied after being left overnight in vacuum (10^{-9} mbar) (Figure 6-29). The shrinkage of the platelets in the vacuum is quantified by measurements in Figure 6-30 where the heights of the three fresh platelets are 9.68, 13.41 and 10.31 nm but those of the three shrunk platelets are only 5.73, 6.01 and 5.03 nm respectively. This shrinkage may be caused by the loss of water, which gives an indication of the non-metallic property of the platelets. Further discussion about the oxide property will be made when the kinetics of the passivation are studied.

Figure 6-29 AFM images: a) swollen platelets on the fresh passivated surface and b)shrunken platelets on the sample surface staying in vacuum overnight after passivation.

a

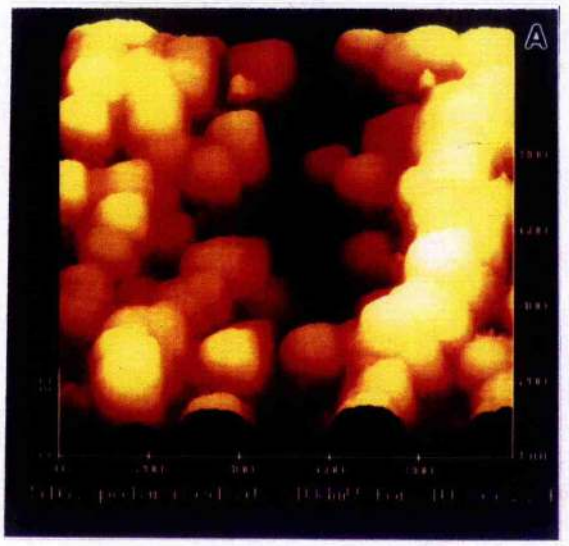

b

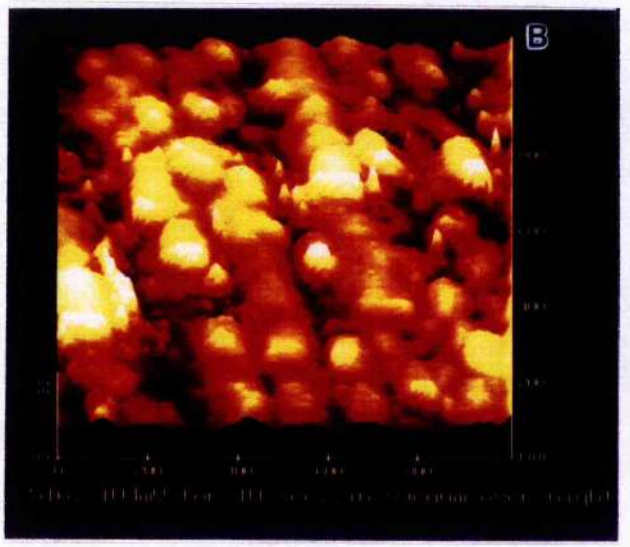

Figure 6-30 AFM measurements of the swollen andthe shrunken platelets, a) the three individual fresh platelets with the height of 9.68, 13.41 and 10.31 nm, and b)the three shrunken plateletswith the height of 5.73, 6.01 and 5.03 nm respectively.

a

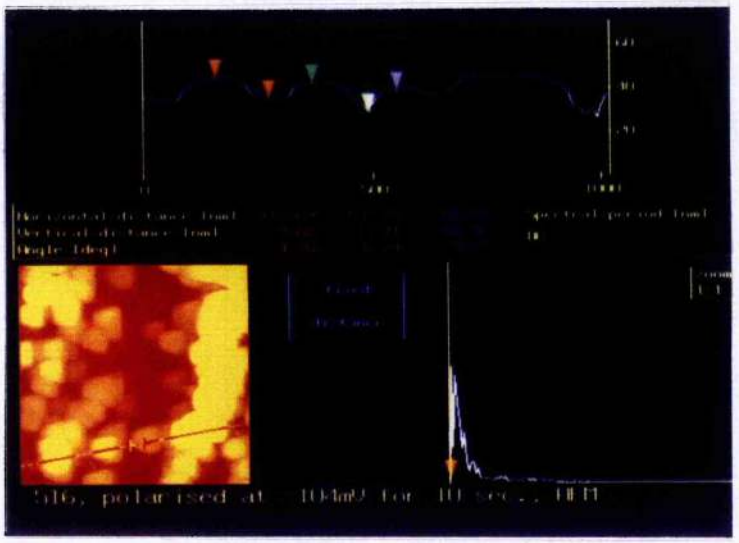

b

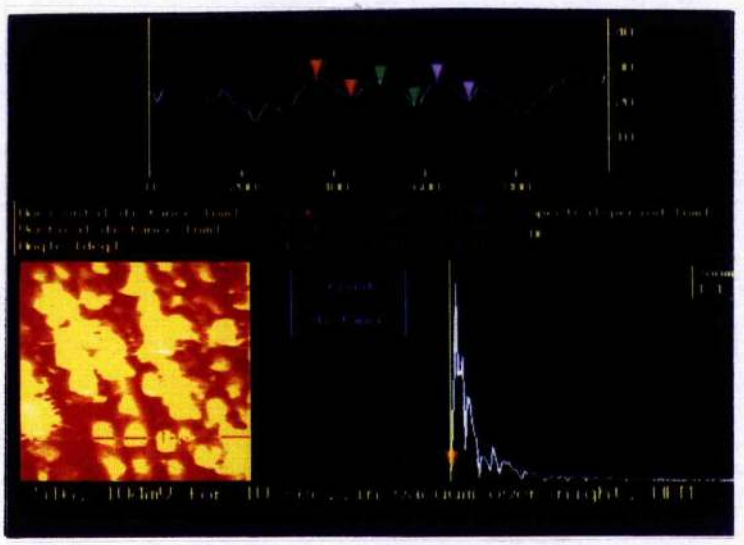

6.1.4.2 The thickness of the passive film

Figure 6-31 The thickness of the platelet measured by AFM is 13.74 nm.

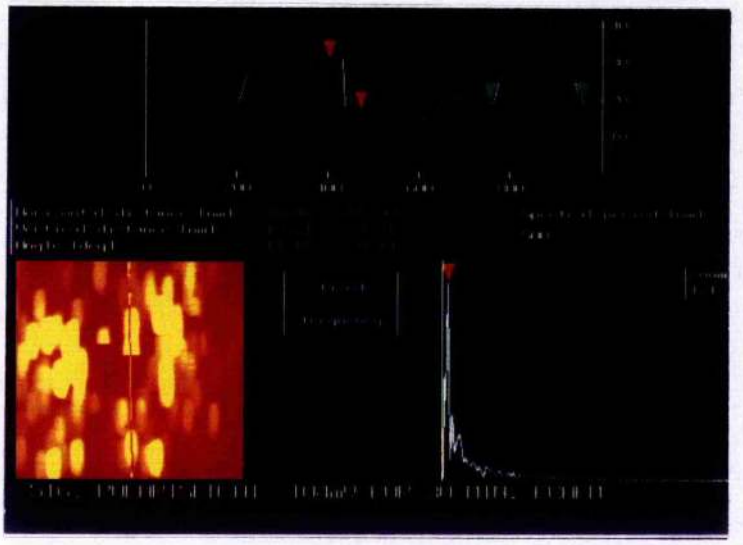

The thickness of a platelet measured by AFM on a broken platelet is shown in Figure 6-31, where the thickness of a broken platelet reaches 13.74 nm. This thickness is much larger than the thickness measured by XPS in the round robin work (2 nm) and by the angle-resolved XPS analysis in this work (1.3 nm). The difference between XPS and AFM measurement is considered to be induced partially by the shrinkage of the platelets as discussed above. Since AFM operated in solution or on a freshly passivated surface in air, the images of the oxide platelets were expected to be swollen with water. During XPS analysis, however, high vacuum and elevated temperature could lead to a rapid dehydration

of the platelets to give a smaller value in thickness.

Another reason which may cause the difference in film thickness by the two techniques lies in the different scales that the two techniques detect. In XPS analysis, the film is assumed uniform which is certainly not true for AFM scans in a much smaller scale. The thickness obtained from XPS analysis is based on the measurement of intensity ratios for the oxidized and unoxidized components of the film, i.e.

$$I_{ox} / I_{met} = \exp(d/\lambda \sin\theta)-1 \qquad (65)$$

where d is the film thickness, θ is the electron take-off angle and λ is the electron inelastic mean free path.

The same intensity ratio may be interpreted as the relative areas of metal exposed between islands of thick oxide. In this case,

$$I_{ox} / I_{met} = A_{ox} / A_{met} \qquad (66)$$

where A is the area of oxide, or metal, according to the subscript, on the exposed surface.

In the study of the film thickness in this work, d is found to be 1.3nm. Using this value together with $\theta = 45°$ and $\lambda = 1.5$ nm as the typical values for iron and chromium, it can be seen that the ratio of intensities which yields a thickness of 1.3nm also yields an oxide covered area of 70%. Thus only 30% exposed or thinly covered metal is required to give the intensity ratio

corresponding to the film thickness measured by XPS: this condition could be met by allowing for an area of thinly covered metal at the boundary between the platelets.

6.1.5 Kinetics of passivation

6.1.5.1 Kinetics of passivation of molybdenum-bearing alloys

The topographic study using AFM gives us a surprising view of the platelets which have never been reported before. In this section, the growth and the development of the platelets are investigated by both ex-situ and in-situ AFM studies.

Figure 6-32 A polished sample surface scanned in pure water by AFM.

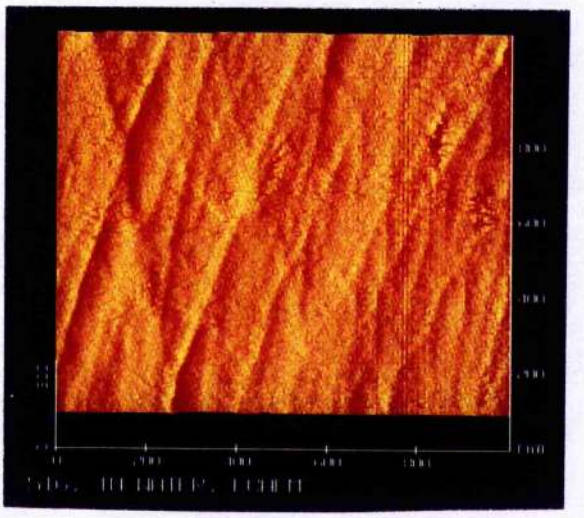

Before the experiment started, the steel was imaged in pure water (Figure 6-32). The same appearance of the steel in water and in air shows that the surface only slightly reacts with pure water.

Figure 6-33a (height mode images) and Figure 6-33b (corresponding force mode images) are two groups of 1 μm square in-situ AFM images which were obtained in the same run to describe a passivation process occurring on 516 alloy in two and a half hours. In each case a scan was made in height mode followed by a scan in force mode, so a comparison between the height-mode and force-mode images can indicate sudden changes of the surface which might have occurred between the two scans. The time series show, very dramatically, the growth of surface deposits. A careful comparison between these two group images reviews:

(a) inter-growth [e.g. the platelet "a" grows in the images of 5 minutes (B), 20 minute (C) and 30 minute (D). The growth can be seen in both force-mode and height-mode images]

(b) loss [e.g. the platelet "b" in the 20 minute image (C) losses in the 30 minute image (D). The loss can be seen in both height-mode and force-mode images]

(c) Breakage [e.g. the completed platelet "c" in 30 minute height-mode image (D) is broken in the corresponding force-mode image]

Figure 6-33a An in-situ AFM image recorded in height mode scans, showing the time series of the passivation of 516 alloy, A) for 1 min, B) for 5 min, C) for 20 min, D) for 30 min, E) for 1 hr, F) for 2.5 hrs.

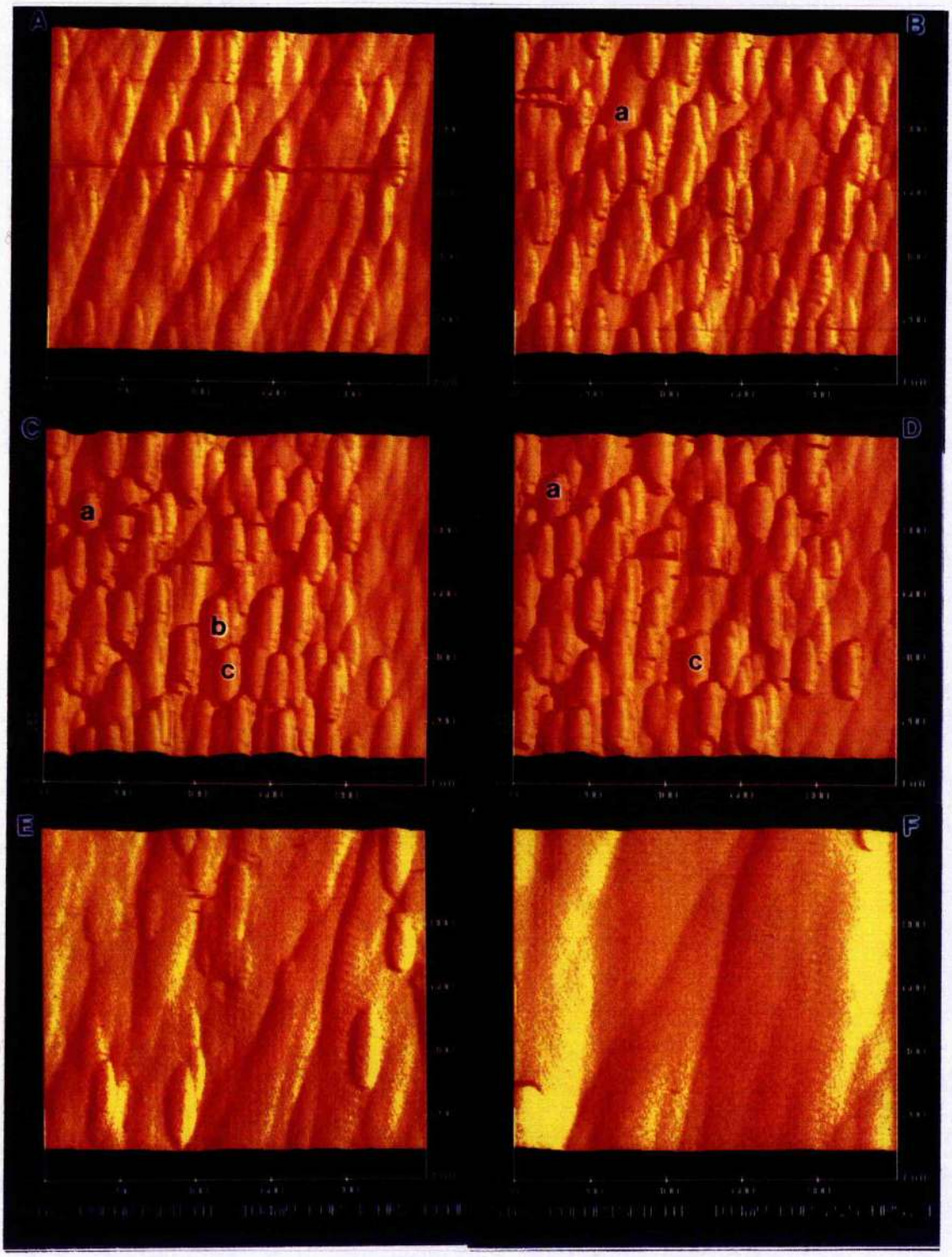

Figure 6-33b An in-situ AFM image recorded in force-mode scans, showing the time series of the passivation of 516 alloy, A) for 1 min, B) for 5 mins, C) for 20 mins, D) for 30 mins, E) for 1 hr, F) for 2.5 hrs.

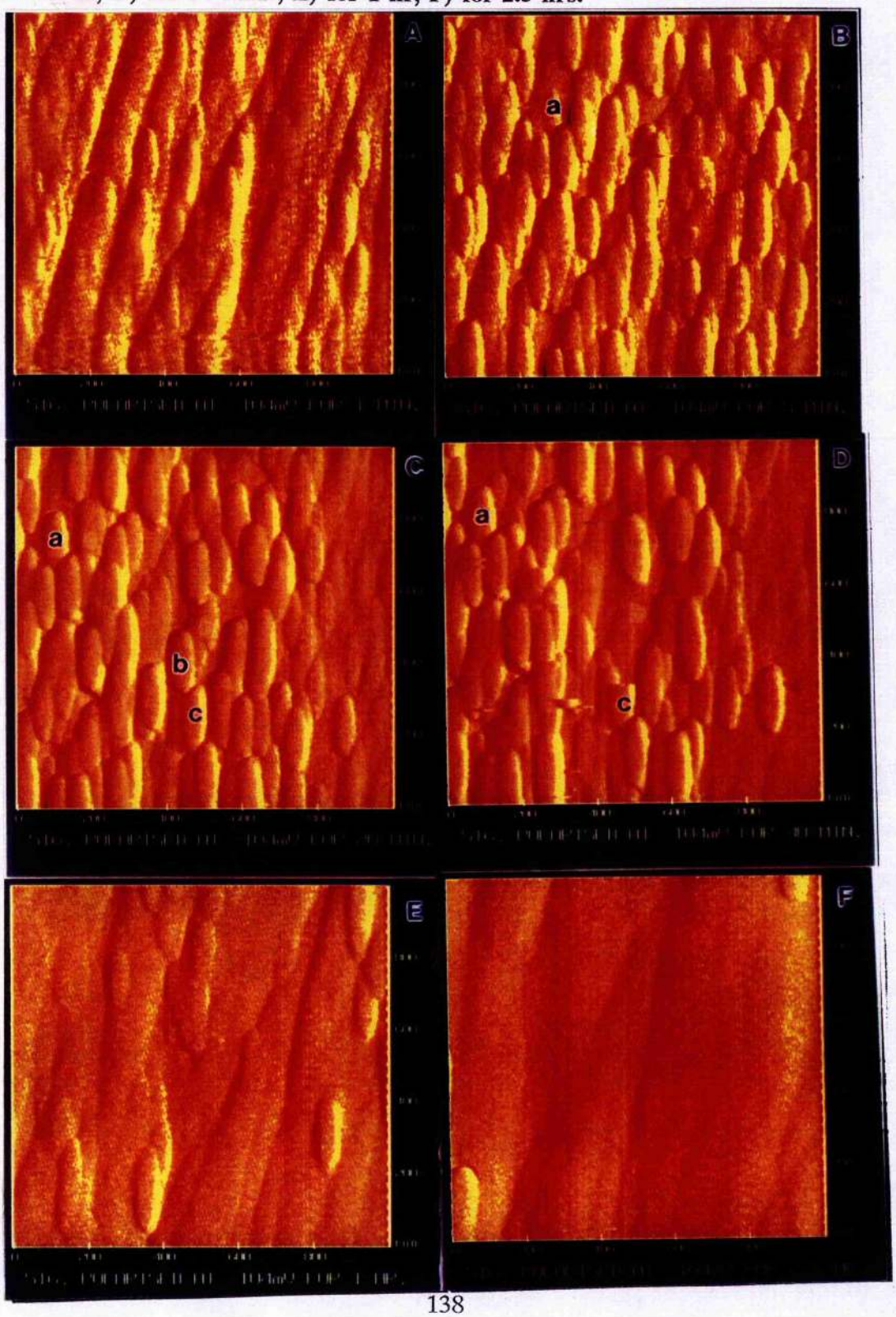

The generation of these platelet deposits, whilst dramatic, is a transient phenomenon and a more mature surface is eventually created. A rapid generation of the platelets on the surface are replaced with a rapid loss or dissolution of the platelets from about 20 minutes and by the one hour scan the platelets on the surface almost disappear. The residual featureless background is the passive film which is identified by the low current density.

A time series in Figure 6-34 is a group of ex-situ AFM images which were obtained from different runs processed in a traditional cell. The ex-situ AFM study repeats the passivation process observed in in-situ AFM study, i.e., the platelets generate and disappear during the passivation. It is concluded that the platelets are not artifacts created in the in-situ AFM studies.

Figure 6-34 An group of ex-situ AFM image obtained from a time series of the passivation of 516 alloy, A) for 10 secs, B) for 1 min, C) for 10 mins, D) for 1 hr, E) for 2 hrs and F) for 24 hrs.

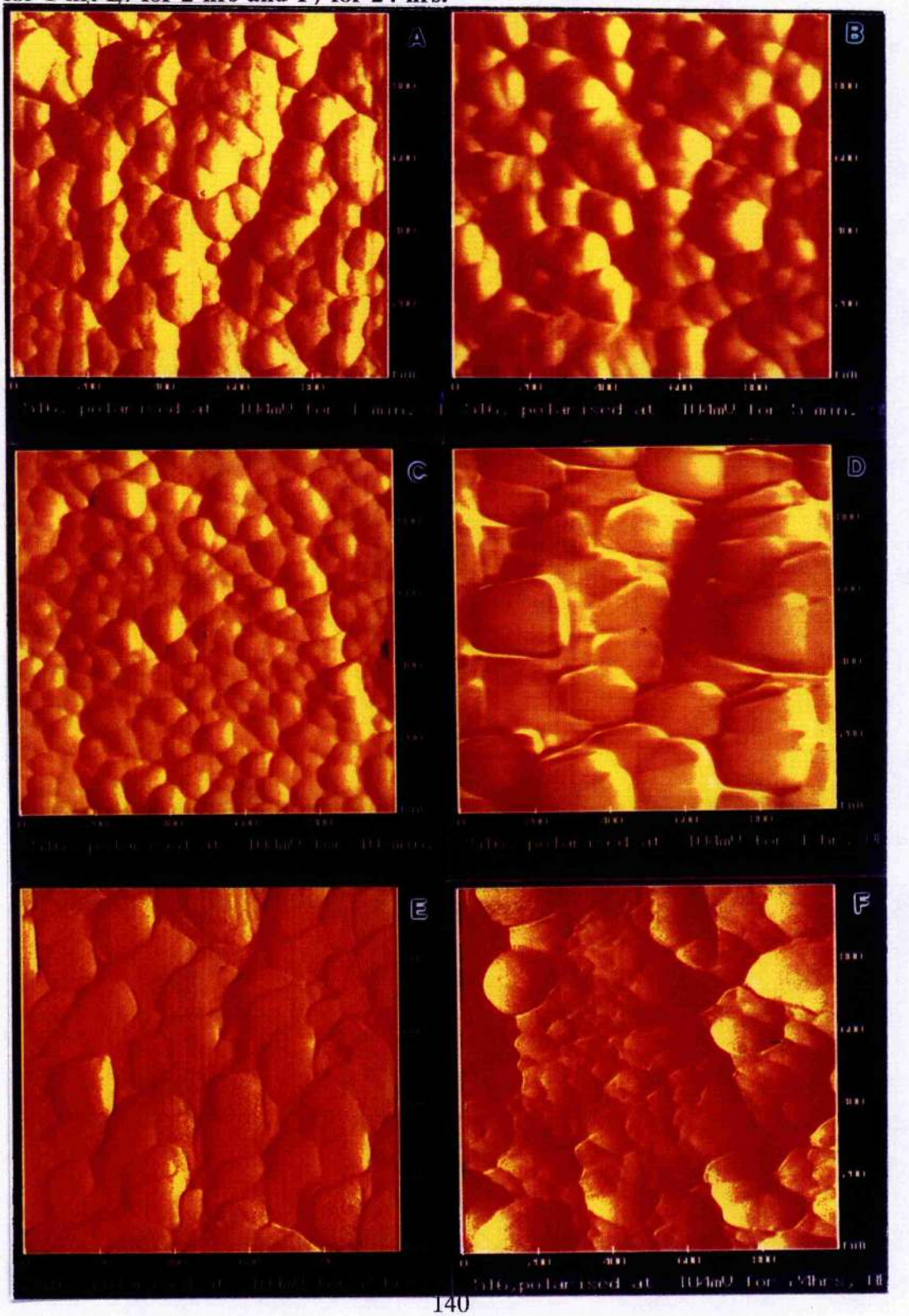

6.1.5.2 Kinetics of molybdenum free alloys

To confirm that the generation of the platelets is associated with the existence of molybdenum in the alloy, the molybdenum free alloys (515 and 304 steel) were studied following the conditions used for 516 as closely as possible. Figure 6-35 and 6-36 record the passivation at a low potential within the passive potential regions (-104 mV for 515 and 250 mV for 304) in 0.1 M H_2SO_4. The results show that no nuclei or platelets can be found during the passivation of molybdenum-free alloys and the new passive films formed on both alloys lack structure and are shapeless, whose existence is only indicated from a low passive current rather than a variation of the surface. After a long elapsed time, the passivated surfaces become smoother.

Figure 6-35 In-situ AFM images show the passivation of 515 alloy in 0.1M H_2SO_4 when it is polarised at the low potential of the passive region A) for 1 min, B) for 5 mins, C) for 15 mins, D) for 30 mins, E) for 1 hr and F) for 3 hrs.

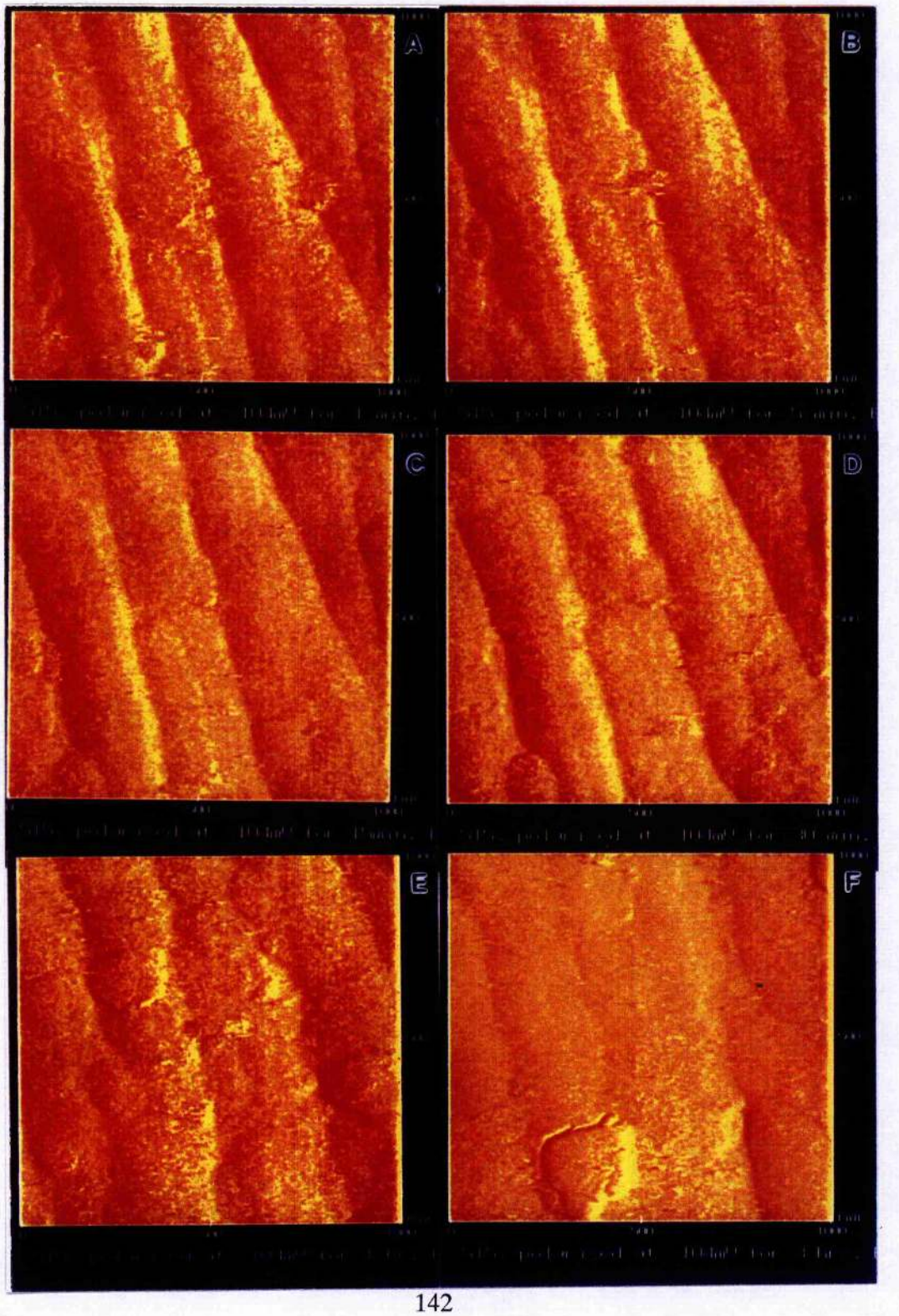

Figure 6-36 In-situ AFM images show the passivation of 304 alloy in 0.1M H_2SO_4, when it is polarised at the low potential of the passive region A) for 5 mins, B) for 10 mins, C) for 20 mins, D) for 30 mins, E) for 1 hr and F) for 3 hrs.

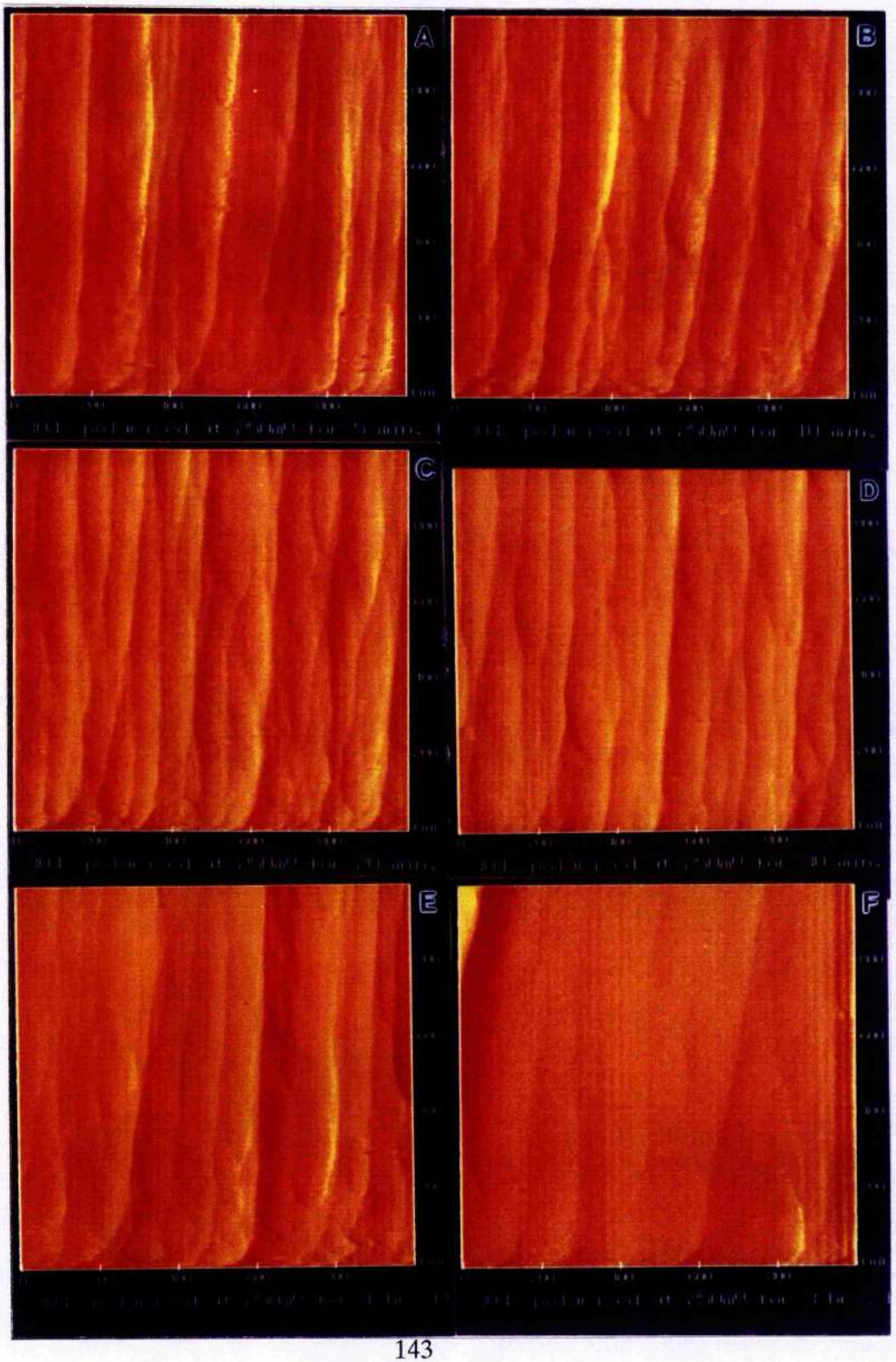

6.1.5.3 Discussion

A comparison between the passivation processes occurring on the molybdenum-bearing alloy and the molybdenum-free alloys indicates that the appearance of the platelets only occurs in the passivation of molybdenum-bearing alloys. Therefore, it is considered that the generation of the platelets is caused by the existence of molybdenum in the alloy and the platelets may be chromium oxide nucleated by molybdenum oxide. However, iron and chromium content in the alloy is much higher than that of molybdenum, the concentrations of both iron and chromium ions in the solution, obviously, should be higher than that of molybdenum in the passivation. Then why can molybdenum oxide reach the supersaturated level before iron and chromium and precipitate on the surface as the first oxide? The answer to this question is found in Pourbaix diagram (Figure 6-37).

Figure 6-37a Pourbaix diagram of Fe-H_2O.

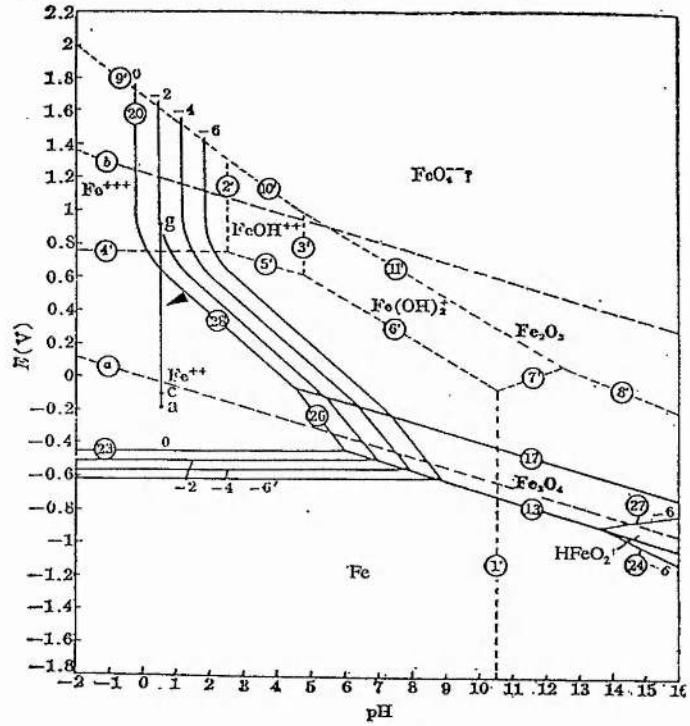

In the Pourbaix diagram of Fe-H_2O (Figure 6-37a), the line indicated by an arrow gives the pH value of the solution and the range of potentials used in this study. The diagram shows that at a potential around -0.2 V (the passivation potential where the passive film begins to form on the surface) in this solution, iron in the surface is dissolved to Fe^{++}, so iron cannot stay on the surface. The Cr-H_2O diagram (Figure 6-37b) shows the similar situation, i.e. at the passivation potential, the chromium is oxidized to soluble ions, Cr^{+++}, which go to the solution as well. However, in this case, if the pH value of the solution at the anode increases by about 1.5 units then, once the concentration of chromium ion reaches 0.01 M at the anode, insoluble oxide, $Cr(OH)_3$, can be formed on the surface.

Figure 6-37b Pourbaix diagram of Cr-H_2O.

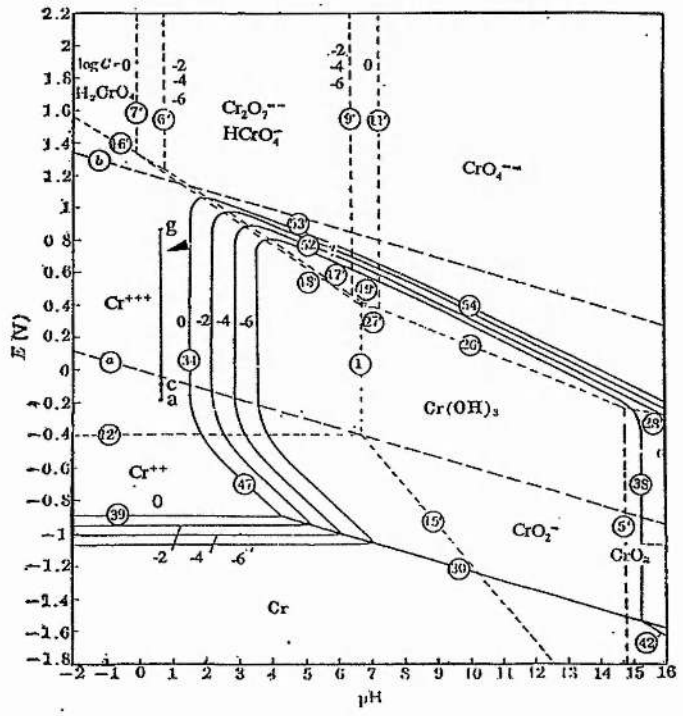

In comparison with Fe and Cr ions, it is easier for Mo ions to form solid deposits from the solution. As can be seen from the Mo-H_2O diagram (Figure 6-37c), around the passivation potential, insoluble molybdenum oxide, MoO_2, can form when the concentration of Mo ions reach 1 M. This requirement is difficult to meet, but when the local pH value increases by 1 unit, MoO_2 will form when the concentration of Mo ions reach 10^{-4} M. Similarly, MoO_2 can form in the condition that the pH value increases by 1.5 units and the concentration of Mo ions reach 10^{-6} M.

Figure 6-37c Pourbaix diagram of Mo-H_2O.

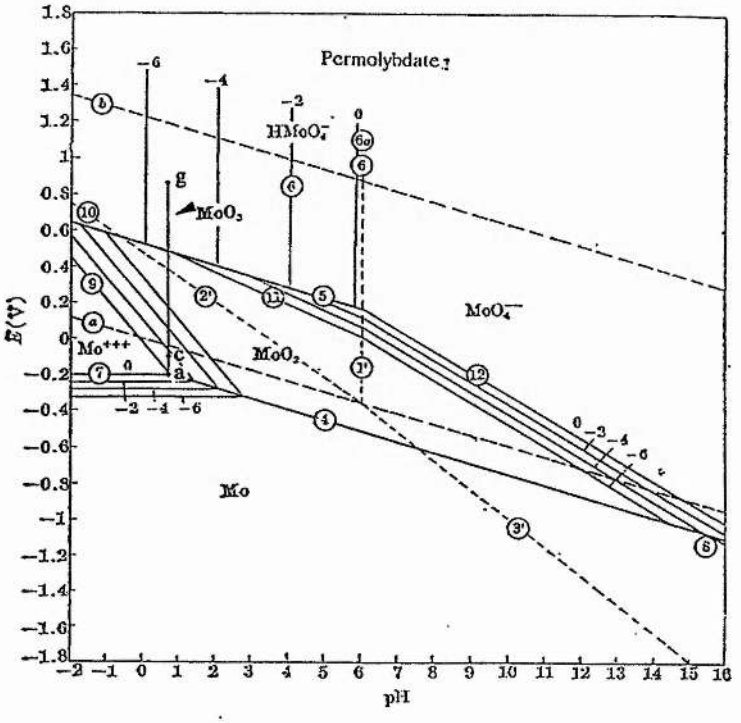

Comparison of the Pourbaix diagrams of Fe, Cr and Mo shows that around the passivation potential, the insoluble molybdenum oxide is likely formed before the formation of chromium oxide, and so it can provide nuclei for the precipitation chromium from the solution.

According to the Pourbaix diagrams, the formation of chromium and molybdenum oxide occurs only under the condition in which the local pH value in the anodic area is slightly higher than that in the solution. The increase of the local pH value may be caused by the dissolution of a large number of metal ions in active dissolution in which the massive positive ions lead to a rapid movement of hydrogen ions in the solution away from the vicinity of the anode surface.

As a result of the active dissolution and the increase of the local pH value, the molybdenum-oxide nuclei form on the surface and they make the precipitation of chromium easier. These nuclei grow up to the oxide platelets, which have been seen in AFM images, by nucleating chromium oxide from super-saturated solution. This platelet layer works as a barrier in the interface of the film and the solution to prohibit the continued dissolution of metal ions and to facilitate the formation of the passive film underneath. This is probably the role of molybdenum in the passivation of such an alloy. In practical applications, molybdenum gives protection against pitting corrosion, crevice corrosion and localised attack which relates to the breakdown of the protective film. Molybdenum is normally sufficient to protect chromium steels against the environment. Breakdown of a film results in momentarily high reaction rates and the key safeguard is a rapid repassivation. These are exactly the conditions in which the provision of seed nuclei would have greatest impact on the film growth and this is the precise function of molybdenum in an alloy steel.

More evidence supporting the oxide property of the platelets was found in the in-situ AFM studies (Figure 6-32). For example, the platelet marked "a" appeared and was growing in the period between 5 minutes (B) to 30 minutes (D), when most of the surface was in a passive state. This shows that the platelet 'a' was not created by a high dissolution current in the early stage of passivation. The passivation product can precipitate in passivation, but the metal structure is most likely to be etched at active dissolution. The close examination also finds that the platelet "a" appears on, but not underneath, the surface of the metal, it cannot be considered as metal structure. Significant loss and breakage of platelets between the height and force mode scans (comparing the 30 minute images at the position "c" from both the height-mode and the force-mode images) indicate the fragile nature of the platelets, which can even be damaged by the tip scan, so they are truly a kind of surface deposit. After 1 hour exposure, the rough surface observed at the early stage of passivation became smooth after the removal of the platelets, which shows that the rough surface was not caused by etching metal structure.

The loss of the platelets found in the in-situ AFM study seems not to occur in ex-situ AFM studies. This is because the refreshment of solution during in-situ AFM study may dilute the local concentration of metal ions below a saturation level, which leads to a subsequent dissolution of deposits and loss of the platelets. The surface changes in ex-situ experiment suggest that if the passivation is not disturbed by the environment, the platelets should be absorbed into the general oxide film. When the tip scans in solution, the loss and the breakage of the wet platelets happen as the wet platelets in solution are weaker than dry ones in air. It should also be remembered that the breakage of the platelets always ran across the plate as if the dendritic structure provided a weak fracture route.

Figure 6-38 In-situ AFM images show the passivation of GGR steel when it is polarised at 400 mV in 0.1 M H_2SO_4, A)1 min, B) 5 mins, C) 10 mins, D) 20 mins, E) 30 mins, F) 2 hrs.

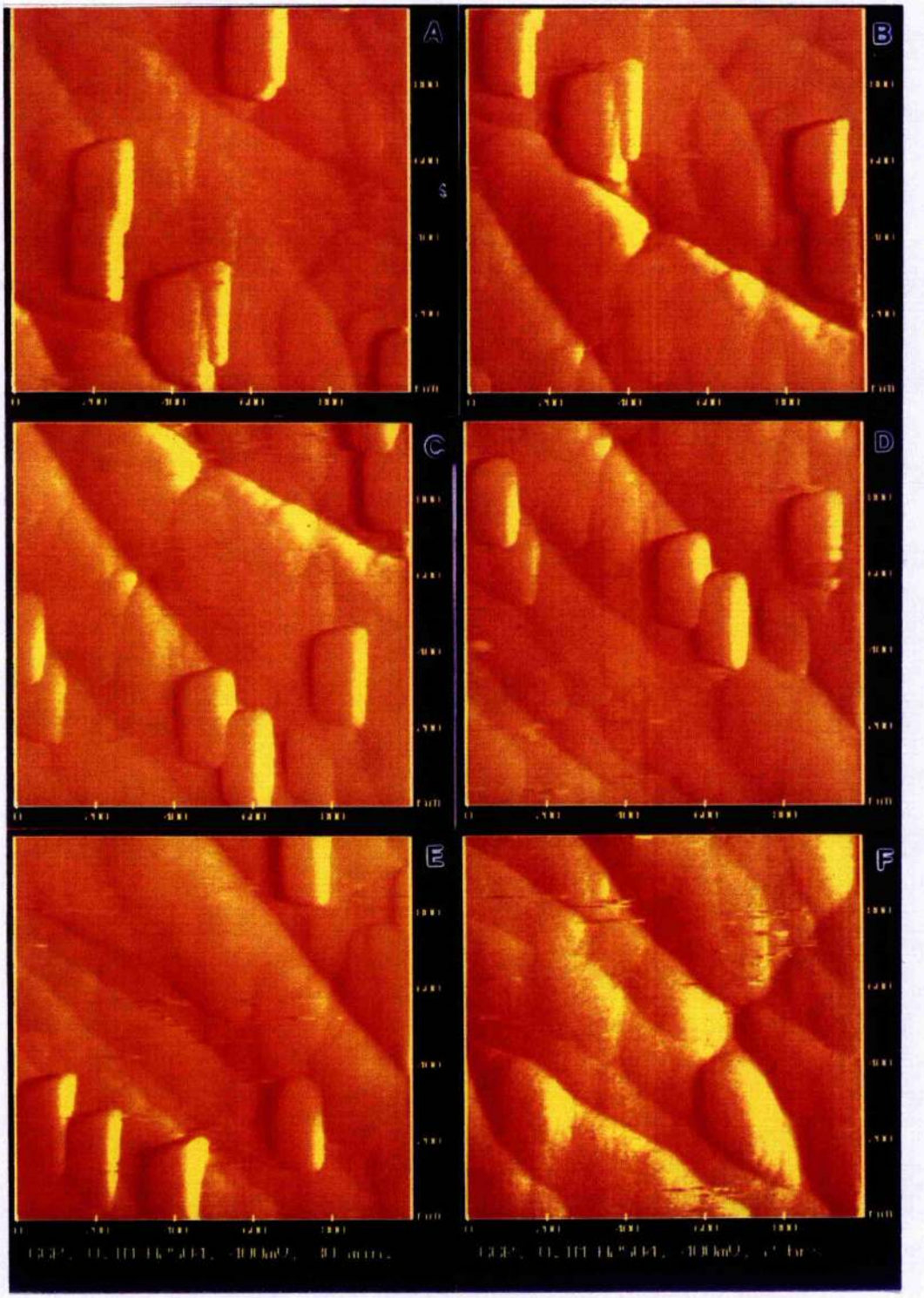

Passivation of molybdenum-bearing alloys is a coordinated function of molybdenum and chromium: the topography of the passivation surface will change with decreasing Mo/Cr ratio in the alloy. Figure 6-38 records the passivation of a duplex stainless steel which contains 22.2% chromium and 3.1% molybdenum (GGR steel). On the passivation surface, instead of forming a compact platelet layer, a few platelets scatter in the field of view. These platelets are too few to be expected to inhibit the dissolution of the metal ions from the metal surface. There are two possibilities to explain the phenomenon: 1) the importance of molybdenum in passivation decreases with decreasing the Mo/Cr ratio in alloys. In the passivation of a low Mo/Cr alloy, chromium plays a main role in passivation while molybdenum nucleation is not necessary, and 2) molybdenum nuclei rapidly merge into the new passive film before they grow up to the big platelets. In the passivation of a low Mo/Cr alloy, the rapid precipitation of chromium oxide on the molybdenum nuclei forms the passive film rather than forms the individual platelets. These two possibilities need to be assessed for relative importance in the future work.

6.1.5.4 Model of the passivation of molybdenum-bearing alloys

A model for the passivation of molybdenum-bearing alloys based on the above results is described as following: at the initial stage of passivation - active dissolution stage -, massive currents of iron, chromium and molybdenum ions dissolve into solution from metal surface, which leads to a rapid accumulation of the metal ions in the vicinity of the sample surface. If there is a sufficient amount of molybdenum in the alloy, its ions in the solution will reach a super-saturated level and precipitate on the surface as the first deposit of an oxide phase. Then molybdenum oxide seeds chromium oxide from supersaturated solution and the

molybdenum nuclei grow up to the big oxide platelets at the early stage of the passivation. The platelet layer works as a barrier in the interface of the metal and the solution to hinder the dissolution of passive species from the metal matrix and to facilitates the formation of the passive film underneath.

Once a compact passive film formed, the dissolution current decreases to a low level which fails to supply sufficient passive species to generate new platelets rapidly. The oxide film, then, grows under the platelet layer by way of the direct reaction with water on the surface. If there is no disturbance from the environment, the initial platelets will stay in the passive film permanently. Figure 6-40 is a schematic diagram to describe the nuclei-growth model for the passivation of molybdenum-bearing alloys.

Figure 6-39 The model for the passivation of the molybdenum-bearing alloy.

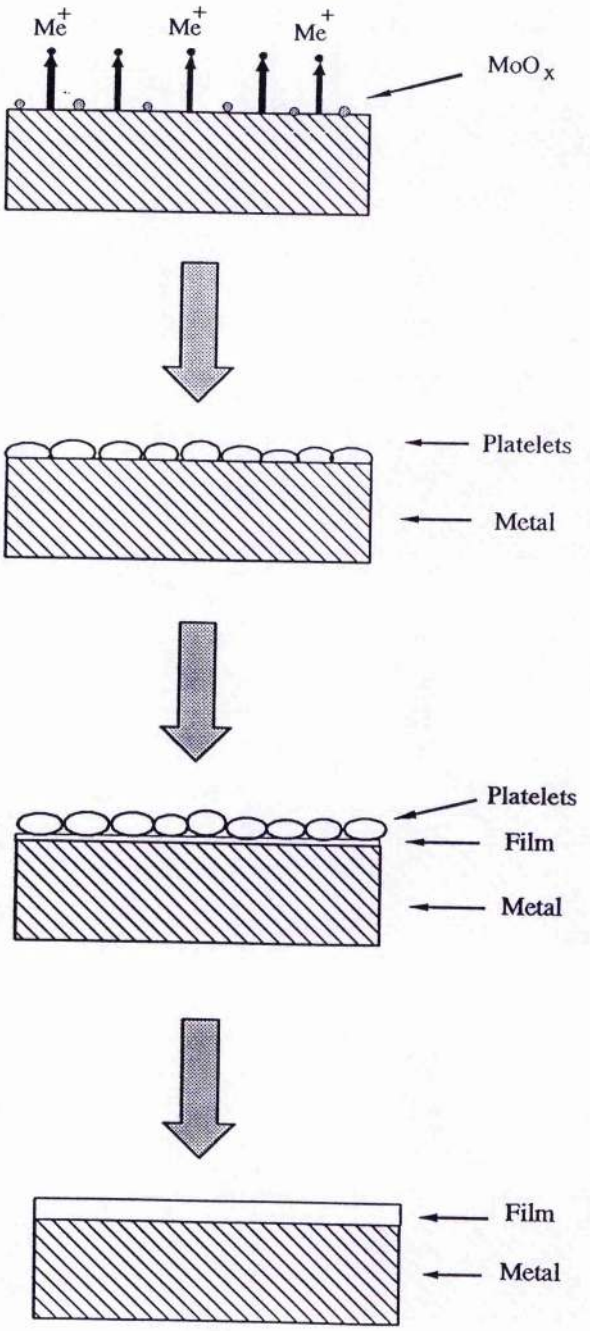

6.2 Introduction to the study of heavily corroded surfaces

6.2.1 Introduction

The previous section concerned on the relatively smooth passivated surfaces. In order to extend the study to the actively corroding surface, it will be necessary to image the etched structures and perhaps the pits on the sample surfaces and this bring out a different problem in the use of in-situ AFM. This type of problem has already been reviewed in chapter 4, and here an experimental inspection on the specifically etched structure in duplex steels. The sloping sidewalls of corroded features and "crystalline structures" on the sidewall were observed in this corrosion study. During studying other materials, some authors had found the similar phenomena and they considered them to be artifacts created by AFM tips (Hellemans *et al*, 1991, Allen *et al*, 1992, Grütter *et al*, 1992, Keller *et al*, 1992, Schwarz *et al*, 1994). To understand fully and interpret correctly AFM images obtained in a corrosion study, the reality of features observed in AFM images is discussed in this thesis before the investigation of corrosion. In this section, the effect of sharpness of a tip and the effect of viscosity on AFM images are discussed separately.

6.2.2 Effect of tip sharpness on AFM images

6.2.2.1 Reality of sloping sidewalls

Several investigators have reported that unsatisfactory sharpness of AFM tips may distort rough structures in AFM images (Hellemans et al, 1991, Allen et al, 1992, Grütter et al, 1992, Keller et al, 1992, Schwarz et al, 1994). For example,

when a tip meets a vertical sidewall during a scan, the tip may describe the vertical sidewall as a steep sidewall because its open angle makes it impossible to scan the "hole region" beside the sidewall (Keller, 1991). The situation is illustrated by the scan line of the tip in Figure 6-40.

Figure 6-40 Distortion of the feature by the AFM tip.

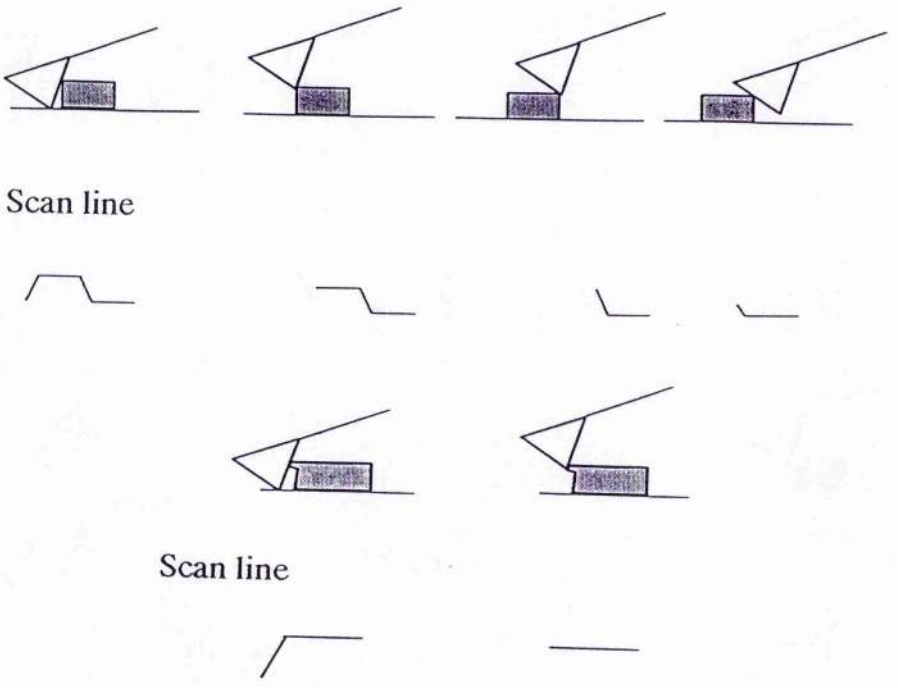

Sloping sidewalls on corroded surfaces are observed in AFM images in different duplex stainless steels throughout this study (Figure 6-41). Are they the artifacts reported in the literature? According to Keller, this kind of artifacts occur only on a sidewall which is steeper than the scanning tip. It is, thus, possible to identify the reality of the gradient of the sidewall by measuring its angle. Figure 6-42 is a schematic diagram of this kind of measurement, where angle A and B are angles of both sidewalls and angle C is the open angle of the

tip. When A(or B) + (1/2)C is less than 90°, the tip scans the sidewall properly, otherwise, it will fail to give the real image of the sidewall but reflect its own shape instead.

Figure 6-41 An AFM image, showing a sloping sidewall of a duplex stainless steel.

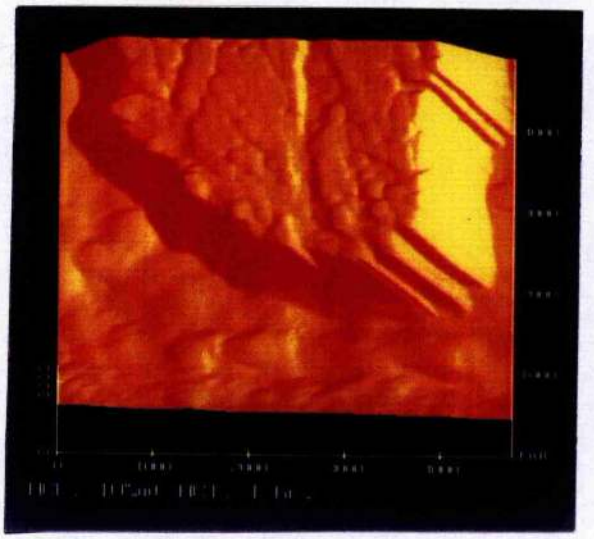

Figure 6-42 Schematic diagram for the measurement of the sidewall.

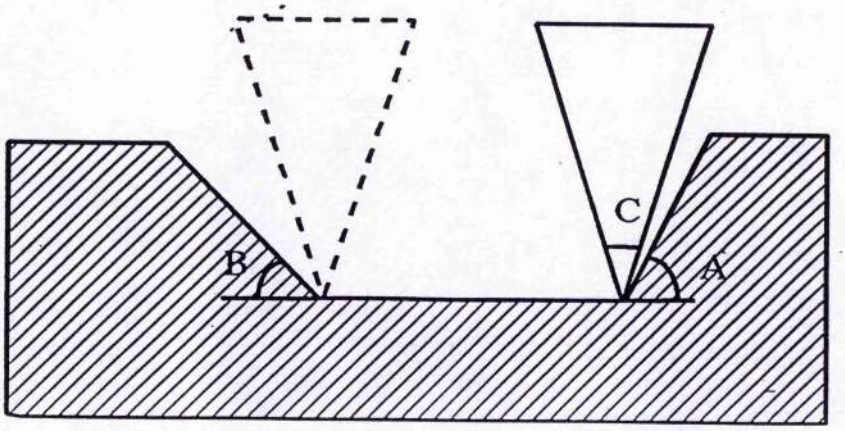

Two examples of the measurements are shown in Figure 6-43 and Figure 6-44. The gradients of the sidewalls of a hole and a high relief which were scanned by a tip having an open angle of 62° are measured separately.

Figure 6-43 AFM measurement of the sloping sidewall of a hole.

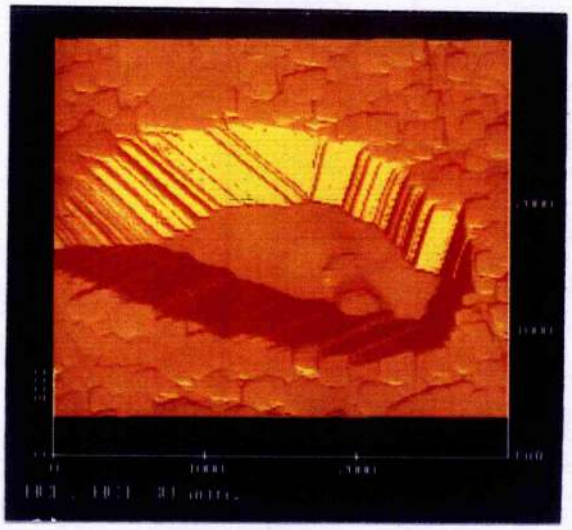

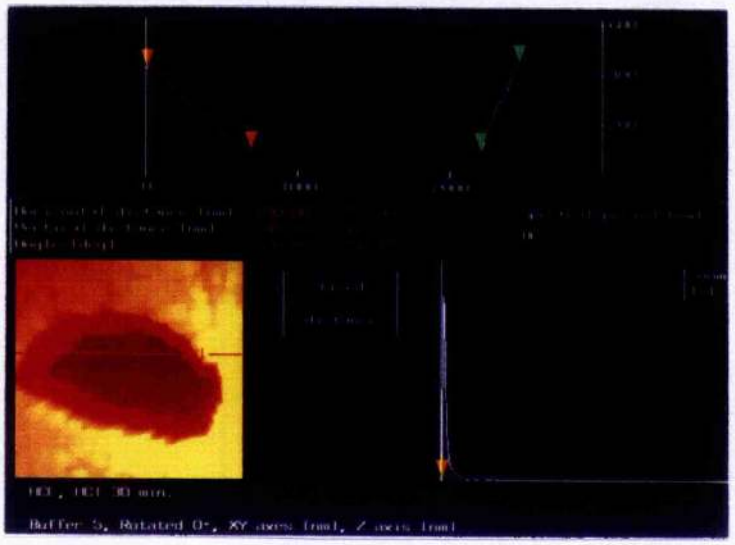

Figure 6-44 AFM measurement of the sloping sidewall of a high relief.

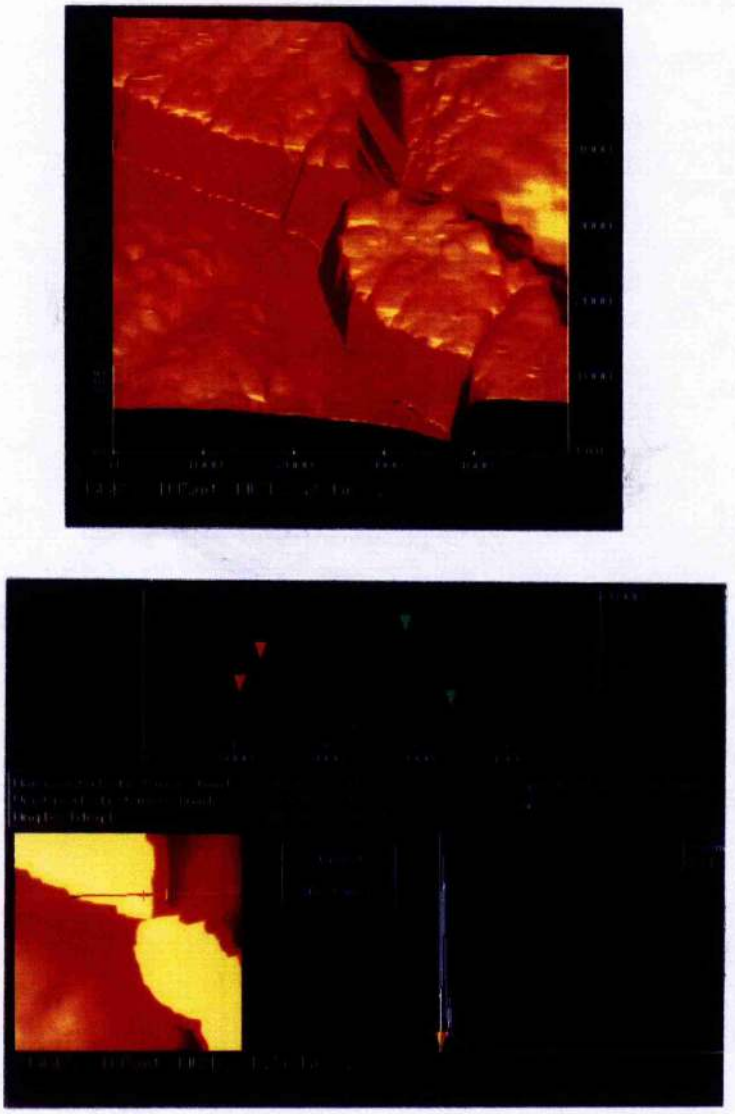

The angles of the both sidewalls of the hole are 26° and 55°, while those of the high relief are 44° and 45° respectively, so the sidewalls in both images satisfied the condition of A(or B) + (1/2)C < 90°, i.e. 56° or 85° for the sidewalls of the hole and 74° or 75° for the high relief. The both images of Figure 6-43 and Figure 6-44, therefore, may give the real appearance of the features.

The other gradient measurement is based on the principle of maintaining a constant angle of the tip relative to the surface in constant force mode operations (height-mode scan), i.e., the sidewall angle of a feature is changeable at different positions while the angle of the tip relative to the surface is constant in height mode scans. Measuring the sidewall angles in different scan lines can identify that the image is the contour of the feature or the shape of the tip. A grain boundary (Figure 6-45a) is measured in two different positions. The angles of both sidewalls are 41^{o} and 53^{o} in the first measurement but 30^{o} and 39^{o} in the second measurement (Figure 6-45b, 6-45c). Therefore, the sidewall angle of the feature in the image is independent of the tip angle.

Figure 6-45 AFM images of a grain boundary and AFM measurements of its sidewall: a) an AFM image of a grain boundary, b) the angles of the both sidewalls are 41 degree and 53 degree in the first measurement and c) the angles of the both sidewalls are 30 degree and 39 degree in the second measurement.

a

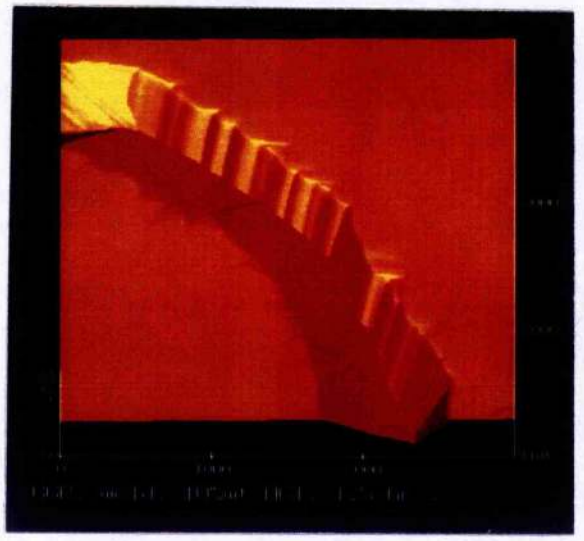

b

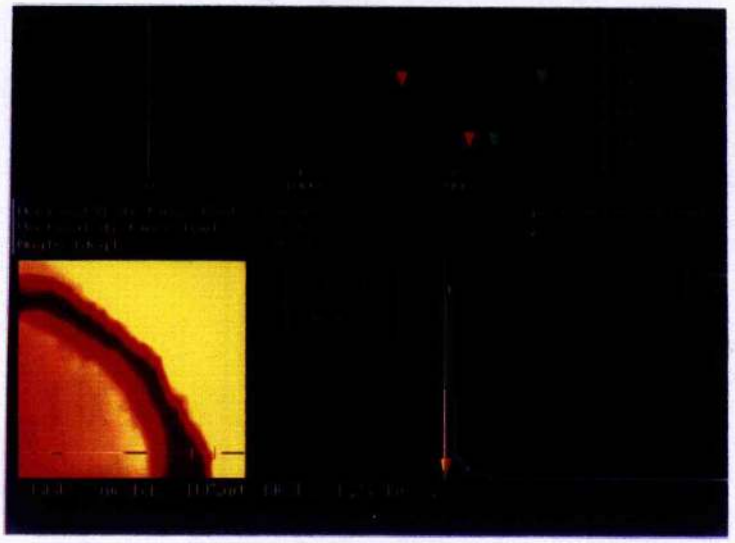

c

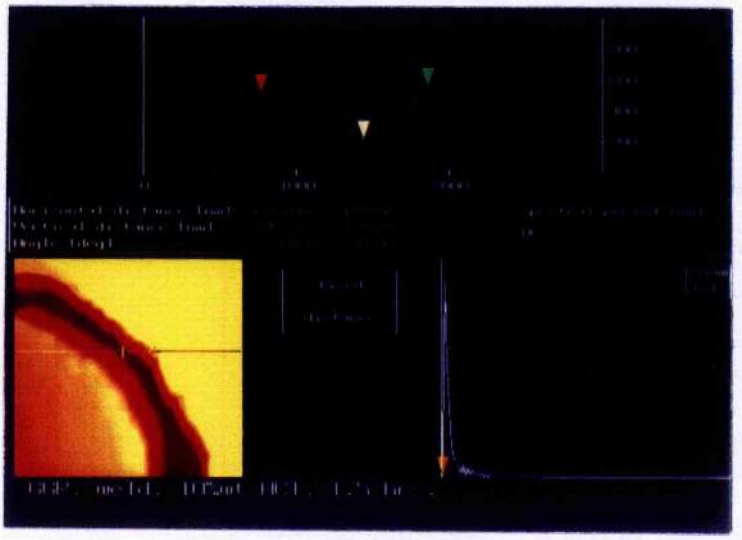

A real feature will show the same appearance when it is scanned by different tips while a tip-created sidewall will present differently. Therefore, the reality of sloping sidewalls scanned by a pyramidal tip in the previous study is examined by comparing them with a scan using a silicon tip (Figure 6-46). Figure 6-47 shows the used tip with an open angle of about 40°. The similar appearance of sidewalls in images scanned by both tips indicates the possible reality of the sloping sidewall.

SEM will give a convincing description of the appearance of sidewalls as it can eliminate the effect of tips entirely. A large field of view of an SEM micrograph (Figure 6-48) shows that gradients of sidewalls vary widely from one to another even in one piece of crystal. Therefore, the sloping sidewall is a common phenomenon of the features studied.

Figure 6-46 An AFM image scanned by a silicon tip shows that the sloping sidewall scanned has the similar appearance to that scanned by a pyramidal tip.

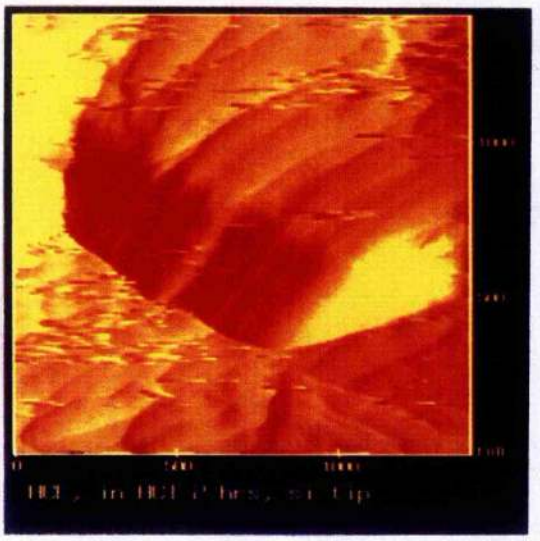

Figure 6-47 An SEM micrograph showing the silicon tip used to obtain the image in Figure 6-46.

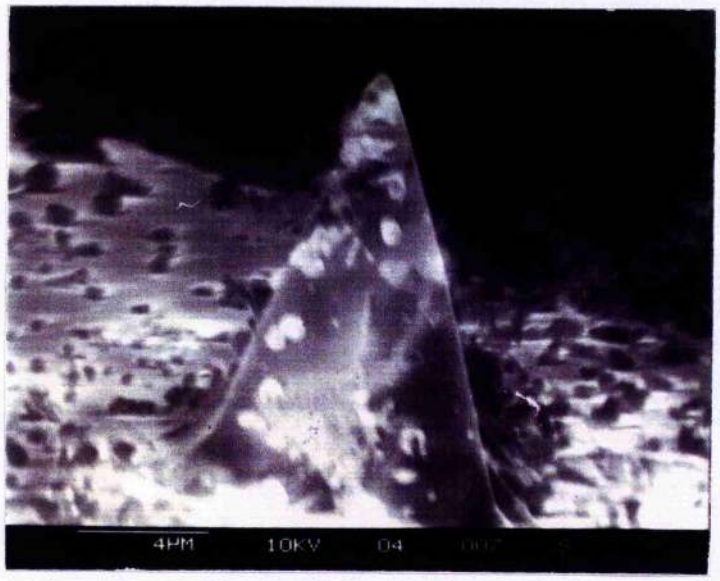

Figure 6-48 An SEM micrograph showing variable gradients of sidewalls.

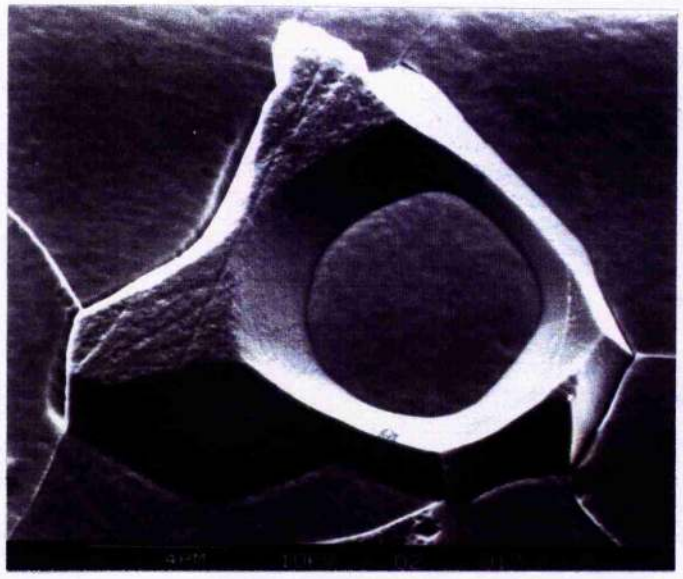

6.2.2.2 Reality of metal structures on sidewalls

In addition to sloping sidewall, crystalline structures, such as ledges and triangular structures on the sidewall, are considered as artifacts by Schwarz and co-workers (1994) as well. They considered the ledge to be the image of the tip edge and the triangular structure to be the image of the side face of the tip.

In this study, similar structures were observed in the sidewalls of the corroded features and their reality is more difficult to identify than the gradients of the sidewalls. One piece of evidence found from the above angular measurements is that crystalline structure is observed on the sidewall with a small gradient which satisfied A(or B) + (1/2)C < 90°, so the structure appears beyond the "hole region".

If a structure is the image of the tip, it will change its appearance as the scan area of the tip changes. Therefore, scanning the structure in perpendicular directions and inspecting the difference in the image is a way to establish the reality of the structure. It can be seen from Figure 6-49a and Figure 6-49b that the triangular structures which were scanned in different directions on the sidewall show the same appearance, so the result indicates that the structure found in this study is not associated with the scan area of the tip.

A bulge on a triangular structure in Figure 6-50 was not scanned as a ledge or triangular structure in the AFM image as Schwarz and his colleagues reported, therefore, it is possible using AFM to scan a bulge on the sample surface without distortion.

Figure 6-49 An AFM image of the triangular structure scanned in different directions.

a

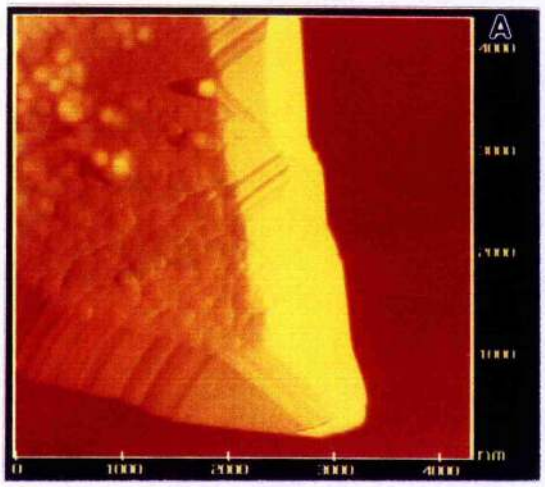

b

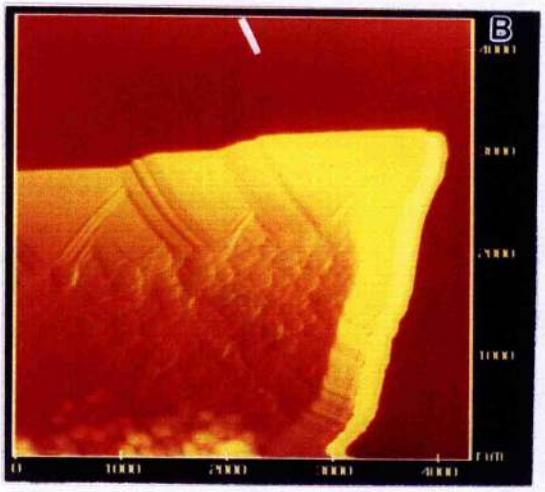

Figure 6-50 A bulge on triangle structure in an AFM image.

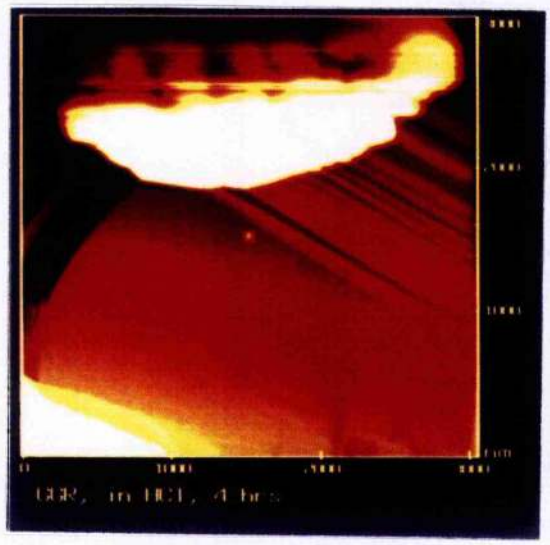

The characteristic structure of a material can only be found in that material while a tip-created structure, if exists, will appear in any material in AFM images. In this study, a silicon wafer (Figure 6-51) was scanned to examine whether the structure observed in steels is present. The repeated scans of 250 nm high sidewalls on the silicon wafer with both pyramidal tip and silicon tip do not show the existence of the structure seen in steels (Figure 6-52). Hence, the structure in the steel is considered to be the characteristic of steels.

Figure 6-51 An AFM image taken from a silicon wafer.

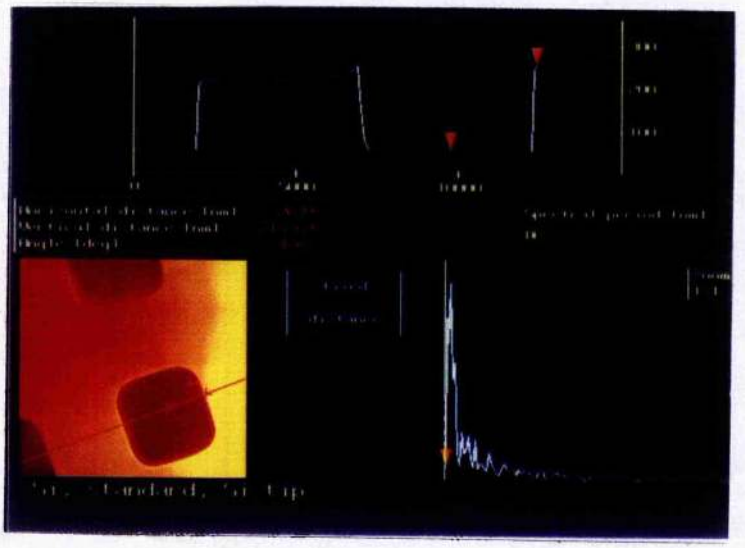

Figure 6-52 No crystalline structure on the sidewall of silicon wafer can be seen from the AFM images a) the image scanned with a pyramidal tip and b) the image scanned with a silicon tip.

a

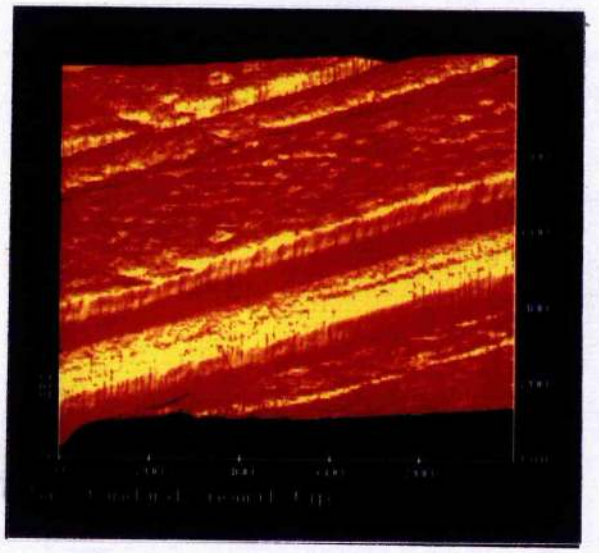

b

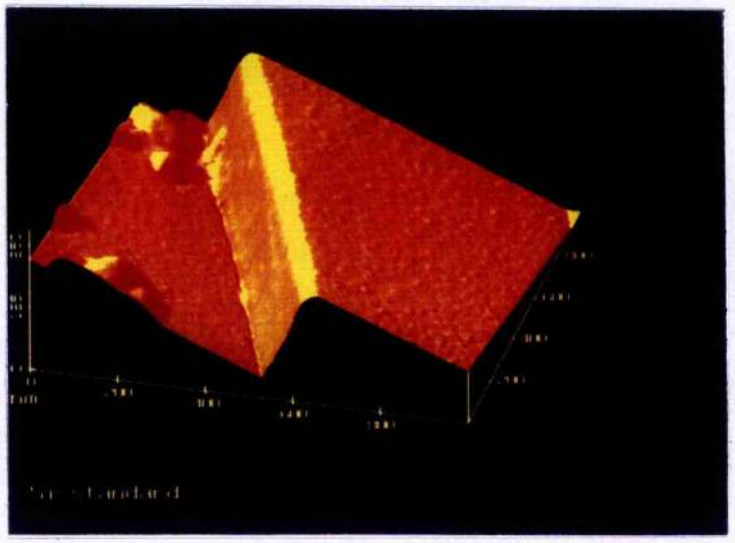

The ledge and the triangular structures observed in pyramidal-tip images are examined further in silicon-tip images. The fine irregular feature is revealed on the ledge structures in the silicon-tip image (Figure 6-53a) and these features show that the ledge structure is not the extension of roughness on the upper rim. This ledge structure is enlarged in Figure 6-53b. Shown in Figure 6-54 is the triangular structure in the AFM images scanned with a silicon tip.

Figure 6-53 A ledge structure in the AFM images scanned using a silicon tip, a) the ledge structure and b) zoomed-in area of the ledge structure.

a

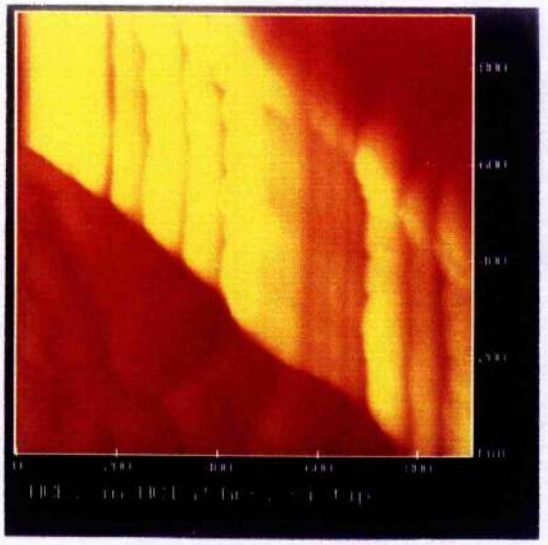

b

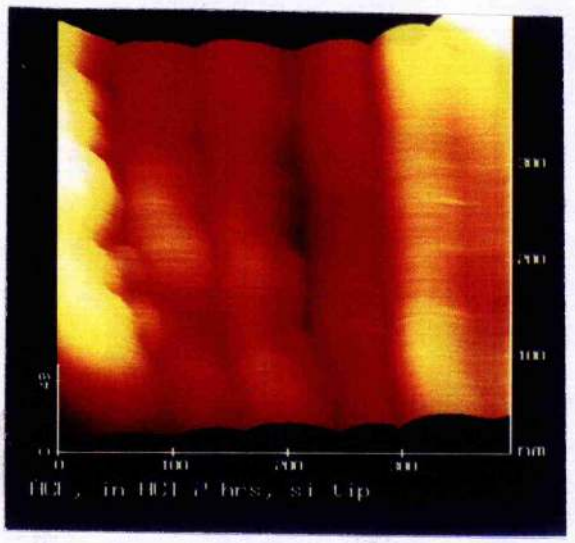

Figure 6-54 A triangular structure in the AFM images scanned using a silicon tip.

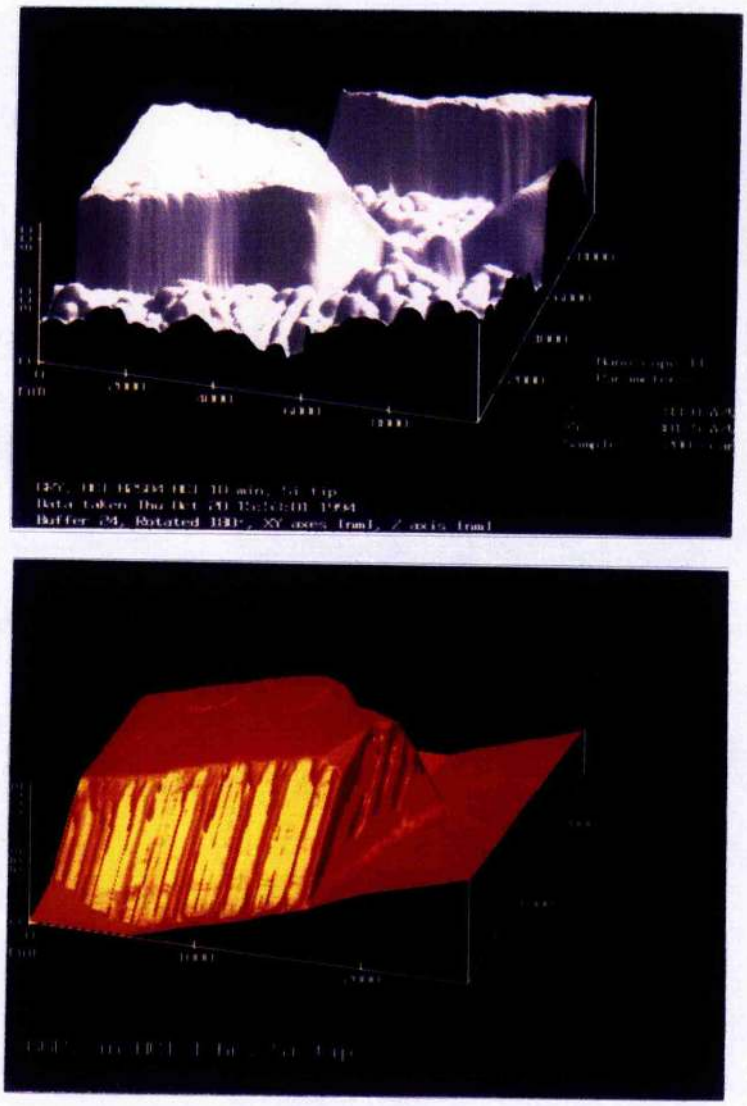

SEM was used to further examine the steps and triangular structures observed in the AFM images to confirm their existence (Figure 6-55). By lowering the accelerating voltage, the fine ledges and the triangular structures present on the sidewall are clearly shown in Figure 6-56 and Figure 6-57.

Figure 6-55 An SEM micrograph showing the step and the triangular structure on the sidewall.

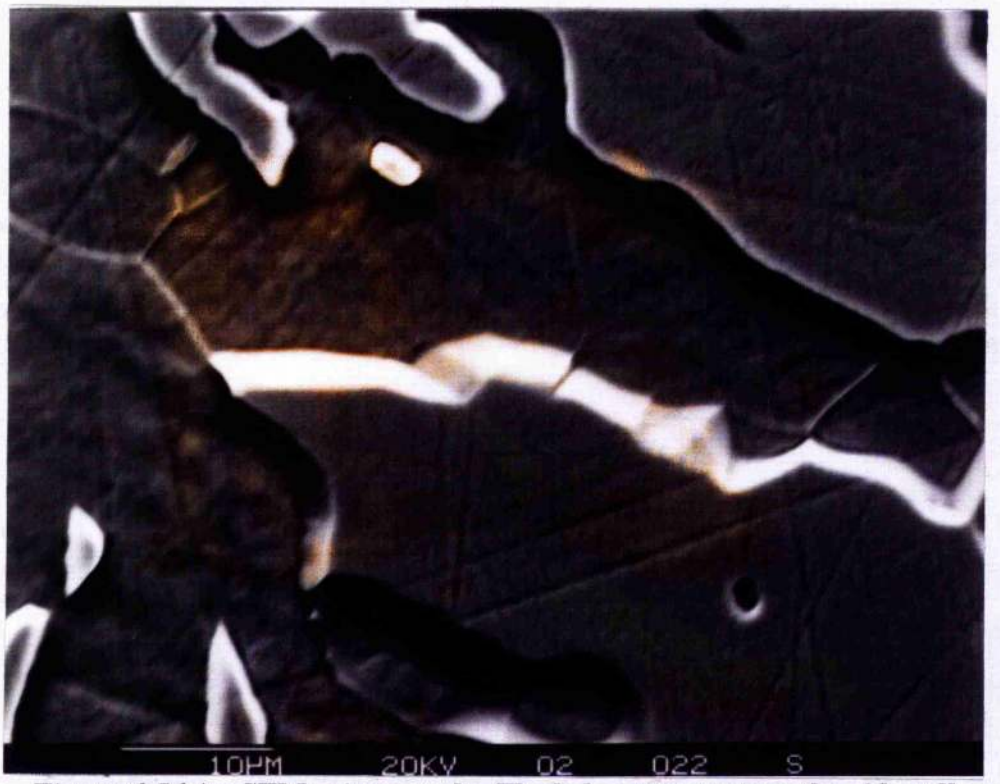

Figure 6-56 An SEM micrograph: The ledge structure on the sidewall can be seen clearly.

a

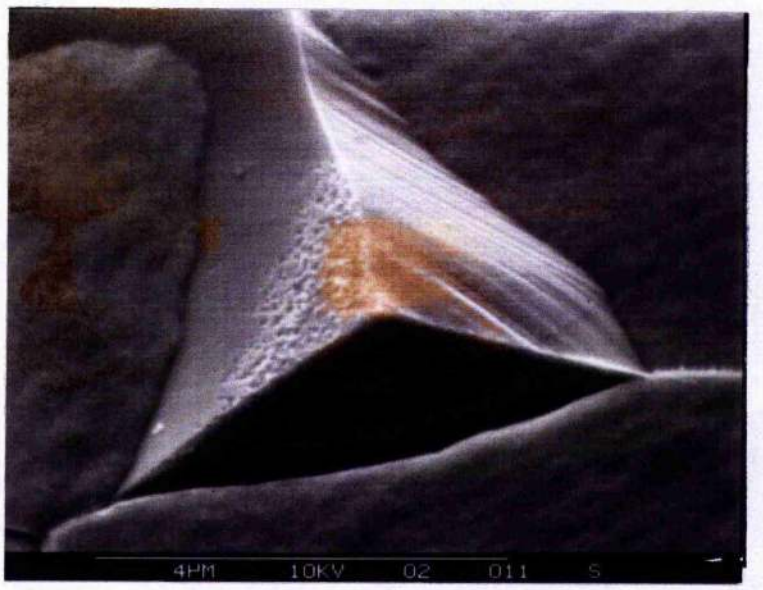

b

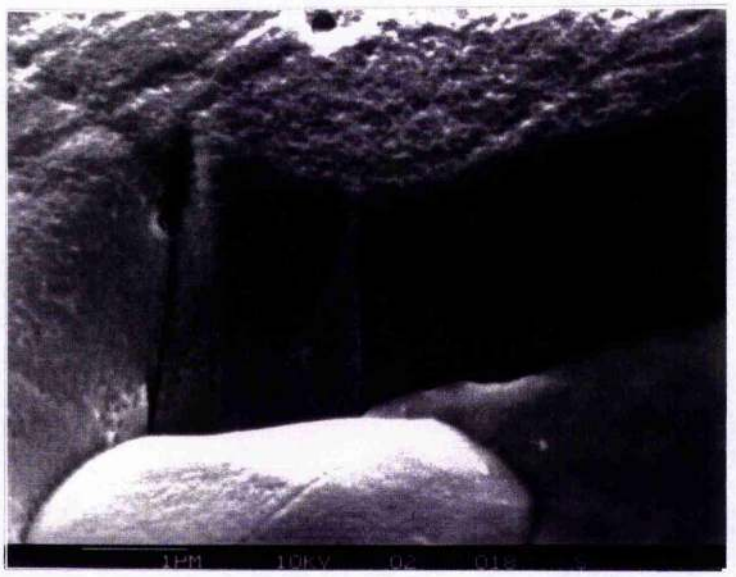

Figure 6-57 A triangular structure on the sidewall observed in an SEM micrograph.

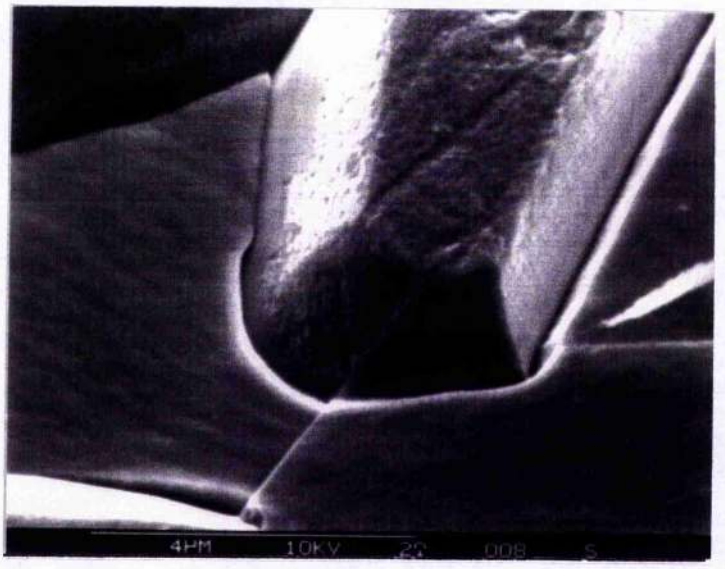

Following above investigation which has provided evidence for the reality of the crystalline structure on sidewalls, it is necessary to examine the situation when a tip scans through a hole region on the sample. The study was carried out on one specimen having different sloping sidewalls (Figure 6-58a). On the right sidewall, rich structures appear but on the left one, the structures are not observed clearly. The same situation is shown in both height mode and force mode images and the visibility of the structure on the left sidewall cannot be improved even by changing the viewing angle and using a front light source which illuminates the sidewall directly (Figure 6-58b and c). The measurements of the angles of both the sidewalls (Figure 6-58d) show that the rich structures appear on the small gradient sidewall (36^{o}) where $A + (1/2)C = 67^{o} < 90^{o}$ (Figure 6-52d) while it can hardly be seen on the steep sidewall (68^{o}) where $B + (1/2)C = 99^{o} > 90^{o}$ As artifacts are more likely to occur on a steep sidewall than a sloping sidewall, it is considered that the metal structure on the sloping sidewall is the real structure.

Figure 6-58 a) Rich structure observed on the right sidewall but not on the left sidewall from an AFM image.

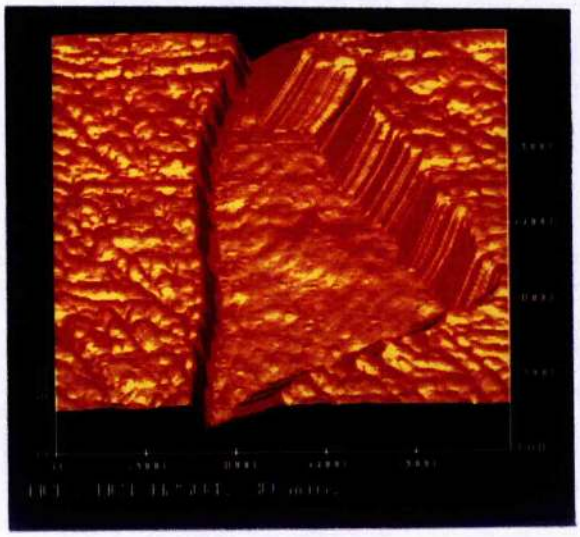

Figure 6-58 b) and c) AFM images, showing the poor visibility of the structure on the left sidewall even changing the view angle, b) a height mode image and c) the corresponding force mode image.

b

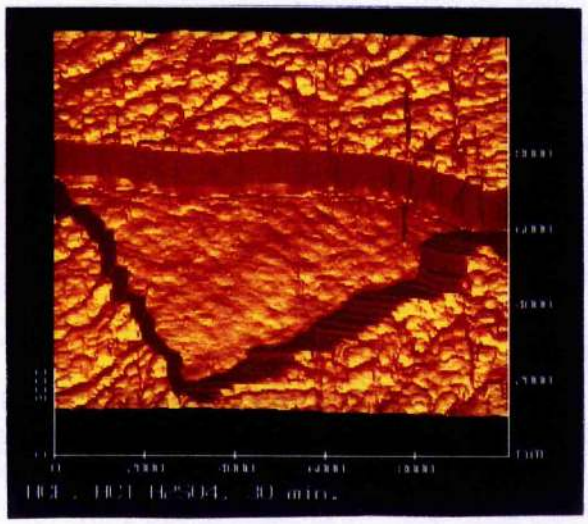

c

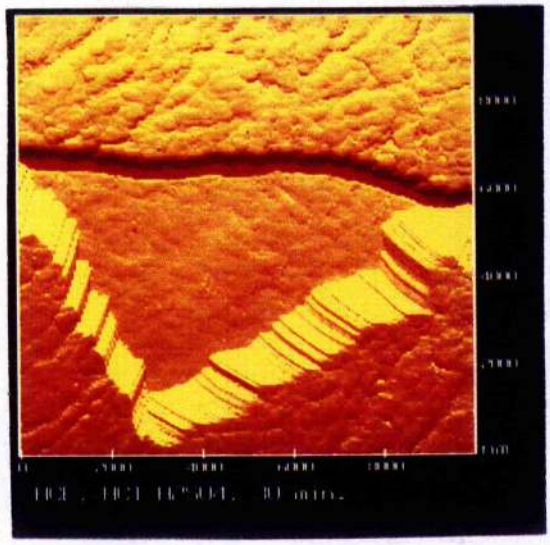

Figure 6-58 d) Measurements of the sidewall angles using AFM, the gradient of the steep sidewall is 68° and the sloping sidewall is 36°.

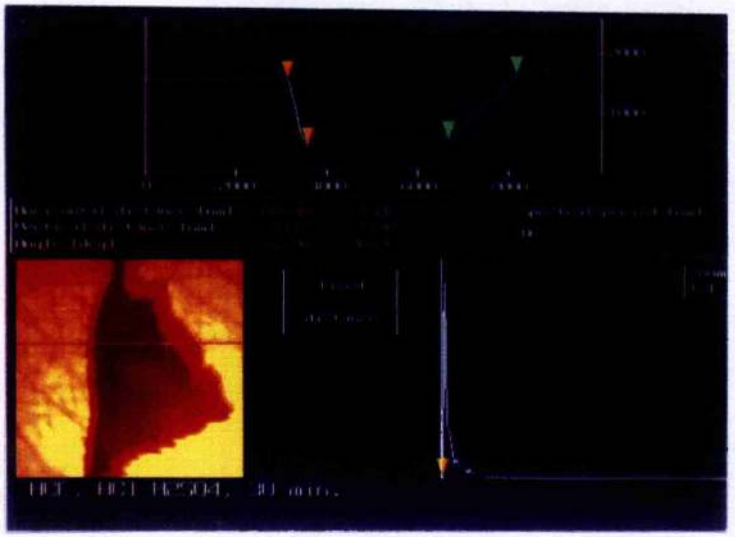

Figure 6-59 shows another example, in which the gradient of the left sidewall of a hole in two measurements is 44° or 40°, while those of the right sidewall is 58° or 60° respectively. Therefore, A + (1/2)C is 74° or 70° for the left sidewall, and 88° or 90° for the right sidewall where the artifact may be created (Figure 6-50a and b).

Figure 6-59 a) and b) Measurements of the hole sidewalls: the left sidewall having the smaller gradient of 44° or 40°, the right sidewall having the larger gradient of 58° or 60° respectively.

a

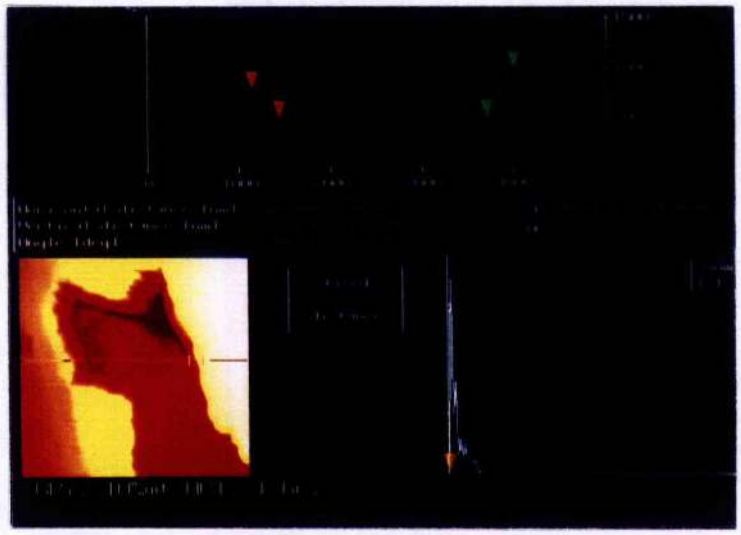

b

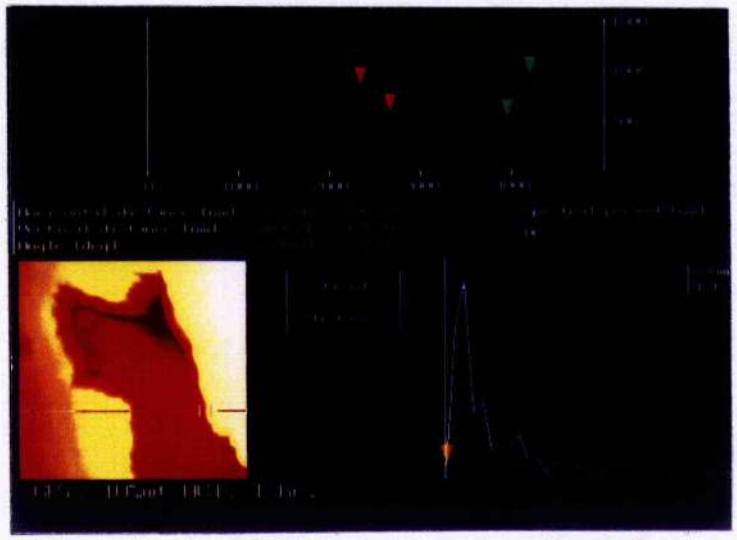

The corresponding height mode and the force mode images are shown in Figure 6-59c and d. As it can be seen that the metal structures only appear on the sidewall with a small gradient in both images.

Figure 6-59 c) and d) In-situ AFM images: the structure on the steep sidewall can hardly be seen in both the height mode scan c) and the force mode scan d).

c

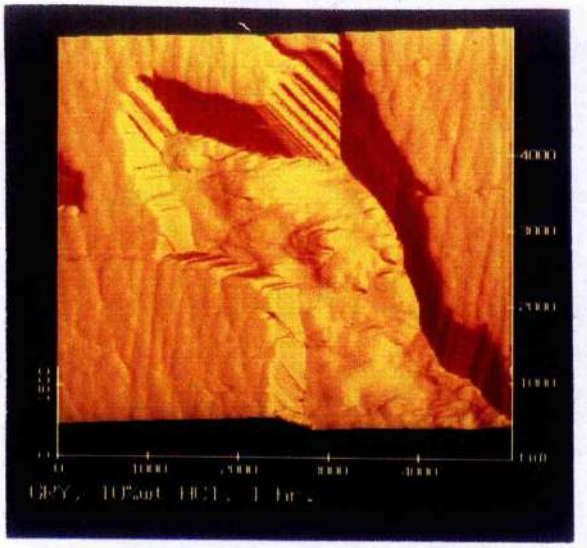

d

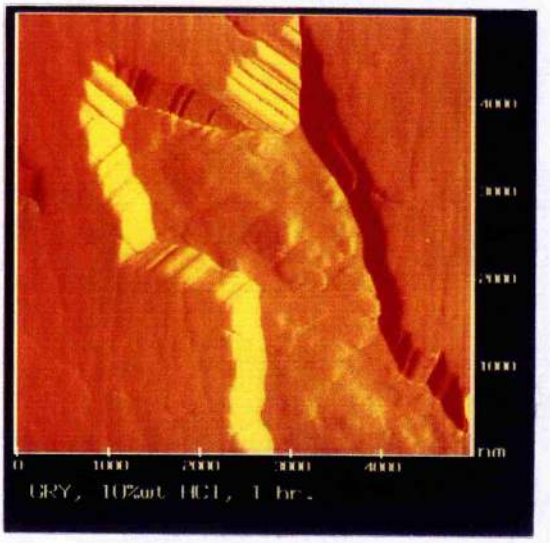

Changing the viewing angle and using a front light source does not show any structure on the right sidewall (Figure 6-59e and f). According to the above investigation, the tip scan is more likely to miss the feature on the sidewall rather than to create it in a "hole region".

Figure 6-59 e) and f) In-situ AFM images: the structure on the steep sidewall is still difficult to see even in a changed view angle in either the height mode scan e) or in the force mode scan f).

e

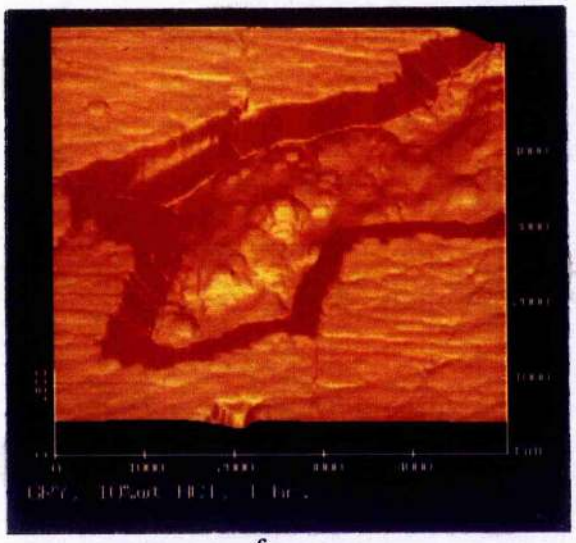

f

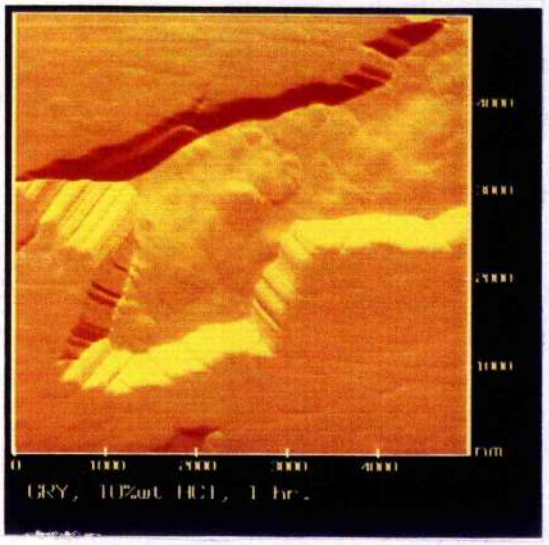

6.2.3 Effect of viscosity on AFM images

The motion of a scan tip in any medium other than vacuum will generate an opposing force arising from viscous drag which may have a significant damping effect on the tip motion, especially in aqueous media. In this case, the scanning tip no longer follows the structural contours of the sample accurately and this will affect, for example, the edge resolution of the steps which are not parallel to the scanned direction.

When a tip passes a cliff, its vertical velocity reaches a terminal velocity, u, from zero. During this period, the atomic force loaded on the tip approaches 10^{-11} N and the drag force changes accordingly. The total force on the tip in this period cannot be measured, so the movement of the tip is difficult to be calculated mathematically. Stokes law ($f = 6\pi\eta ru$) refers only to the terminal velocity once a steady state has been reached, however, the velocity of the tip will not reach a steady state, so using Stokes law to describe the force on the tip moving in aqueous medium is likely to underestimate the effect of the viscous drag. Nevertheless, the calculation by Stokes law is still carried out in this study as if the exact value is not necessary, it will simplify the situation and give a concept of the movement of the tip under the function of viscosity.

The Stokes law is described as $f = 6\pi\eta ru$, where η is the viscosity of the medium, r is the radius of the sphere which is moving in the medium, u is the terminal velocity and f is the drag force. An AFM tip moved in the medium can be estimated by simulating the tip as a sphere with a radius, r, of 5 μm and assuming it weightless (Figure 6-60). It is known that for pure water, η is in the order of $10^{-2}N(sec)(m^{-2})$. The drag force is assumed to be equal to the typical atomic

force, f, in value (10^{-11}N) but is opposite in direction. The terminal velocity, u, can then be easily determined to be 10^4 nm/sec according to Stoke law.

Figure 6-60 A schematic diagram of simulating the tip as a sphere in solution.

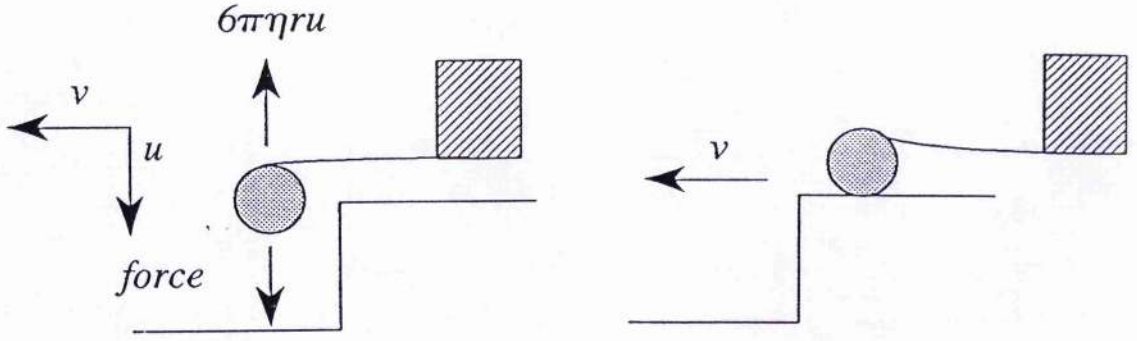

Whether the damping action calculated above will influence the image quality depends on the scan rates used for mapping the sample surface. By considering a tip scans a sidewall with a length of l, as shown in Figure 6-62a, the tip will move lsinθ vertically at a vertical velocity of u in time t_a and scan lcosθ at a horizontal velocity of v in time t_b. If $t_a < t_b$, the tip will move too fast to follow the feature contour, leading to the situation as shown in Figure 6-61a. On the contrary, if $t_a > t_b$, the tip can scan the surface properly.

Figure 6-61 Schematic diagram showing the effect of the scan rate on the resolution of AFM images under the function of drag force.

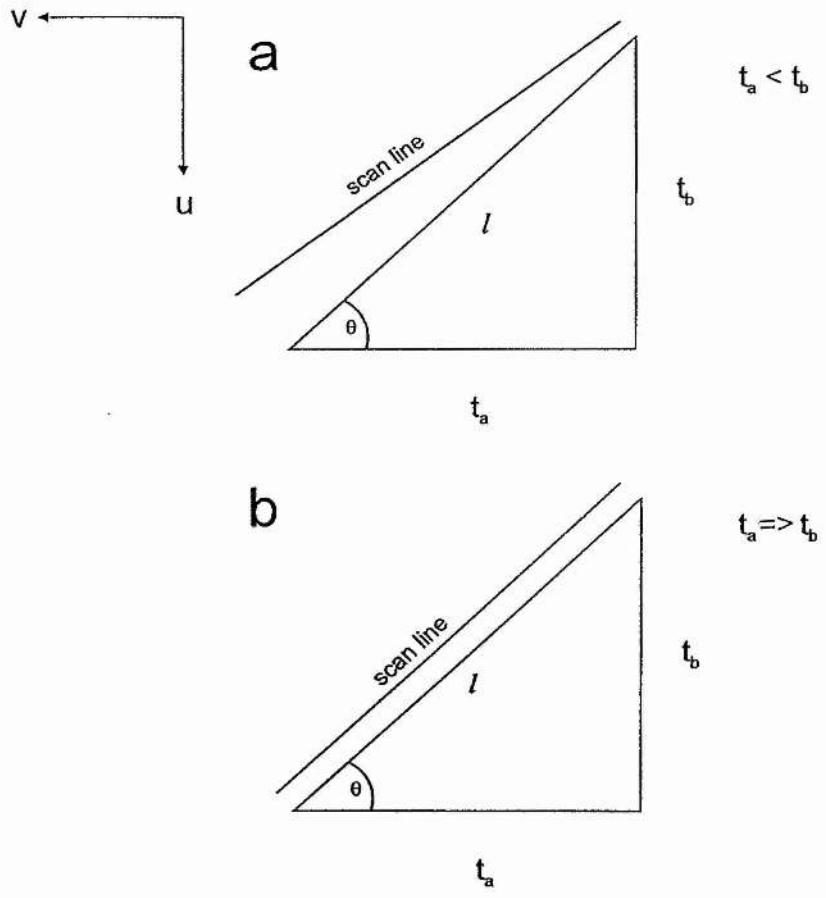

Figure 6-62 is an example which shows the effect of the scan rates on the resolution of in-situ AFM images in aqueous solution HCl. A poor-resolution image (Figure 6-62a) was obtained at a high scan rate (5 lines/sec) and its resolution was improved by reducing the scan rate to 3 and 1 lines/sec (Figure 6-62b, c). From the line scan picture (Figure 6-63) it can be seen that the sharp corner marked as "a" takes the form of a distinct rounding of the edges at the high scan rate pictures and the feature "b" is not able to be scanned properly

Figure 6-62 In-situ AFM images obtained by scanning the feature in HCl at differing scan rates.

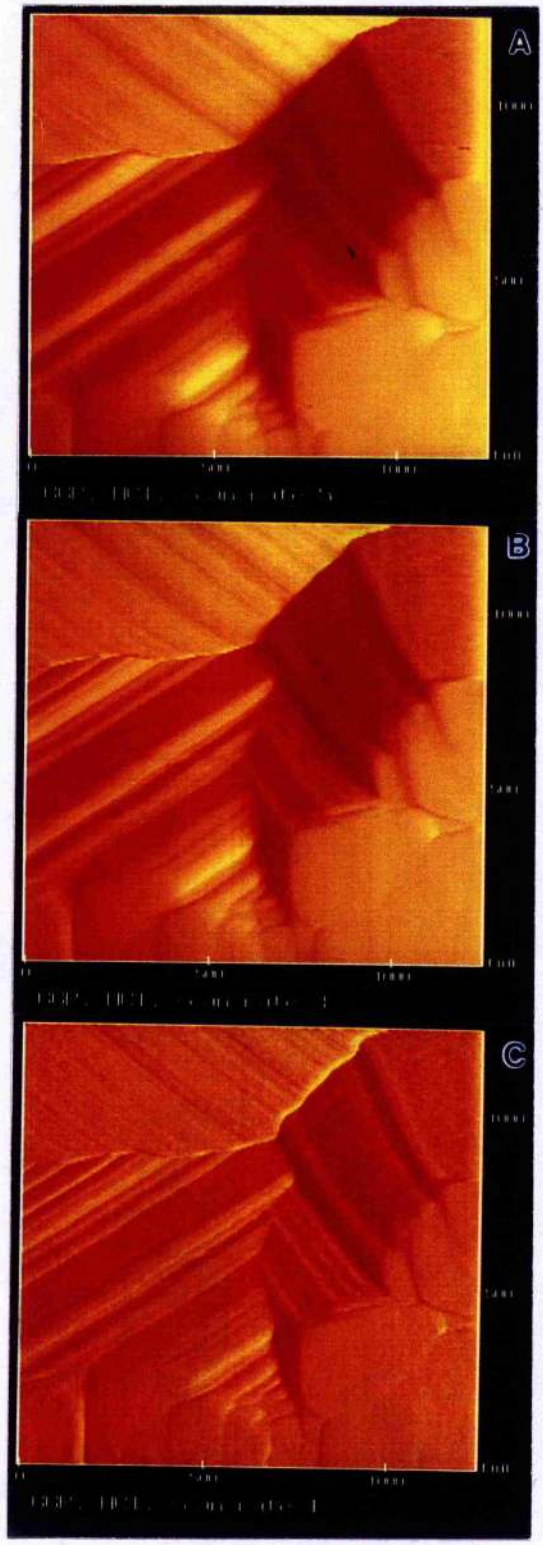

Figure 6-63 Line scan pictures of Figure 6-62 images, showing the sharp corner loosing the sharp shape in the high-scan-rate image.

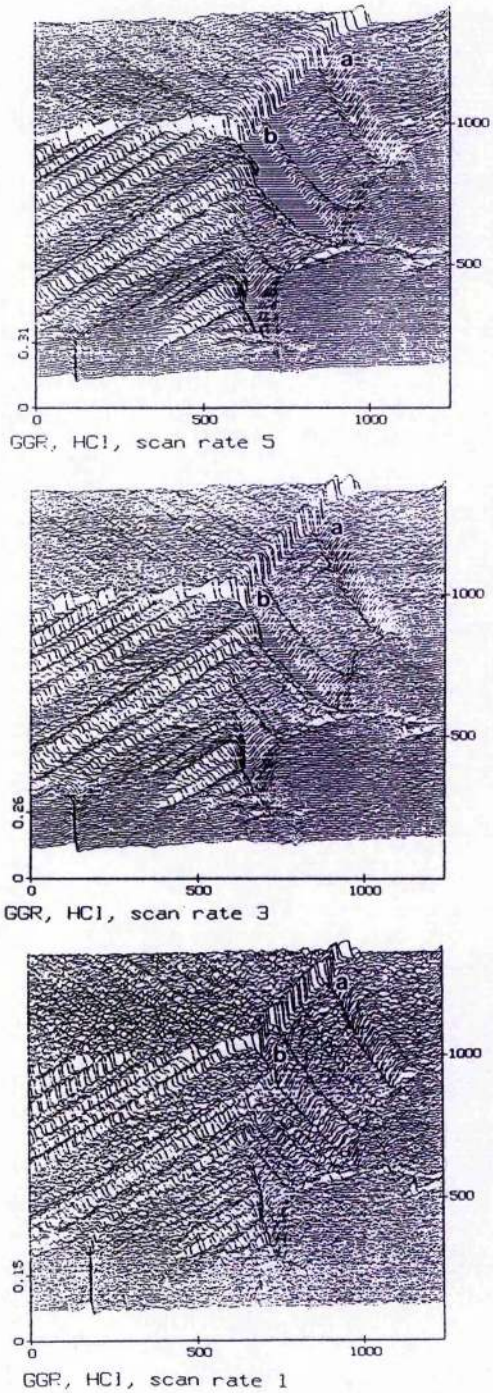

in the high scan rate pictures. This is very likely to be influenced greatly by drag.

The other example is shown in Figure 6-64. By reducing the scan rate from 3 lines/sec (Figure 6-64a) to 1 line/sec (Figure 6-64b), the fine feature on the structure is revealed, so the smooth surface shown in the high-scan-rate image becomes rough in the low-scan-rate image.

Figure 6-64 Drag force degrading the resolution of the high-scan-rate AFM image, A) 3 lines/sec and B) 1 line/sec.

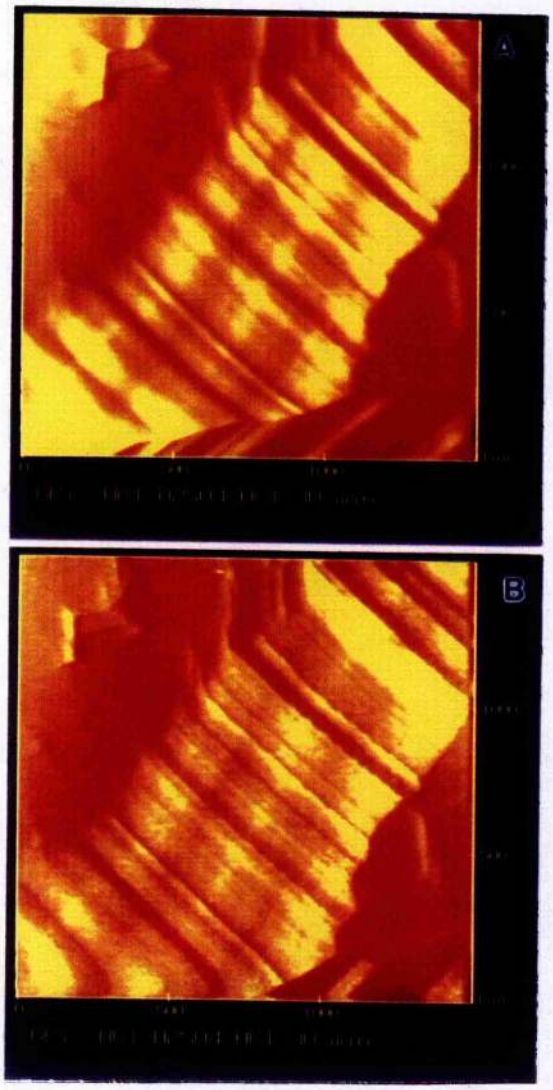

The same situation is observed in the high magnification images. The poor resolution of the 7.8 lines/sec image is improved gradually when the scan rate reduces to 5.7 lines/sec, 3.1 lines/sec and at last to 0.9 lines/sec. With reducing the scan rate, more and more fine structures appear in the lower-scan-rate images (Figure 6-65).

Figure 6-65 The resolution of in-situ AFM images is improved by reducing the scan rate, A) 7.8 lines/sec, B) 5.7 lines/sec, C) 3.1 lines/sec and D) 0.9 line/sec.

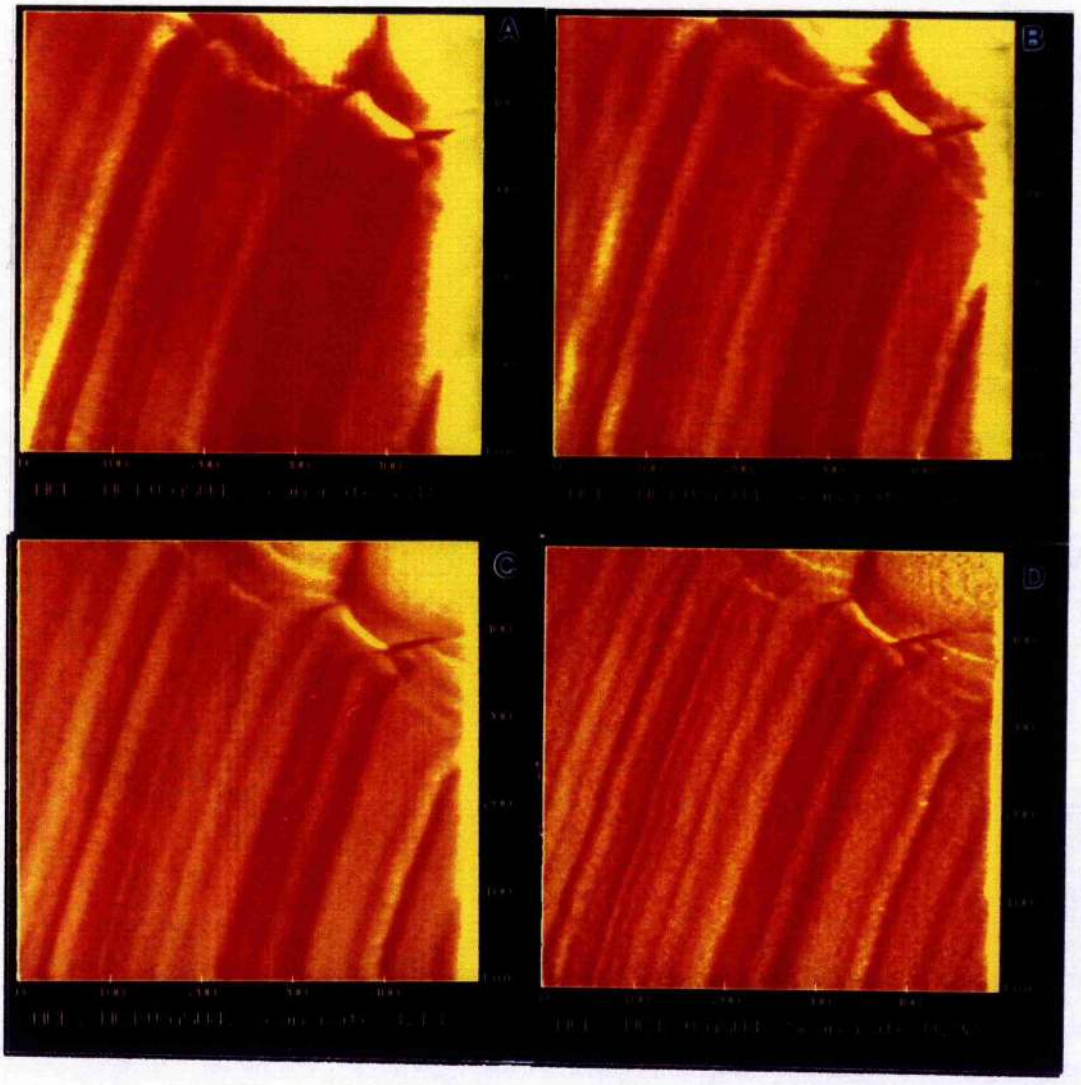

The small η of air lowers the drag force and decreases the influence of the scan rate when the tip scans in air. Though the difference between the AFM images induced by the different scan rate can still be seen in the ledge structure (Figure 6-66), the fine features appearing in 1 line/sec image are also observed in the 4 lines/sec image.

Figure 6-66 The low drag force of air decreasing the importance of the scan rate, a) 4.3 lines/sec, and b) 1 line/sec.

a

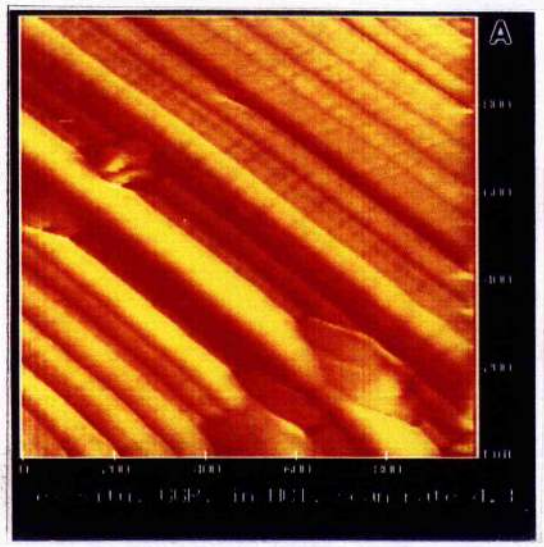

b

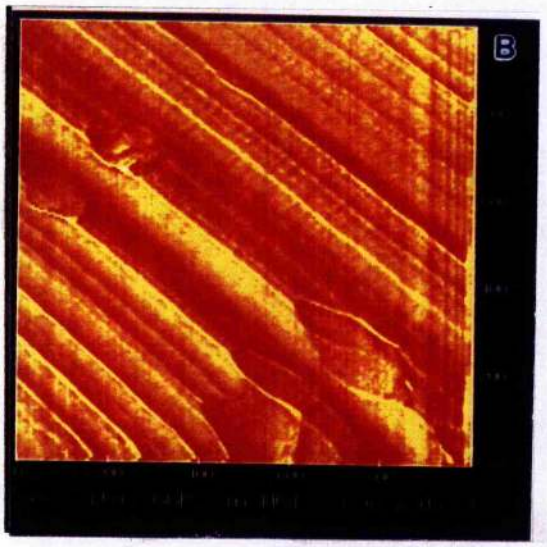

6.2.4 Discussion

Fine ledge structures observed in AFM images are very difficult to be seen under SEM though the spacial resolution of SEM is sufficient. This is because the depth of the fine ledge structures is only in the order of tens of nanometres, which must be inspected in SEM using a low accelerating voltage. In addition, an oxide film formed in air will gradually hide the metal structure behind after a sample is removed from solution. In this study, by using a freshly etched sample and 10 kV accelerating voltage, ledge structure having similar intervals to that in AFM images is observed under SEM successfully.

6.3 Corrosion of molybdenum-bearing alloys in HCl

6.3.1 Introduction

Using AFM to study rough metal surfaces created by corrosion is the first attempt and problems which has been discussed in the previous section may occur during the study. The reality of corroded structures in AFM images has been confirmed. In this section, the interest is transferred to corrosion investigation in which attention is paid to the difference in corrosion rate of the austenite and the ferrite in duplex stainless steels.

Although the total dissolution current of the metal can be measured by traditional electrochemical measurements, the information about localized corrosion cannot be obtained. For example, the three polarisation curves of the three duplex stainless steels GGR, HCE and GRY in 0.1 M H_2SO_4 (Figure 6-67a) indicate total corrosion current of the alloys in the solution, but, they cannot describe the subtle distinctions for each phase in the corrosion process. The two austenite alloys, GRP and GRK, in Figure 6-67b show the different polarisation curves from those of the duplex stainless steels, which means that austenitic phases and ferritic phase are dissolved in a different way in the solution and their combining function give the observed current which is different from the real current.

By measuring the three dimensional nature of the corroded feature using AFM, it is expected that an estimation can be made for the differential corrosion rate between the two phases, so it is possible to establish the different corrosion properties of the two phases in the duplex stainless steels.

Figure 6-67 a) Polarisation curves of duplex stainless steels and b) polarisation curves of austenite stainless steels.

a

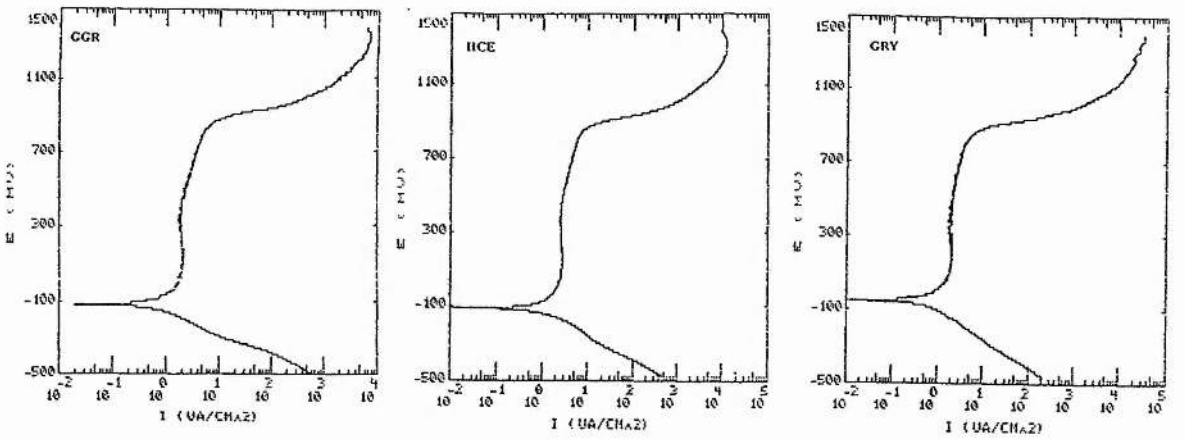

b

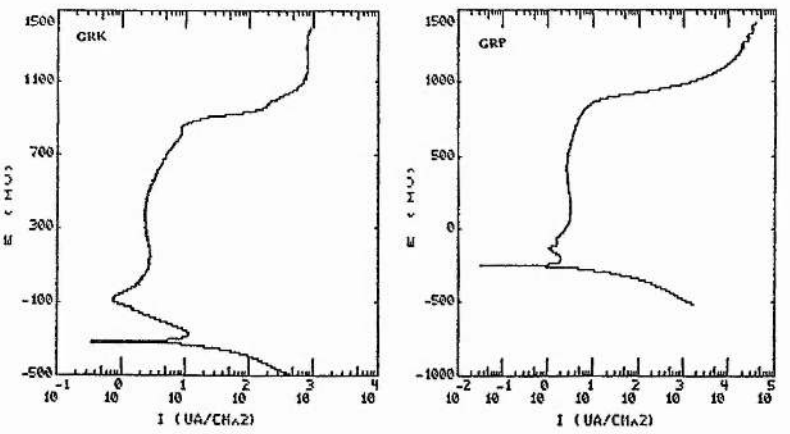

6.3.2 Samples used for corrosion studies

Table 6-6 Chemical composition of the steels.

Sample	GGR duplex	HCE duplex	GRY duplex
Cr	22.2	23.0	25.98
Ni	6.1	6.36	6.98
Mo	3.1	3.34	3.51
N	0.1	0.18	0.226
Cu	----	----	0.72
W	----	----	0.708
C	0.031	0.010	0.028
Si	0.46	0.52	0.469
Mn	1.60	1.36	0.84
P	0.02	0.019	0.016
S	0.01	0.001	0.010
Fe	66.38	65.21	60.51

Studying corrosion of duplex stainless steels in HCl is of practical importance, especially for the oil and gas industry. This project was supported by British Gas, and the samples of the duplex stainless steels coded GGR, HCE and GRY used in this study were also provided by British Gas Company. All the samples were Cr-Mo-Ni steels with a microstructure of 50% austenitic and 50%

ferritic phase. Their chemical compositions listed in Table 6-6.

6.3.3 Topography of the corroded surfaces

In the corrosion of duplex stainless steels, the two phases show different corrosion behaviour and their differentiation in corrosive solutions was reported in the literature. In this study, the two modes of corrosion have also been observed in all three steels in HCl, as shown in the SEM micrographs (Figure 6-68 - 6-70). To make a discussion easier, the phase with a low dissolution rate is called phase A and the other is called phase B.

Figure 6-68 An SEM micrograph taken from the GGR steel sample exposed in 10%wt HCl for 2 hours.

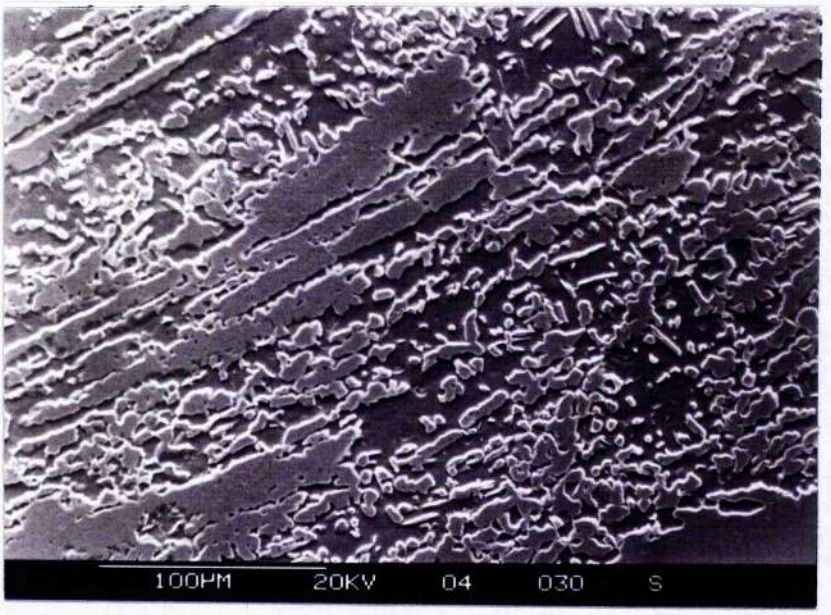

Figure 6-69 An SEM micrograph taken from the HCE steel sample exposed in 10% HCl for 2 hours.

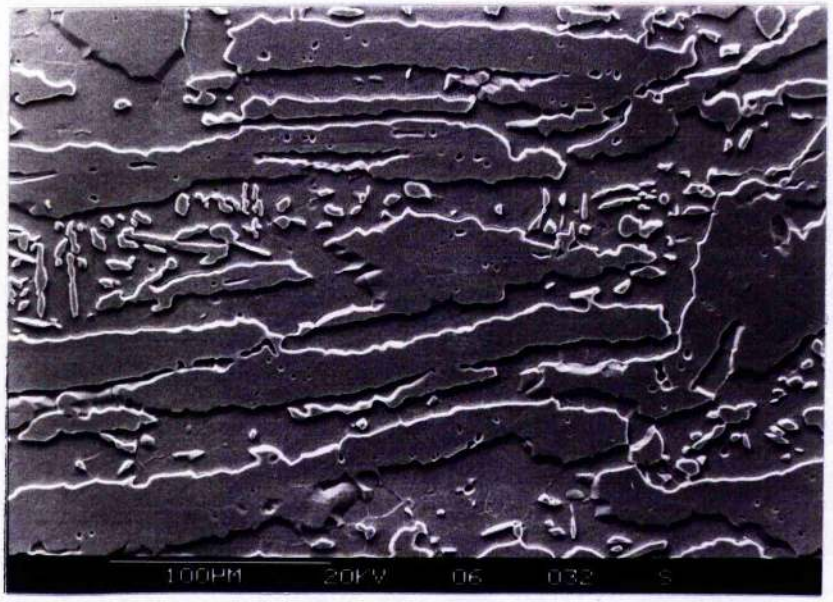

Figure 6-70 An SEM micrography taken from the GRY steel sample exposed in 10%wt HCl for 2 hours.

Figure 6-71 AFM images for studying the differentiation of the two phases during corrosion in HCl and no obviously topographic difference can be seen from A) GGR, B) GRY and C) HCE three steels.

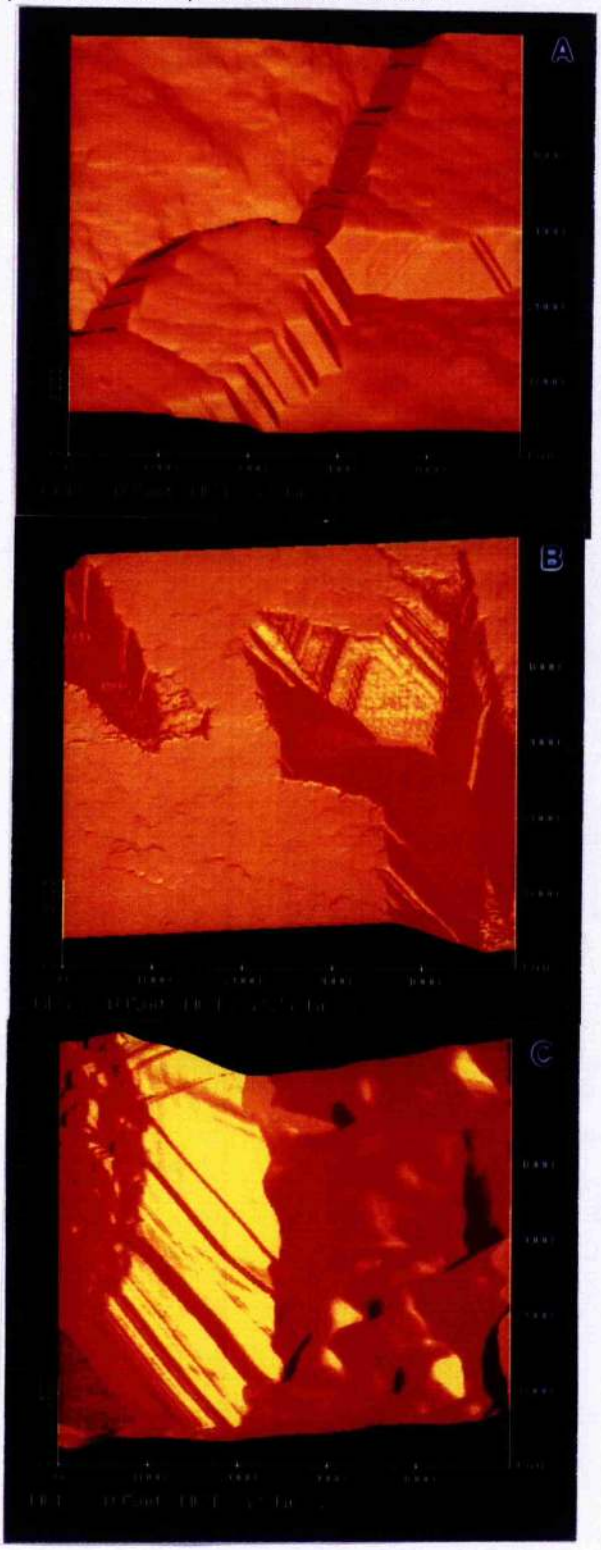

The distinct difference observed in SEM micrographs among the three steels, which possess different chemical compositions, lies in the size of phase A. As it can be seen in Figure 6-68, 6-69 and 6-70, most of the phase A in a shape of island in the GGR steel are small, but in the HCE are large whereas in the GRY steel are medium. The different dissolution rates of the two phases are also observed in AFM (Figure 6-71), but, the three steels cannot be differentiated by topography of AFM.

6.3.4 Identification of the phases

As the microstructure of steels strongly depend on their compositions, the identification of phases A and B can be worked out by analysing their phase compositions in two steps: 1) analysing the compositions of the austenitic and the ferritic phases in the metal matrix, and 2) analysing the compositions of phase A and phase B on the corroded surface. The microstructures of phase A and phase B can be determined by comparing their compositions.

A composition analysis in matrix was carried out in the HCE alloy, in which the phases were identified by electron diffraction and then their compositions were analyzed using EDX. The result is shown in Figure 6-72, in which though the molybdenum difference in the two phases is not obvious because of its small content, a high Ni/Fe ratio in austenitic phase and a high Cr/Fe ratio in ferritic phase are noticeable. Therefore, the austenite stabilising element, nickel, is enriched in the austenitic phase while the ferrite stabilising element, chromium, is enriched in the ferritic phase. Meanwhile, Electron Probe Micro Analysis (EPMA) shows that phase B contains more chromium and molybdenum while phase A contains more nickel. The results of quantitative analysis on this alloy

Figure 6-72 The composition of the HCE alloy analyzed using EDX. The evidence for nickel enrichment in austenite while chromium and molybdenum enrichment in ferrite is clear.

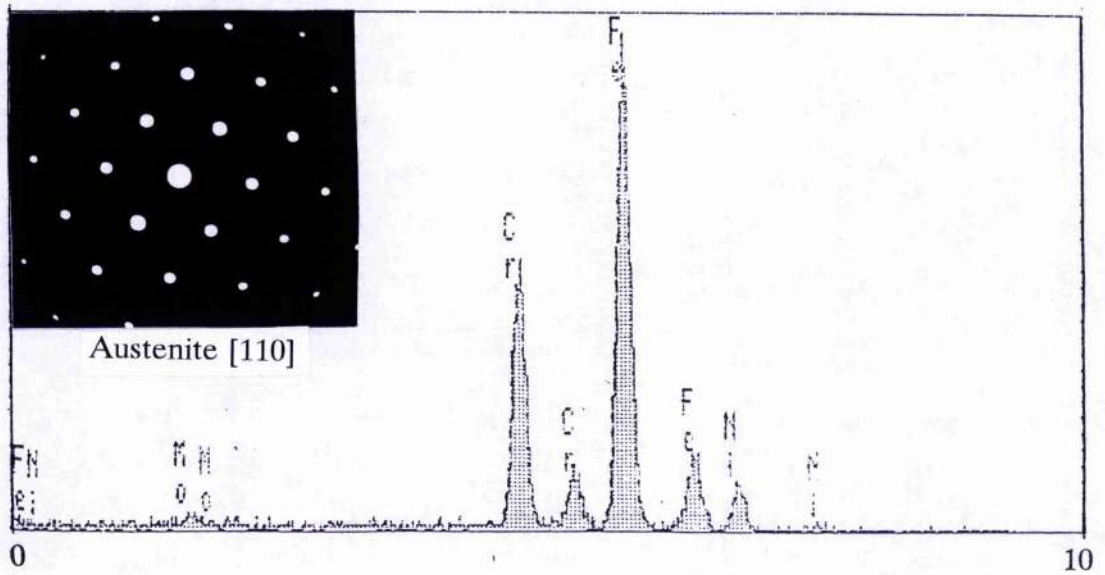

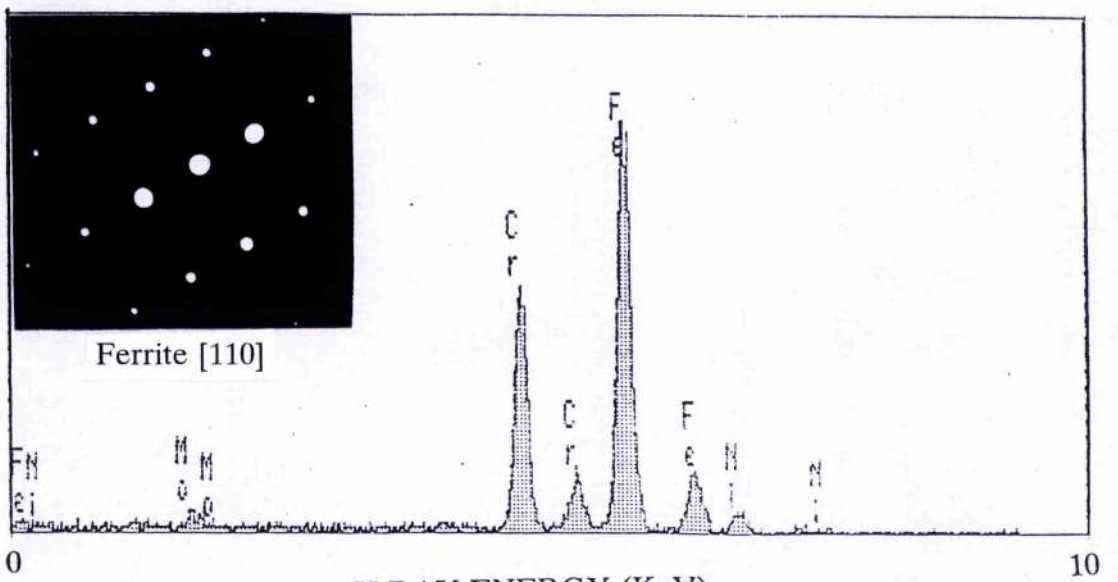

are listed in Table 6-7. Therefore, the composition of phase A corresponds to that of austenite and the composition of phase B corresponds to that of ferrite.

Table 6-7 Quantification of the chemical composition of the two phases on the corroded surfaces

	Si	Cr	Mn	Fe	Ni	Mo	Cr%+3.3Mo
phase A wt%							
GGR	0.7	20.7	1.4	66.6	8.1	2.6	29.3
HCE	0.7	21.7	1.5	65.2	8.4	2.5	30.0
GRY	1.0	24.6	0.9	61.7	9.2	2.8	33.8
at%							
GGR	1.4	22.0	1.4	66.0	7.6	1.5	
HCE	1.4	23.1	1.5	64.6	7.9	1.5	
GRY	2.0	26.1	0.9	60.9	8.6	1.6	
phase B wt%							
GGR	0.8	23.4	1.4	64.0	5.5	4.8	39.2
HCE	0.8	24.4	1.4	61.5	6.0	6.0	44.2
GRY	1.2	26.9	0.6	60.0	6.8	4.5	41.8
at%							
GGR	1.6	25.1	1.4	63.8	5.3	2.8	
HCE	1.5	26.3	1.4	61.6	5.7	3.5	
GRY	2.3	28.7	0.6	59.4	6.4	2.6	

The efficiency sum: Cr% + 3.3Mo% is an important parameter to assess the pitting corrosion resistance of alloys. Therefore, the efficiency sum: Cr% + 3.3Mo% of the two phases in the duplex stainless steels is listed in table 6-8 though it will be not discussed in this study.

6.3.5 Electrochemical differentiation of the two phases

The previous study in this work has shown that the ferritic phase dissolves more rapidly than the austenitic phase in HCl. This may be caused by a potential difference between the two phases which have different compositions. During corrosion, the anode might then dissolve rapidly enough to protect the cathode sacrificially.

Such a potential difference between the two phases does exist and it was shown by a copper deposition experiment, in which a freshly corroded HCE alloy was exposed in 0.1 M H_2SO_4 + 0.1 g $CuSO_4$ solution for 10 minute. This makes it possible to inspect the copper precipitation which would map the cathodic area on the surface. In the SEM micrograph (Figure 6-73), it is observed that massive numbers of fine Cu deposits are on the austenitic phase, which is consistent with a cathodic potential on the austenite.

This subjective impression is confirmed by Auger mapping (Figure 6-74), which was reconstructed from the pixels rich in copper or iron taken from the circled regions in a scatter diagram. Thus the austenitic phase is cathodic towards the ferritic phase.

Figure 6-73 An SEM micrograph, showing copper deposit on austenite phase.

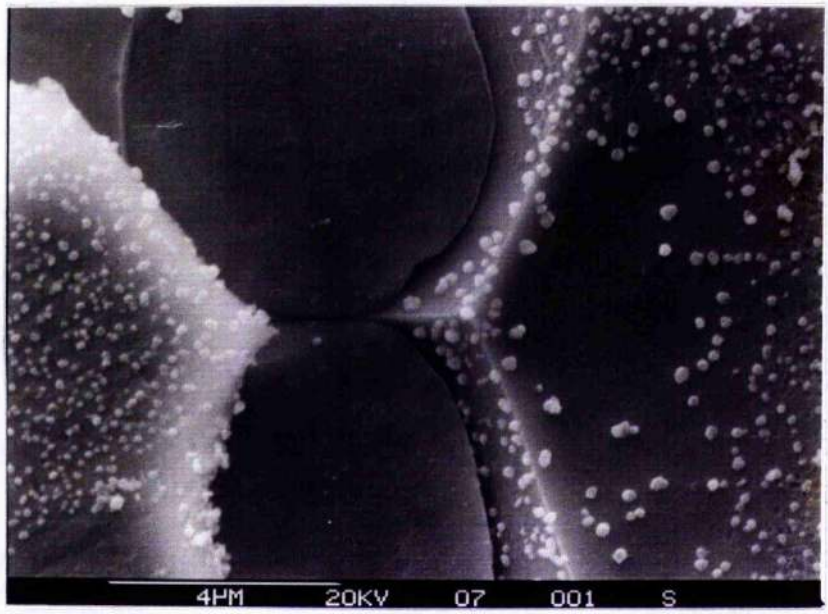

Figure 6-74 Auger mapping giving the evidence for copper decorating across the austenitic phase.

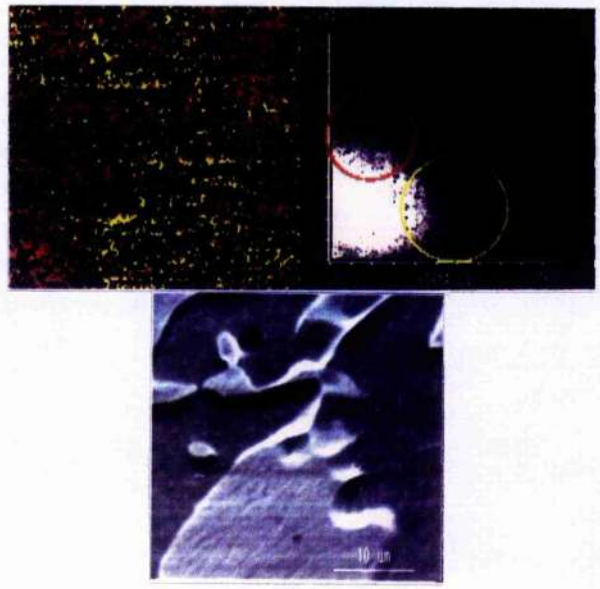

6.3.6 Kinetics of the corrosion of duplex stainless steels

To study the kinetics of corrosion, the circular samples were used for in-situ AFM study. Before the corrosion, all steels were in the same appearance in pure water as in Figure 6-75, which look smooth. The corrosion of the three steels started once the HCl was replaced and it led to a gradual differentiation of the two phases, as shown in Figure 6-76, 6-77 and 6-78 by height mode scans of 5000 nm square. Along with a rapid dissolution of the ferritic phase, the austenitic phase was gradually exposed on the surface and after a long elapsed time, some of the phase islands such as the crystal marked "b" in Figure 6-76 disappeared suddenly by undercutting. The three steels show the similar corrosion behaviour and the topography during the corrosion.

Figure 6-75 A polished HCE sample scanned by AFM in pure water.

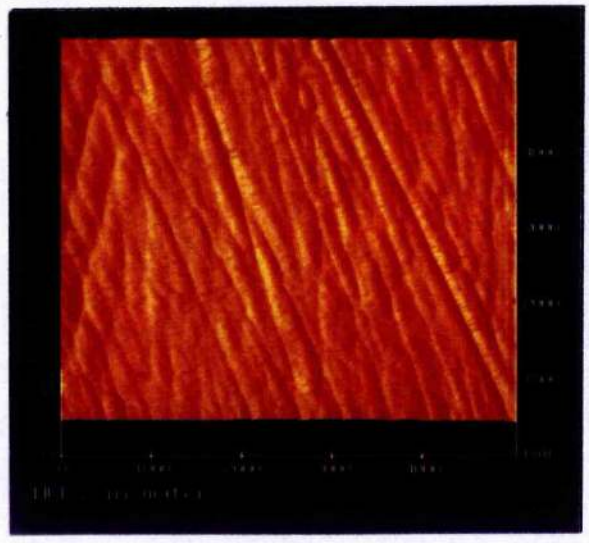

Figure 6-76 In-situ AFM images taken from GGR sample during its exposure in HCl.

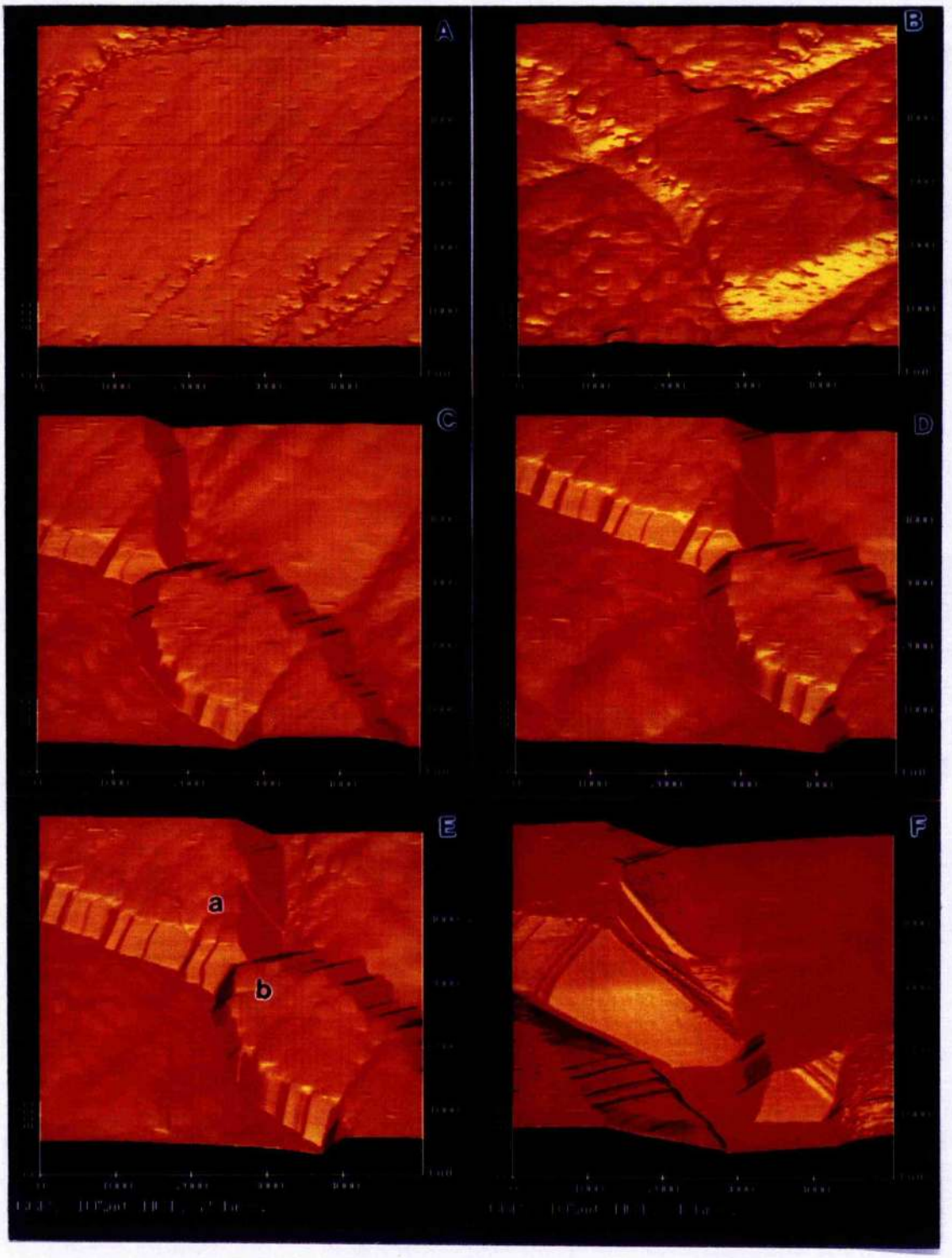

Figure 6-77 In-situ AFM images taken from HCE sample during its exposure in HCl.

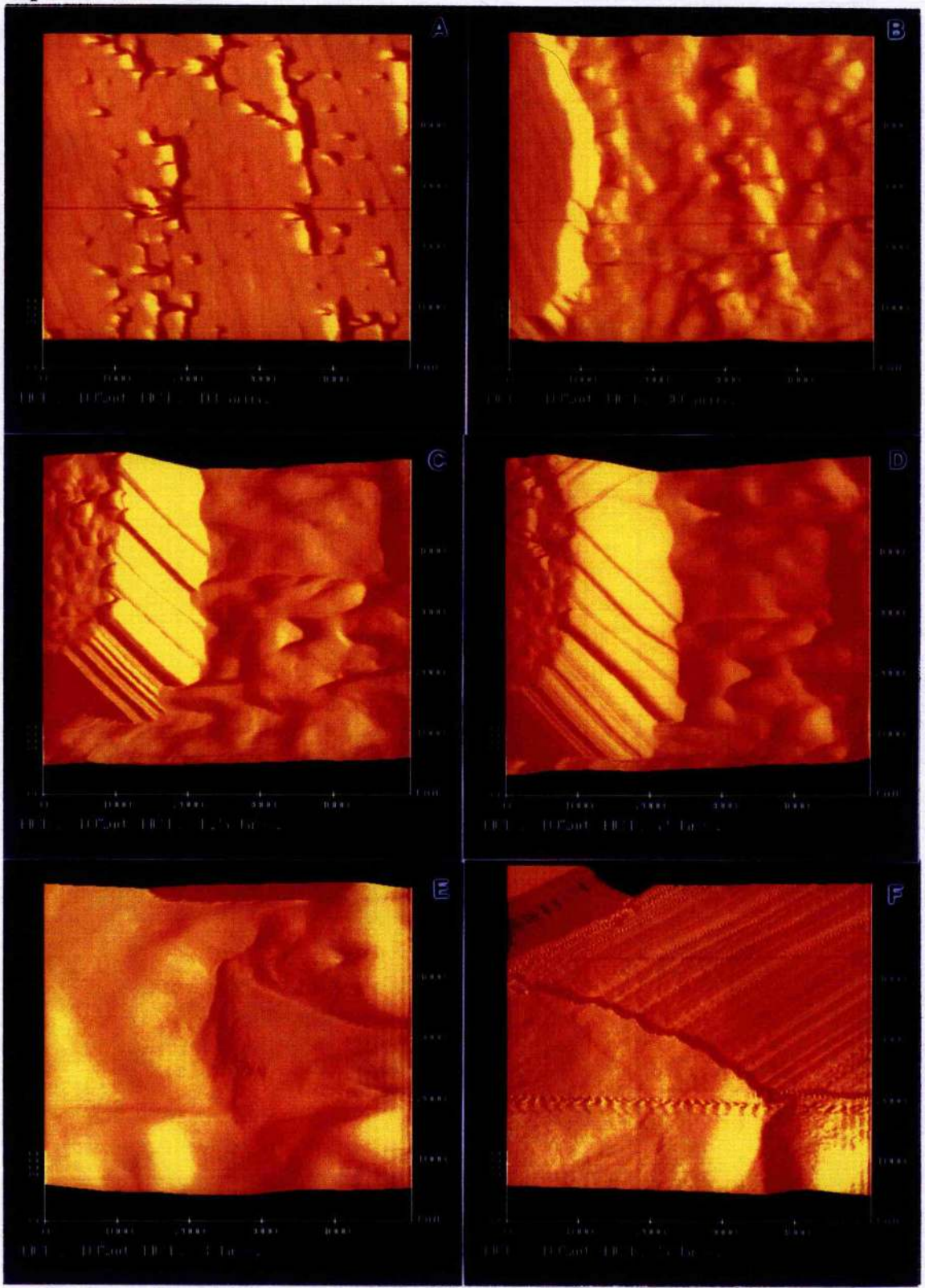

Figure 6-78 In-situ AFM images taken from GRY sample during its exposure in HCl.

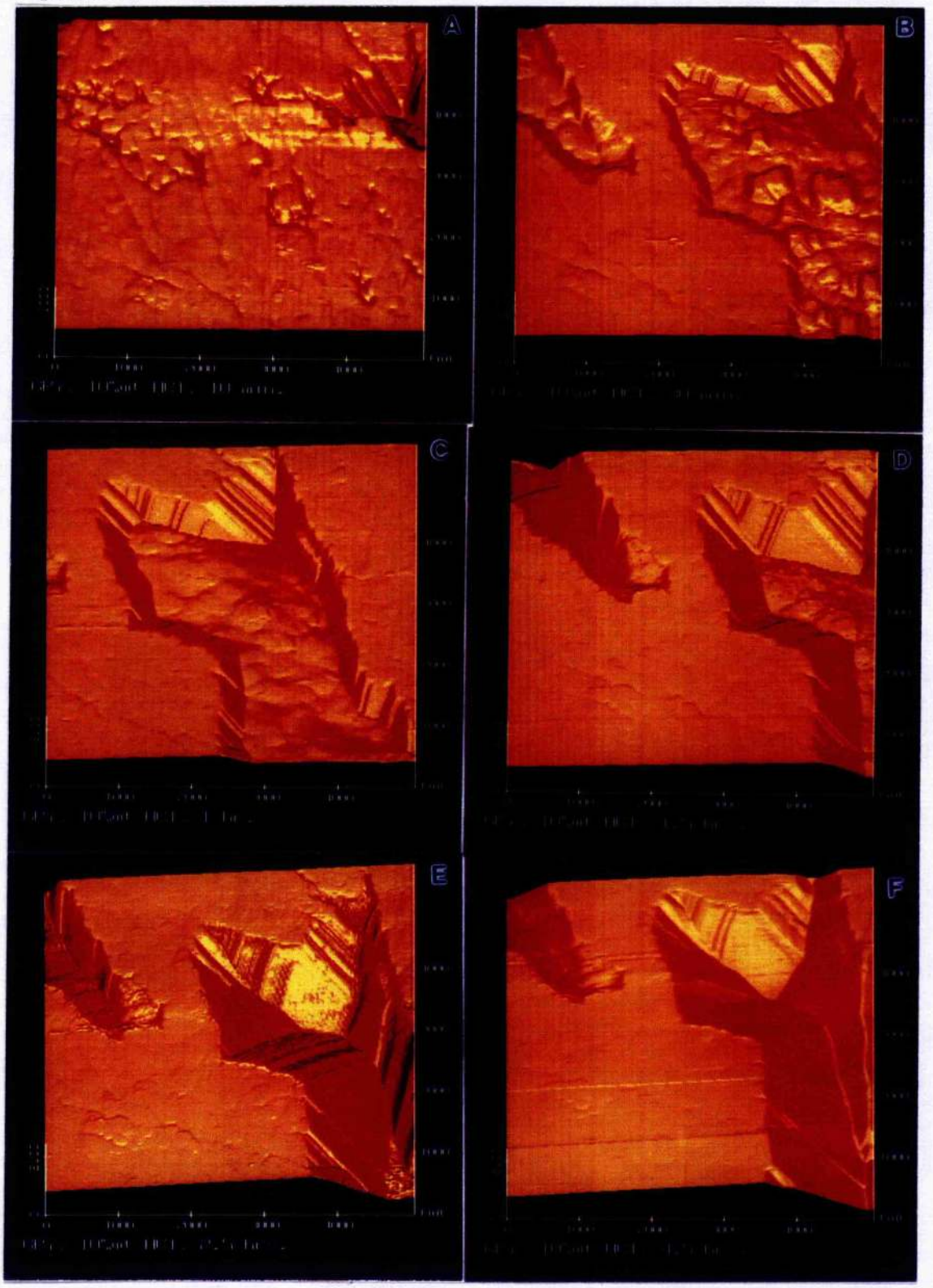

The differential etching rate was measured in different samples by measuring the thickness change of the austenitic-phase islands as schematically indicated in Figure 6-79. The rapid increase in the thickness of the islands of the phase A corresponds to the differential corrosion rate of the ferritic phase relative to the austenitic phase. The measurement in a sample was carried out in the same position after the sample being etched in different times and the results are listed in Table 6-8. The thickness of the islands of phase A in the three steels obviously increases with prolonging etching time. Therefore, the ferritic phase dissolves more rapidly than the austenitic phase. Though the differential etching rate of the HCE steel seems greater than those of the other two steels in Table 6-8, it must be remembered that these measurements were made at one point on the sample. Therefore, it may not be safe to draw this conclusion.

Figure 6-79 The increase of the thickness of the islands of phases A is the result of the differential etching rate of the two phases.

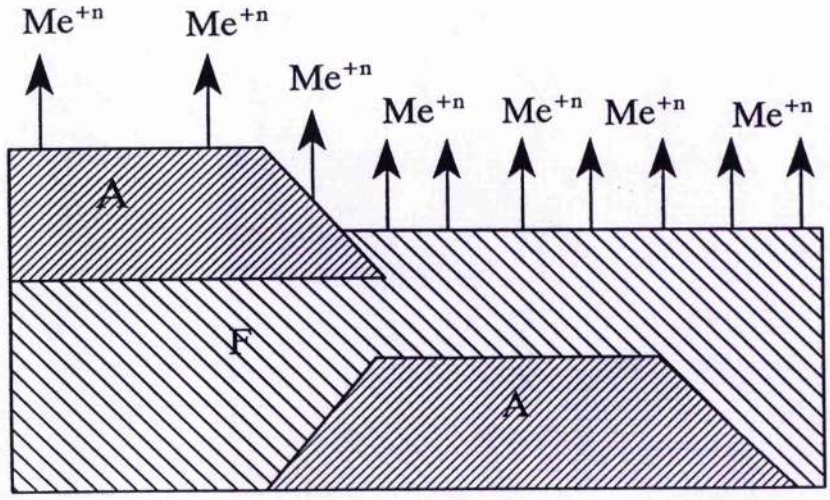

Table 6-8 Austenite/Ferrite Differential Etching Rate (nm)

	20 min	30 min	1 hr	1.5 hrs	2hrs	2.5 hrs
GGR	200		373	523	580	
HCE		225	700	825	940	
GRY	109	162	308	587		996

Though the austenitic phase was protected cathodically by the ferritic phase, the dissolution of the austenitic phase is still observed on the polished surface and sidewalls which become rougher by chemical etching (Figure 6-80).

Figure 6-80 An in-situ AFM image, showing the etched surface of the sidewall on the GRY sample.

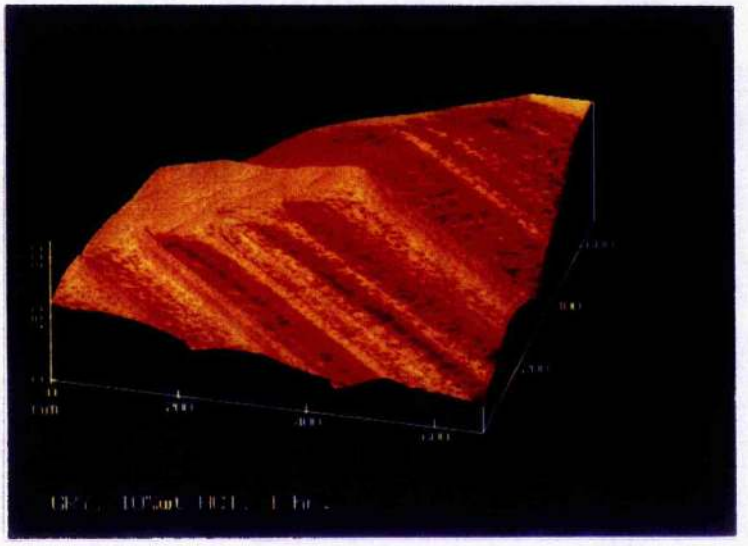

A projecting triangular surface pointed by an arrow in Figure 6-81 was lost after 4 hour exposure in HCl. The same phenomenon was also observed from another sample. Figure 6-82 shows an enlarged image for the etched triangular structure.

Figure 6-81 An in-situ AFM image taken from the GGR sample, showing an etched triangular structure in HCl.

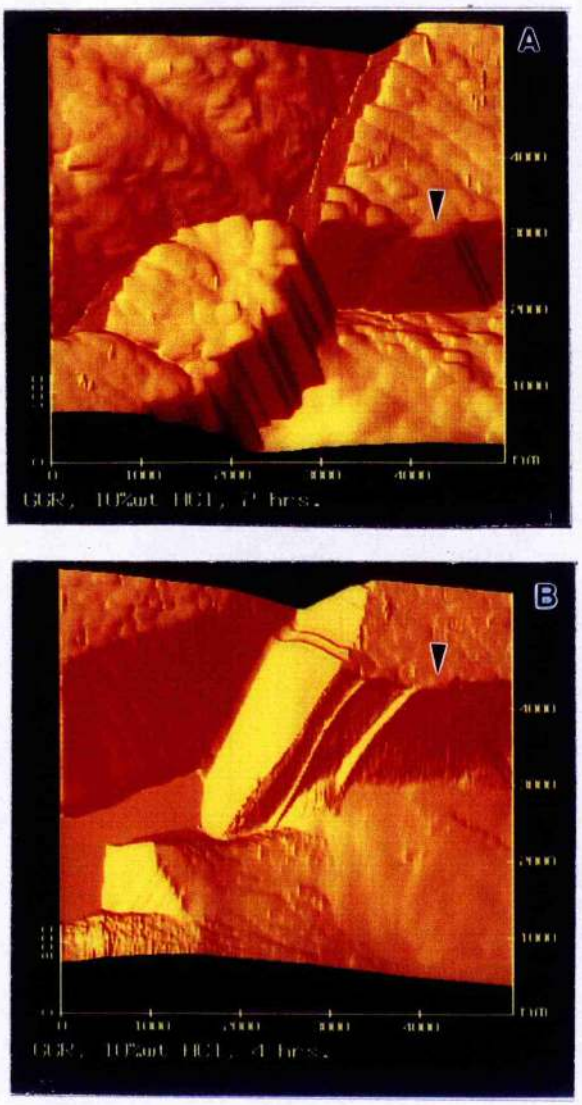

Figure 6-82 An in-situ AFM image taken from the GGR sample, showing another example of the etched triangular structure in HCl.

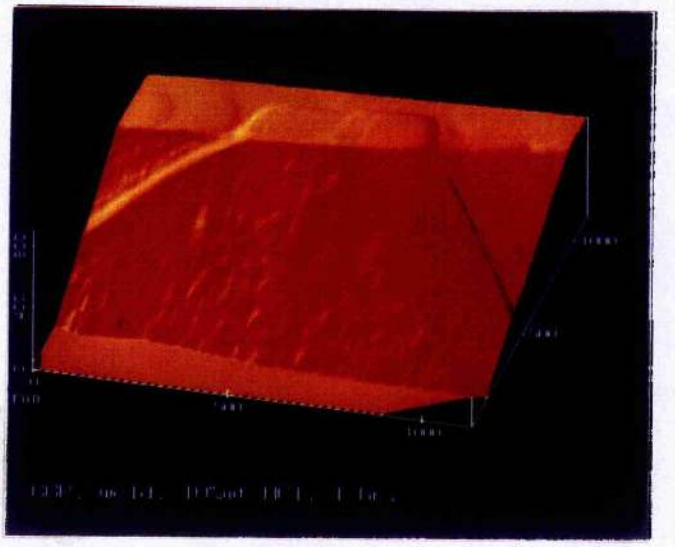

Figure 6-83A and 6-83B are two images showing the corrosion of the HCE duplex stainless steel in HCl and the second image was collected 10 minutes after the first. Here a sudden change happening on the sidewall of the austenitic phase (arrow pointed area) indicates the occurrence of preferential corrosion. In the subsequent investigation, therefore, the preferential corrosion of this kind of structure was studied in detail.

Figure 6-83 In-situ AFM images taken from the HCE steel in HCl: A) exposed for 30 mins, and B) exposed for 40 mins. By comparing these two images, it is evident that a selective dissolution of the sidewall of the austenitic phase occurred simultaneously with a selective dissolution of the ferritic phase surrounded by the austenitic phase.

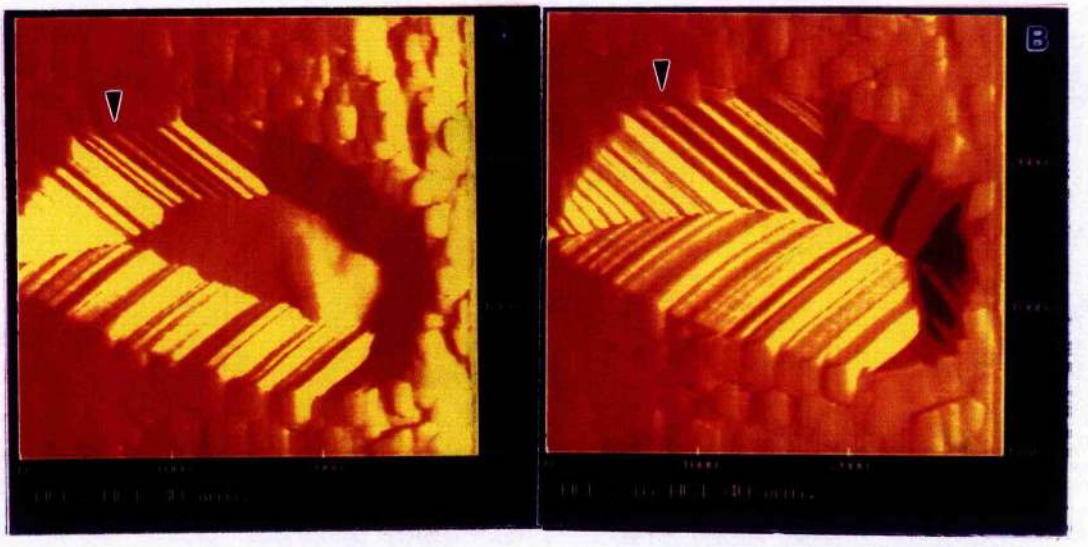

In Figure 6-76, a complete loss of the lower part of the austenitic crystal is observed during the corrosion. The austenitic phase in the images is broken at a narrow waist which is a boundary of the two grains of austenite, as a high angle interface between them has been found from an enlarged area in Figure 6-84. Removal of the lower grain is so complete that it implies that this grain boundary is selectively attacked, leaving behind a smooth surface of the upper grain marked "a" in the images. As rapid dissolution of the lower grain is not found throughout

the exposure, the sudden disappearance of the lower austenitic grain results from undercutting of the ferritic phase boundary which was caused by selective dissolution.

Figure 6-84 An enlarged area of the time series of AFM images in Figure 6-78 showing the broken region with a high angle interface between the grains.

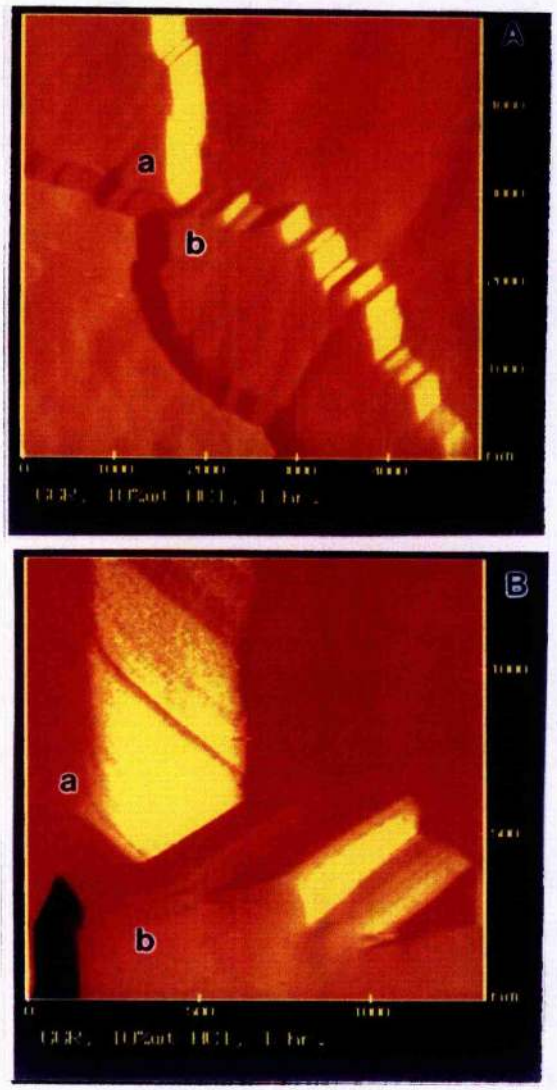

Another sudden change to the side wall may be associated with the detachment of complete columnar sub-grains. Figure 6-85 shows this by the loss

of the grain structure numbered 6, between the HCE steel corroded in HCl for 1.5 hours and for 2 hours, where corrosion preferentially occurs along the sub-boundary.

Figure 6-85 In-situ AFM result for the HCE steel after immersion in HCl for 1.5 hours and 2 hours. The disappearance of the subgrain structure is marked 6.

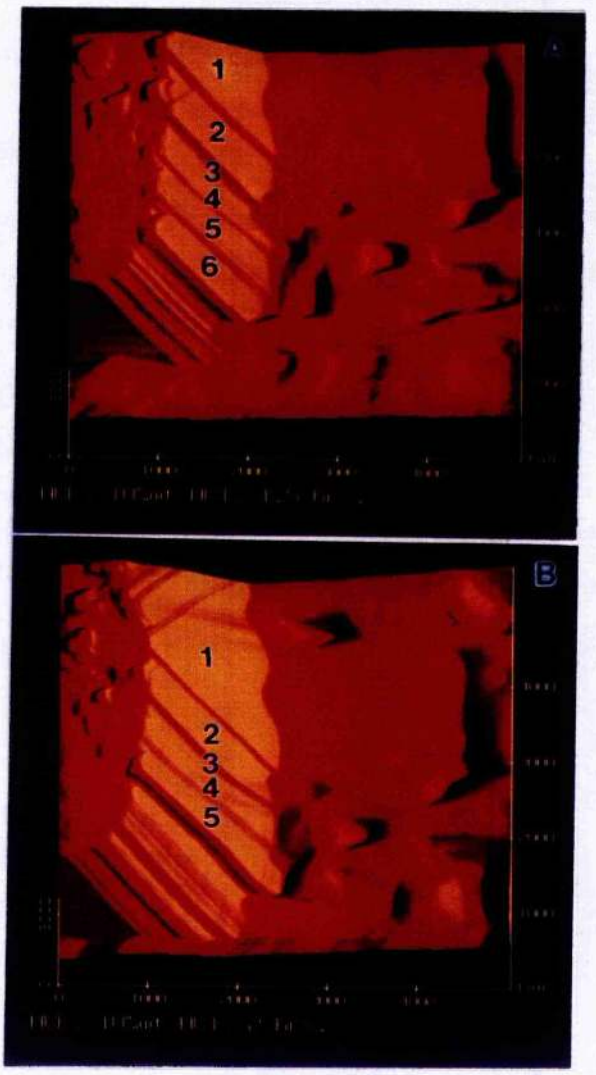

Figure 6-86 shows a dramatic change of a step structure on the austenite during the corrosion. The repeated frames of a sequence were taken at a nominal time of 30 minutes. In the first scan of this sequence, the step indicated with the

letter x commences to dissolve, the rapid dissolution leaves half of the step x in the position in the second scan and at last it disappears completely in the third scan. The step x was dissolved in 50 seconds. It gives an example of the dissolution of the planes with high energy.

The other example (Figure 6-87) shows the dissolution of a step structure in different direction. During the three scans, the risers on the step-like structure appear to split, narrow and vanish under the action of corrosion. The consequence of the selective dissolution occurring on certain steps or crystallographic directions is shown in the large field of view in Figure 6-88, in which the second image was collected half an hour later the first image. It can be seen that the corrosive attack on the surface was extended further and deeper following a certain orientation while other features preserve or change slowly. All the examples described above show that the corrosion preferentially occurs along the grain boundary, sub-boundary and certain high energy planes.

Figure 6-86 An in-situ AFM image from the GGR steel immersion in HCl, showing the kinetic dissolution of the step feature during the course of the central scans.

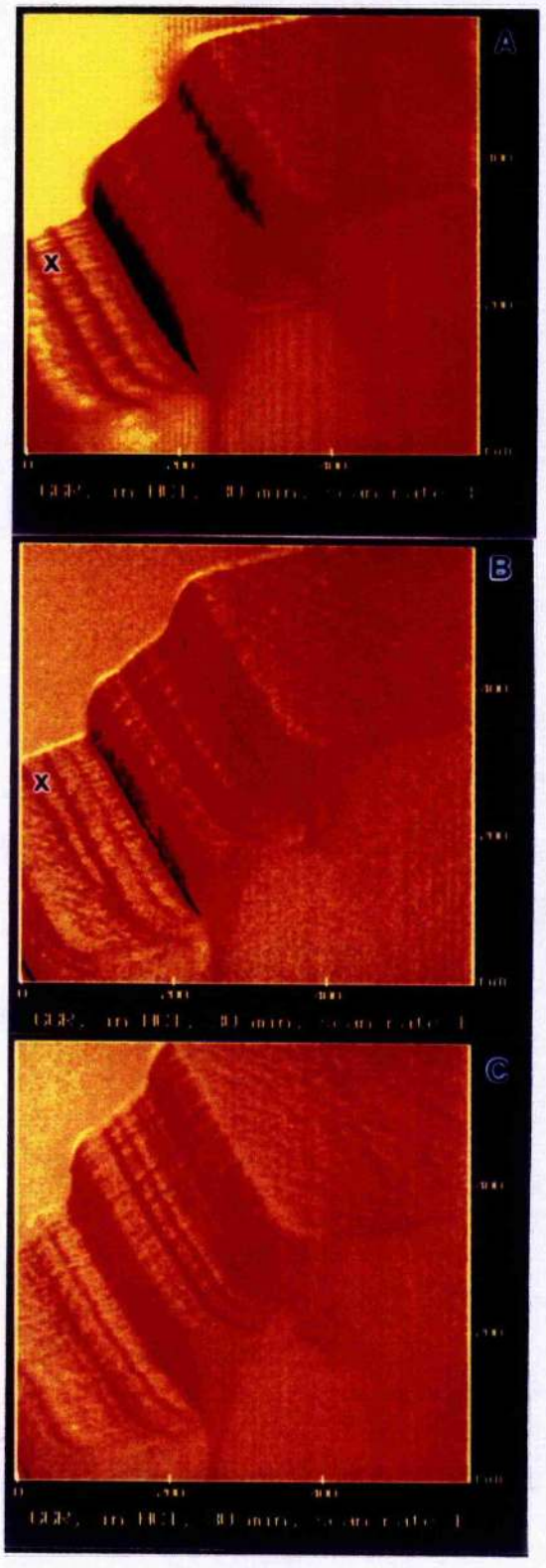

Figure 6-87 An in-situ AFM image from the GRY steel immersion in HCl, showing the development of corrosion.

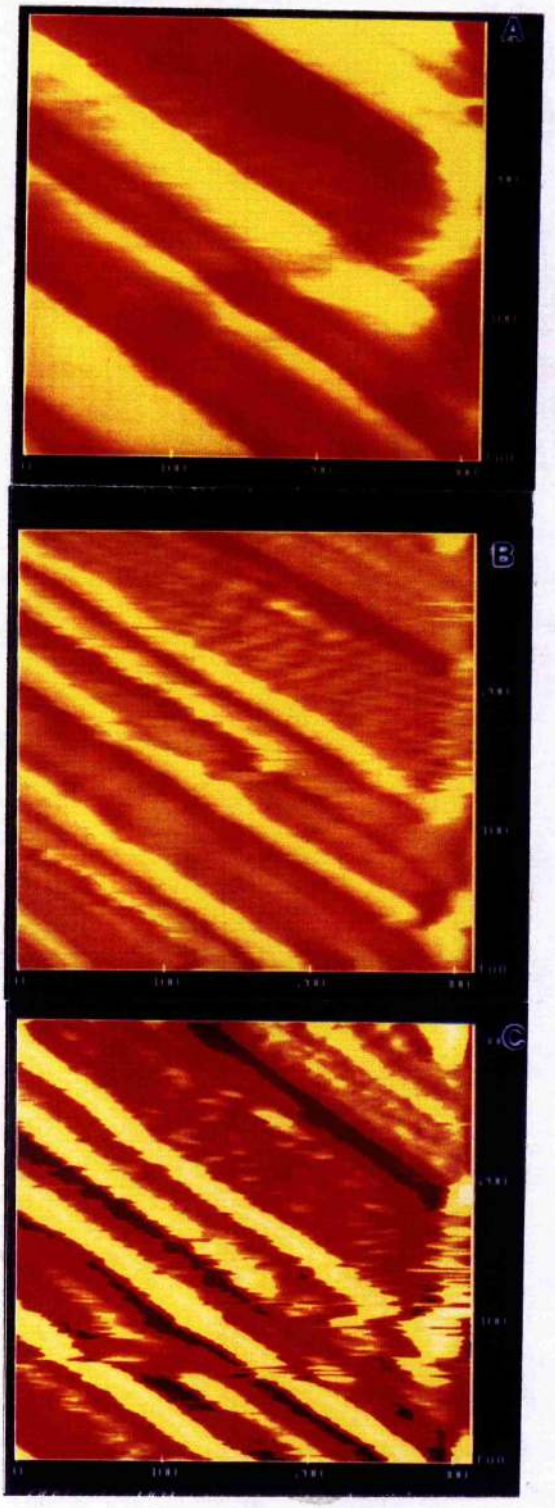

Figure 6-88 An in-situ AFM image from the GRY steel immersion in HCl, showing the development of corrosion in a large field of view.

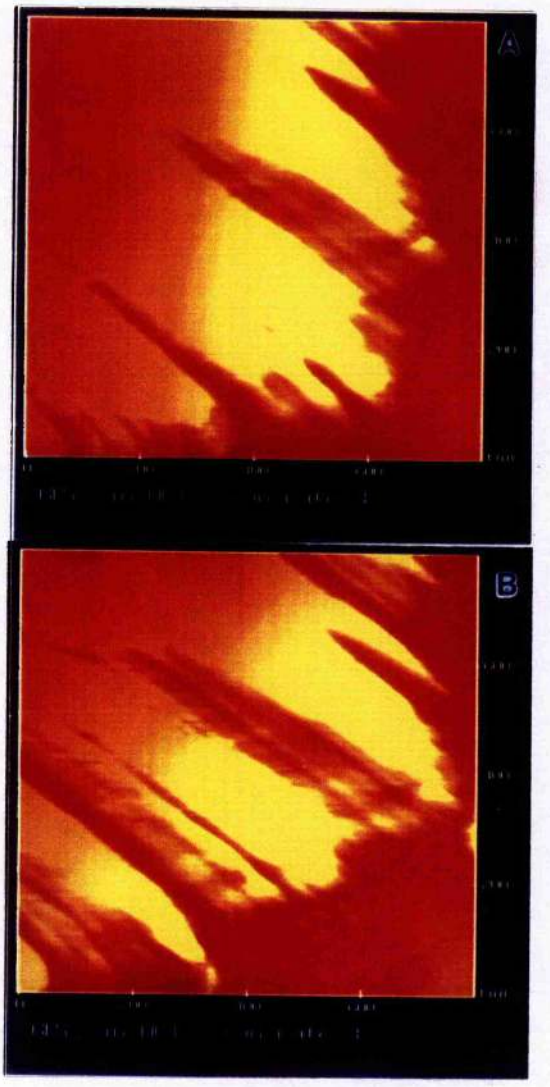

Sudden changes on the austenitic phase occur in HCl frequently, which give an impression that a selective dissolution along grain boundaries or subgrain boundaries may lead to peeling off a whole piece of metal. Figure 6-89A shows a microcrack running parallel to the step tread towards the grain boundary which is zoomed in Figure 6-89B.

Figure 6-89 An in-situ AFM image from the GRY steel immersion in HCl. Evidence of a microcrack on austenite can be seen clearly.

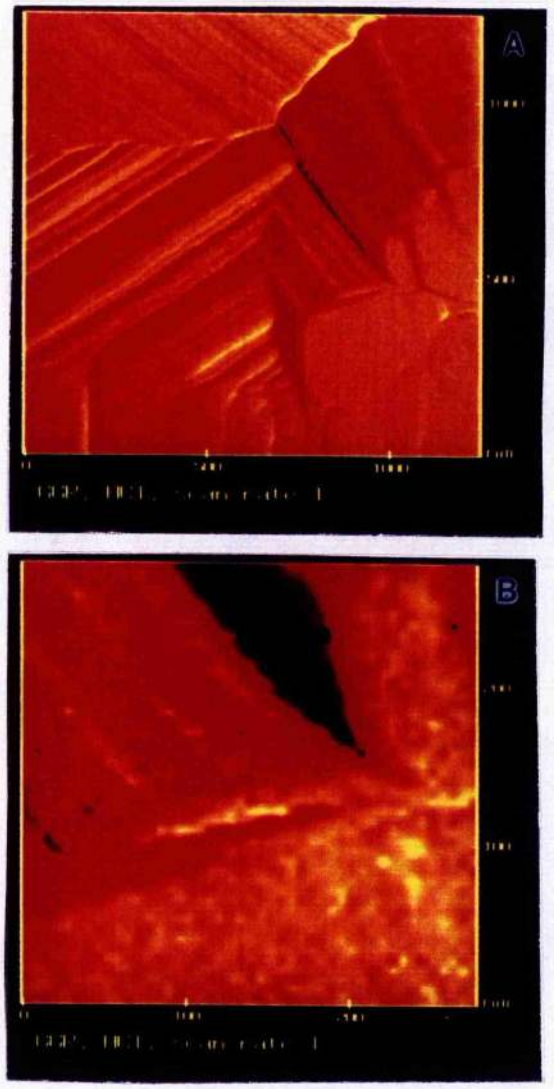

Figure 90 shows that a triangular structure in the HCE steel was broken after 4 hour corrosion in HCl. It is considered that the broken layers, as seen in the front of aligned triangular structures, are attributed to the preferential dissolution along the subgrain boundaries. The change of the triangular structure in corrosion provides a further evidence for the reality of the structure.

Figure 6-90 In-situ AFM images taken from the HCE steel in HCl after A) 3 hour exposure and, B) 4 hour exposure, showing the breaking process of the triangular structure.

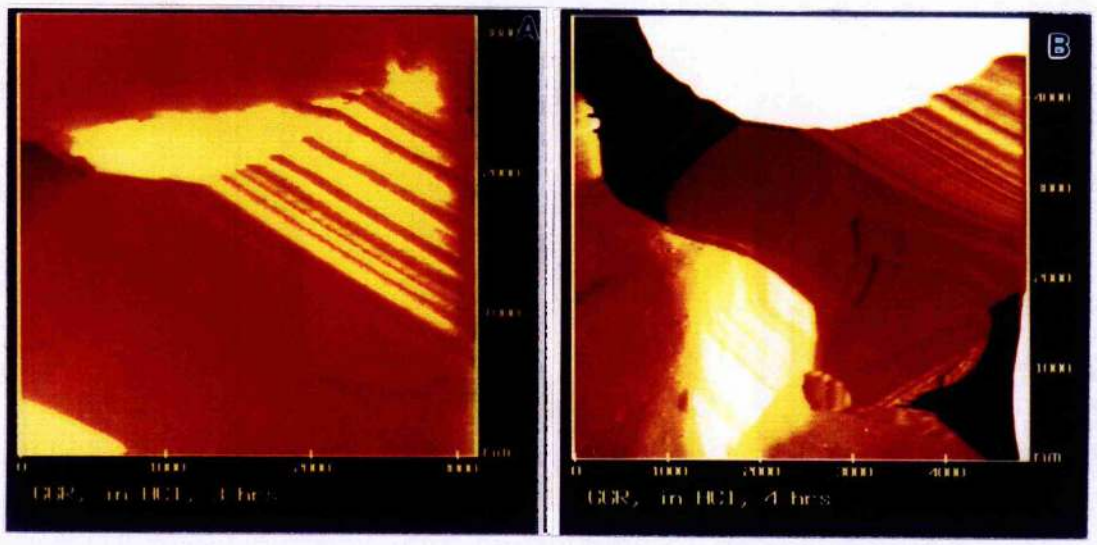

6.3.7 Repassivation of the duplex stainless steels

Because of rapid oxidation of an active surface in air, it is impossible to investigate the initiation and early development of the passivation occurring on an active surface by ex-situ study. In this work, a group of corrosion-passivation and corrosion-passivation-corrosion experiments were designed and conducted for in-situ AFM studies, which link the active and passive conditions in the same experiment for the first time to study the change of the surface when the

electrochemical condition jumps from one to the other.

The experiments can be divided into different stages: active dissolution and passivation, and the two stages might be repeated when it was required. In other words, the experiment started with active dissolution in which the sample was dissolved in 10%wt HCl solution until the two phases were separated. Then the passivation stage began by replacing HCl solution with 0.1 M H_2SO_4 solution and applied a passive potential (400 mV/SHE). If needed, the HCl solution could be changed back and the potentiotat was switched off after the passivation to study active corrosion occurred on a passivation surface.

Figure 6-91 records the corrosion and the passivation occurring in the GGR steel. The selective dissolution of the ferritic phase surrounded by the austenitic phase forms a hole at the active dissolution stage and a completed stop of the further increase in depth of the hole happens after a few minutes of exposure under the passive condition. The passivation does not cause any obvious change in the topography of the surface as in the passivation of 516 steel and it only can be defined by the depth measurement in Table 6-9 and the current-time curve which shows a sharp decrease of the dissolution current in the first a few minutes of passivation (Figure 6-92). The decrease of the hole depth after 1 hour passivation may result from pilling up the passivation products.

Figure 6-91 In-situ AFM images taken from the GGR steel, a) in HCl for 10 minutes, b) in HCl for 30 minutes, c) in HCl for 30 minutes and in H_2SO_4 for 10 minutes, d) in HCl for 30 minutes and in H_2SO_4 for 30 minutes and e) in HCl for 30 minutes and in H_2SO_4 for 60 minutes.

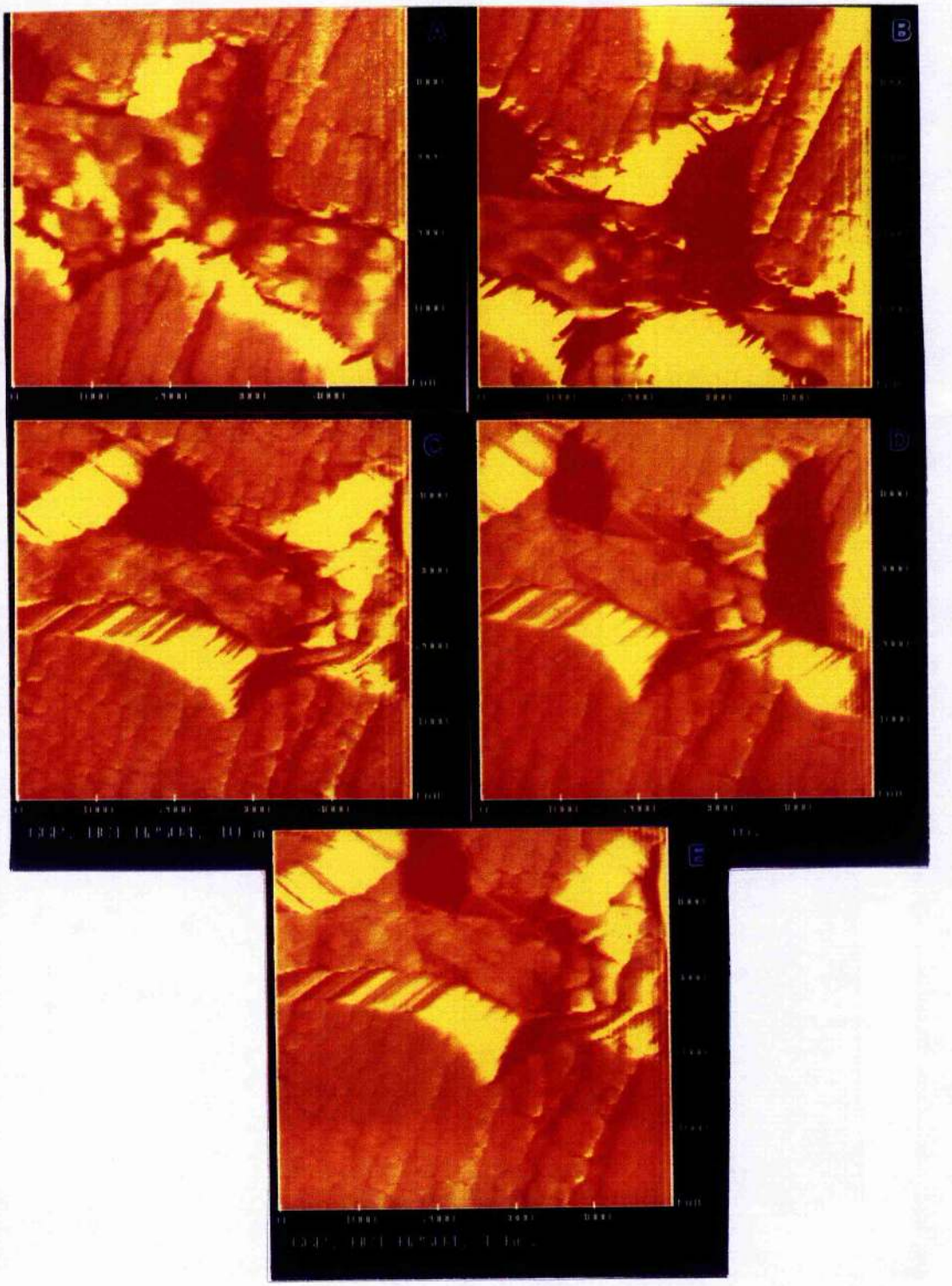

Table 6-9 Differential removal (nm) of Austenite/Ferrite in the GGR steel.

A*10min,	A30min,	A30min-B**10min,	A30min-B30min,	A30min-B1hr
136	375	485	488	437

* HCl
** H_2SO_4, passive potential

Figure 6-92 Current decay curve of the GGR steel in H_2SO_4 at 400 mV.

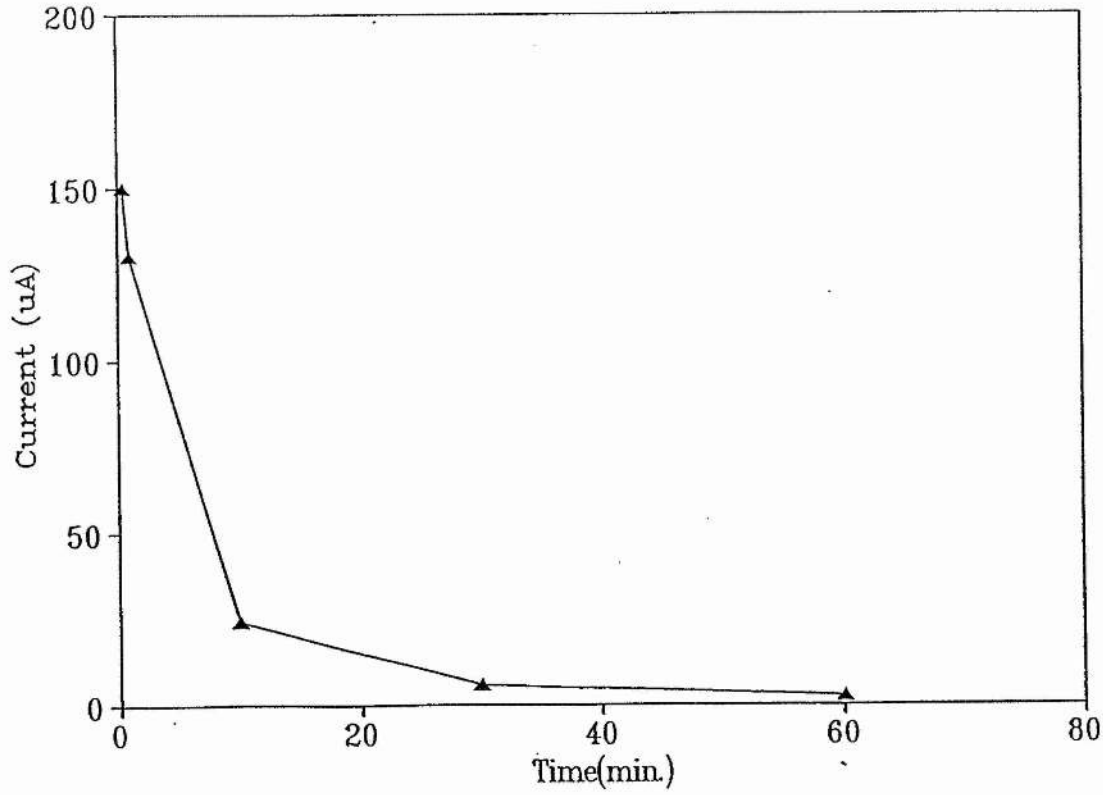

When the electrochemical condition changes from active dissolution to passivation, not only the differential corrosion between the two phases ceases, but the corrosion on the sidewall of the austenitic phase is prohibited as well. For example, the metal structure on the sidewall observed in Figure 91A to 91C gives a sign of the highly localised attack under the active condition, but the change is frozen under the passivation condition. In Figure 6-91D and 6-91E, the structure obtained stands close comparison in a way which is not possible for similar structure under active conditions. Nevertheless, the dissolution still carries on at an extremely low rate, which provides the passive current and it can be observed by the vanishing of fine structures (Figure 6-93).

Though the structure on the surface is relatively stable under the passivation condition, once the electrochemical condition is switched to the active dissolution at the open-circuit potential in HCl, the characteristic step structure begins to fade and the surface eventually becomes quite smooth, as shown in Figure 6-94 and Figure 6-95. The main structures on the sidewall in Figure 6-94 remain in 1 hour passivation while they begin to vanish once the HCl is replaced (Figure 6-95). The following active dissolution following removes all sharp structure from the surface and leaves a smooth surface eventually.

The same situation is observed in the images scanned by a sharp silicon tip (Figure 6-96). The ledge structures which appear constantly in the sidewall in 1 hour passivation (Figure 6-96B and 6-96C) disappear under the active condition in 10 minutes (Figure 6-96D and 6-96E).

Figure 6-93 In-situ AFM images recorded from the GRY steel, showing the fine structure vanishing in passive stage, A) after 2.5 hour passivation and B) after 3 hour passivation.

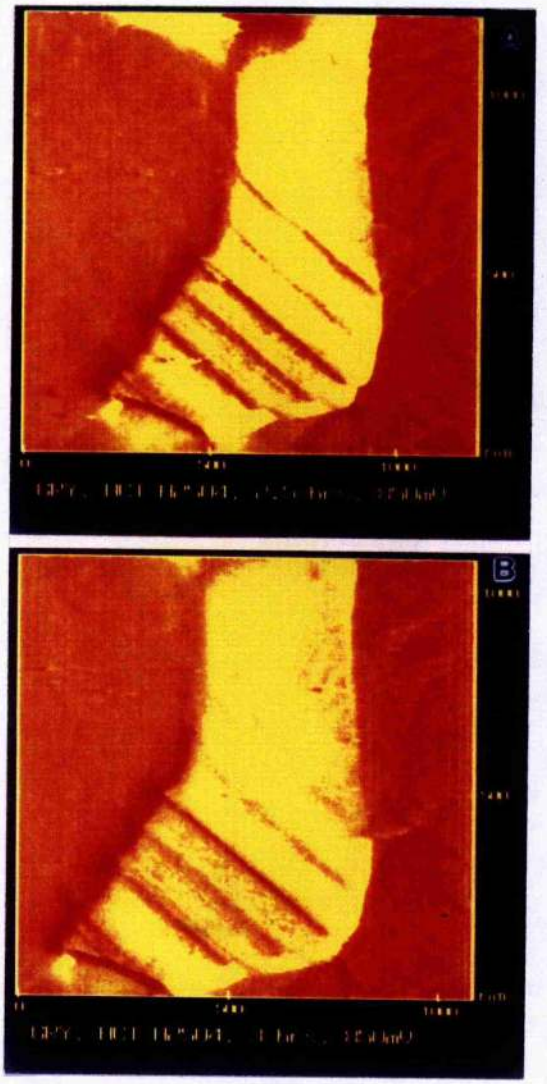

Figure 6-94 In-situ AFM images recorded from the GRY steel. It can be seen that most of the metal structures remain unchanged in the passivation, A) in HCl for 1 hr and in H_2SO_4 for 10 min, B) in HCl for 1 hr and in H_2SO_4 for 30 minutes and C) in HCl for 1 hr and in H_2SO_4 for 1 hr.

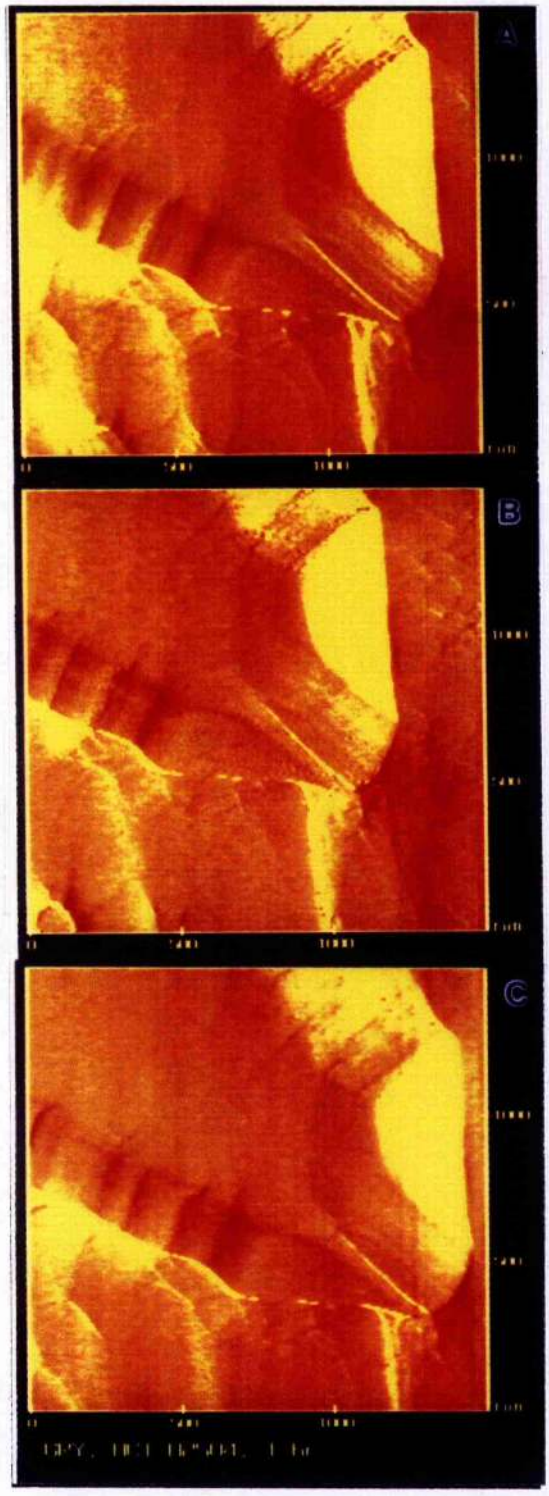

Figure 6-95 In-situ AFM images recorded from the GRY steel, A) in HCl for 1 hr, in H_2SO_4 for 1 hr and in HCl for 30 minutes B) in HCl for 1 hr, in H_2SO_4 for 1 hr and in HCl for 1 hr, and C) in HCl for 1 hr, in H_2SO_4 for 1 hr and in HCl for 1.5 hrs. The active dissolution after the passivation removes all the metal structures from the surface.

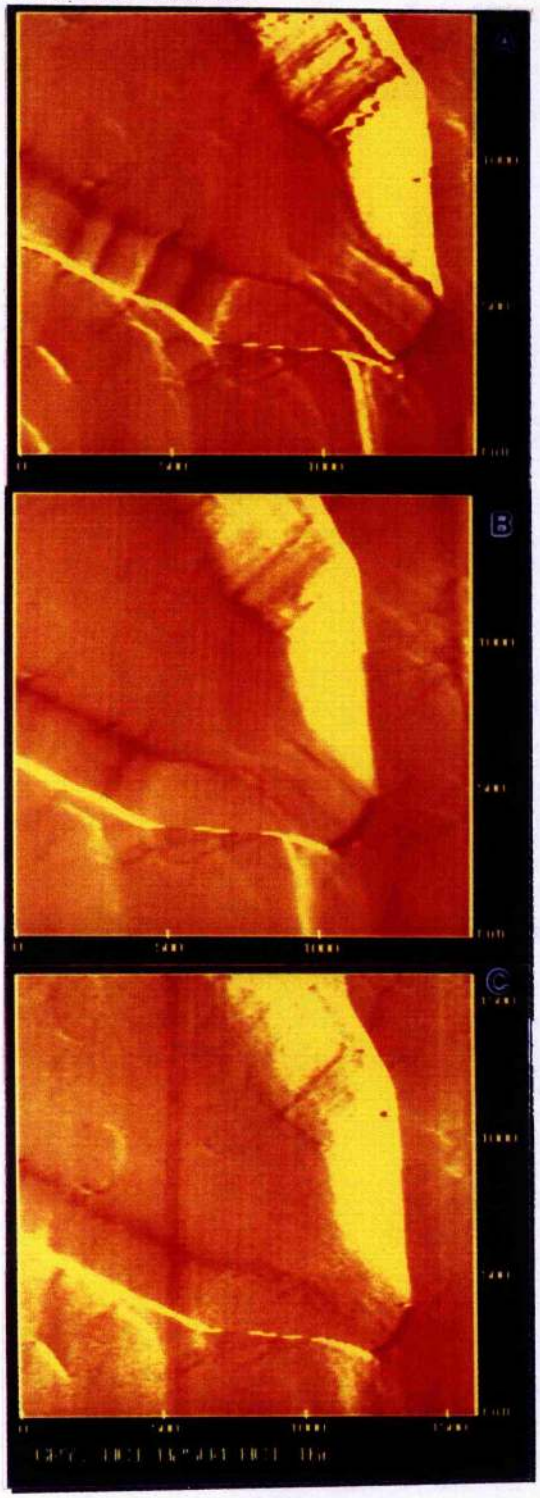

Figure 6-96 In-situ AFM images recorded from the GRY steel, A) in HCl for 1 hr, B) in HCl for 1 hr and in $H_2SO_4$for 30 minutes, C) in HCl for 1 hr and in $H_2SO_4$for 1 hr, D) in HCl for 1 hr, in $H_2SO_4$for 1 hr and in HCl for 10 minutes and E) in HCl for 1 hr, in $H_2SO_4$for 1 hr and in HCl 30 for minutes.

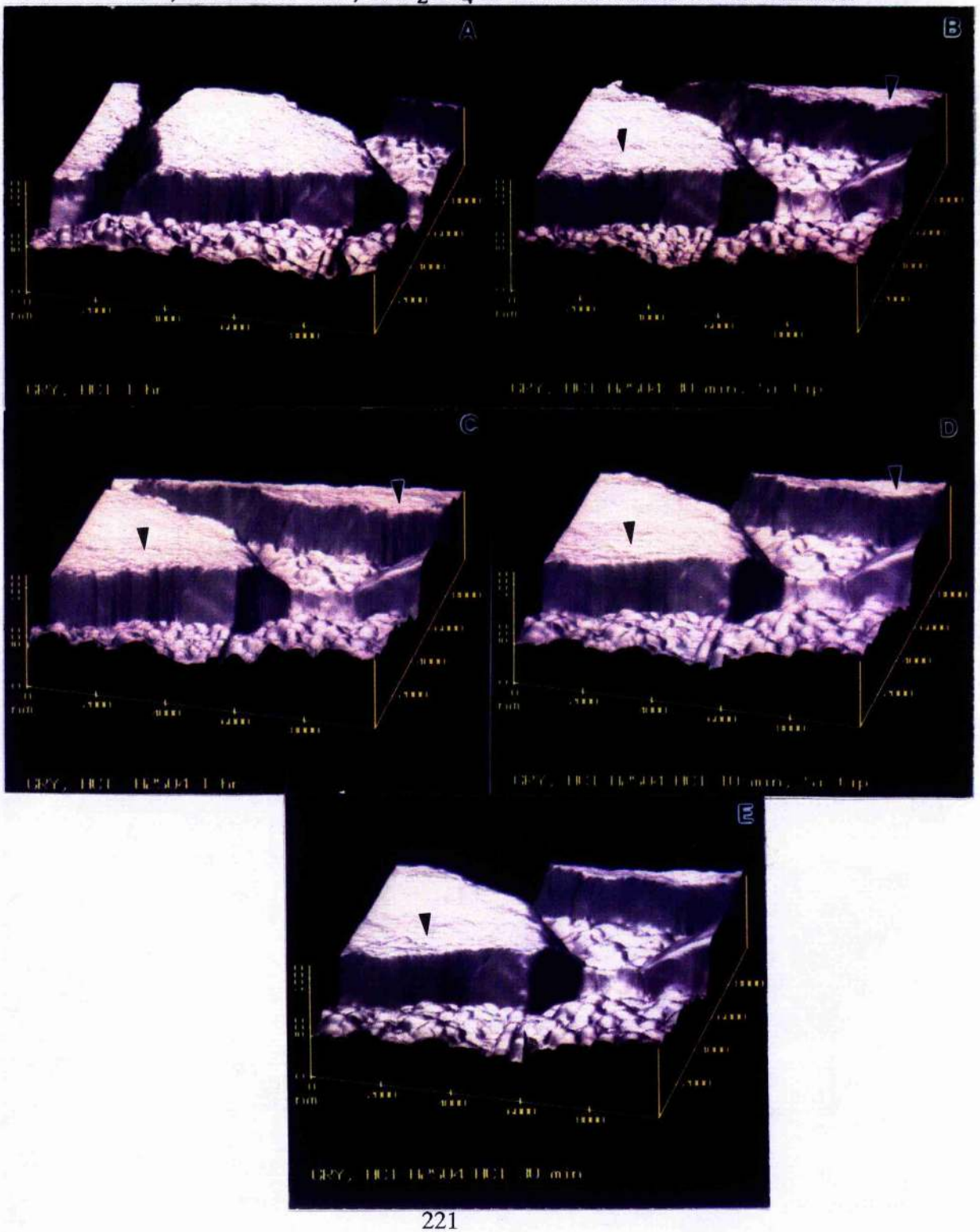

6.3.8 Discussion:

The structure appeared on the sidewall of the austenitic phase may be a low energy surface created by corrosion or a low energy structure created as the equilibrium phase boundary during metallurgical processing of these alloys, which merely revealed by corrosion. In order to examine whether such structures are present within the alloy, TEM was used to investigate the phase boundaries between the ferritic and the austenitic phase in the HCE duplex stainless steel (Figure 6-97). A fine parallel fringe contrast was found at an inclined austenite/ferrite interface and the similar appearance has been reported by Howell and Honeycombe (1984) in their studies of the similar alloys.

Figure 6-97 A TEM result showing the boundary of the ferritic and austenitic phases in the HCE steel.

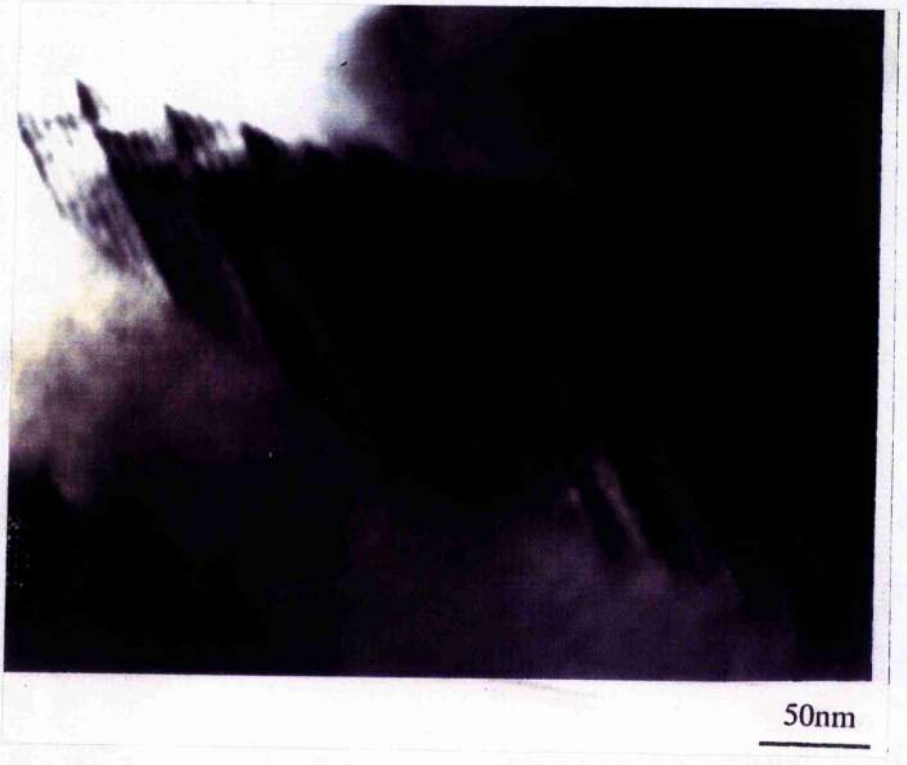

The fringe pattern consists of strong features at an interval of approximate 30 nm, which corresponds to the frequency of the finest steps on the boundary walls in the AFM micrographs. A high magnification image of AFM shows, very clearly, the correlation between the AFM and TEM results in Figure 6-98. Therefore, this boundary will be expected to be in a low energy configuration and the structures observed after corrosion are essentially pre-existing in the alloy boundaries.

Figure 6-98 An in-situ AFM image under high magnification, showing the structure on the boundary of the ferritic and the austenitic phase in the HCE steel, which is very similar to that observed in the TEM micrograph

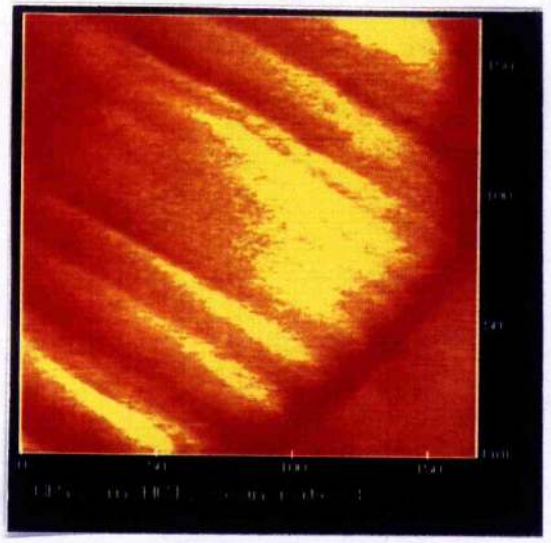

The removal of columnar grains and the loss of materials from the crystallographic step features possibly proceed from the formation and development of microcracks. These microcracks may be created by the selective dissolution of sub-grain boundaries, whose development permits the loss of the

layers from the triangular and similarly aligned surfaces.

In general corrosion, metal cations are more readily dissolved from an irregular area where the atom has fewer bonds than a flat area and the dissolution proceeds, therefore, from grain boundaries and emergent dislocations etc (Scully, 1975). Accordingly, the fading and the disappearance of the structures during the passivation and the subsequent active dissolution are the result of general corrosion. The change of the corrosion mode from selective dissolution to general corrosion in the dissolution-passivation-dissolution experiment may be associated with molybdenum exposed in the surface in the initial corrosion, but this suggestion need evidence to prove and it will be another topic to investigate how molybdenum works.

CHAPTER 7

CONCLUSIONS

In the passivation study, XPS and AFM were used to investigate the molybdenum role in the passivation of stainless steels. In order to establish the electrochemical condition where molybdenum exerts its great function, XPS analyses were carried out under different electrochemical conditions and the results show that when 516 alloy is anodically polarised in sulphuric acid, both molybdenum and chromium are enriched in the surface. Comparison of the molybdenum enrichment in a range of concentrations (0.05M, 0.1M and 0.5M) of sulphuric acid indicates that the molybdenum enrichment is more pronounced in the low potential region than in the high potential region and the greatest enrichment is obtained in 0.1 M sulphuric acid.

Close examination on surface molybdenum and chromium were then carried out in 0.1 M sulphuric acid and it is found that the enrichment of the both elements in the surface varies with potential in contrasting behaviour. Molybdenum enrichment factors clearly exceed those of chromium throughout the active region, the active/passive region and at the lower potentials of the passive

region. The peak value of molybdenum is at the low potential of the passive region close to Flade potential (-104 mV/SHE) where F(Mo) is 3, or molybdenum in the surface is three times higher than in the matrix. Correspondingly, the maximum concentraion of molybdenum oxide is also found at this potential. However, the molybdenum enrichment remains at the high value only in a limited potential region, so the value of the enrichment factors is lower at higher potentials of the passive region. On the contrary, the chromium enrichment in the surface increases steadily with potential and the maximum content is found at the high potential of the passive region, where F(Cr) is 3.2, though F(Mo) is only 1.9.

XPS measurment in the thickness of the passive film which is formed at the highest molybdenum concentration potential shows that after 1 hour polarisation, it is 1.3 nm thick.

Using AFM and in-situ AFM, the topography of the passive film and the kinetics of the passivation of 516 alloy were studied at the highest molybdenum concentration potential. It is found that on the passivation surface, a platelet layer is formed. The in-situ AFM study shows that the platelets generate at the early stage of the passivation and they will gradually merge into the passive film if they are not disturbed by the environment. TEM analysis shows that these platelets mainly consist of chromium oxide and molybdenum oxide. As they were only found in molybdenum-bearing alloy, their generation is most likely associated with the molybdenum nucleation function in passivation.

The model of the passivation of a molybdenum-bearing alloy based on the above results suggests : an initial active dissolution in passivation leads to an accumulation of metal ions in solution; molybdenum compound, as the first oxide

precipitates on the surface, seeds the chromium oxide from the supersaturated solution; by nucleating chromium oxide, the seeds grow up to be the big platelets seen on the high molybdenum/chromium ratio alloy, form the platelet barrier between the surface of the metal and the solution, and prohibit the dissolution of passive species from the metal surface; and they then facilitate the formation of the underlying passive film.

The tremendous influence of molybdenum in passivation is found in the initiation of passivation. The ability of molybdenum compounds to nucleate chromium oxide retains more chromium in the film both in the platelets and beneath the platelet layer. The molybdenum alloying element protects chromium steels against pitting corrosion, crevice corrosion and localised attack by assisting in nucleating chromium oxides at active sites where the alloy is dissolved with a high etching rate, i.e. to block the dissolution current and to facilitate the growth of the new passive film.

Another subject of this thesis is studying the kinetics of the corrosion of the duplex stainelss steels (GGR, HCE and GRY) in 10%wt HCl. It is found in the in-situ AFM studies that during the corrosion of duplex stainless steels in 10%wt HCl, the austenitic phase and the ferritic phase are differentiated by different corrosion rates. TEM and EPMA analyses show that the ferritic phase dissolves more rapidly than the austenitic phase in HCl. A copper deposition experiment determined that the ferritic phase is the anode toward the austenitic phase in the duplex stainless steels in this condition. Therefore, during the corrosion of duplex stainless steels, the ferritic phase is the sacrificed anode, which protects the austenitic phase by rapid dissolution.

The exposed austenitic phase in the duplex stainelss steels in corrosion shows sloping sidewalls with different gradients, and on the sidewall, there are crystalline structures, such as ledges, steps and triangular structures. These structures are pre-existing in the alloy for metallurgical reasons and they are revealed during the corrosion.

A study of corrosion kinetics by in-situ AFM shows that corrosion on the austenitic phases does not develop evenly and the preferential route of corrosion appears to be along grain boundaries, sub-grain boundaries and some planes with high energy.

The corrosion-passivation experiments show that the crystallographic features exposed in HCl mainly remain under the passivation condition except some fine features fading gradually. When the electrochemical condition changes back from the passivation to the active dissolution, the structures fade rapidly and they vanish eventually in the field of view. The change in behaviour of the surface may be associated with the irreversible electrochemical oxidation of species, perhaps molybdenum, which were present on the austenitic/ferritic interface revealed by the first expose to HCl.

Using AFM to study corroded rough surfaces is a new application of AFM. In this study, a large amount of work has been complished to identify the reality of the rough structure in AFM iamges. Several methods which were used here is very useful for the future AFM study:

1. Measuring the angles of sidewalls: when the angle of the sidewall plus the half angle of the tip less than 90°, the gradient of the sidewall and the structure on the

sidewall is not the tip image.

2. Measuring the angle of the sidewalls at different positions in height mode scans: if the angle of the sidewall changes at different positions, the angle of the feature in the image is not the tip angle.

3. Scaning the feature in different directions: if the feature shows the same appearence when it is scanned by different tip surface, the feature appearence in the image is not the tip image.

4. Scanning the feature using different tips: if the feature shows the same appearence when it is scanned by different tips, it is not the tip image.

5. If possible, comparison of the AFM image and the corresponding SEM micrograph can provide evidence for identifying the reality of the structrue in the AFM image.

CHAPTER 8

SUGGESTIONS FOR FUTURE WORK

The role of molybdenum in passivation of stainless steels has been discussed in this study. Though the platelets have been observed repeatly throughout the study of 516 alloy, they have not been found readily in high chromium content alloys i.e. duplex stainless steel containing about 3% molybdenum and more than 20% chromium. The difference may be caused by two possible reasons: 1) the chromium oxide film is self-nucleated because of the generally higher level of chromium and 2) the molybdenum oxide nuclei are buried in the passive film before they grow big enough to be observed, again because of higher concentration of chromium ions on the surface of these alloys. The precise mechanism of oxide nucleation on these high chromium alloys might be identified by future work using AFM.

The experiments involving a sequence of corrosion and passivation show that when corrosion conditions were re-established following passivation the selective dissolution of crystallographic structure changed into general corrosion. This phenomenon is noted for the first time in this work. There are also two

possibilities for the interpretation: 1) the appearance of crystallographic structures in the first exposure of the sample surface to HCl is evidence in support of molybdenum atoms blocking dissolution sites. The loss of the crystallographic structures would then correspond to the loss of these key atoms, perhaps by oxidation of molybdenum during the passivation of the surface, and 2) the selective dissolution in the first exposure in HCl is caused by the thermodynamic selection along the grain boundaries and sub-grain boundaries. The molybdenum oxide produced at the active sites at the early stage of passivation prohibits the boundary dissolution, so when the corrosion medium is changed back to HCl, this local passivation remains and general corrosion is observed for a relatively long time in HCl. In future work, Auger analysis on the phase boundaries at every individual stage (corrosion, passivation, corrosion and repassivation) would enable the mechanism of this phenomenon to be determined.

In the corrosion-passivation experiments, it was also found that when the sample surface returned to the conditions for active corrosion from passivation, the passive film was not dissolved as rapidly as described in some literature citations. In contrast, the passive film seems to stay on the surface for a rather long time. As it is shown in Figure 88 and Figure 89, the passivated duplex stainless steel does not show obvious change in HCl for 1 hour though it changed rapidly before passivation. A similar situation was also found when the steel was passivated in air. This phenomenon leaves a topic for the further study in the investigation of the driving force for the reversal of passivation.

During the current study of the passivation of 516 alloy, a structureless passive film under the platelet layer was found. Therefore, apart from the mechanism of dissolution and precipitation, the other process in which chromium

oxide may form by the direct reaction with water or O_2 at the interface of metal and solution must continue to be researched. The local increase of pH value, which was discussed early in this thesis may facilitate this process, i.e. the anodic surface reaches the Cr_2O_3 region during the passivation, so chromium forms chromium oxide directly on the surface. In future work, the measurement of the gradient of pH value in the vicinity of the surface will provide strong evidence to support the above suggestion.

In addition to molybdenum, nickel is also another important alloying element which benefits the passivation of stainless steels. Although the role of nickel in passivation has been studied by the previous work of this laboratory, AFM study in the future work will give more evidence and may modify the model for the role of nickel in passivation. The above research work may lead to the new finding of the coordinated function of molybdenum, chromium and nickel in passivation and it will approach the aim of obtaining a full understanding of the passivation of stainless steels.

REFERENCE

Albrecht T R, 1989, Advances in atomic force microscopy and scanning tunneling microscopy. Ph.D. Dissertation, Stanford University, Stanford, CA

Albrecht T R and Quate C F, 1987, J.Appl. Phys. **62**, p 2599

Alexander S, Hellemans L, Marti O, Schneir J, Elings V, Hansma P.K, Longmire M and Gurley J, 1989, J.Appl. Phys. 65, 164

Allen M J, Hud N V, Balooch M, Tench R J, Siekhaus W J & Balhorn R,, 1992 Tip-induced artefacts in AFM images of protamine-complexed DNA fibers. Ultramicroscoopy, 42-44, 1905-1100

Ambrose J R, 1978, in Passivity of Metals (Edited by R.P.Frankenthal and J.Kruger), pp 740-748, Electrochem. Soc. Princeton

Amer N M and Meyer G, 1988, Bull. Am. Phys. Soc. 33, 319

Armstrongm R D, 1971, Corros. Sci., 11, 693-697

Asami K, De Sa M S, and Ashworth, 1986, Corr. Sci., 26, 15

Asami K, Hashimoto K and Shimodaira S, 1976 Corros, Sci. vol.16, pp387-391

Asami K, Hashimoto K and Shimodaira S, 1978 Corros, Sci. vol.18, pp151

Asami K, Naka M, Hashimoto K and Masumoto T, 1980, J.Electrochem.Soc. 127, 2130

Azzerri N et al, 1982, Corr. Sci., v22, no7, p675

Baer D R and Thomas M T, 1982,"Use of Surface Analytical Techniques to

Examine Metal Corrosion Problems" In: Casper & Powell ed. "Industrial Applications of Surface Analysis" p251-282, American Chemical Society,Washington,D.C.

Berneron R, Charbonnier J C, Namdar-Irani R and Manenec, 1980, J. Corros, Sci. **20**, 899

Bernhardsson S, Mellström R, Oredsson J, 1981 "Properties of Two Highly Corrosion Resistant Duplex Stainless Steels", Papper No 124, NACE Corrosion/81, Tooronto, Ontario, Canada, April 1981.

Bernhardsson S, Duplex Stainless Steels '91, 28-30 October 1991, Beaune Bourgogne, France, Vol.1, Edited by J.Charls-S.bernhardsson

Binnig G, Quate C F and Gerber C, 1986, Phys.Rev.Lett. 56, 930

Binnig G, Rohrer H (1982) Scanning tunneling microscope. Helv. Phys. Acta **55**, 726-735

Bockris J O'M and Reddy A K N, 1970, Modern Electrochemistry Vol.2, P1317 Plenum Press, New York

Bond A P et al, Corrosion/85, paper 68, NACE, Houston Texas

Brandis H and Kiesheyer H, 1985, Stainless Steels '84, The Institute of Metals, London, p217

Briggs D and Seah M P, 1987, Practical Surface Analysis by Auger and X-ray Photoelectron Spectroscopy, John Wiley & Son Ltd., Chichester, p181-214

Brooks A R, Clayton C R, Doss K and Li Y C, 1986, J. Electrochem. Soc., Vol 133, 2459

Cahoon J R and Bandy R, 1982, Corr. NACE **38**, 299

Calinski C and Strehblow H H, 1989, J. Electrochem. Soc., Vol. 136, p1328

Charbonnier J C, Maitrepierre Ph, Noual P and Namdar-Irani R, 1977, 7th Proc. Int. Vac. Congr. 3rd Int. Conf. Solid Surf. pp 2375-2378

Castle J E, 1977, Surface Science 68, pp, 583-602

Castle J E 1980 "Applied Surface Analysis ASTM STP699", ed. Barr T L and Davis L E, Am. Soc. Test.Mat.

Castle J E, Abu-Talib I and Richardson S A, 1985, Mat. Res. Soc. Symp. Proc.

Vol. 48, Materials Research Society

Castle J E, Ke R and Watts J F, 1990[1], Corrsion Science, Vol 30, no 8/9, pp 771-798

Castle J E and Qiu J H, 1989, Corro. Sic. 29, No.5, pp591-603

Castle J E and Qiu J H, 1990, J. Electrochem. Soc., 137,2031-2038

Clayton C R and Lu Y C, 1986, J. Electrochem. Soc., 133, No.12 2465-2473

Cunha Belo M da, Rondot B, Pons F, Hericy J Le and Langeron J P, 1977, J. Electrochem. Soc., **124**, p1317

Davison R & Redmond J, 1990, Practical Guide to Using Duplex Stainless Steels. Materials Performance, p57, Jan.

Drake B, Prater C B, Weisenhorn A L, Gould S A C, Albrecht T R, Quate C F, Cannell D S, Hansma H G and Hansma P K, 1989, Science 243, 1586

Degerbeck J, Karlsson a and Berglund G, 1979, British Corrosion Journal, v14, p220

Eckenrod J J and Kovach C W, Properties of Stainless Steels and Their Weld Metals, ASTM, STP 679, Philadelphia PA, p17.

Ericson C, 1988, "The first Years of the Duplex Staianless STeels", Bergsmannen 6, p 255 (in Swedish)

Evans U R, 1927, J. Chem. Soc. (London), 1020

Evans U R, 1960, The Corrosion and Oxidation of Metals, London, Edwl. Arnold

Faraday M, perinted in 1965, "Experimental Researches in Electricity, Vol.2, pp.234-250. Dover Pub. New York

Flade F, 1911, Z. Phsik. Chem.,76, 513

Fontana M G and Greene N D, 1967, Corrosion Engineering, McGraw-Hill, 337

Franck U F, 1949, Z. Naturforsh., 49, 378

Galvele J R, Lumsden J B and Staehle R W, 1978, J. Electrochem. Soc., **125**, 1204
Gise P and Smith I, 1992, review the cooperating princples and characteristics of the contacting and non-contacting versions of AFM and STM, European Semiconductor, Sept. 1992, p22-24

Gmelin, 1929-1932, "Heandbuch der Anorganischen Chemie", Teil 59A, P313,Berlin

Goetz R and Landolt D, 1982, Electrochimica Acta. **27**, 1061

Goetz R and Landolt D, 1984, Electrochimica Acta. 29 No.5 667-676

Gould S A C, Drake B, Prater C B, Weisenhorn S M, Kelderman G L, Butt H-J,

Grütter P, Zimmermann-Edling W & Brodbeck D, 1992, tip artefacts of microfacbricated force sensors for atomic force microscopy. Apply. Phys. Lett.. 60,.2741-2743

Haber F, 1904, Z. Elekrochem.,10, 697

Halada G P and Clayton C R, 1991, J. Electrochem. Soc. 138, 2921
Hansma H, Hansma P K, 1990, Ultramicroscopy, 33, 93-98, North-Holland

Hashimoto K, Asami K and teramoto K, 1979[1], Corros. Sci., 19, 3-14

Hashimoto K, Naka M, Asami K and Masumoto T, 1979[2], Corros. Sci., 19, 165-170

Heathcote H, 1907, J.Soc. Chem. Ind. (London), 26, 899

Hellemans L, Waeyaert K & Hennau F (1991) Can atomic force microscopy tips be inspected by atomic force microscopy? J. Vac. Sci.. Technol. B, 9, 1309-1312

Hertz H, 1887, Ann.Physik. 31, 983

Howell P R and Honeycombe R W, (1984), p339, in "Crystallographic Aspects of Diffusional Phase Transformations in Metals and Alloys", ed: Aoronson H.I, TMS-MIME, Warrendale, PA

Jahanmir J, Haggar B G and Hayes J B, 1992, scanning Micorscopy, Vol. 6, No. 3 p625-660

Keller D, 1991, Sur. Sci. 253, 353

Keller D, Deputy D, Alduino A and Luo K, 1992, Ultrmicrosccopy 42-44, 1481-1489

Kruger J, et al, 1990, Corr. Sci., v31, p111

Langmuir I, 1916 Trans. Electrochem. Soc., **29**, 260

Leygraf C, Hultquist G, Olefjord I, Elfstrom B-O, Knyazheva V M, Plaskeyev A V and Kolotyrkin Ya M, 1979, Corros, Sci. **19**, 343

Lumsden J B, 1978, in Passivity of Metals (Edited by R.P.Frankenthal and J.Kruger), pp.730-739, Electrochem. Soc., Princeton

Lumsden J B and Staehle R W, 1972, Scripta Metallurgica **6**, 1205

Lumsden J B and Staehle R W, 1976, Passivaty: Its Breakdown: Iron Iron Base Alloys (Edited by Staehle R W and Okada H), U.S.A.-Japan Semin. 1975, pp 75 and 76

Mahla E M and Nielsen N A, 1948, Trans. Electrochem. Soc., **93**, 1

Maivald P, Butt H J, Gould S A C, Prater C B, Drade B, Gurley J A, Elings V B and Hansma P K, 1991, Nanotechnology 2, 103-106, Printed in the UK

Mamin H J, Rugar D, Sterm J E, Terris B D and Lambert S E, 1988, Appl. Phys. Lett. 53, p1563

Marcus P and Charbonnier J C, 1981, J. Microsc. Spectrosc. Electron. **6**, 329

Marcus P and Herbelin J -M, 1993, Corrosion Science, Vol 34, No 7, pp 1123-1145

Marcus P and Olefjord I, 1988, Surface and interface analysis, Vol 11, 569-576

Marti O, Drake B, Gould S and Hamsma P K, 1988, J. Vac. Sci. Technol. 6, 287

Marti O, Drake B and Hansma P K, 1987, Appl. Phys. Lett. 51, 484

Martin Y, Williams C C, Wickramasinghe H K, 1987, J. Appl. Phys., 61, p4723

Matsuda S, Kikuchi T and Sugimoto K, Corr. Sci., v31, 1990, p161

McBee C L and Kruger J, 1972, Electrochim.Acta, 17, 1337

McClelland G M, Erlandsson R, Chiang S, 1987, in "Review of Progrss in Quantitative Nondestructive Evaluation", vol.6B, p307, Thompson.D.O, Chimenti.D.E eds., Plenum, New York

Meisel W, Stumm U and Gutlich P, 1988, Surface and interface analysis, 12, 430

Meyer G and Amer N M, 1988, Appl. Phys. Lett. 53 1045

Meyer E, Heinzelmann H, Grütter P, Jung T, Weisskopf T, Hidber H R, Lapka

R, Rudin H and Güntherodt H J, 1988, J Microscopy, **151**, 268

Mischler S, Mathieu H J and Landolt D, 1988, Surf. INterf. Anal., Vol 11, p182

Mischler S, Vogel A, Mathieu H J and Landolt D, 1991, Corrosion Science, Vol.32, No.9. pp 925-944

Miyasaka A and Ogawa H, 1990, Corr. Sci., v31, p99

Monnartz P, 1911, Metallurgie, 8, 161

Müller W J, 1927, Z. Elecktrochem., 33, 401

Nordling C, Sokolowski E and Sieghahn K, 1958, Ark. Fys., 13, 483

Ogawa H, Omata H, Itoh I and Okada H, 1978, Corr. NACE, **34**, 52

Okamoto G, 1973, Corros, Sci. 13, 471

Olefjord I, 1980, Materials Science and Eng., 42, 161-171

Olefjord I and Elfstrom.B-O, 1982, Corrosion-Nace, 38, No1, 46-52

Olefjord I and Brox B, 1983, in Passivity of Metals and Semiconductors, Froment M, Editor, p561, Elsevier, Amsterdam

Olefjord I and Wegrelius, 1990, Corr. Sci., v31, p89

Olivier R, 1955, 6th meet. Int. Comm. Electrochem. Thermodynamics and Kinetics, Poitiers, France, Butterworth, England, 312

Oshe E K and Rosenfeld I L, 1975 Extended Abst. 6th ICMC-Sydney No. 1-23

Pourbaix M, 1945, thesis, Delft and Brussels

Qiu J H, 1989, Thesis, Univerisity of Surrey, p 220.

Rhodin T N, 1956, Corrosion No12 123t

Rondot B, Pons F, Hericy J Le, Cunha Belo M da and Langeron J P, 1975, Vide **20**, 70

Roscoe C V, Gradwell K J, Watts M and Nisbet W J, Stainless Steel '87, 1988, The Institute of Metals, London, p87

Rugar D and Hansma P, 1990, Physics Today, Oct. p23-30

Sarid D, 1991 "Scanning Force Microscope", Oxford University Press, New York

Sato N, Kudo K and Noda T, 1975, Z.Phys.Chem., N.F.,98, 271

Schwarz U D, Haefke H, Reimann P & Güntherodt H-J, 1994, J. of Micorscopy, Vol.173, Pt 3, 183-197

Scully J C, 1975, "The Fundamentals of Corrosion" 2nd edition, Pergamon Press oxford.

Seah M P and Deanch W A, 1979, Quantitative electron spectroscopy of surfaces: a standard data base for electron inelastic mean free paths in solids, Surf. Interf. Anal., **1**, 2-11

Sedriks A J, 1979, Corrosion of Stainless Steel, John Wiley & Sons, New York p56

Siegbahn K, ed Beta and Gamma-Ray Spectroscopy, North Holland, Amsterdam (1957), revised 1965

Smith D P E aned Binnig G, 1986, A piezoelectric tube-translator, Rev.Sci.Instr. 57, p2630

Sogimoto K and Sawada Y, 1977, Corros. Sci. **17**, 425

Soulignac P and Dupoiron F (1990) Duplex Stainless Steel, Past, Present and Future, Stainless Ssteel Europe, June, p18. Thum, E (1935) Handbook of Stainless Steels, ASM, Clleveland, Ohio, USA

Stranski I and Mutafschiew Z, 1929, Z. Electrochem., 35, 393

Stout D A, Lumsden J B and Staehle R W, 1979, Corr. Nace 35, 141

Sugimoto K, Stainless Steel '84, p198

Sugimoto K and Matsuda S, 1988, Stainless Steel '87, The Institute of Metals, London, p 201

Suutala N and Kurkela M, 1985, Stainless Steel'84, Ihe Institute of Metals, 1985, p240.

Sugimoto K and Sawada Y, 1977, Corros.Sic. 17, 425-445

Thurn E E, ed., 1935, Handbook of Stainless Steels, ASM Cleveland, Ohio, USA

Tomashov N D and Chernova G P, 1967 "Passivity and Protection of Metals Against Corrosion", Plenum Press, New York

Tronstad L and Borgmann C, 1934, Trans. Faraday Soc., 30, 349

Truman J E et al, 1977, Br. Corr. J., v12, p236.

Uhlig H H, 1948, Corrosion Handbook, Wiey, New York, p20-30

Uhlig H H, 1971, Corrosion and Corrosion Control, 2nd Edition, John Wiley & Son Inc., New York, p51

Uhlig H H, 1978, "History of Passivity Experiments and Theories" In: Frankenthal.R.P and Kruger.J, ed. "Passivity of Metals" 6, The Electrochem. Soc. Inc., Preston

Wagner C D, Riggs W M, Davis L E, Moulder J F, Muilenberg G E (Editor), 1979, "Handbook of x-ray photoelectron spectroscopy", Perkin-Elmer Corporation, Physical Electronics Division, Minnesota

Wagner C and Traud W, (1938), Z. Electrochem., Band 44, p391

Watts J F, 1990, "An Introduction to Surface Analysis by Electron Spectroscopy", Oxford University Press. Royal Microscopical Society

Whitney W R, 1903, J.Am.Chem.Soc., Vol.25, p394

Wolter O, Bayer T H, Greschner J, 1991, micromachined silicon sensors for scanning force microscopy. J. Vac. Sci. Technol. B9, 1353-1357

Yang W P, Costa D and Marcus P, 1994[1], J.Electrochem. Soc., Vol.141, No.10, p2669-2676

Yang W P, Costa D and Marcus P, 1994[2], J.Electrochem. Soc., Vol.141, No.1, p111-116

Yaniv A E, Lumsden J B and Staehle R W, J. electrochem. Soc. **124**, p490

Zhang Wenqi, Metal Corrosion Handbook,p39 Shanghai Science and Technology Publishing, Shanghai, 1987

APPENDIX

PUBLICATIONS AND PRESENTATIONS

J E Castle, X F Yang and P Zhdan, "Atomic Force Microscopy studies on passivation of FeCrMo alloy", The 33rd Corrosion Science Symposium, Oxford, 9-11 September, 1992.

J E Castle, X F Yang, J H Qiu and P Zhdan, " Modifications of Passive Films - papers presented at the European Symposium on Modifications of Passive Films", in Paris, France 15-17 February 1993, Eds P Marcus, B Baroux and M Keddam, published by the Institute of Materials, p70-75.

J E Castle, X F Yang, "XPS and AFM Studies of Role of Mo in the Passivation of Stainless Steel", presented at the research colloquium of the Department of Materials Science & Engineering , University of Surrey, 29, June, 1993.

J E Castle, X F Yang, "the Role of Mo in Passivation of Iron/Chromium Alloys" the paper has been accepted by "Corrosion Science".

J E Castle and X F Yang " Does Viscous Drag Make a Noticeable Impact on Spacial Resolution in AFM of Surfaces Immersed in Aqueous Media?", the paper was presented at Quantitative Surface Analysis-Eighth International Conference

(QSA-8), Surrey, U.K.23-26 August 1994.

J E Castle, X F Yang and P A Zhdan "In-situ AFM and SEM Study of Active Corrosion of Duplex Stainless Steel in HCl" the paper was presented at The 35th U.K. Corrosion Science Symposium, Manchester, 21-23 September, 1994.

J E Castle, X F Yang and K Prosser "AFM Studies of the Repassivation of Molybdenum Containing Duplex Steels", the paper was presented at International Symposium on Localized Dissolution and Corrosion, Pennsylvania, 3-6, October, 1994.